306319513V

Seismic Source Parameter Determination Using Regional Intermediate-Period Surface Waves

by

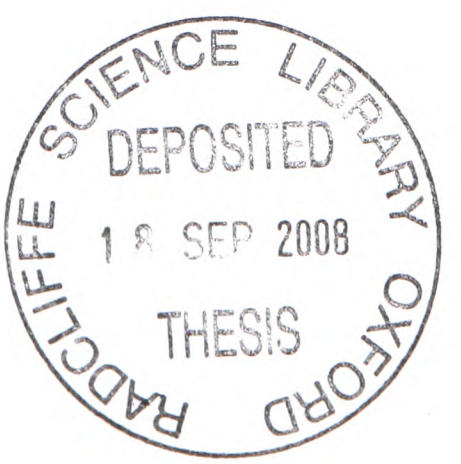
Benjamin Daniel Fox

Thesis submitted to the University of Oxford
for the degree of Doctor of Philosophy



Department of Earth Sciences & Exeter College
University of Oxford
Trinity Term, 2007

Supervisors:
Professor John Woodhouse & Dr Neil Selby



"The lecturer should give the audience full reason to believe that all his powers have been exerted for their pleasure and instruction."

Michael Faraday (1791–1867)

Seismic Source Parameter Determination Using Regional Intermediate-Period Surface Waves

Benjamin Daniel Fox

Department of Earth Sciences & Exeter College

University of Oxford

Trinity Term, 2007

Abstract

In general, the depths of shallow earthquakes are poorly resolved in current catalogues. Variations in depth of ± 10 km can significantly alter the tectonic interpretation of such earthquakes. If the depth of a seismic event is in error then moment tensor estimates can also be significantly altered. In the context of nuclear-test-ban monitoring, a seismic event whose depth can be confidently shown to exceed say, 10 km, is unlikely to be an explosion.

Surface wave excitation is sensitive to source depth, especially at intermediate and short periods, owing to the approximate exponential decay of surface wave displacements with depth. The radiation pattern and amplitude of surface waves are controlled by the depth variations in the six components of the strain tensor associated with the surface wave eigenfunctions. The potential exists, therefore, for improvements to be made to depth and moment tensor estimates by analysing surface wave amplitudes and radiation patterns.

A new method is developed to better constrain seismic source parameters by analysing 100–20 s period amplitude spectra of fundamental-mode surface waves. Synthetic amplitude spectra are generated for all double-couple sources over a suitable depth range and compared with data in a grid-search algorithm. Best fitting source parameters are calculated and appropriate bounds are placed on these results.

This approach is tested and validated using a representative set of globally-distributed events. Source parameters are determined for 14 moderately-sized earthquakes ($5.4 \leq M_{\mathrm{w}} \leq 6.5$), occurring in a variety of tectonic regimes with depths calculated between 4–39 km. For very shallow earthquakes the use of surface wave recordings as short as 15 s is shown to improve estimates of source parameters, especially depth.

Analysis of aftershocks ($4.8 \leq M_{\mathrm{w}} \leq 6.0$) of the 2004 great Sumatra earthquake is performed to study the depth distribution of seismicity in the region. Three distinct tectonic regimes are identified and depth estimates calculated between 3–61 km, including the identification of one CMT depth estimate to be in error by some 27 km.

Seismic Source Parameter Determination Using Regional Intermediate-Period Surface Waves

Benjamin Daniel Fox

Department of Earth Sciences & Exeter College

University of Oxford

Trinity Term, 2007

Extended Abstract

In general, the depths of shallow earthquakes are poorly resolved in current catalogues. The reliable constraint of shallow source depths is crucial in seismo-tectonic studies of deformation in the Earth's crust, and seismic discrimination studies of the depth and nature of suspect seismic events.

Surface wave excitation is sensitive to earthquake depth, especially at intermediate and short periods, due to the approximate exponential decay of surface wave displacements with depth. The radiation pattern and amplitude of surface waves are controlled by the depth variations in the six components of the strain tensor. Therefore the potential exists for improvements to be made to depth and moment tensor estimates by analysing surface wave amplitudes and radiation patterns.

The accurate modelling of fundamental-mode surface wave amplitude spectra has long been known to provide constraints on source depths as well as focal mechanisms. In particular, frequency-dependent notches in the Rayleigh wave amplitude spectra have been previously identified as containing important information about seismic source depth.

A method is presented here for estimating seismic source parameters from recordings of intermediate-period (100–20 s), fundamental-mode surface waves. Rayleigh and Love waves are identified and isolated from other arrivals in regional station recordings using predictions of group arrival times calculated using a 3-D Earth model.

Synthetic seismograms are generated by determining local modes of oscillation at the source and receiver. For the path term, the propagation contribution is calculated by integrating the phase velocity along the great circle path through the Earth model. Synthetic amplitude spectra are generated for all double-couple sources over a suitable depth range and compared with those isolated from data recordings in a grid-search algorithm. Best fitting amplitude spectra are selected by calculating the minimum least-squares misfit in log amplitude space and an F-test is performed over all solution space to calculate the global range of statistically acceptable source parameters.

Due to the 180° symmetries in strike and rake of the surface wave amplitude radiation pattern, the

best fitting synthetic amplitude spectra can be generated by one of four possible source mechanisms. 100–50 s waveform comparisons, incorporating source phase information, are performed to identify the optimum mechanism. Typically, at depths greater than 10 km this is a definitive procedure, but at shallower depths, where the resolution of two components of the seismic moment tensor is poor, an ambiguity arises and the selection of a focal mechanism has to be guided by other results and independent geological observations.

Events previously studied by other methods have been chosen to help develop, test and validate these new methods of surface wave analysis. Seismic source parameters are determined for 14 moderately-sized earthquakes ($5.4 \leq M_{\mathrm{w}} \leq 6.5$) and are shown to be in agreement with the results of previous studies. Depths are generally well constrained, especially for shallow sources and in the instances where frequency-dependent notches appear in the recorded Rayleigh wave amplitude spectra. The fault plane solutions determined here describe a wide variety of faulting styles, attributable to the various tectonic regimes in which the earthquakes are located. Confidence in these results emanates from the wide variety of studies that are used as comparisons, including the Harvard and USGS centroid catalogues, long-period body-wave modelling, relocated aftershocks, InSAR, GPS, strong-motion studies and observations of surface ruptures in the field.

Depths are calculated in the range 4–39 km and for deep crustal earthquakes reliable source parameter estimates can be made using amplitude spectral observations at periods greater 20 s. However, for very shallow sources it is demonstrated that the addition of periods as short as 15 s can significantly improve the resolution of seismic source parameters. In the case of the 2004 Parkfield earthquake, the use of these shorter periods is shown to be necessary in calculating trustworthy estimates of the centroid depth and in determining a style of faulting consistent with that observed on the San Andreas Fault.

Aftershocks of the great 2004 Sumatra earthquake provide an opportunity to study a suite of earthquakes with varying depths and consistent data coverage, as they occurred over a short space of time. Source parameters are determined for 16 events ($4.8 \leq M_{\mathrm{w}} \leq 6.0$) and these earthquakes are found to exhibit a wide range of faulting styles with depths calculated between 3–61 km. Three distinct regimes of seismicity are identified, including the Offshore Banda Aceh region where the relocation of eight, similarly-oriented, aftershocks demonstrate the improved depth estimates provided by this method compared to those in the CMT catalogue. In particular, the determination of one CMT depth estimate to be in error by some 27 km further highlights the merit of this approach.

Where a good azimuthal distribution of receivers is not available, the ability of this method to determine source parameters is not significantly affected. The insensitivity of the Love wave radiation pattern to source depth is clearly demonstrated; when used exclusively, Love wave recordings do not constrain depths or focal mechanisms. Synthetic seismograms, generated to cut-off periods below

50 s, are shown to provide close matches to the recorded waveforms to at least 30 s; no improvement, however, is seen in the resolution they afford when used in waveform comparisons.

The Earth model used in the calculation of synthetic seismograms and the prediction of the dispersive surface wave arrivals is analysed and shown to accurately represent the local velocity structure of the Earth. Predictions of peak group velocity arrival times are found to be in general agreement with those observed at regional stations and synthetic seismograms generated at periods as short as 30 s period compare favourably with recorded waveforms. The analysis of earthquakes occurring on three separate continents highlights the applicability of this model to the study of global seismic events.

The determination of trustworthy source parameters for seismic events shallower than 10 km, especially with the addition of shorter-period data, demonstrates the value of the method presented here. It is anticipated that the accuracy, especially at shallow depths, of seismo-tectonic studies and seismic discrimination investigations can be greatly increased by the application of this source parameter determination methodology.

Acknowledgements

Firstly, I would like to thank John and Neil for their supervision over the past 4 years. They have consistently provided me with support, guidance and above all else, enthusiasm for this project, and for that I am extremely grateful. I would also like to thank Ana Ferreira for the help she provided at the start of this project. Ana was a constant 'source' of help over the first two years of this study and I am grateful to her for the time and patience she afforded me in the early days. Thanks also to my examiners, Barry Parsons and Keith Priestley, who have provided the necessary constructive criticism of this thesis.

My time in the department has been enhanced through discussions of varying natures with my colleagues in the Seismo-lab^{TM}, be they political (Ross), pedantic (Kit), linguistic (Ana), argumentative (Eoin), feministic (Anna), unprintable (Dave), class-related (Anneka), technical (Andrew) or, on occasions, seismological ('Baby' Dave). Those who kindly proof read the initial drafts of this thesis and provided helpful comments can take a bow. In addition, as my college supervisor, Shamita Das has always taken a keen interest in my progress here and has provided invaluable updates on the latest test match score. Elsewhere in the department, I am grateful to those who have provided me with both technical and administrative support.

As well as providing financial and scientific assistance, I am grateful to all the staff at AWE Blacknest for their help and encouragement over the course of this studentship.

I'd like to thank all my family for their support during my time here, especially my parents who have made many sacrifices for me over the years. I'll always be grateful to them despite their insistence that "We didn't send you to a good school so you'd try and become an academic!".

A final 'thank you' to everyone else who has enhanced and enriched my life in Oxford and have helped this work to be completed over time and over budget... especially those in Park End.

Declaration

The contents of this thesis are all my own work, except where otherwise stated. The views and opinions expressed herein are mine and not necessarily those of any person or body unless so attributed.

Contents

Abstract i
Extended Abstract ii
Acknowledgements v
Declaration vi
Table of Contents vii
List of Figures xi
List of Tables xiv

1 Introduction **1**
1.1 Overview 1
1.2 Depth Determination Techniques 2
1.3 Previous Surface Wave Studies 3
1.4 Surface Wave Amplitude Spectra 4
1.5 Seismic Discrimination 5
1.6 Depth Distribution of Earthquakes 6
1.7 Thesis Outline 7

2 Method **9**
2.1 Overview 9
2.2 Synthetic Seismograms 11
2.2.1 Theory 11
2.2.2 Local Modes 14
2.2.3 Implementation 19
2.2.4 1-D Earth Seismograms 23
2.2.5 3-D Earth Seismograms 23
2.3 Isolating the Fundamental-Mode Arrivals 27

2.3.1 Data Selection 27
2.3.2 Frequency-Time Analysis and the Multiple Filter Technique 28
2.3.3 Phase-Matched Filtering 30
2.4 Source Parameter Determination 34
2.4.1 Amplitude Spectral Modelling 34
2.4.2 The Search for Optimal Source Parameters 36
2.4.3 Source Parameter Constraints 44
2.5 Summary 48

3 Validation **51**
3.1 Overview 51
3.2 1999 South Xinjiang, China, earthquake (013099A) 54
3.2.1 Introduction 54
3.2.2 Previous Studies 55
3.2.3 Results 55
3.3 2002 Andaman Islands earthquakes (091302C & 091402B) 65
3.3.1 Introduction 65
3.3.2 Previous Studies 65
3.3.3 Results 67
3.4 1995 Kozani-Grevena, Greece, earthquake (051395B) 70
3.4.1 Introduction 70
3.4.2 Previous Studies 70
3.4.3 Results 71
3.5 1995 Dinar, Turkey, earthquake (100195B) 74
3.5.1 Introduction 74
3.5.2 Previous Studies 74
3.5.3 Results 75
3.6 1997 Lake Tanganyika, Zaire, earthquake (092197C) 77
3.6.1 Introduction 77
3.6.2 Previous Studies 77
3.6.3 Results 78
3.7 2002 Molise, Italy, earthquakes (103102B & 110102F) 81
3.7.1 Introduction 81
3.7.2 Previous Studies 81

3.7.3 Results 83
3.8 2004 Parkfield, California, USA, earthquake (092804H) 86
3.8.1 Introduction 86
3.8.2 Previous Studies 86
3.8.3 Results 88
3.9 Summary 93

4 Sumatra Aftershocks 2004–2005 **95**
4.1 Overview 95
4.2 Introduction to Sumatra 95
4.3 Transect 98
4.4 Results 99
4.5 Summary 103
4.6 Interpretations 105

5 Discussion **108**
5.1 Overview 108
5.2 The CUB Earth Model 109
5.3 Source-Receiver Distance 114
5.4 Azimuthal Receiver Coverage 117
5.5 Rayleigh Waves vs Love Waves 119
5.6 Spectral Notches 121
5.7 Scalar Seismic Moment Estimates 123
5.8 $Q(F|\nu_1, \nu_2)$ Confidence Levels 124
5.9 Amplitude Spectra: Above 20 s 127
5.10 Amplitude Spectra: Below 20 s 129
5.11 Parkfield Revisited 130
5.12 Synthetic Seismograms: Below 50 s 132
5.13 Source Locations and Origin Times 136
5.14 Summary 140

6 Conclusions **141**
6.1 Summary 141
6.2 Future Work 143

A 3-D CUB Earth Model 145

B Isolating the Fundamental Mode 149

B.1 Multiple Filter Technique 149

B.2 Time Variable Filtering 151

B.3 Phase-Matched Filtering 152

C Source Determinations for Chapter 3 Earthquakes 158

C.1 1999 South Xinjiang, China, earthquake (013099A) 158

C.2 1999 Chi-Chi, Taiwan, earthquake (102299A) 161

C.3 2005 Qeshm Island, Iran, earthquake, (112705I) 164

C.4 1993 Gulf of Aqaba, Egypt, earthquake (080393G) 167

C.5 1999 Lake Baikal, Siberia, earthquake (022599H) 169

C.6 1999 Athens, Greece, earthquake (090799C) 171

D Spectra and Waveforms for Earthquakes in Chapter 3 173

E Solution Space Slices for Chapter 3 Earthquakes 204

F Spectra and Waveforms for Earthquakes in Chapter 4 219

G Calculations of the Subduction Zone dip in Chapter 4 252

Bibliography 256

List of Figures

2.1 Flowchart of procedure developed in this study 10
2.2 Calculations of local eigenfunctions 15
2.3 Local eigenfunctions and model discontinuities 16
2.4 Dispersion curves calculated in Tibet and the Pacific Ocean 17
2.5 Global 3-D Earth phase and group velocity maps 18
2.6 Excitation kernels for event 013099A 22
2.7 1-D Earth mode summation synthetic seismograms 24
2.8 3-D seismograms for event 051395B 26
2.9 Conversion of raw data to displacement 28
2.10 Calculation of an FTAN contour plot 29
2.11 Undispersing seismograms using predictions of phase velocities 31
2.12 Depth dependency of amplitude spectra 35
2.13 Assignment of azimuthal weightings 37
2.14 Assignment of dispersion weightings 40
2.15 Strike and rake symmetries in amplitude spectra 43
2.16 Global variations in amplitude spectral misfit 46
2.17 Identification of 95% solution space confidence bounds 49

3.1 Regional map of event 013099A and station locations 54
3.2 Misfit-depth profile calculated for event 013099A 57
3.3 Rayleigh wave amplitude spectra and waveforms for event 013099A 58
3.4 Love wave amplitude spectra and waveforms for event 013099A 59
3.5 Depth-dependent variations in synthetic amplitude spectra 60
3.6 Depth-dependent variations in synthetic waveforms 61
3.7 Solution space defined by 95% confidence limits for event 013099A 63
3.8 Regional map of events 091302C & 091402B 66

3.9 Misfit-depth profile calculated for events 091302C & 091402B 68
3.10 Solution space defined by 95% confidence limits for event 051305B 73
3.11 Misfit-depth profile calculated for event 092197C 79
3.12 Regional map of events 103102B & 110102F 82
3.13 Misfit-depth calculated profile for event 092804H 89
3.14 Solution space defined by 95% confidence limits for event 092804H 91

4.1 Regional map of Sumatra 96
4.2 Sumatra CMT solutions from 1 January 1990 to 31 December 2006 97
4.3 Regional map of Sumatra mainshocks and the receivers used in this study . . 100
4.4 Map and cross-section view of calculated source parameters 101
4.5 Synthetic amplitude spectra and waveforms for event 123104M 104
4.6 Comparison of rupture models and aftershock locations 106

5.1 Rayleigh wave group velocity discrepancies 110
5.2 Love wave group velocity discrepancies 111
5.3 Love and Rayleigh wave group velocity discrepancies for Sumatra aftershocks 112
5.4 Diurnal Sumatra aftershocks 113
5.5 Group velocity discrepancies by distance for events from Chapter 3 115
5.6 Individual station amplitude spectral misfits 116
5.7 Receiver coverage for 1995 Dinar earthquake 118
5.8 Rayleigh wave spectra for event 022599H 122
5.9 Love wave spectra for event 022599H 122
5.10 Solution-space histograms of $Q(F|\nu_1, \nu_2)$ 126
5.11 Misfit-depth profiles for cut-off periods of 50 s, 40 s, 30 s, 25 s and 20 s 128
5.12 Misfit-depth profiles for cut-off periods to 15 s for event 100195B 129
5.13 Misfit-depth profiles for cut-off periods to 15 s for event 092804H 131
5.14 Rayleigh wave amplitude spectra and waveforms for event 092804H 133
5.15 Love wave amplitude spectra and waveforms for event 092804H 134
5.16 Synthetic seismograms to 20 s cut-off period for event 080393G 135
5.17 Synthetic seismograms to 20 s cut-off period for event 092804H 137
5.18 Synthetic waveforms for event 090799C at different source locations 138
5.19 Waveforms misfit values for event 090799C 139

A.1 CUB global elevation 146

A.2 CUB crustal thickness 147
A.3 CUB global dispersion 148

B.1 Multiple Filter Technique 150
B.2 Time Variable Filtering 153
B.3 Phase-Matched Filtering (i) 154
B.4 Phase-Matched Filtering (ii) 155
B.5 Phase-Matched Filtering (iii) 157

C.1 013099A misfit-depth profile for 13 km discontinuity 159
C.2 013099A misfit-depth profile for 33 km discontinuity 159
C.3 102299A misfit-depth profile 162
C.4 112705I misfit-depth profile 165
C.5 080393G misfit-depth profile 167
C.6 022599H misfit-depth profile 170
C.7 090799C misfit-depth profile 172

List of Tables

3.1 NEIC hypocentral parameters for earthquakes in Chapter 3 52
3.2 Source parameters determined in Chapter3 53
3.3 Source parameters published for event 013099A 55
3.4 Source parameter bounds for event 013099A 62
3.5 Source parameters published for events 091302C & 091402B 67
3.6 Source parameter bounds for events 091302C & 091402B 69
3.7 Source parameters published for event 051395B 71
3.8 Source parameter bounds for event 051395B 72
3.9 Source parameters published for event 100195B 75
3.10 Source parameter bounds for event 100195B 76
3.11 Source parameters published for event 092197C 78
3.12 Source parameter bounds for event 092197C 80
3.13 Source parameters published for events 103102B & 110102F 84
3.14 Source parameter bounds for events 103102B & 110102F 85
3.15 Source parameters published for event 092804H 87
3.16 Rake-dip trade-offs for event 092804H 90
3.17 Source parameter bounds for event 092804H 90

4.1 NEIC hypocentral parameters of Sumatran aftershocks 98
4.2 Source parameters of Sumatran aftershocks 102

5.1 Receiver distribution effects for event 100195B 117
5.2 Source parameter perturbations using solely Rayleigh waves 120
5.3 Grid-search and scaling seismic moment estimates 124
5.4 Range of source parameters for $Q(F|\nu_1, \nu_2) = 0.32$ 125
5.5 Source parameters for event 100195B at cut-off periods between 50–15 s . . . 130

5.6 Event 100195B depth estimates with cut-off periods between 50–15 s 130
5.7 Source parameters for event 092804H at cut-off periods between 50–15 s . . . 131
5.8 Source parameters published for event 092804H 132
5.9 NEIC and CMT source locations of event 090799C 139

C.1 013099A source parameters 158
C.2 102299A source parameters 161
C.3 102299A source parameter estimates 163
C.4 112705I source parameters 164
C.5 112705I source parameter estimates 166
C.6 080393G source parameters 167
C.7 080393G source parameter estimates 168
C.8 022599H source parameters 169
C.9 022599H source parameter estimates 170
C.10 090799C source parameters 171
C.11 090799C source parameter estimates 172

G.1 Depth estimates of Offshore Banda Aceh earthquakes 253
G.2 Subduction interface dip estimates 254

Chapter 1

Introduction

"It is no good to try to stop knowledge from going forward.
Ignorance is never better than knowledge."

Enrico Fermi (1901–1954)

1.1 Overview

The reliable estimation of the depths of shallow earthquakes is a fundamental seismological problem. For example, the tectonic significance of an earthquake can vary greatly depending on whether it occurs in the upper crust, the lower crust or in the upper mantle. Similarly, in seismic discrimination, a trustworthy determination of an earthquake depth deeper than 10 km is sufficient to screen a seismic event as a naturally-occurring earthquake, and not a potential man-made explosion. There are few seismic events in current catalogues that have reliably determined depths, with the majority of shallow earthquakes fixed at certain standard depths. It has long been known that surface wave amplitudes and radiation patterns can provide robust constraints on seismic source depths. It is the aim of this thesis to generate synthetic amplitude spectra to compare with recorded data in order to determine reliable source parameters for shallow depth earthquakes.

1.2 Depth Determination Techniques

Earthquake depths are generally calculated in one of three different ways: (i) by analysis of body wave travel times; (ii) by modelling long-period body waves; (iii) by utilising short-period 'depth phases' (surface reflections such as pP and sP). Body wave travel times, while useful for analysing deep earthquakes, lack sufficient resolution to tightly constrain intermediate and shallow depth seismic sources. This is because there is little variation in the travel-time versus distance curve for depth for shallow events, so travel-time trades off with origin time unless very local recordings are made available.

Long-period body wave modelling has proved to provide accurate depth constraints on relatively large earthquakes; however, because long-period body waves are poorly recorded for smaller magnitude events ($M_{\mathrm{w}} < 5.0$), the application of this technique is somewhat limited. Short-period depth phases have been shown to provide highly accurate depth estimates, when they are detected and reliably identified. However, for shallow events, depth phases arrive very soon after the direct P arrival, so the clear identification of each discrete phase can be difficult. For many focal mechanisms clear P, pP and sP arrivals are not recorded at the same station because of the earthquake radiation pattern; in addition source characteristics and the above-source structure can also affect the transmission and detection of these signals. In cases where the clear identification of depth phases is not available, broadband modelling of their interference can be peformed (e.g. see Choy & Boatwright, 1988). This method relies on accurately calculating the delays and amplitudes of the P, pP and sP phases and is strongly influenced by uncertainties in the local Earth structure, attenuation and the spatial and temporal characteristics of the source.

It has been recently suggested that accurate shallow depth determinations can be made without clear identification of individual depth phases by modelling their collective interference (Warren & Shearer, 2005) on P-wave spectra. For a range of depths synthetic spectra calculated using pre-determined focal mechanisms are compared with the observed data. The accuracy of this method is currently subject to some debate (Douglas, A., 2008, pers. comm.) with a wide range of depth estimates determined for selected events. The requirement for pre-determined focal mechanisms reduces its use in the study of small ($M_{\mathrm{w}} \leq 5.0$) events.

In many seismo-tectonic studies, estimates of source depths and focal mechanisms are taken

from global earthquake catalogues and used to characterise and quantify the nature of seismicity in tectonically active regions. From the early 1980s Harvard Centroid Moment Tensor (CMT) solutions (Dziewonski et al., 1981; Dziewonski & Woodhouse, 1983) have been routinely determined for earthquakes of $M_w \geq 5.0$ and United States Geological Survey (USGS) fast moment tensor solutions (Sipkin, 1982) have been produced for earthquakes of $M_w \geq 5.5$. The Harvard CMT method uses body waves greater than 45 s (and, for large earthquakes, long-period (T > 135 s) surface waves) in an inversion for the seismic moment tensor. The magnitude threshold for which robust seismic moment tensors can be calculated in this way is controlled by the signal-to-noise ratio at teleseismic distances and prevents the determination of trustworthy source parameters for earthquakes with $M_w \leq 5.0$.

USGS moment tensor solutions (Sipkin, 1982) are generated by the inversion of composite P body waveforms consisting of P, pP and sP and are independent of the moment tensors produced using the Harvard CMT methodology. Orientations of the moment tensors are generally similar, though some differences exist due to the different types of data used by the two methods (Sipkin, 1986).

1.3 Previous Surface Wave Studies

At periods greater than 20 s, most of the seismic energy recorded at regional and teleseismic distances propagates as surface waves and moderate sized-earthquakes ($M_w \sim 5.5$) have significant signal-to-noise ratios. Surface wave recordings contain information about both the character of the seismic source and the Earth structure along the source-receiver path. The separation of these effects has long been a challenge to seismologists, especially at short-periods and for small events, where corrections for path effects need to be accurately applied.

Path corrections can be determined using a 'reference event'– an earthquake for which a robust source mechanism has previously been determined – these corrections can then be applied to neighbouring seismic events of interest. Following the approach of Weidner & Aki (1973), Patton (1977) developed a method to calculate source parameters and infer propagation effects for a group of closely located events recorded over teleseismic distances. However, it was shown by Aki & Patton (1979) that in order to calculate reliable moment tensor solutions from 100–20 s period data, estimates of phase velocities along a path required an accuracy of

0.5%.

Intermediate-period surface waves exhibit high signal-to-noise ratios, especially when recorded at short ($< 10°$) epicentral distances (e.g. Fukushima et al., 1989; Patton & Zandt, 1991; Ritsema & Lay, 1993; Romanowicz, 1995; Thio & Kanamori, 1995). Until recently these surface waves have been excluded from regional source studies due to the lack of knowledge of their propagation characteristics. However, the development, in the last 10 years, of accurate upper mantle and crustal velocity maps now allows path effects to be better modelled, allowing more reliable surface wave source parameter studies to be performed.

These advances in mapping global surface wave dispersion (e.g. Trampert & Woodhouse, 1995; Ekström et al., 1997) have allowed the Harvard CMT algorithm to be updated (in the so-called Global CMT project[1]) and the studies of Arvidsson & Ekström (1998) and Morelli et al. (2000) have generated source mechanisms for earthquakes where $M_w \geq 4.5$. The motivation behind the updating of the CMT method is to allow the determination of focal mechanisms for small earthquakes in regions where dense, local seismic networks are not available. Even with the addition of shorter-period data, shallow depth resolution remains poor in the CMT catalogue and typically shallow source depths are fixed at 15 km.

1.4 Surface Wave Amplitude Spectra

Tsai & Aki (1970) first proposed the possibility of using surface wave amplitude spectra to constrain earthquake depths. In particular these authors demonstrated that 50–10 s period Rayleigh wave amplitude spectra were especially sensitive to changes in focal depth compared to variations in crustal structure, spatial and temporal source behaviour and attenuation. Frequency-dependent 'notches' in these spectral signals are most pronounced for vertical dip-slip and 45° focal mechanisms and have been shown to provide tight constraints on source depth. The absence of such features in Love wave amplitude spectra has limited their application in source depth determination studies (Tsai & Aki, 1970, 1971).

The exact frequency at which a notch occurs is dependent on mechanism, depth and source-receiver azimuth; but not all nulls observed in Rayleigh wave amplitude spectra are at-

[1]Henceforth the various versions of the CMT methodology will simply be referred to as 'CMT', with no explicit reference to either 'Harvard' or 'Global', unless it is deemed necessary.

tributable to source. Tsai (1969) matched nulls in the Rayleigh wave amplitude spectra of mid-ocean ridge earthquakes and concluded that source depths could be identified as deep as 65 km. Weidner & Aki (1973) analysed the same events and concluded that the spectral nulls were not indicative of the seismic source and were actually propagation effects (e.g. interference due to multipathing) and demonstrated that these earthquakes occurred at depths shallower than 10 km. Spectral holes attributable to path effects are also identified in Love wave amplitude spectra; indeed their occurrence at similar frequencies to those occurring in corresponding Rayleigh wave recordings would often indicate that they are a propagation effect (e.g. Tsai & Aki, 1971).

The frequency-depth dependence of spectral notches has been used in the identification of shallow focal earthquake depths (e.g. Nguyen & Herrmann, 1992; Patton, 1998) and has been identified as a key difference between Rayleigh wave amplitude spectra from earthquakes and those from explosions (Tsai & Aki, 1971; Selby et al., 2005). However, when using just amplitude spectra, a source mechanism ambiguity is introduced due to the 180° symmetries exhibited by surface wave radiation patterns in both strike and rake. As such, additional information about the source phase will need to be provided to distinguish between four possible focal mechanisms, but this ambiguity does not influence depth estimates.

1.5 Seismic Discrimination

Seismology is the principal tool used in the monitoring of the global comprehensive nuclear test ban treaty (CTBT, e.g. van der Vink & Park, 1994). Surface waves are important in seismic discrimination studies because the most successful tool for distinguishing man-made explosions from naturally-occurring earthquakes is the ratio of body wave to surface wave magnitude, the $m_b : M_s$ criterion. Brune et al. (1963) and Press et al. (1963) were the first to report the possible use of this discriminant, although widespread acceptance did not come until detailed analysis of seismic data in the wake of the 1965 LONGSHOT underground nuclear explosion in the Aleutians by Marshall et al. (1966) and Liebermann et al. (1966).

If a seismic event is suitably large, discrimination using this method is fairly straightforward. Explosions release their energy in a small volume, efficiently producing P body waves but exciting surface waves relatively weakly. Indeed, Brune et al. (1963) reported that in the

California-Nevada region earthquakes generated surface waves with amplitudes of the order of 5–10 times greater than those generated by explosions.

Carpenter (1965) reported that there was a finite probability that the first motion P waveforms from an earthquake observed at large distances (3000–9500 km) would be compressive everywhere and thus appear as an explosion. Douglas et al. (1971) showed that, using the $m_b : M_s$ criterion, a shallow compressional earthquake occurring on a 45° dip-slip fault could well be misinterpreted as an explosion. Earthquakes producing explosion-like $m_b : M_s$ signatures have been observed historically (Landers, 1972; Douglas, 1981) and Bowers & McCormack (1997) demonstrated, through analysis of the Harvard and USGS published moment tensors, that earthquakes with compressional dip-slip mechanisms are the most prevalent in seismic source catalogues.

These observations suggest that the identification of a source mechanism consistent with the tectonic release from an earthquake is not sufficient to preclude a seismic event from being considered a possible explosion. Accurate depth determinations are of great importance in seismic discrimination; if an event can be located at depths greater than, say, 10 km, then it can be confidently screened as a naturally-occurring earthquake. This is especially important for small magnitude events where there is diminished trust in the use of the $m_b : M_s$ discriminant.

1.6 Depth Distribution of Earthquakes

In seismo-tectonic studies reliable estimates of earthquake depths help illuminate the manner of continental crustal deformation. The theory of plate tectonics has succeeded in accurately describing the observed patterns of deformation in oceanic tectonic settings, but fails somewhat when it is applied to continental regions because they do not, typically, behave as rigid plates. Seismicity occurs in discrete, narrow bands around the edges of oceanic plates, but is much more broadly distributed in the continents. Features such as mountain belts, plateaus and basins owe their existence to the behaviour of deformation of the crust and underlying upper mantle. As such, the character and interaction between the crust and mantle is the subject of much debate, especially concerning the depths of relative 'strength' and 'weakness' in the lithosphere.

Current views on the distribution of earthquake depths in the continents are divided into two camps. The first is the so-called 'Jelly Sandwich' view, which describes a bimodal distribution of earthquakes with depth; brittle deformation occurs in the upper crust (top 10–20 km) and in the upper mantle, with a weaker lower crust separating these two seismogenic layers. The lack of seismic activity found in the lower crust by Chen & Molnar (1983) and Chen (1988) was a significant observation in the development of this view. If a weak lower crust separates a strong upper crust and upper mantle then these two strong, seismogenic, regions will be at least partly decoupled over local and regional length scales (Royden, 1996).

An alternative view has been proposed by Maggi et al. (2000a,b). These authors re-examined the depth distribution of continental earthquakes and determined that most naturally occurring seismic sources occurring on the continents are confined within a crustal layer varying in thickness from 10 to ~40 km. Despite earthquakes being definitively found in the oceanic mantle lithosphere (Wiens & Stein, 1983), Maggi et al. (2000a,b) found no convincing evidence of such seismicity beneath the Moho in continental regions. This view would suggest that the mantle and crust are mechanically coupled (England & Jackson, 1989) and deform coherently, and therefore that crustal deformation may be taken to directly reflect deformation in the mantle (Silver, 1996).

The nature of the depth distribution of earthquakes in the crust and upper mantle is open to intense debate and the techniques developed in this study have the potential to increase our capability of assigning earthquakes either to the crust or to the mantle. Some of the earthquakes studied in this thesis occur close to the continental Moho, for these we seek to determine whether they are in the crust or in the upper mantle.

1.7 Thesis Outline

In this thesis surface wave amplitude spectra are modelled to place constraints on seismic source parameters. Rayleigh and Love wave synthetic amplitude spectra are generated using a suitable 3-D Earth velocity model, and group arrival predictions from this model are used to identify and isolate the fundamental-mode surface wave arrivals from recorded seismograms. All double-couple solutions are grid-searched over an appropriate range of depths; a least squares misfit calculation is performed to identify the best fitting source parameters and

appropriate constraints are placed on the source solution. These procedures are outlined in full in Chapter 2.

In Chapter 3 source parameters are presented for 14 events used in the testing and validation of this method. These earthquakes have been studied previously using other seismological techniques and reliable source estimates are determined over the magnitude range $5.4 \leq M_{\mathrm{w}} \leq 6.5$.

Aftershocks of the 2004 Sumatra earthquake are studied in Chapter 4 and reliable focal mechanism and depths determined for seismic events as small as $M_{\mathrm{w}} = 4.8$. Constraints placed on source depth are used to identify the orientation of the subduction zone, the likely down-dip extent of the mainshock rupture and the approximate location of the brittle-ductile transition in this region.

The effects of perturbing the method are analysed in Chapter 5 to assess the performance of the approach undertaken here. In addition a critique of the 3-D Earth model is performed by comparing its predictions of the dispersive properties of the Earth with those calculated from data recordings. The accuracy of amplitude spectral matches with the data is assessed, as is the closeness of fit of waveforms generated here with those observed over regional distances.

The main conclusions of this work and opportunities for further work are outlined in Chapter 6.

Chapter 2

Method

"A child of five would understand this. Send someone to fetch a child of five."

Groucho Marx (1895–1977)

2.1 Overview

This chapter contains descriptions of the techniques developed here in order to use intermediate-period surface wave observations to constrain seismic source parameters. For chosen events Rayleigh and Love wave recordings are selected at stations in the minor-arc epicentral range 10–60°. Predictions of the great circle dispersion characteristics of these waves are used to identify and isolate the 100-20 s period fundamental-mode arrivals from unwanted signals and noise. Synthetic seismograms are calculated for all source-receiver pairs over a suitable depth range and amplitude spectra generated from all possible double-couple focal mechanisms are compared with those retrieved from the processed data in a grid-search algorithm. The best fitting synthetic spectra are identified using a least-squares misfit calculation in logarithmic amplitude space and appropriate constraints placed on the source parameters. The methodology developed here is outlined in Figure 2.1.

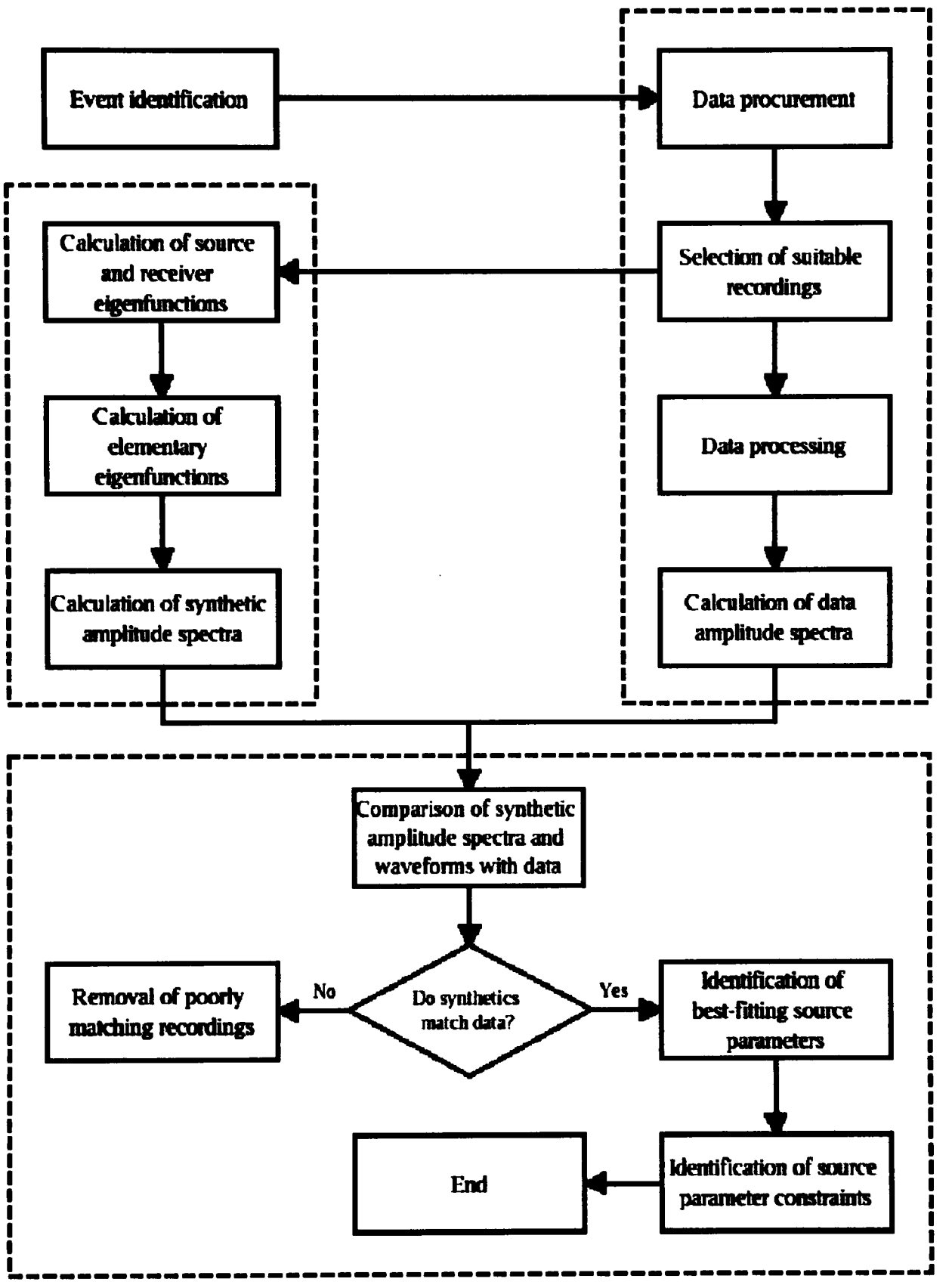


Figure 2.1: Flow chart depicting the various processes undertaken in this study for the determination of seismic source parameters. The three dashed regions identify the different sections of the method presented in this chapter: the generation of synthetic seismograms (upper left), the procurement, selection and processing of seismic data (upper right) and the search for best fitting source parameters (bottom).

2.2 Synthetic Seismograms

2.2.1 Theory

In this thesis synthetic surface waves are generated in a 3-D, laterally-heterogeneous, Earth. Calculations are made which take into account (1) wave excitation based upon the local Earth structure at the source; (2) amplitude and path corrections due to propagation through a 3-D Earth; and (3) seismic displacement dependent on the local Earth structure at the receiver. The methodology of Ferreira (2005) is closely followed; only a general outline of the theory behind the technical procedure applied here is presented; a more rigorous description is available from that author.

Considering a smooth, laterally heterogeneous, slightly anisotropic, anelastic, non-rotating, self-gravitating Earth model; for a given source-receiver pair, the surface wave displacement in the frequency domain (Woodhouse, 1974) may be approximated as:

$$u(\omega) = A(\omega)e^{-i\psi(\omega)}, \tag{2.1}$$

where

$$A = A_s A_p A_r, \tag{2.2}$$

and

$$\psi = \psi_s + \psi_p + \psi_r. \tag{2.3}$$

The subscripts s, p and r, are used to indicate those terms evaluated at source, those dependent on the path and those evaluated at the receiver respectively. Here the amplitude, A, is given by the product of the amplitude terms and the phase, ψ, is given by the sum of the respective phase contributions.

The terms A_s, A_p, A_r, ψ_s, ψ_p and ψ_r are given by:

$$A_s e^{-i\psi_s} = \frac{1}{\sqrt{C_s}} \mathbf{M} : \mathbf{E_s^*} e^{i\frac{\pi}{4}}, \tag{2.4}$$

$$A_p e^{-i\psi_p} = \sqrt{\frac{1}{\sin\Delta}} \exp\left(-i\omega a \int_{gc} \frac{1}{c}\, \mathrm{d}\Delta\right), \tag{2.5}$$

$$A_r e^{-i\psi_r} = \frac{1}{\sqrt{C_r}}\ \mathbf{s_r}. \tag{2.6}$$

M is the seismic moment tensor (after Gilbert, 1970) expressed in spherical components, $\mathbf{E_s}$ is the strain tensor evaluated at the source (* denotes the complex conjugate) and $\mathbf{s_r}$ is the local displacement eigenvector at the receiver. ω is angular frequency, C_s and C_r are the group velocities at the source and receiver respectively.

To account for the amplitude and phase contributions due to propagation along the source-receiver path, a great circle (gc) approximation is used. Geometric spreading is accounted for by assuming that the amplitude decays based on a $\sqrt{\frac{1}{\sin\Delta}}$ spherical divergence relationship, where Δ represents the source-receiver distance. The propagation phase contribution is calculated by integrating the phase slowness ($\frac{1}{c}$, where c is phase velocity) along the great circle path.

The local phase velocity is given by $c = \frac{\omega}{k}$ and the local group velocity (the wave energy speed) is given by $C = \frac{\delta\omega}{\delta k}$, where k is the local wavenumber and is related to wavelength, λ, by:

$$k = \frac{\lambda}{a} = \frac{l+\frac{1}{2}}{a}, \tag{2.7}$$

where a is the radius of the Earth and l is the angular order of the equivalent free-oscillation multiplet; equation (2.7) describes the travelling-wave and standing-wave correspondence of seismic surface waves propagating on a sphere.

In a laterally varying Earth, the phase and group velocities vary as a wave propagates from the source to a receiver. In this thesis, so-called 'local' phase and group velocities for any location are derived from the normal modes of vibration of a spherically symmetrical Earth whose radial structure is given by the variation of seismic velocities with depth at that location. These oscillations occur at discrete frequencies ('local eigenfrequencies') and are described by displacement fields termed 'local eigenfunctions'.

For Rayleigh waves, the quantity $\mathbf{M}$:$\mathbf{E_s^*}$ in Equation 2.4 is given by:

$$\begin{aligned}\mathbf{M} : \mathbf{E_s^*} = \{&-[\dot{U}_s M_{rr} + \frac{1}{2r}(2U_s - \lambda^2 V_s)(M_{\theta\theta} + M_{\phi\phi})] \\ &i\lambda[M_{r\phi}\cos\xi + M_{r\theta}\sin\xi][\dot{V}_s + \frac{1}{r}(U_s - V_s)](-1)^{\alpha}\end{aligned}$$

$$+\lambda^2 \frac{V_s}{r}[\frac{1}{2}(M_{\theta\theta} - M_{\phi\phi})\cos 2\xi + M_{\theta\phi}\sin 2\xi]\}_s, \tag{2.8}$$

(following Dahlen & Tromp, 1998) and $\mathbf{s_r}$ in Equation 2.6 is calculated as:

$$\mathbf{s_r} = U_r\hat{\mathbf{r}}_r - iV_r\hat{\mathbf{k}}_r. \tag{2.9}$$

Likewise for Love waves:

$$\begin{aligned}\mathbf{M} : \mathbf{E_s^*} = \{&i\lambda[M_{r\theta}\sin\xi + M_{r\theta}\cos\xi][\dot{W}_s + \frac{1}{r}W_s](-1)^\alpha \\ &+\lambda^2\frac{W_s}{r}[\frac{1}{2}(M_{\theta\theta} - M_{\phi\phi})\sin 2\xi + M_{\theta\phi}\cos 2\xi]\}_s,\end{aligned} \tag{2.10}$$

and

$$\mathbf{s_r} = \hat{i}W_r(\hat{\mathbf{r}}_r \times \hat{\mathbf{k}}_r). \tag{2.11}$$

U_s, V_s, W_s, $\dot{U}_s$, $\dot{V}_s$ and $\dot{W}_s$ are the values of the local radial eigenfunctions and their radial derivatives at the seismic source depth. Their calculation, along with that of U_r, V_r and W_r, the radial eigenfunctions evaluated at the receiver, are discussed in 2.2.2. $\hat{\mathbf{r}}_r$ and $\hat{\mathbf{k}}_r$ are the vertical component and radial component directions respectively. ξ is the azimuth of the surface wave ray path on the unit sphere and $\mathbf{k}$ is the local wavevector. The variable r represents the radius at which the excitation is calculated.

In order to account for the ellipticity of the Earth, all geographic latitudes (θ) are converted to geocentric latitudes (θ') using:

$$\tan\theta' \approx (1 - 2\epsilon_a)\tan\theta, \tag{2.12}$$

where ϵ_a, is the Earth's ellipticity and has the value 3.36×10^{-3} (e.g. Dahlen, 1982).

At very long periods seismometer recordings are affected by changes in the Earth's gravitational field caused by the redistribution of the Earth's mass due to seismic wave propagation (Dahlen & Tromp, 1998). The mode calculation program used in this study includes the effect of this mass redistribution in the calculation of the U and V eigenfunctions (toroidal modes are unaffected). However, in the period range of interest in this thesis (100–20 s), the effect of self-gravitation is insignificant (e.g. see Udias, 1999).

2.2.2 Local Modes

In order to calculate the surface wave displacements defined in Equations (2.1) to (2.6), determinations of the local radial source eigenfunctions (U_s, V_s, W_s) and their radial derivatives ($\dot{U}_s$, $\dot{V}_s$, $\dot{W}_s$) at the seismic source radius are required. At each receiver, calculations of the local eigenfunctions at the Earth's surface (U_r, V_r, W_r) must be made, along with the estimations of local phase and group velocities.

The determination of local modes of oscillation (Woodhouse, 1974) in this study follows the methodology of Woodhouse (1988). The MINOS computer program distributed by G. Masters, based on earlier programs by F. Gilbert and J. H. Woodhouse, is used here. Radial eigenfunctions are calculated for each discrete eigenfrequency and estimates of phase and group velocities are generated. Whilst the functionality exists to search through user-specified minimum and maximum angular order numbers (l_{min} to l_{max}), angular frequencies (ω_{min} to ω_{max}) and overtone numbers (n_{min} to n_{max}); in this study $n_{\text{min}} = n_{\text{max}} = 0$ as only the fundamental-mode is considered. For the full synthetic seismograms presented here, local modes are calculated to a cut-off frequency of $\omega_{\text{max}} = 58.8\,\text{mHz}$, corresponding to a cut-off period (T_{cut}) of $\approx 17\,\text{s}$. Separate calculations are performed for the spheroidal and toroidal modes of vibration to generate the eigenfunctions and dispersion curves required for the synthesis of Rayleigh and Love wave seismograms respectively.

Seismic surface waves can be modelled in a laterally homogeneous Earth using the one-dimensional (1-D) Preliminary Reference Earth Model (PREM, Dziewonski & Anderson, 1981). However, for accurate Earth synthetic calculations, a laterally heterogeneous model is required and here we use the CUB Earth model provided by Shapiro & Ritzwoller (2002) (see Appendix A for more details). The CUB model is a 3-D crust and upper mantle shear velocity model and was calculated using group velocity measurements between 200–16 s and the phase velocity measurements of Trampert & Woodhouse (1995) and of Ekström et al. (1997). The final database is described on a $2° \times 2°$ geographic grid and consists of 16,020 individual velocity models centred on even latitudes and longitudes. This model is only described to depths of 400 km; however, the calculation of local modes requires a full description of the Earth's velocity structure, core to crust, so the PREM model is used below these depths. Surface waves in the 100–20 s period range are not sensitive to the velocity structure below 400 km so calculated eigenfunctions, eigenfrequencies, phase and group velocities are representative

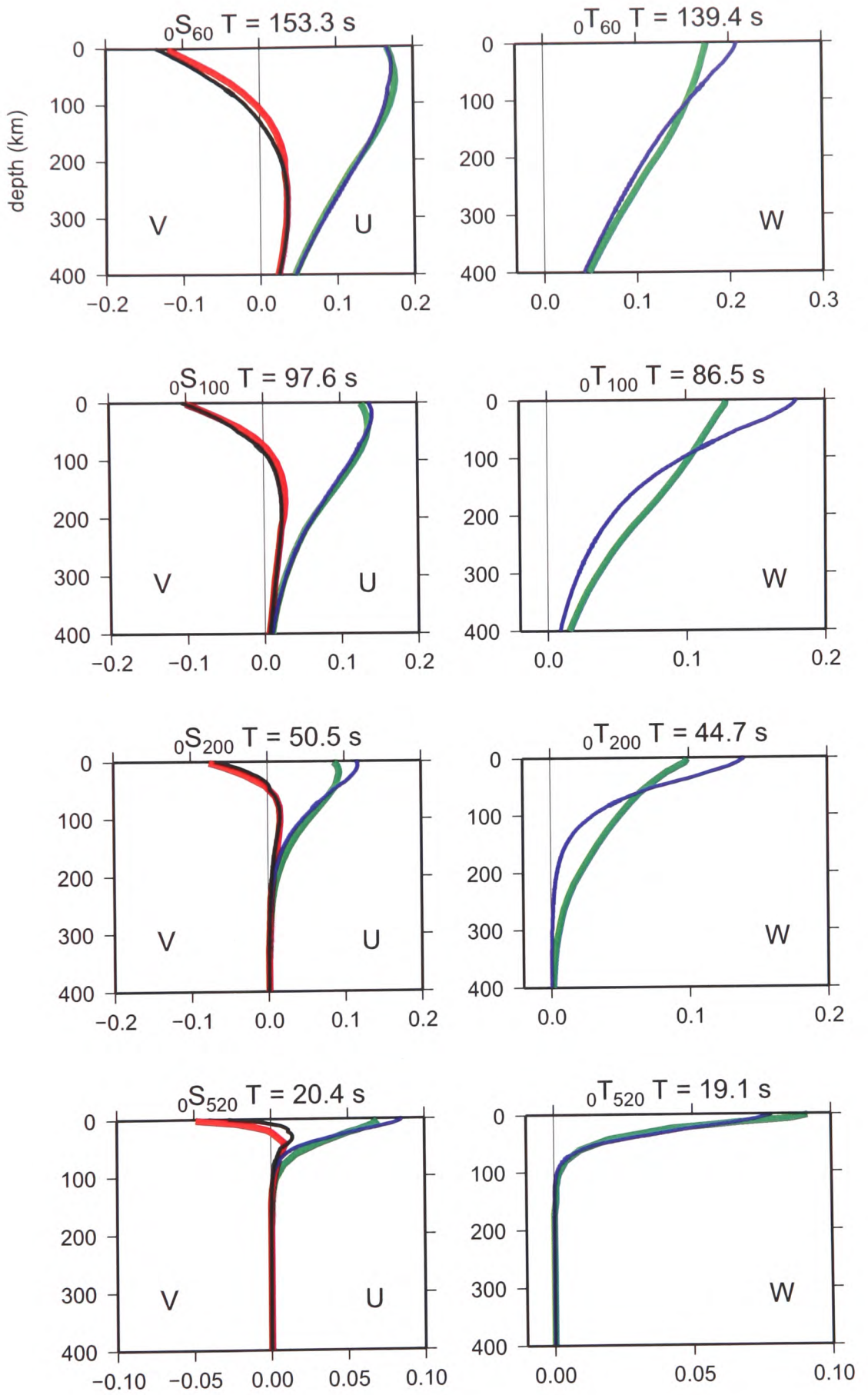


Figure 2.2: A comparison of the CUB and PREM local eigenfunctions calculated for grid square 30°N 90°E in central Tibet using the MINOS modes calculation program. Horizontal (V) and vertical (U) spheroidal eigenfunctions are plotted in red and green (PREM), and black and blue (CUB) respectively; whist the horizontal (W) toroidal eigenfunctions are shown in green (PREM) and blue (CUB). At short-periods, eigenfunction amplitudes are seen to be greatest near the surface.

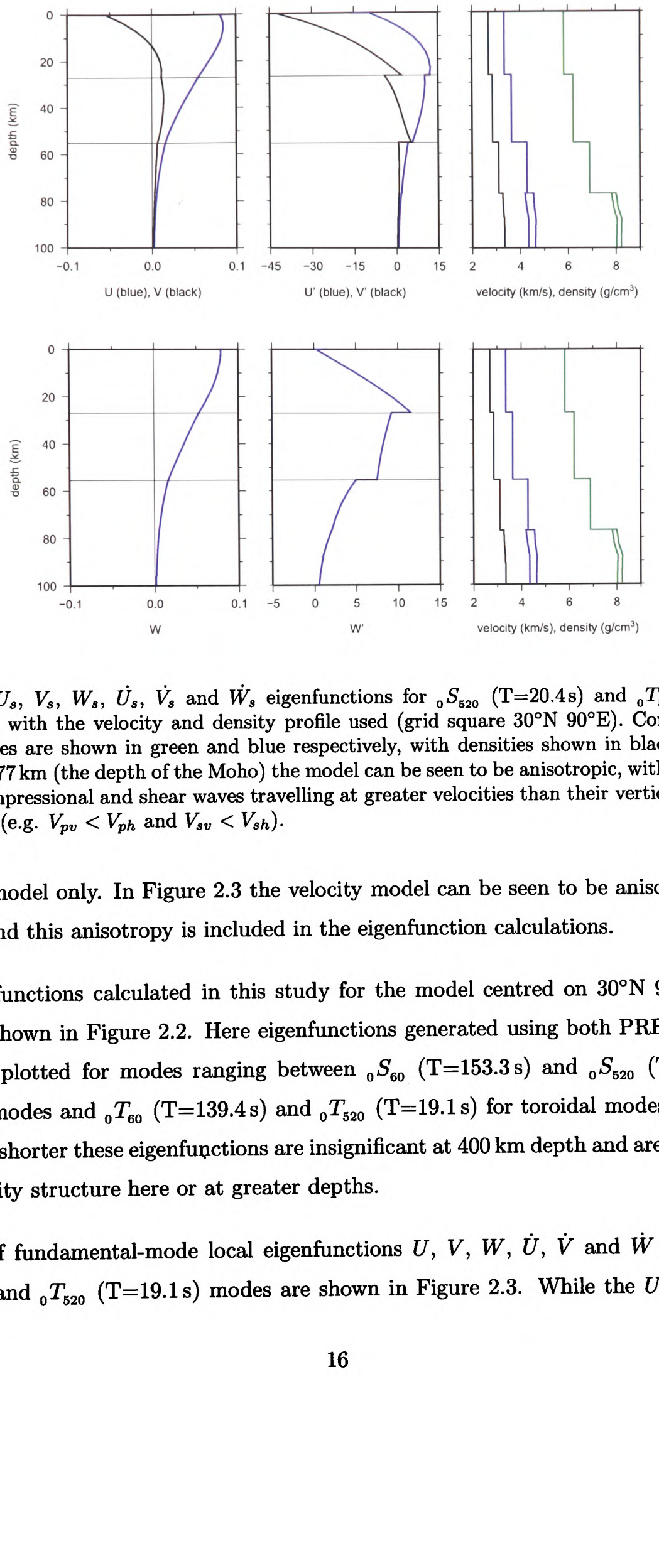


Figure 2.3: U_s, V_s, W_s, $\dot{U}_s$, $\dot{V}_s$ and $\dot{W}_s$ eigenfunctions for ${}_0S_{520}$ (T=20.4 s) and ${}_0T_{520}$ (T=19.1 s) modes, along with the velocity and density profile used (grid square 30°N 90°E). Compressive and shear velocities are shown in green and blue respectively, with densities shown in black. At depths greater than 77 km (the depth of the Moho) the model can be seen to be anisotropic, with horizontally-polarized compressional and shear waves travelling at greater velocities than their vertically-polarized counterparts (e.g. $V_{pv} < V_{ph}$ and $V_{sv} < V_{sh}$).

of the 3-D model only. In Figure 2.3 the velocity model can be seen to be anisotropic below the Moho and this anisotropy is included in the eigenfunction calculations.

Local eigenfunctions calculated in this study for the model centred on 30°N 90°E (central Tibet) are shown in Figure 2.2. Here eigenfunctions generated using both PREM and CUB models are plotted for modes ranging between ${}_0S_{60}$ (T=153.3 s) and ${}_0S_{520}$ (T=20.4 s) for spheroidal modes and ${}_0T_{60}$ (T=139.4 s) and ${}_0T_{520}$ (T=19.1 s) for toroidal modes. At periods of 100 s and shorter these eigenfunctions are insignificant at 400 km depth and are not sensitive to the velocity structure here or at greater depths.

Examples of fundamental-mode local eigenfunctions U, V, W, $\dot{U}$, $\dot{V}$ and $\dot{W}$ for the ${}_0S_{520}$ (T=20.4 s) and ${}_0T_{520}$ (T=19.1 s) modes are shown in Figure 2.3. While the U_s, V_s and W_s

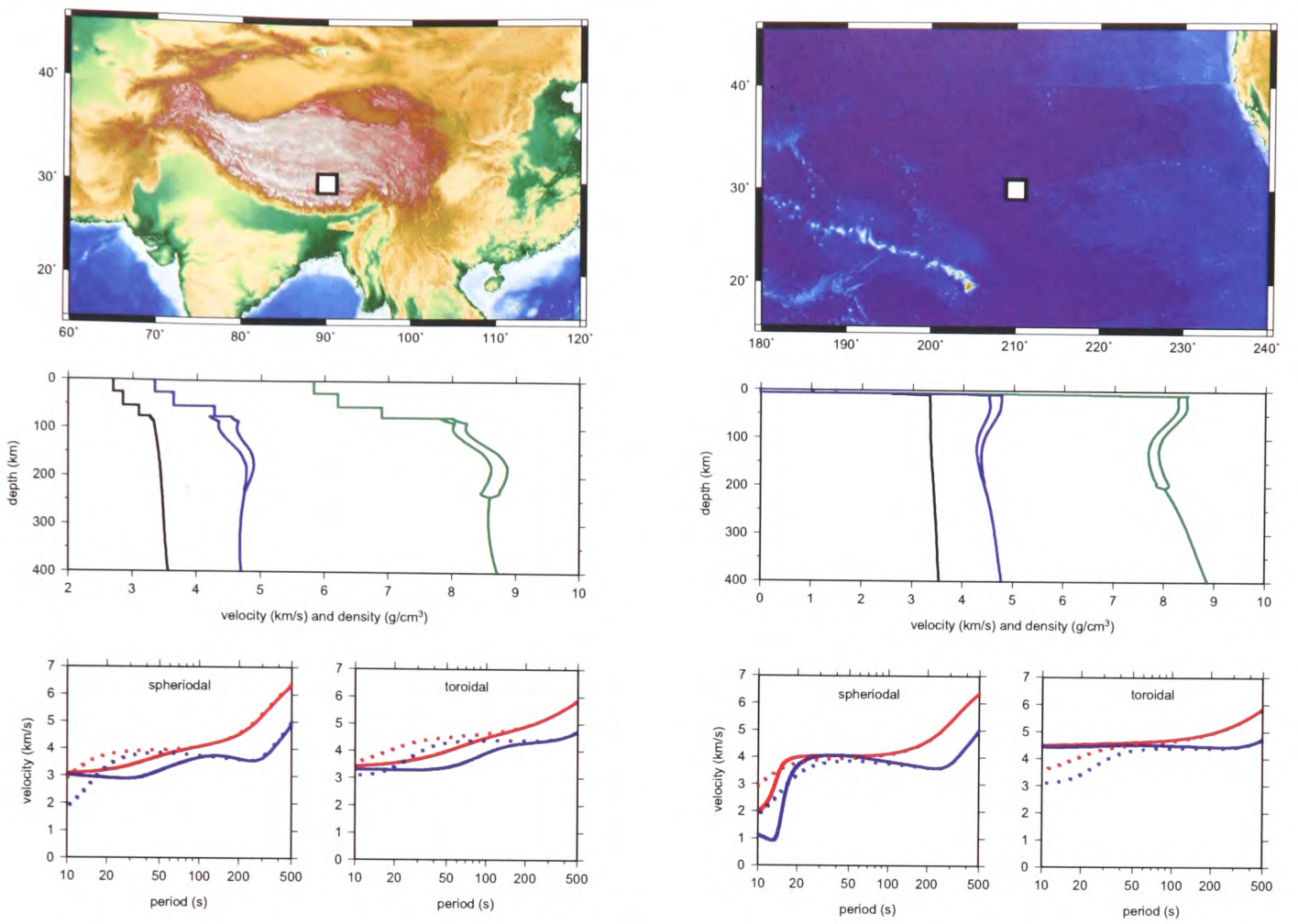


Figure 2.4: Left hand side (LHS): map of central Eurasia, with the grid square centred on 30°N 90°E shown (top); velocity and density profile described by the CUB model (centre), key as Figure 2.3; spheroidal and toroidal phase (red) and group (blue) velocity dispersion curves (bottom). Right hand side (RHS): as left, but for the grid square centred on 30°N 210°E, in the Pacific Ocean. Dashed lines show the corresponding dispersion curves generated using PREM. Again, the models can be seen to describe an anisotropic upper mantle.

eigenfunctions are, on the whole, smooth curves, the effect of boundaries in the model is clear on their radial derivatives. Discontinuities in the seismic velocities at depths of 27 km and 55 km cause jumps in the radial derivatives, along with small deviations in the displacement eigenfunctions. The values of U_s, U_r, V_s, V_r, W_s, W_r, $\dot{U}_s$, $\dot{U}_r$ and $\dot{V}_s$ are used in Equations 2.8 and 2.10 to generate synthetic seismograms at specified depths. It can be expected that seismograms generated either side of these discontinuities may differ more significantly than those generated at incremental depths either side of these boundaries. These deviations in the eigenfunctions and their radial derivatives are inevitable consequences of using a 3-D Earth model with velocity discontinuities.

In the local mode calculations, phase and group velocities are calculated for each discrete eigenfrequency, examples of which can be seen in Figure 2.4. Spheroidal and toroidal phase

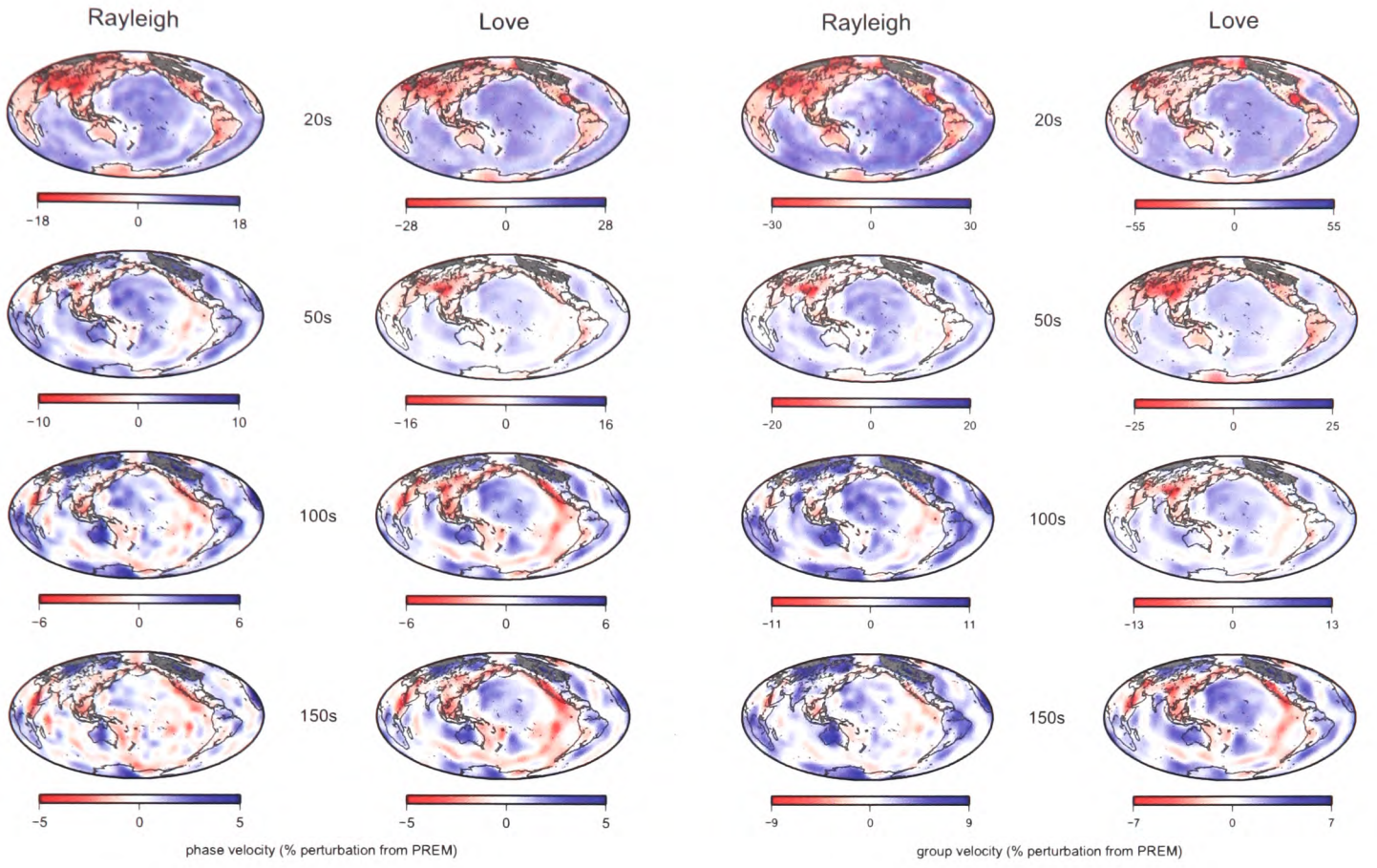


Figure 2.5: Rayleigh and Love phase (left) and group (right) velocity maps for 20 s, 50 s, 100 s and 150 s period surface waves generated here using the CUB Earth model. Velocities are plotted as % perturbations from those calculated using the PREM model.

and group velocity curves are shown for two different Earth models, one in Tibet and the other in the Pacific Ocean and the corresponding PREM dispersion curves are plotted for comparison. For both models, the dispersion curves are similar at longer-periods, reflecting the sensitivity of surface waves to the Earth's structure below ~400 km. At shorter-periods (i.e. 100 s and below) the two CUB model dispersion curves deviate from PREM and also from each other, indicating an increased sensitivity to the laterally heterogeneous upper mantle and crustal velocity structure described by the 3-D Earth model.

Dispersion curves are generated for each of the 16,020 $2° \times 2°$ model grid squares and phase and group velocity maps can be plotted for the entire Earth. Examples of global phase and group velocity maps at 20 s, 50 s, 100 s and 150 s periods are shown in Figure 2.5. It is the integration of the phase slowness through these maps that provides the propagation phase information (Equation 2.5).

2.2.3 Implementation

The synthetic seismogram calculation program of Ferreira (2005) has been adapted for use in this study. An earlier modes calculation routine, EOSANI, was replaced by the MINOS modes calculation program to allow the cut-off period to be lowered from 40 s to 10 s; although only the fundamental-mode is considered here, this change also allows the generation of synthetics with the addition of overtones. A new path calculation routine was added to account for the phase and amplitude contributions caused by propagation along the great circle path. Synthetic seismograms can be generated for both PREM and CUB models allowing comparisons of the two with recorded data to be made.

For a specified source, synthetic seismograms are generated for all required stations. The local Earth model is selected which contains the source epicentre, and receiver local models are selected for each station location. Local displacement eigenfunctions and their radial derivatives, along with calculations of phase velocity, group velocity and attenuation are determined for both source and receiver; estimations of the propagation contributions are found by tracing the great circle path through the phase velocity maps calculated in each of the $2° \times 2°$ model grid squares between the source and the receiver.

At the source, values of U_s, V_s, W_s, $\dot{U}_s$, $\dot{V}_s$ and $\dot{W}_s$ are calculated for each discrete eigenfrequency to a specified cut-off period ($T_{\text{cut}} = 17.5\,\text{s}$) and applied in Equations 2.8 and 2.10. For the receiver term, the values of U_r, V_r and W_r are evaluated at the free surface.

Along the great circle path, the phase and group velocities in each $2° \times 2°$ cell are calculated at each frequency interval, along with the distance travelled through each given grid square. Because the dispersion characteristics differ from model square to model square, the eigenfrequency calculated for a given angular order of vibration will vary along the path. To account for this, dispersion curves in each square are interpolated and mapped onto the $\omega - l$ pairs calculated for PREM. As a result, phase velocities corresponding to identical frequencies of vibration are summed along the great circle path through the model. Estimates of the average

phase and group velocities, $\bar{c}(\omega)$ and $\bar{C}(\omega)$, respectively, along the path are thus given by:

$$\bar{c}(\omega) = \frac{\sum_{k=1}^{N} l_k}{\sum_{k=1}^{N} \frac{l_k}{c(\omega)_k}}, \tag{2.13}$$

and

$$\bar{C}(\omega) = \frac{\sum_{k=1}^{N} l_k}{\sum_{k=1}^{N} \frac{l_k}{C(\omega)_k}}, \tag{2.14}$$

where l_k is the length of the great circle path through the kth square and N is the total number of grid squares traversed between the source and receiver.

In this study, the source is considered to be a single point dislocation; the seismic moment tensor, $\mathbf{M}$, is a symmetric 3×3 matrix whose elements define the nine different couples that can act at a given point (Aki & Richards, 1980). The eigenvectors of this tensor define the source orientation, and the source type is described by the eigenvalues. By symmetry, the moment tensor contains only six independent quantities M_{rr}, $M_{\theta\theta}$, $M_{\phi\phi}$, $M_{r\theta}$, $M_{r\phi}$ and $M_{\theta\phi}$, where the subscripts r, θ and ϕ refer to the radial (up), latitudinal (South) and longitudinal (East) components. These components are also referred to as f_1, f_2, f_3, f_4, f_5 and f_6 respectively.

The seismic moment tensor can contain isotropic, compensated linear vector dipole (CLVD) and double-couple (D-C) components (Frohlich & Apperson, 1992). It might be expected that an explosion, where all P-wave arrivals are positive, would contain a significant isotropic component. Slip on a curved fault surface (Agnieszka & Sipkin, 1987; Frohlich, 1990), a series of sub-events rupturing non-parallel fault surfaces (Wallace, 1985), the fluid-driven opening of tensile cracks (Chouet & Julian, 1985; Chouet, 1986) and earthquakes close to volcanoes (Nettles & Ekström, 1998) have all been shown to give rise to the presence of CLVD components.

Despite global earthquake catalogues containing many solutions with non D-C components, a tectonic earthquake is considered to be a shear dislocation described by a D-C source. Shallow earthquakes, in particular, are not associated with substantial volume changes (i.e. the

isotropic component is considered to be zero) and observations of significant CLVD components are also rare, found mostly in complex tectonic settings. Non-source deviations from pure D-C mechanisms have been attributed to incorrect focal depths and faults intersecting major structural discontinuities, such as the Moho (Dziewonski & Woodhouse, 1983); small signal-to-noise ratios and poor station distributions (Panza & Sarao, 2000) or poor resolution of the $M_{r\theta}$ (f_4) and $M_{r\phi}$ (f_5) components of the moment tensor (Kuge & Lay, 1994; Henry et al., 2002).

Considering a pure D-C source, describing the orientation of a shear fault and the slip occurring on it, the seismic moment tensor components are described in terms of strike (ϕ_s), dip (δ) and rake (λ) angles as follows:

$$\begin{pmatrix} M_{rr} \\ M_{\theta\theta} \\ M_{\phi\phi} \\ M_{r\theta} \\ M_{r\phi} \\ M_{\theta\phi} \end{pmatrix} = M_0 \begin{pmatrix} \sin 2\delta \sin\lambda \\ -(\sin\delta\cos\lambda\sin 2\phi_s + \sin 2\delta \sin\lambda \sin^2\phi_s) \\ \sin\delta\cos\lambda\sin 2\phi_s - \sin 2\delta\sin\lambda\cos^2\phi_s \\ (\cos\delta\cos\lambda\cos\phi_s + \cos 2\delta\sin\lambda\sin\phi_s) \\ \cos\delta\cos\lambda\sin\phi_s - \cos 2\delta\sin\lambda\cos\phi_s \\ -(\sin\delta\cos\lambda\cos 2\phi_s + \frac{1}{2}\sin 2\delta\sin\lambda\sin 2\phi_s) \end{pmatrix}. \tag{2.15}$$

M_0 is the scalar seismic moment defined as:

$$M_0 = \mu A u, \tag{2.16}$$

where μ is the rigidity in the source region, A is the area of the fault estimated to have ruptured and u is the fault slip (after Aki & Richards, 1980).

The point-source is fixed at the origin time and the latitude and longitude as listed in the National Earthquake Information Center (NEIC) Bulletin[1]. The depth of the centroid location is varied across a suitable range and at each discrete depth interval and source-receiver pair, six synthetic seismograms (e_1, e_2, e_3, e_4, e_5 and e_6) are generated which represent the unit excitation relating to each of the six components of the seismic moment tensor. Using Equations 2.8 and 2.10 for Rayleigh and Love waves respectively, the first elementary seismogram (e_1) is calculated for the moment tensor (1,0,0,0,0,0); the second elementary seismogram (e_2) is calculated for (0,1,0,0,0,0) and so on. The final seismogram ($u(t)$) is obtained by summing

[1]http://neic.usgs.gov/neis/epic/epic_global.html

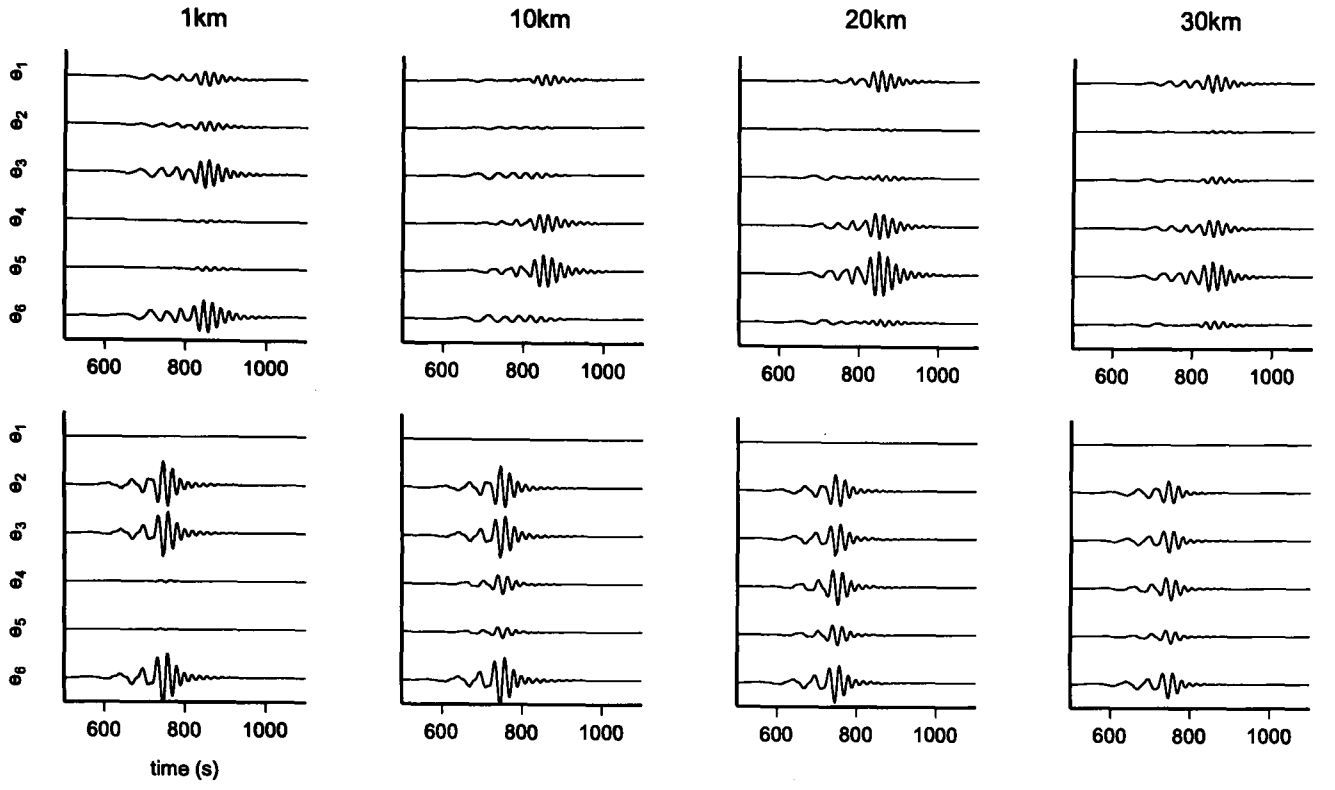


Figure 2.6: Rayleigh (top) and Love (bottom) wave excitation kernels (e_1–e_6) for an event in Southern Xinjiang, western China (event 013099A, studied in more detail later), calculated at station HIA (Hailar, Inner Mongolia) for depths (h) between 1 km and 30 km. The station is located at a distance of 2566 km and an azimuth of 60.1° from the source.

each elementary seismogram multiplied by the corresponding moment tensor component:

$$u(t) = \sum_{i=1}^{6} f_i e_i(t), \tag{2.17}$$

where i is the corresponding number of the element of the seismic moment tensor.

Figure 2.6 shows examples of six Rayleigh and Love wave excitation kernels (labelled e_1 to e_6) generated for an event in Southern Xinjiang, western China (event 013099A, epicentre 41.67°N 88.46°E) and recorded at station HIA (Hailar, Inner Mongolia, 49.27°N 119.74°E) in this study for 1 km, 10 km, 20 km and 30 km source depths (h) using the CUB Earth model. For both types of waves the e_4 and e_5 components are very small at 1 km and ground motion is relatively insensitive to the f_4 and f_5 components of the moment tensor as the tangential stress related to them is required to vanish at the free surface.

After these excitation kernels have been calculated for all receivers, they can be combined with the six corresponding components of the moment tensor, summed together and multiplied by an appropriate scalar seismic moment in order to generate full synthetic seismograms allowing

comparisons with recorded data to be made.

2.2.4 1-D Earth Seismograms

Full, three-component synthetic seismograms using the 1-D PREM Earth model are generated for event 013099A in western China and are shown in Figure 2.7. These waves are computed for all periods down to $T_{\text{cut}} = 100\,\text{s}$ at ten stations with varying epicentral distance and azimuth from the source. For comparison, PREM synthetic seismograms generated using an established mode summation program (APSYNAH, after Woodhouse, 1988) are also shown. Both sets of synthetics were computed using the same Earth model and the same source mechanism, that listed in the CMT catalogue. In all traces the waves are in phase, with the only differences being some small variations in amplitudes attributable to round-off errors in the calculations. All of these raw displacement seismograms are shown as they were calculated with no filtering applied, which is why they all exhibit a degree of ringing. This can be removed with the application of a frequency domain taper around the cut-off frequency, and this is applied to all further synthetics shown in this study.

2.2.5 3-D Earth Seismograms

Examples of synthetic seismograms calculated using the 3-D CUB Earth model are presented in Figure 2.8. Here both 1-D and 3-D Earth synthetics are shown along with recorded waveforms at ten stations located at various azimuths from the 1995 Kozani-Grevena, Greece, earthquake (event 051395B). Synthetic seismograms, converted to displacement and corrected for instrument response, are generated for Love (transverse, T channel) and Rayleigh (vertical, Z channel) waves. All traces are bandpass-filtered between 100–50 s and undergo time variable filtering (TVF, after Pilant & Knopoff, 1964; Landisman et al., 1969) which removes noise and additional signals (body wave and surface wave overtone arrivals), allowing waveform comparisons to be representative of the fundamental-surface wave arrivals (see Appendix B). The CUB synthetics can be seen to provide better matches to the data than the PREM waveforms. For the Love waves, 3-D synthetics are markedly better than the 1-D synthetics at stations ATD (Arta Tunnel, Djibouti), BGCA (Bogoin, Central African Republic) and KIEV (Kiev, Ukraine). For the Rayleigh waves, 3-D waveform matches at stations ARU (Arti, Russia), BRKV (Borovoye, Kazakhstan), DBIC (Dimbokro, Cote d'Ivoire) and KEV

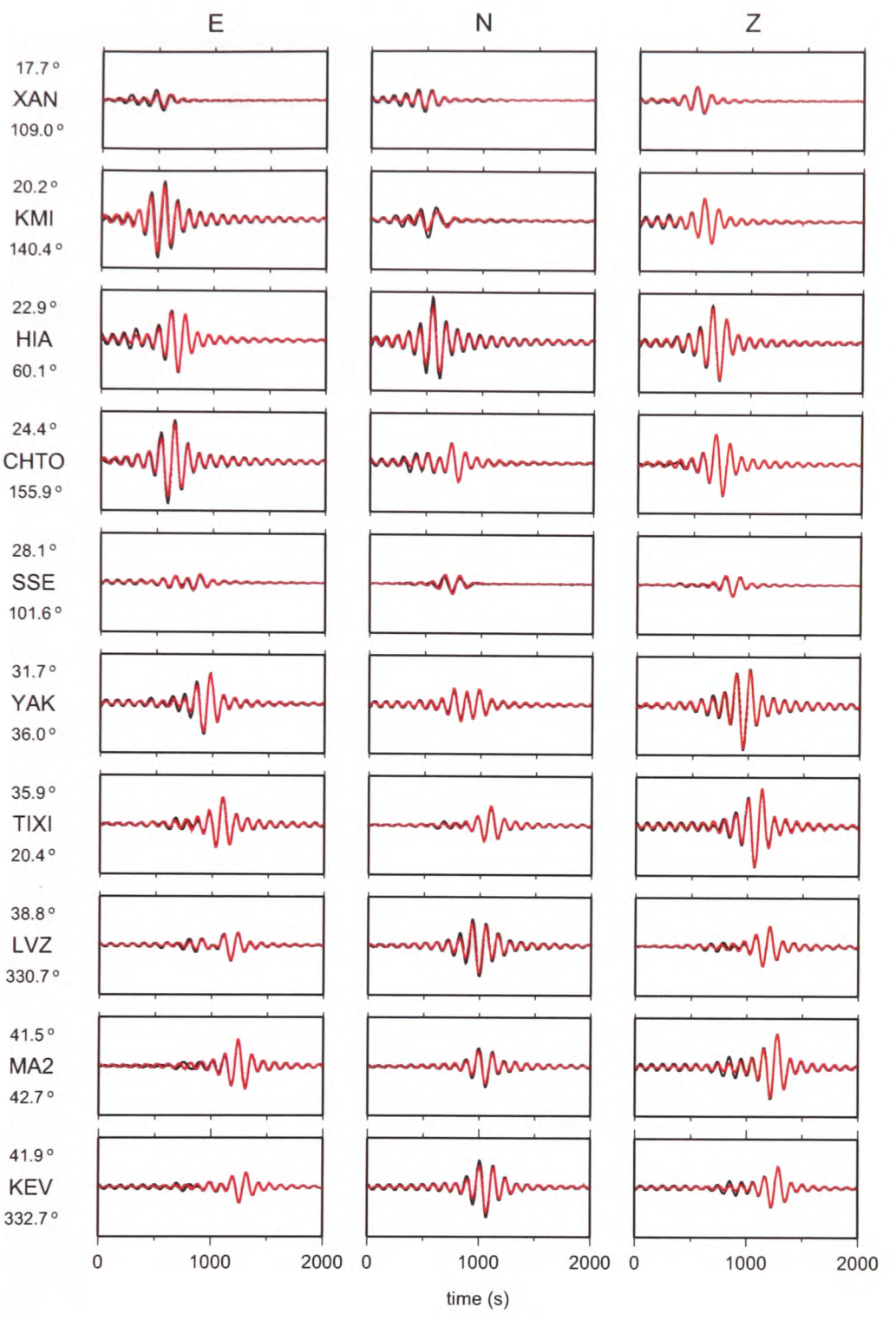


Figure 2.7: Full, three-component synthetic seismograms for event 013099A in western China using the PREM model and CMT mechanism (ϕ_s=116°, δ=36°, λ=99°, h=23 km). Black traces are those generated by an established mode summation program whilst red traces are those calculated in this study. East and North channels are denoted by 'E' and 'N', respectively, whilst the vertical channel is indicated by 'Z'. Station codes are shown by each set of traces, the numbers above and below each code are the epicentral distance and azimuth (both in degrees) respectively of the station from the source. A common amplitude scale is used for all traces.

(Kevo, Finland) are much closer than those using 1-D synthetic seismograms.

Considering amplitude estimates, the PREM synthetics do provide close matches to the data waveforms in Figure 2.8. In addition, the source mechanism used to generate these synthetics (ϕ_s=244°, δ=44°, λ=-106°, h=7 km) was selected as it was close to that determined by the CMT method, but it is not necessarily the best fitting mechanism and as a result the waveforms may not optimised. Nonetheless, it is clear that the 3-D Earth synthetics are more accurate, promoting confidence that seismograms generated in this study are likely to be representative of those observed in the Earth.

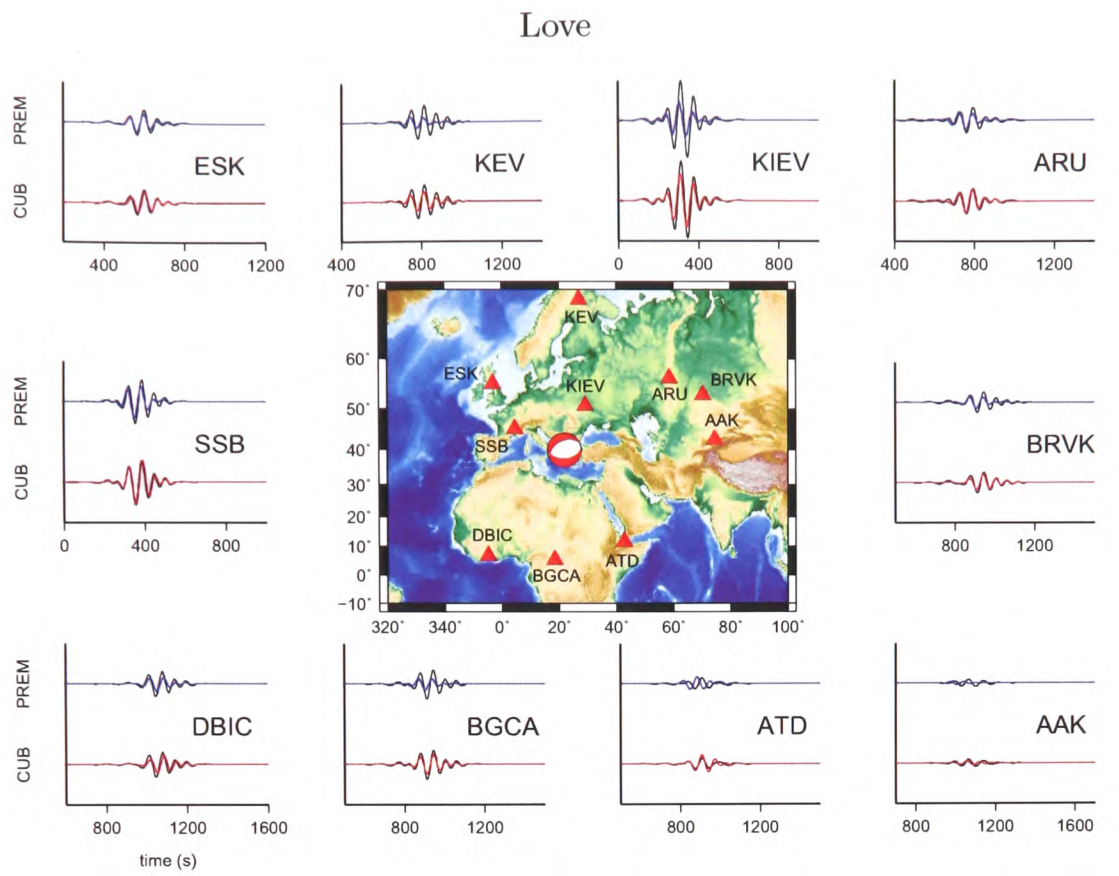


Figure 2.8: 1-D PREM (blue) and 3-D CUB (red) synthetic Love and Rayleigh wave seismograms calculated at ten azimuthally distributed stations for event 051395B (13 May 1995, Kozani-Grevena, Greece). Recorded waveforms are shown in black for comparison and all traces are band-pass filtered between 100–50 s. The similarity in amplitudes between the 1-D and 3-D seismograms is due, in part, to the common attenuation model used in the two models (see Appendix A).

2.3 Isolating the Fundamental-Mode Arrivals

2.3.1 Data Selection

East, North and vertical channel recordings are selected from stations lying in the minor-arc epicentral range $10° < \Delta < 60°$ for events of interest. Recordings at stations where $\Delta < 10°$ are not considered because the fundamental-mode surface waves arrive along with body waves and overtones and it is difficult to separate the individual arrivals. Stations where $\Delta > 60°$ are generally discarded as the wavetrain becomes highly dispersed over these distances, errors in the velocity model can become accentuated and accurate predictions of group velocity arrival times are difficult to make. However, in instances where there are few available recordings, it may be necessary to identify recordings outside of this range and analyse their suitability for inclusion in the study. All data used in this study is obtained from the IRIS (Incorporated Research Institutions for Seismology) DMS (Data Management System)[2].

Recordings with low signal-to-noise ratios are discarded; all traces are corrected for instrument response and converted to displacement. In this study the channel names of recordings are kept for continuity, e.g. LHE, LHN, LHZ, LHL and LHT refer to the East (E), North (N), vertical (Z), longitudinal (L) and transverse (T) components respectively. The horizontal components, LHE and LHN, are rotated into the longitudinal and transverse directions, LHL and LHT respectively. Each LHZ and LHT channel trace is then bandpass-filtered to produce two separate waveforms; firstly, with cosine tapers at 100 s (high-pass) and 20 s (low-pass) and secondly between 100 s (high-pass) and 50 s (low-pass). The amplitude spectra of the 100–20 s traces are used in the determination of source parameters here, with the 100–50 s seismograms being used in waveform comparisons with recorded data and analysed to assess the accuracy of the resultant synthetic seismograms. Examples of original seismic recordings and their subsequent conversion to 100–20 s and 100–50 s displacement waveforms are shown in Figure 2.9. LHZ, LHE, LHN and the rotated LHL and LHT channels are shown here for recordings of event 013099A at station TLY (Talaya, Russia).

What follows in this section is a discussion of the various techniques employed in the processing of the data used to best identify, isolate and analyse the fundamental-mode arrivals in a seismic wavetrain.

[2] www.iris.edu

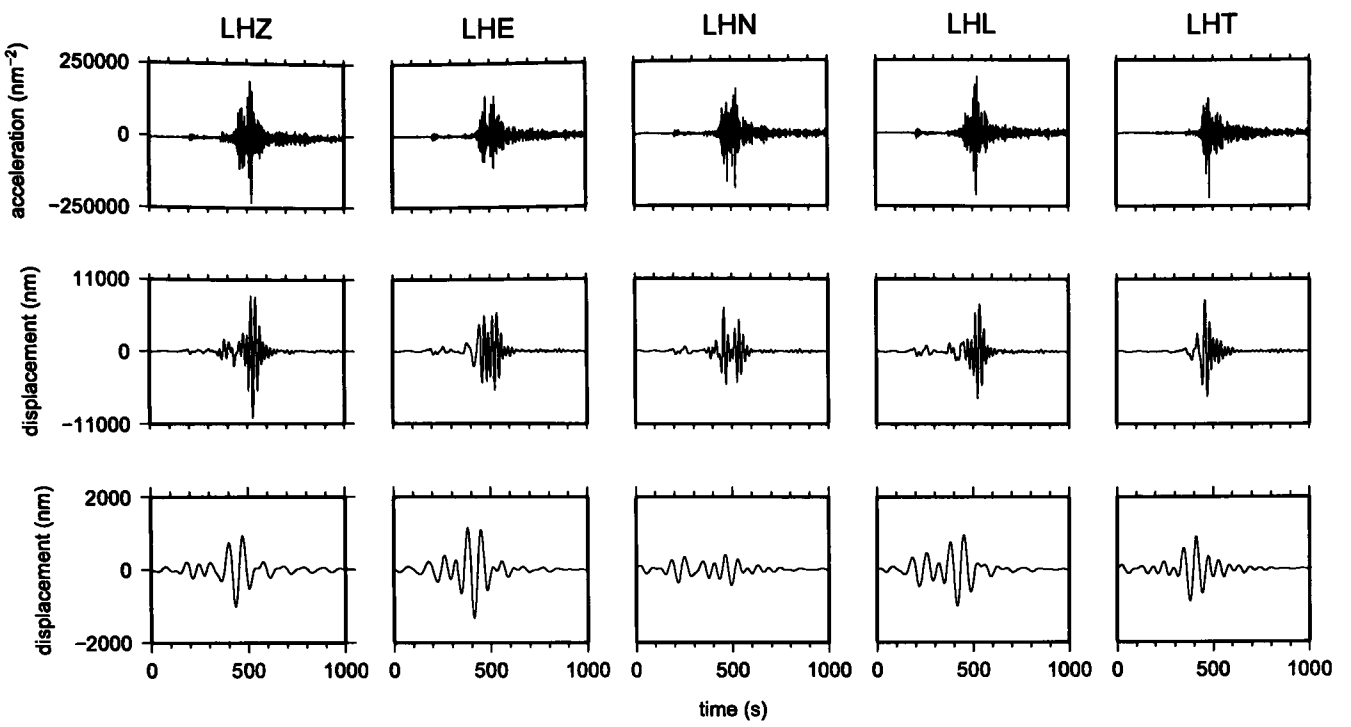


Figure 2.9: Examples of original traces (top) and their subsequent conversion to displacement waveforms filtered between 100–20 s (middle) and 100–50 s (bottom) for event 013099A recorded at station TLY in Russia. The horizontal LHE and LHN channels were rotated to generate the LHL and LHT channels.

2.3.2 Frequency-Time Analysis and the Multiple Filter Technique

Frequency-Time Analysis (FTAN, Levshin et al., 1989) is the method by which a recorded seismogram can be analysed in the frequency-time domain and, in the case of a dispersive wavetrain, this is a particularly advantageous method of study. By plotting a seismic signal in both frequency and time an analyst can identify the times of the frequency-dependent peak energy arrivals and determine a group velocity curve as a result. In the absence of accurate Earth models this type of analysis was necessary to allow the derivation of the Earth's structure in terms of elastic parameters from observations of its dispersive properties (Dziewonski & Hales, 1972). In this study, all estimates of dispersion are calculated from tracing source-receiver paths through the CUB Earth model and averaging the frequency-dependent phase and group velocities. As such, FTAN is not used for analysis but it still provides a useful visualisation tool, especially in the verification of the processing techniques described later in this section.

In order to optimise the identification of a seismic signal, the Multiple Filter Technique (MFT) is used. The MFT has been shown to be a fast and efficient means of studying multi-mode dispersed signals (Dziewonski et al., 1969). A wavetrain is passed through many filters centred

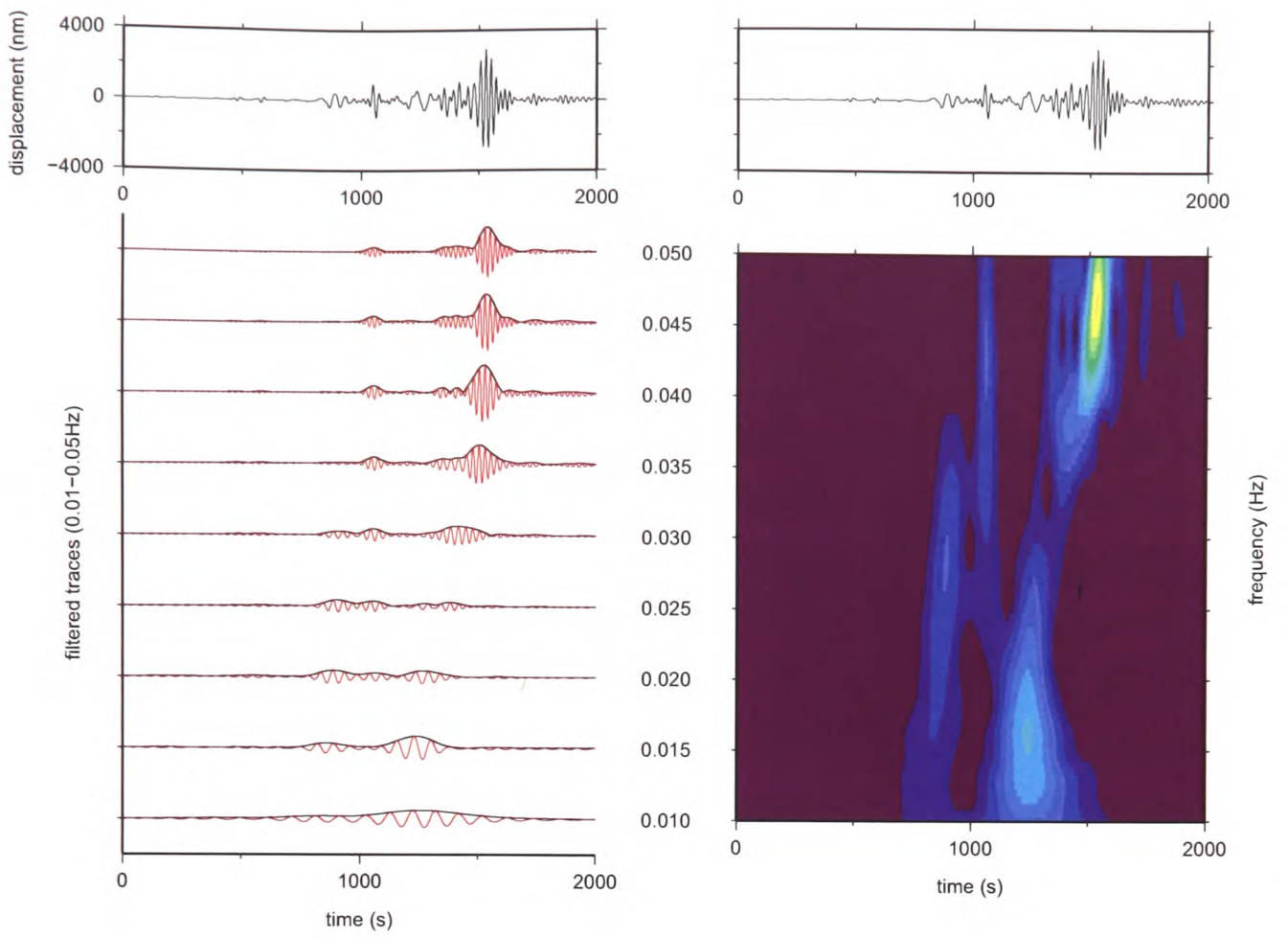


Figure 2.10: LHZ channel recording of event 013099A at station MA2 in Russia (top). Narrow-bandpass-filtered traces and envelope functions are shown from 0.01–0.05 Hz at 0.005 Hz intervals. The combination of these envelopes creates the FTAN contour plot on the right, where the brighter colours indicate higher amplitude energy arrivals. Many more frequency intervals are used in the creation of this frequency-time plot than just the nine shown. The dispersive fundamental-mode surface wave arrival is clearly seen in this contour plot, as well as the non-dispersive body wave arrivals. For clarity the frequency-time plot is shown in increments of linear frequency increments; this is in contrast to later figures where logarithmic frequency scales are used.

on a range of frequencies, with the result being a contour plot of intensity of the wavetrain content resolved in frequency and time. The technical details of the choice of filter parameters are best described by Inston et al. (1971) and Cara (1973); a condensed analysis can be found in Appendix B.

An example of a calculated contour plot is presented in Figure 2.10. The LHZ recording of event 013099A at station MA2 (Magadan, Russia) is shown along with the calculated filtered traces and their envelope functions. In addition to the clear fundamental-mode surface arrivals, the non-dispersive body wave arrivals are also evident. The highest amplitude arrivals can be seen to occur between 0.04 Hz and 0.05 Hz; because the waveforms are cosine-filtered between 20 s and 17.5 s there is little discernible signal at periods shorter than 20 s. This

cut-off is selected because at periods below 20 s it become increasingly difficult to distinguish the fundamental-mode from other arrivals (e.g. overtones and late arriving body waves) and model predictions of peak group velocity arrival times become less trustworthy.

2.3.3 Phase-Matched Filtering

The effective isolation of the surface wave fundamental-mode of dispersion is paramount in this study. Phase velocity estimates are calculated from the Earth model and used to remove the dispersion from a waveform, collapsing it about specific point in time. Once compressed, it is possible to window out noise and unwanted signals. By calculating the amplitude spectrum of the resultant waveform in a narrow time window, the amplitude spectrum is extracted from a signal considered to be representative of the fundamental-mode arrival.

This Phase-Matched Filtering technique (PMF, after Herrin & Goforth, 1977) is commonly used and well documented elsewhere (e.g. Levshin & Ritzwoller, 2001; Stevens & McLaughlin, 2001). Figure 2.11 shows examples of the use of predicted phase velocity curves to undisperse recorded seismograms around the centre of the time window (i.e. around 1000 s for a 2000 s window). Four recordings of event 013099A are shown along with their corresponding FTAN contour plots (a plot of their dispersive characteristics).

Phase velocity estimates from the CUB model are used to calculate the predicted frequency-dependent phase, $\Phi(\omega)_p$, at the receiver as follows:

$$\Phi(\omega)_p = \frac{D\omega}{\bar{c}(\omega)}, \tag{2.18}$$

where D is the source-receiver distance (in km). The phase at the centre of the time window, $\Phi(\omega)_c$, is calculated as:

$$\Phi(\omega)_c = \frac{L}{2}\omega, \tag{2.19}$$

where L is the total length of the time window (2000 s). The difference between these two phases, $\Phi(\omega)_d$, is the phase shift required to collapse the predicted group arrivals around the centre of the time window. Here $\Phi(\omega)_d$ is simply given by:

$$\Phi(\omega)_d = \Phi(\omega)_c - \Phi(\omega)_p. \tag{2.20}$$

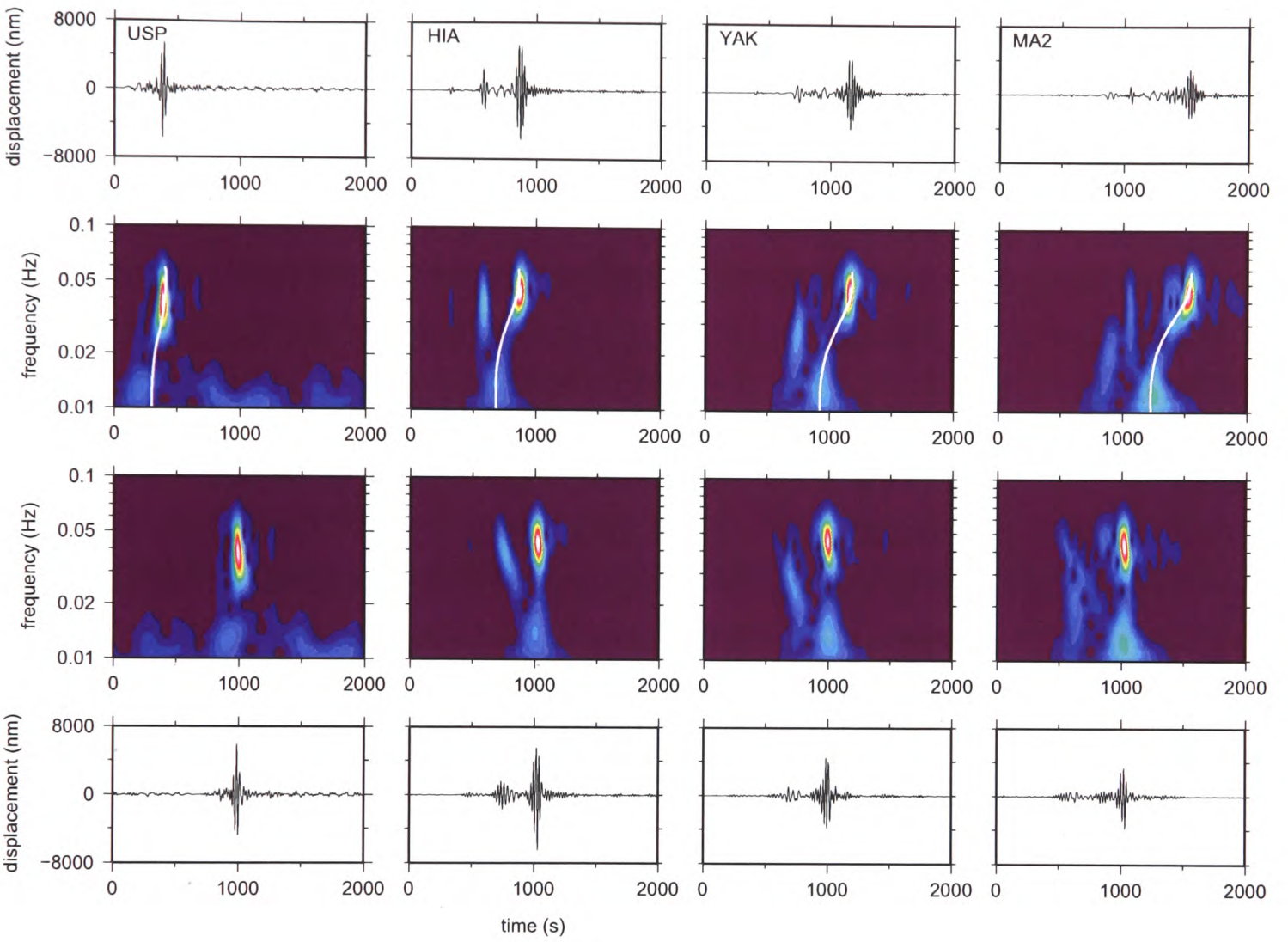


Figure 2.11: Four vertical displacement recordings of the 013099A earthquake in western China. Seismograms are shown in increasing epicentral distance from the source, with stations between 1161 km (USP, Uspenovka, Kazakhstan) and 4630 km (MA2, Magadan, Russia). Beneath the original seismograms are the respective FTAN contour plots showing the frequency-dependent energy arrivals and the predicted group velocity arrival times (white line) and below these are the resulting contour plots with the dispersion removed. The bottom waveforms are the resultant undispersed seismograms, centred about the middle of the time windows.

By applying this phase shift to the recorded data the fundamental-mode surface wave peak group arrivals are centred about the middle of the time window. Any deviations in this resultant, compressed, seismogram from the centre of the time window are attributable to differences in the predicted and recorded dispersion in the signal. In all cases in Figure 2.11 it is clear that the dispersive characteristics predicted by the CUB model appear to closely match those seen in the data. The ability to compare model predictions with recorded measurements of dispersion offers an opportunity to validate the performance of the dispersion characteristics predicted by the CUB model; this analysis is performed in Chapter 5.

Unwanted signals and noise are removed by applying a cosine bell window around the compressed signal. This time-domain filter is described by a maximum width, t_{win}, and a parameter, p, which corresponds to the fraction of the window that is cosine tapered. For example a window 100 s wide with $p = 0.1$ would have cosine tapers of width 10 s at each end. As such the parameter p can take any value between 0, where no tapers are applied (i.e. a boxcar), and 0.5, where the window is of the form of two, back-to-back, cosine tapers. Here choices of $t_{win} = 300$ s and $p = 0.1$ are made; the effects of varying these parameters are discussed in Appendix B. The selection of a windowing function 300 s wide is in agreement with Stevens & McLaughlin (2001) who report that, while a window as narrow as 100 s could be used in this kind of study, a 300 s time window was sufficiently wide to capture the complete surface wave arrival for nearly all paths while still providing significant noise reduction. As a result the time-domain windowing function ($W(t)$) applied in this study is described as follows:

$$W(t) = \begin{cases} \frac{1}{2}\left[1 - \cos(\pi\left[\frac{t-t_1}{t_2-t_1}\right])\right] & t_1 < t < t_2 \\ 1 & t_2 \leq t \leq t_3 \\ \frac{1}{2}\left[1 - \cos(\pi\left[\frac{t-t_1}{t_2-t_1}\right])\right] & t_3 < t < t_4 \end{cases} \tag{2.21}$$

So, for a signal in a 2000 s time window, collapsed around 1000 s, t_1=850 s, t_2=880 s, t_3=1120 s and t_4=1150 s.

The amplitude spectra of the windowed signal is extracted using a Discrete Fourier Transform (DFT, after Cooley & Tukey, 1965). The Fourier transform ($F(\omega)$) of this signal is a complex function of frequency and is given by:

$$F(\omega) = R(\omega) + iI(\omega), \tag{2.22}$$

where $R(\omega)$ and $I(\omega)$ are the real and imaginary parts respectively. It can also be expressed as

$$F(\omega) = A(\omega)e^{-i\Phi(\omega)}, \tag{2.23}$$

where

$$A(\omega) = \frac{\sqrt{[R(\omega)^2 + I(\omega)^2]}}{N\Delta}, \tag{2.24}$$

and

$$\Phi(\omega) = \tan^{-1}\left[\frac{I(\omega)}{R(\omega)}\right]. \tag{2.25}$$

Here $A(\omega)$ is the amplitude spectrum and $\Phi(\omega)$ is the phase spectrum. The amplitude spectrum is normalised by the quantity $N\Delta$, where N is the smallest power of 2 that is greater than the number of points in the original seismogram (e.g for a 2000 s long seismogram, sampled at 1 s, $N = 2048$), and Δ is the sampling interval (always 1 s in this study).

The size of the frequency steps ($\delta\omega$) of $A(\omega)$ and $\Phi(\omega)$ are determined by the number of points in the original time series, n, and the sampling interval as follows:

$$\delta\omega = \frac{1}{n\Delta}, \tag{2.26}$$

with the maximum frequency, called the Nyquist frequency (f_N), given by:

$$f_N = \frac{1}{2\Delta}. \tag{2.27}$$

Equations 2.26 and 2.27 show that the Nyquist is only ever determined by the sampling interval, Δ, but the number of discrete frequencies in an amplitude spectra depends proportionally on the number of points in the original seismic signal. As a result of this relationship, the windowing (and reduction in size) of seismograms in this study results in an increase in the size of the frequency intervals and a decrease in the number of discrete frequencies in the spectra; that corresponds to smoothing of the raw amplitude spectra in addition to the removal of unwanted signals.

2.4 Source Parameter Determination

2.4.1 Amplitude Spectral Modelling

It has long been known that the accurate modelling of fundamental-mode surface wave amplitude spectra can be used to constrain earthquake source parameters. Rayleigh wave amplitude spectra, in particular, have been demonstrated to be highly sensitive to changes in source depth as well as source mechanism. Until recent times the use of this approach has been restricted by the lack of accurate Earth models and the small number of seismic stations available.

Using the Equations (2.8) and (2.10) for the excitation of surface wave displacement, excitation kernels are generated for selected source-receiver pairs. In order to generate synthetic amplitude spectra, these elementary seismograms are converted into real ($R(\omega)$) and imaginary ($I(\omega)$) parts by the application of a DFT and then combined with the corresponding components of the seismic moment tensor as follows:

$$A(\omega_j) = \frac{\sqrt{\left(\sum_{i=1}^{6} R_i(\omega_j) f_i\right)^2 + \left(\sum_{i=1}^{6} I_i(\omega_j) f_i\right)^2}}{N\Delta} \tag{2.28}$$

where the amplitude at a given jth frequency, $A(\omega_j)$, is calculated by the sum of the square root of the sum of the squares of the product of the real and imaginary parts of the six excitation kernels combined with their corresponding moment tensor components. These amplitude spectra are then multiplied by an appropriate scalar seismic moment to best match the amplitudes of the recorded data.

Examples of synthetic amplitude spectra are presented in Figure 2.12. Synthetic Rayleigh and Love wave amplitude spectra are determined at four stations for an earthquake in western China, using a common focal mechanism (ϕ_s=300°, δ=40°, λ=100°) at depths between 10–25 km. The Rayleigh wave sensitivity to source depth is clearly evident, especially in the positions of notches in the amplitude spectrum at station TLY. At shallow depths, these nulls are seen to lie at higher frequencies; as the source depth is increased they migrate to the longer-periods. The Love wave amplitude spectra show little sensitivity to source depth, highlighting their primary dependence on source mechanism.

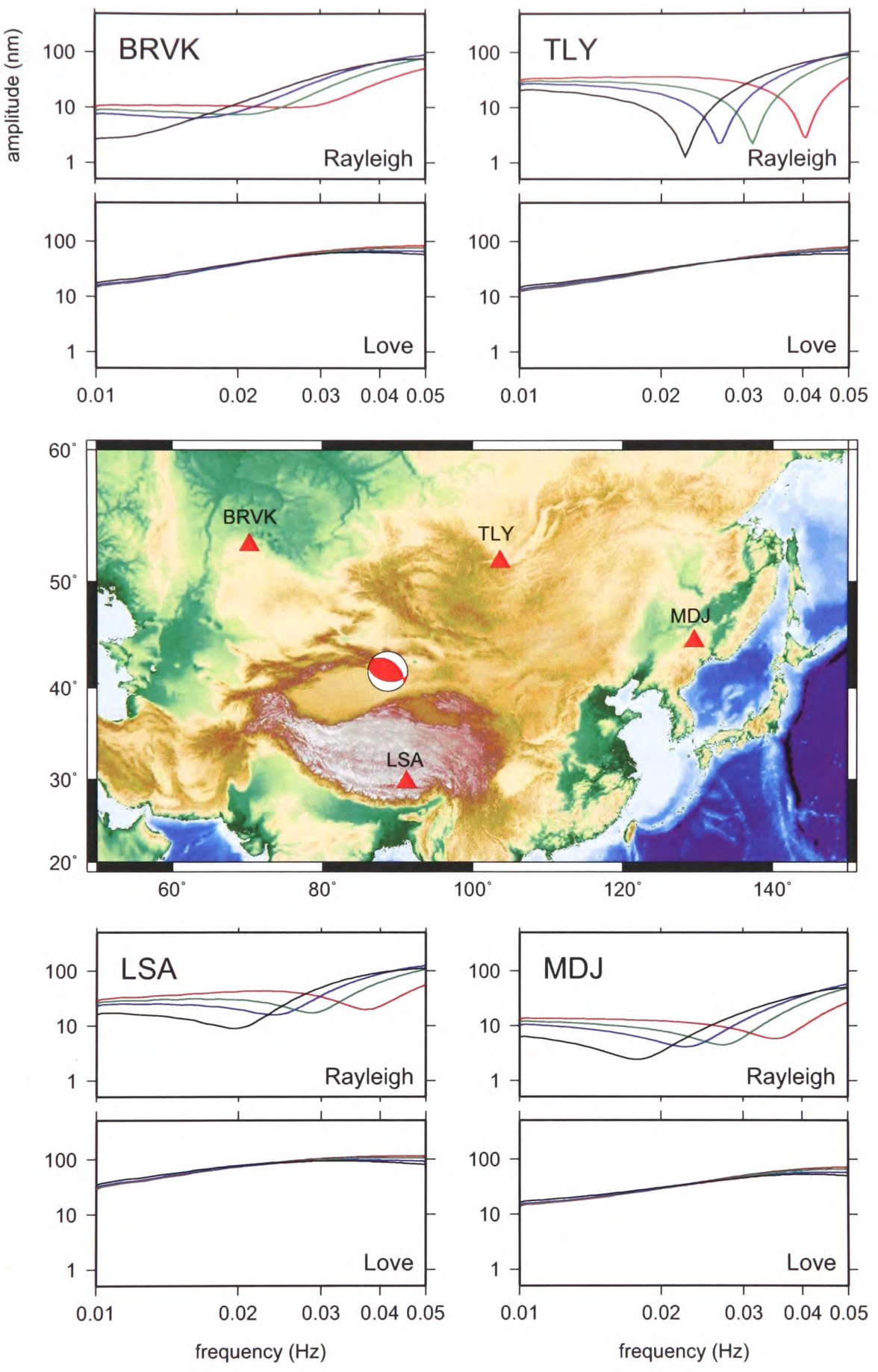


Figure 2.12: Synthetic amplitude spectra calculated at four stations for a source (ϕ_s=300°, δ=40°, λ=100°) in western China (indicated by the position of the 'beach ball' representation of the fault plane solution). Note the strong variations in the patterns of the Rayleigh wave amplitude spectra compared to the Love waves. Amplitude spectra are plotted for source depths at 10 km (red), 15 km (green), 20 km (blue) and 25 km (black).

2.4.2 The Search for Optimal Source Parameters

The processes described in this section are summarised at the bottom of Figure 2.1. So far it has been described how, for an identified event, appropriate data sets are procured, records with good signal-to-noise ratios are selected and processed. Synthetic amplitude spectra are generated for each source-receiver pair and then compared with data in a grid-search to determine the selection of optimum source parameters.

In order to consider every possible D-C source, a four-dimensional (4-D) grid-search is performed over the source parameters strike, dip, rake and depth. Strike, dip and rake space is searched in 2° increments and depths are systematically varied in 1 km steps. For each $(\phi_s,\delta,\lambda,h)$ combination, the six components of the seismic moment tensor are calculated using Equation (2.15) and are combined with the real ($R(\omega)$) and imaginary ($I(\omega)$) parts of the corresponding excitation kernels as described in Equation (2.28).

A series of weights is assigned in this work to account for variations across the data sets used. To account for non-uniform distribution of receivers, an azimuthal weighting is imposed across all stations. Relative weights are assigned to stations according to the number of other receivers within a 15° azimuth range of the source as follows:

$$\Psi_{az} = \frac{1}{S}, \tag{2.29}$$

where S is the total number of stations lying within a 15° azimuthal sector from the source. For instance, a station with no other stations within $\pm 7.5°$, would receive a weighting of 1.0. In the case of three other stations lying with 15°, the station would get a weighting of 0.25. This weighting is performed separately for both Love and Rayleigh wave recordings, so Love and Rayleigh wave data recorded at a station with no other receivers within $\pm 7.5°$ would both be weighted 1.0.

Figure 2.13 shows examples of this azimuthal weighting in two different cases. The first example is of the regional receiver coverage around the 1995 Kozani-Grevena, Greece, earthquake. The abundance of continental landmass in all directions leads to a good azimuthal coverage of stations such that many recordings are weighted 1.0; the closely spaced stations to the north-west being appropriately down-weighted. The second example shows the regional coverage for the 2004 Parkfield, California, earthquake. Here, with the bulk of the landmass being to the

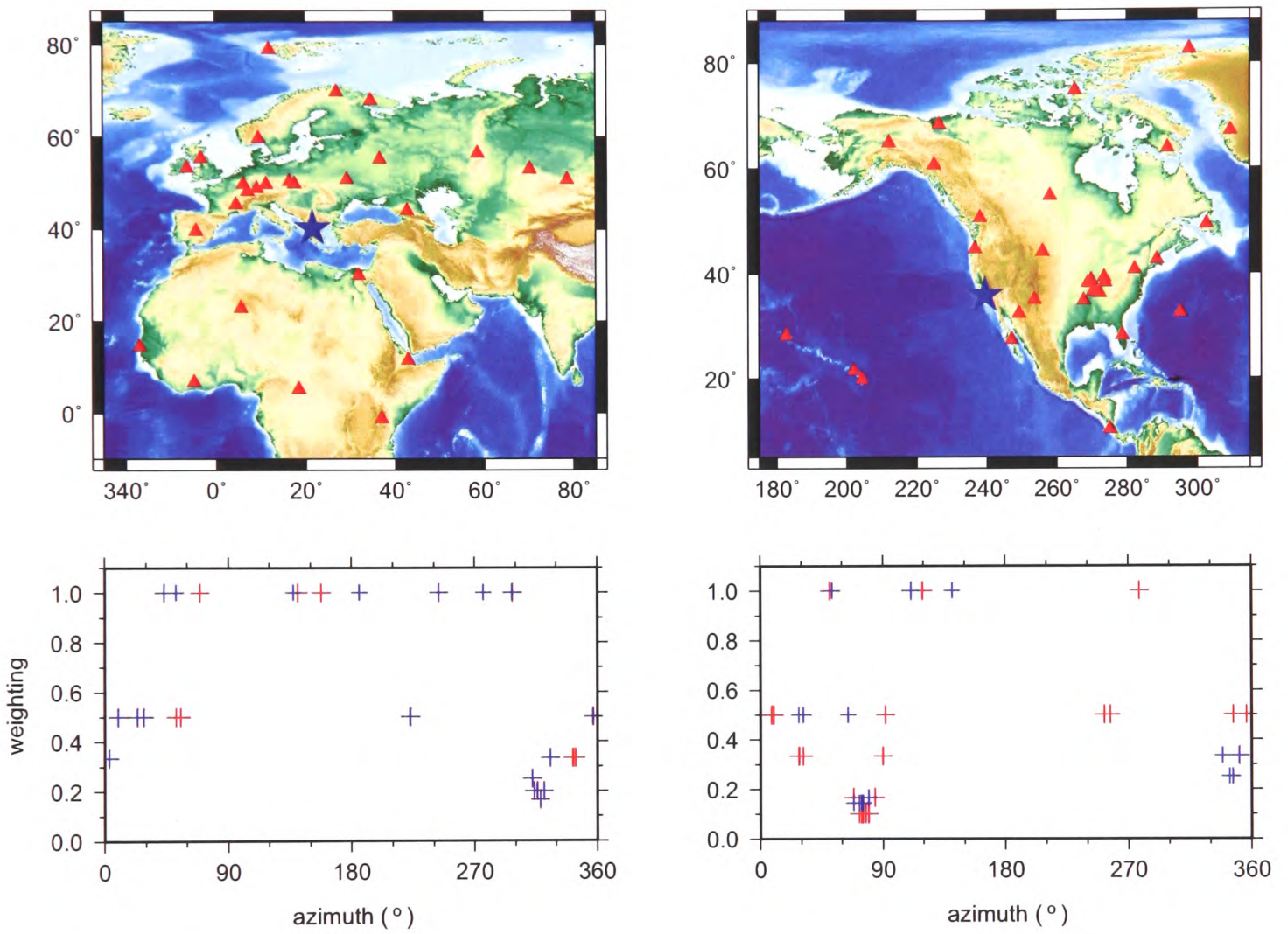


Figure 2.13: Examples of differences in the azimuthal coverage of regional recordings of two earthquakes according to their location. LHS: map of the 1995 Kozani-Grevena, Greece, earthquake and the regional receiver distribution (top). Below the map is a graph of weightings against azimuth, showing that many stations receive high weightings due to the good azimuthal cover provided (red crosses denote Rayleigh wave recordings, Love wave recordings are shown in blue). In contrast the RHS plots show the 2004 Parkfield, California, earthquake and the available receiver coverage. The azimuthal distribution of stations is very much constrained by the Pacific Ocean to the west, with the bulk of receivers lying on the North American continent, those almost due east of the source are especially bunched.

east (i.e. continental North America), there are few recordings that are not down-weighted, indeed the cluster of stations due east of the earthquake can be seen to be weighted between 0.1–0.2.

More confidence is placed in both the recorded data and synthetic seismograms at the longer-periods; to reflect this a frequency-dependent weighting is also applied. It allocates greater weight to the longer-period end of the amplitude spectra and is defined as follows:

$$\Psi_\omega = \frac{1}{\omega}. \tag{2.30}$$

The final weighting pertains to how well the CUB model is determined to have predicted the dispersion for a given source-receiver path. In addition to accounting for frequency-dependent variations by applying the Ψ_ω weighting, allowances are also made for serious discrepancies in the model predictions of group velocity arrivals. At the higher frequencies, in particular, predicted and recorded dispersions deviate somewhat and when this occurs, it is appropriate to reduce the influence of specific observations further. At the frequencies at which these large deviations occur, a wavetrain will not be accurately undispersed, and any subsequent windowing function will not capture all of the recorded surface wave arrival. Thus analysis is performed on the undispersed arrival at a given frequency and if this falls outside of a pre-described range, the observation is accordingly downweighted as:

$$\Psi_C = \begin{pmatrix} 1 & |(t_{arr}(f) - t_0)| \leq \frac{t_{win}}{4} \\ \{\ 1 - \left(\frac{|t_{arr}(f) - t_0| - \frac{t_{win}}{4}}{\frac{t_{win}}{4}} \right) & \frac{t_{win}}{4} < |(t_{arr}(f) - t_0)| < \frac{t_{win}}{2} \\ 0 & |(t_{arr}(f) - t_0)| \geq \frac{t_{win}}{2} \end{pmatrix}, \tag{2.31}$$

where $t_{arr}(f)$ is the frequency dependent arrival time, t_0 is the centre of the time window (e.g. 1000 s for a 2000 s seismogram) and t_{win} is the width of the windowing function determined earlier (300 s). In this study if an energy peak arrives within $\pm$ 75 s of the predicted arrival time, then an observation is weighted 1.0, those arrivals which are between either -150 s and -75 s or 75 s and 150 s are weighted linearly as they increase distance away from the predicts arrival time. Any observations falling outside $\pm$ 150 s of the prediction are weighted 0.0 as they fall outside of the windowing function.

Examples of the application of this weighting are shown in Figure 2.14. FTAN contour

plots of the LHZ channel recording at station DBIC (Dimbokro, Ivory Coast) and the LHT channel recording at station BNG (Bangui, Central African Republic) of the 1995 Dinar, Turkey, earthquake are shown, along with their subsequent undispersing and the calculation of dispersion-related weights. At station DBIC the dispersion is accurately predicted until ~0.035 Hz when the peak energy arrives significantly later. These arrivals are not from the fundamental-mode and are therefore downweighted accordingly. At station BNG, clear fundamental-mode arrivals cease at around 0.04 Hz, after which the peak arrivals are significantly offset from the centre of the window and are assigned a series of weights appropriately.

In instances where the recorded dispersion is not well predicted by the model the windowing function could be widened to account for such discrepancies. However, this could potentially lead to the inclusion of unwanted signals at other periods and so this option is rejected. In addition, the introduction of a series of weights relating to source-receiver epicentral distance was considered, but this was similarly rejected due to the lack of evidence in the 10–60° epicentral distance range that recordings at distant stations were less trustworthy than those close to the source. Ammon et al. (2003) analysed misfits between data and computed synthetics and also drew this conclusion. Further evidence supporting this decision is presented in Chapter 5.

Unlike strike, dip, rake and depth, which are easily discretised (and lend themselves to a grid-search algorithm), the scalar seismic moment is not and the choice of a suitable incremental step in such a grid-search is not necessarily straightforward. To keep the number of grid-search parameters as low as possible, with computer run times in mind, estimates of the scalar seismic moments are derived by scaling the unit synthetic amplitude spectra to the observed data as follows:

$$M_0 = \frac{\sum_{j=1}^{T}\sum_{i=1}^{N} d_{ij}\Psi_{ij}}{\sum_{j=1}^{T}\sum_{i=1}^{N} s_{ij}\Psi_{ij}}, \tag{2.32}$$

where d_{ij} and s_{ij} represent the amplitude spectra of data and synthetic traces respectively, T is the total number of traces, N is the number of discrete frequencies in the amplitude spectra and Ψ_{ij} is the combination of applied weights $(\Psi_{az}, \Psi_{\omega}, \Psi_{C})$ for a given trace and frequency.

Synthetic amplitude spectra are generated for every strike, dip, rake, depth combination in 2° increments for strike (0–180°), dip (0–90°) and rake (0–180°) and 1 km increments in depth

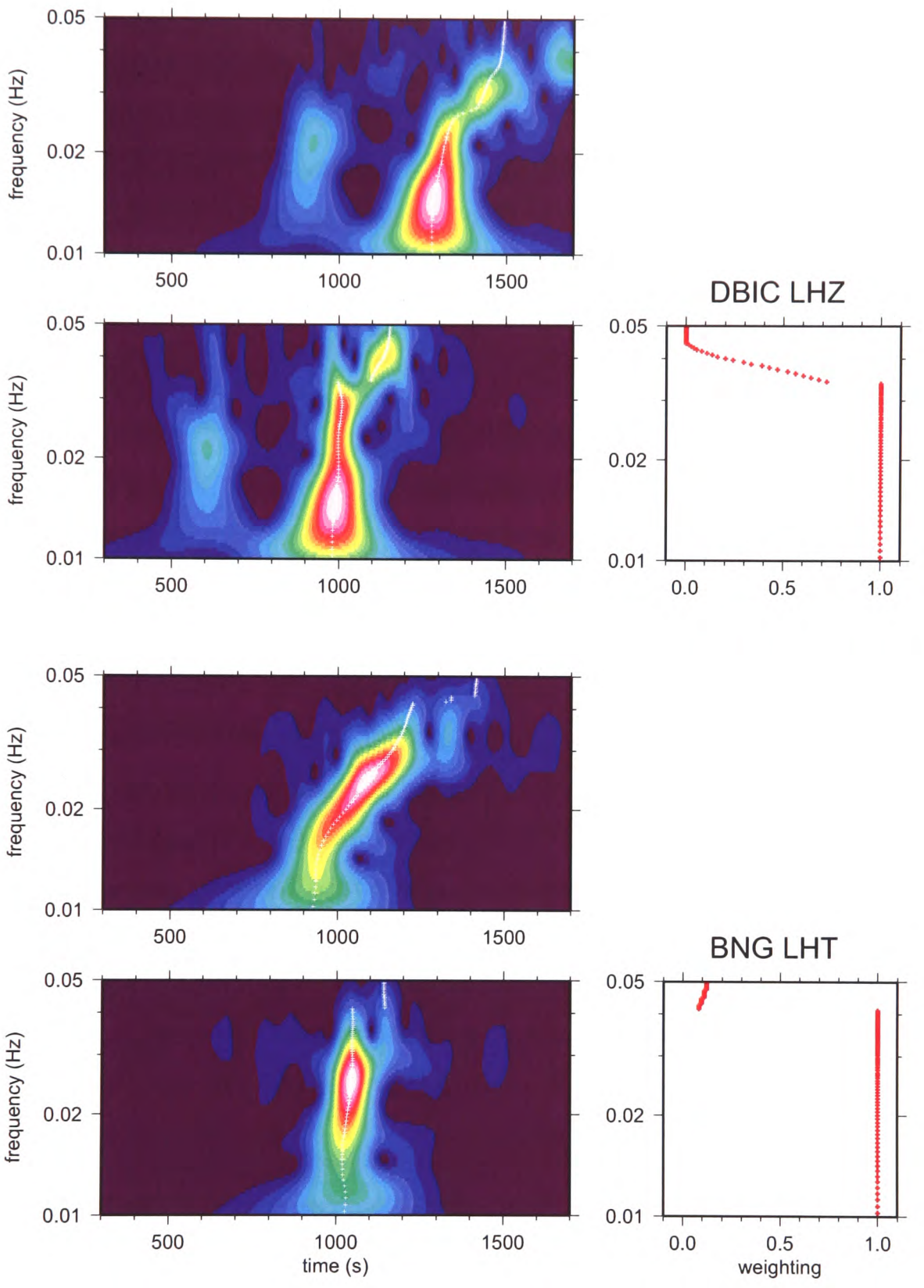


Figure 2.14: Examples of weighting according to the accuracy of the dispersion curves predicted by the CUB model for the 1995 Dinar, Turkey, earthquake as recorded at stations DBIC (Dimbokro, Ivory Coast) and BNG (Bangui, Central African Republic). The upper three plots pertain to the LHZ channel recording at DBIC and show the original FTAN contour plot (top), the undispersed FTAN contour plot (below) and a weighting chart to the right. The white crosses on the FTAN contour graphs show the position of maximum amplitude at a given frequency, i.e. the peak group arrivals. The lower three plots show the same information, but for the LHT recording at BNG.

over a suitable range. Only the interval range 0–180° in strike and rake is considered because of the 180° symmetry in both strike and rake in the surface wave amplitude radiation patterns (Mendiguren, 1977); thus reducing computing run times by a factor of four.

A least squares calculation of the misfit, m, between the synthetics and the processed data is performed in logarithmic amplitude space to identify the source parameters which generate the best-matching amplitude spectra. This misfit value is determined as follows:

$$m = \frac{\sum_{j=1}^{T}\sum_{i=1}^{N}(\log d_{ij} - \log s_{ij})^2 \Psi_{ij}^2}{\sum_{j=1}^{T}\sum_{i=1}^{N}(\log d_{ij})^2 \Psi_{ij}^2}, \tag{2.33}$$

where T and N are the the total number of amplitude spectra and total number of discrete frequencies in a given amplitude spectrum, respectively; d_{ij} and s_{ij} represent the amplitudes of the data and synthetic amplitude spectra at the jth frequency in the ith trace

The smallest (optimum) misfit value calculated in the grid-search, m_0, identifies the best fit between the data and the synthetics with the sum of the squared residuals taken as a measure of goodness of fit. The optimum strike, dip, rake and depth values are referred to in the text as ϕ_{s0}, δ_0, λ_0 and h_0 respectively. The misfit calculation is performed in logarithmic amplitude space so it is receptive to changes in the shapes of the amplitude spectra. In some cases spectral amplitudes can vary over three orders of magnitude in the frequency range studied here (e.g. in the presence of a spectral notch) and it is necessary that the misfit calculation is sensitive to more than just absolute amplitudes.

Due to the 180° strike and rake symmetries in the surface wave radiation patterns, the best fitting amplitude spectra correspond to four different focal mechanisms: (ϕ_{s0}, δ_0, λ_0), (ϕ_{s0}+180°, δ_0, λ_0), (ϕ_{s0}, δ_0, λ_0+180°) and (ϕ_{s0}+180°, δ_0, λ_0+180°).

In order to select between these four possible mechanisms, a waveform comparison is used to choose between synthetic seismograms generated for each source and the recorded seismograms. A least squares calculation of the waveform misfit (m_w) is performed, with m_w given

by:

$$m_w = \frac{\sum_{j=1}^{T}\sum_{i=1}^{N}(d_{ij} - s_{ij})^2 \Psi_{az}^2}{\sum_{j=1}^{T}\sum_{i=1}^{N} d_{ij}^2 \Psi_{az}^2}, \tag{2.34}$$

where T is the total number of traces, N is the total number of samples in the seismograms and d_{ij} and s_{ij} now refer to the amplitudes of the data and synthetic seismograms at the jth sample in the ith trace. This misfit calculation is performed over a time window 800 s wide, centred on the model prediction of the peak 50 s group arrival time; waveforms are bandpass-filtered between 100–50 s. Of the four mechanisms over which the waveform comparison is run, the one resulting in the smallest value of m_w being computed is selected as the most likely source in combination with the optimum depth and seismic moment estimate.

Examples of synthetic waveforms and amplitude spectra corresponding to the strike and rake symmetries of the surface wave radiation patterns are shown in Figure 2.15. Rayleigh and Love wave synthetics are shown for event 013099A at four stations with varying azimuth from the source. At each station the amplitude spectra are the same for all four sources, while phase differences are seen in the variation of waveforms. It is comparisons of these waveforms with data that results in the identification of the best source parameters.

Waveforms with differences in rake of 180° (where all other source parameters equal) are readily identifiable from each other as they exhibit opposite polarities; as a 180° rotation of the rake angle causes all components of the moment tensor to change sign. If two rakes are considered, λ_α and λ_β, where $\lambda_\beta = \lambda_\alpha + 180°$, then their corresponding components of the seismic moment tensor are:

$$\begin{aligned} f_1^{\lambda_\alpha} &= -f_1^{\lambda_\beta} \\ f_2^{\lambda_\alpha} &= -f_2^{\lambda_\beta} \\ f_3^{\lambda_\alpha} &= -f_3^{\lambda_\beta} \\ f_4^{\lambda_\alpha} &= -f_4^{\lambda_\beta} \\ f_5^{\lambda_\alpha} &= -f_5^{\lambda_\beta} \\ f_6^{\lambda_\alpha} &= -f_6^{\lambda_\beta} \end{aligned}, \tag{2.35}$$

where the superscripts refer to the source rake and the subscripts refer to the component of the moment tensor.

The effect of changing the strike of a source mechanism by 180° is to change the sign of the

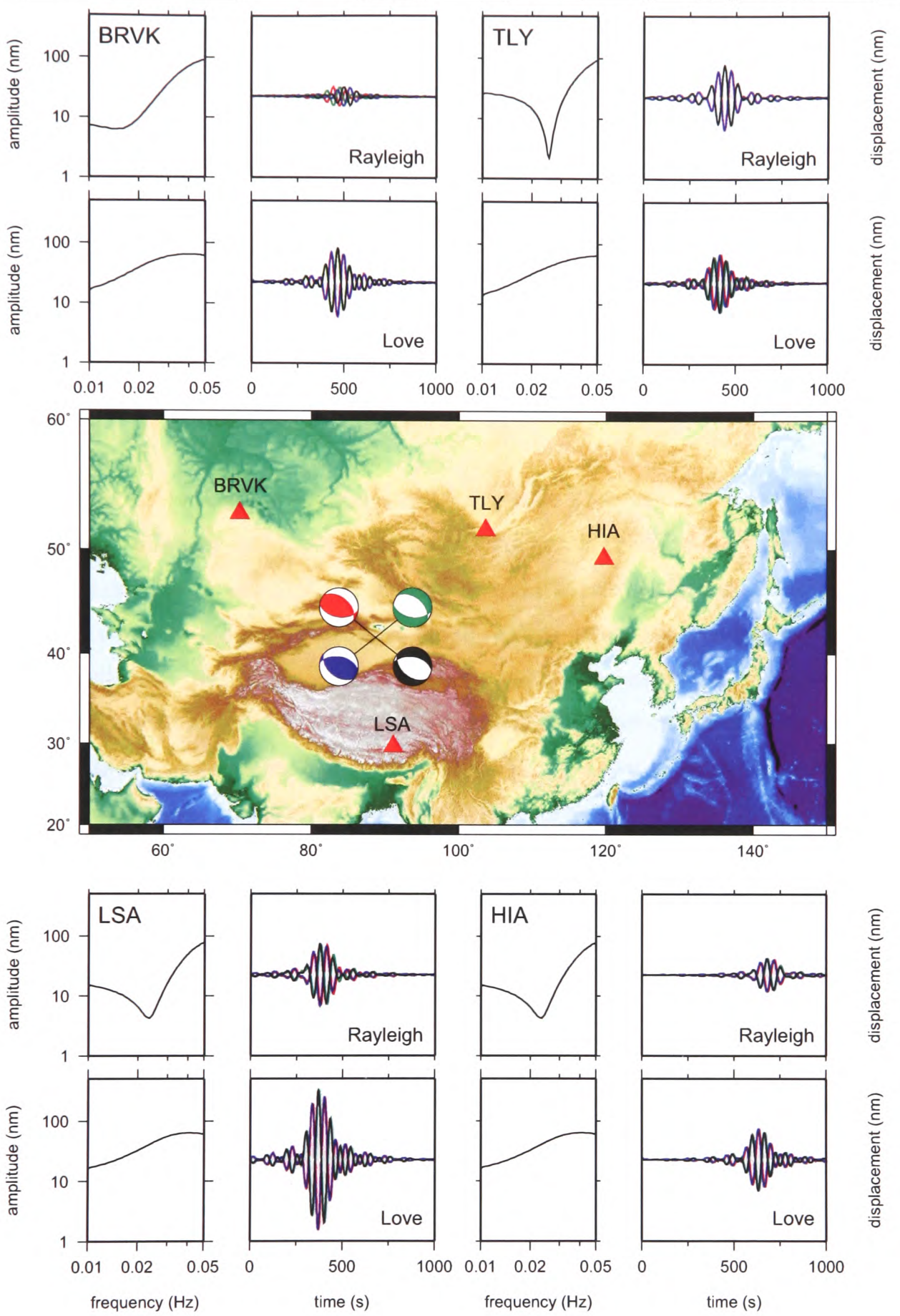


Figure 2.15: Rayleigh and Love wave amplitude spectra and waveforms calculated at stations BRVK (Borovoye, Kazakhstan), TLY, LSA, and HIA for event 013099A, a source located in western China. The four sources shown are coloured according to their focal mechanism and the amplitude spectra and waveforms are similarly coloured. Synthetics are generated for a 22 km source depth with $(\phi_s, \delta, \lambda)$ combinations of (100,48,70) in red, (100,48,-110) in green, (280,48,70) in blue and (280,48,-110) in black.

f_4 and f_5 components of the moment tensor. That is to say for two source strikes, $\phi_{s\alpha}$ and $\phi_{s\beta}$, where $\phi_{s\beta} = \phi_{s\alpha}+180°$, the moment tensor components are:

$$\begin{aligned} f_1^{\phi_{s\alpha}} &= f_1^{\phi_{s\beta}} \\ f_2^{\phi_{s\alpha}} &= f_2^{\phi_{s\beta}} \\ f_3^{\phi_{s\alpha}} &= f_3^{\phi_{s\beta}} \\ f_4^{\phi_{s\alpha}} &= -f_4^{\phi_{s\beta}} \\ f_5^{\phi_{s\alpha}} &= -f_5^{\phi_{s\beta}} \\ f_6^{\phi_{s\alpha}} &= f_6^{\phi_{s\beta}}. \end{aligned} \tag{2.36}$$

In this case differences in the synthetic waveforms come from just the reversal of the f_4 and f_5 contributions. In many instances there will be sufficient difference in these waveforms for an optimum strike to be selected, although it should be noted that in cases where either the f_4 and f_5 components are themselves small and/or when the corresponding excitation kernels are small (e.g. for a very shallow sources, where the tangential shear stresses vanish at the surface, see Figure 2.6) then there may be little difference in the two sets of waveforms (see the Rayleigh waveforms at TLY in Figure 2.15). The use of many recordings helps to determine any ambiguity in the strike parameter, but there may be occasions when either the results of other studies or independent geological information (e.g. surface ruptures and dip angles) are required to identify the likely value of the correct strike orientation.

For each focal mechanism determined here, one of the nodal planes will be the fault plane and the other will be the auxiliary plane (over which the fault rupture is equally likely to have occurred). As with many other seismic source studies, only with the addition of local geological information can a sensible selection of the likely rupture plane be made to solve this ambiguity.

2.4.3 Source Parameter Constraints

In addition to the identification of the source parameters resulting in the best fitting amplitude spectra, estimates are made of the range of sources that are statistically acceptable for a given seismic event. Whilst the presentation of the results of a 4-D parameter grid-search on a 2-D medium is non-trivial, it is possible to show variations in two source parameters whilst holding the others fixed. Figure 2.16 shows the results of a source parameter search performed for

event 013099A. Calculated logarithmic misfit ($\log(m)$) values are plotted for variations in two of the three focal mechanism parameters (ϕ_s,δ,λ) with the other being held fixed at its optimum value along with the best fitting centroid depth. Figure 2.16 can be interpreted as a series of 2-D slices taken from a 3-D volume, which itself has been extracted from a 4-D parameter space. Values of strike and rake are varied between 0° and 360° in order to clearly emphasis the 180° symmetries in the surface wave patterns for these parameters.

The white stars in Figure 2.16 show the location of the best fitting source mechanism. The purple regions indicate the lowest regions of misfit, around which are a cluster of similar source mechanisms that provide close spectral fits to the data; it is desirable to identify the range of statistically acceptable solutions that lie around the optimum.

In this study the F-test is used to place constraints on the source parameters. The F-test is used to determine if two distributions have significantly different variances by trying to reject the null hypothesis that their variances are actually consistent (Press et al., 1996). F-statistics are based on the assumption that the variable errors are normally distributed. While surface wave amplitudes are not normally distributed, logarithmic amplitudes are more likely to exhibit a normal distribution. Errors in the source parameters determined here may be influenced by: the data sets used (the inclusion of noise in data recordings and measurement errors); inaccuracies in the CUB Earth model which affect 1) source eigenfunction calculations, 2) phase and amplitude contributions from the great circle path, 3) receiver eigenfunction calculations; and errors associated with the modelling of a non-finite source. It is unlikely that these errors are, themselves, normally-distributed. However, it has long been known that the probability distribution of large numbers of small random deviations almost always converge to a normal distribution (see Press et al., 1996; Huber, 1981). This so-called 'central limit theorem' permits the application of F-statistics in this study on the assumption that the cumulative influence of the factors listed above allows errors in the source parameters determined here to be treated as Gaussian.

The statistic F is the ratio of one variance to another, and here it is defined as:

$$F = \frac{m}{m_0}, \tag{2.37}$$

where m is the misfit, defined in Equation (2.33), calculated for a given set of source parameters and m_0 is the optimum misfit. It follows that the value of F in the optimum cell is 1.0

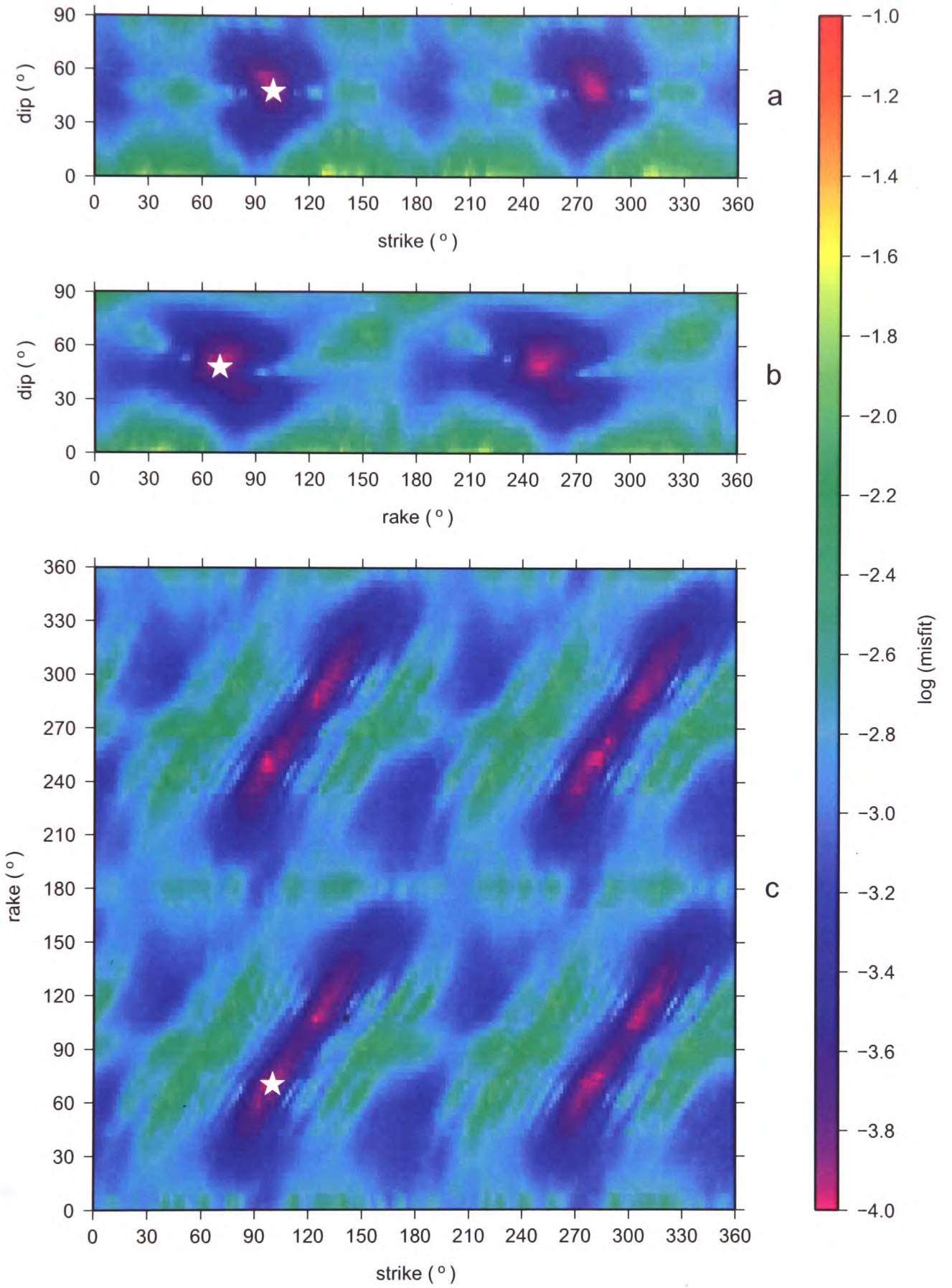


Figure 2.16: Calculated values of logarithmic misfit ($\log(m)$) for changes in source parameters at a fixed depth of 22 km for event 013099A. Plot a) shows how the misfit changes with strike and dip for a fixed rake angle (70°); plot b) show variations in rake and dip for a fixed strike (100°); and plot c) shows strike and rake varying when the dip is held fixed (48°). The white stars indicate the position of the best-determined source parameters and the eight regions of lowest misfit in plot c) indicate the areas around the four symmetrical best fitting mechanisms and their associated auxiliary planes. Note that logarithmic misfit is plotted simply for aesthetic purposes.

and all other values will be greater than 1.0 given that the value of m_0 is the global minimum.

Following Press et al. (1996), the distribution of F is given by:

$$Q(F|\nu_1,\nu_2) = I_{\frac{\nu_2}{\nu_2+\nu_1 F}}\left(\frac{\nu_2}{2},\frac{\nu_1}{2}\right), \tag{2.38}$$

where $Q(F|\nu_1,\nu_2)$ is the significance level at which the misfit of a given source (m) varies from that of the global optimum (m_0); or put another way, the confidence that a given source has the same misfit as the optimum. Here ν_1 and ν_2 are the numbers of degrees of freedom in each sample and are defined here, following Shumway (1971), as:

$$\nu_1 = \nu_2 = \left(\sum_{j=1}^{T} t_{win}\Delta\omega\Psi_{az}\right) - N_{in}, \tag{2.39}$$

where t_{win} is the width of the windowing function (300 s), $\Delta\omega$ is the bandwidth of the data used (0.04 Hz) and N_{in} the number of independent variables (4: $\phi_s, \delta, \lambda, h$).

$I_{\frac{\nu_2}{\nu_2+\nu_1 F}}(\frac{\nu_2}{2},\frac{\nu_1}{2})$ is the incomplete beta function (see Press et al., 1996), which is included here for completeness and is defined as:

$$I_x(a,b) \equiv \frac{B_x(a,b)}{B(a,b)} \equiv \frac{1}{B(a,b)}\int_0^x t^{a-1}(1-t)^{b-1}\mathrm{d}t, \tag{2.40}$$

where a and b are greater than 0 and has the limiting values $I_0(a,b)$=0 and $I_1(a,b) = 1$.

For each cell in the grid-search $Q(F|\nu_1,\nu_2)$ is evaluated. For the optimum set of source parameters (e.g. where $F = 1.0$) the function returns a value of 1.0, that is to say that there is a 100% confidence that the solution is the optimum or, considered another way, the solution can be rejected with 0% certainty that it is not the optimum. All combinations of source parameters falling within 95% confidence bounds are considered plausible solutions statistically and are retained to place constraints on the range of acceptable source parameters. This 95% confidence bound corresponds to a value of $Q(F|\nu_1,\nu_2) = 0.05$; as a result all solutions that fall below this level are rejected with a 95% confidence that they have worse misfits than the global optimum.

The application of this 95% confidence bounds allows the identification (in 4-D solution space) of mechanisms with statistically significant misfit values clustered around the best

fitting solution and Figure 2.17 shows how the results of this test can be best illustrated. Rake-dip planes are plotted at constant depth intervals, with the colour of the grid cell showing the highest value of $Q(F|\nu_1, \nu_2)$ existing for that given (ϕ_s,δ,λ,h) rake-dip-depth-strike combination. Of the independent parameters varied here, the strike is found to be well constrained within a given (λ,δ,h) cell and typically only varies by a few degrees when the other parameters are fixed. Thus the minimum and maximum values of strike are plotted as vectors from the centre of each cell and in most cases the difference between the two is indistinguishable by eye.

In order to place constraints on the four source parameters, the maximum and minimum value of each parameter falling within the set of statistically acceptable solutions can be quoted. These values of $\phi_{s\,\mathrm{min}}$, $\phi_{s\,\mathrm{max}}$, δ_{min}, δ_{max}, λ_{min}, λ_{max}, h_{min} and h_{max} need to be treated with caution as it cannot be considered that solutions of ($\phi_{s\,\mathrm{min}}$, δ_{min}, λ_{min}, h_{min}) or ($\phi_{s\,\mathrm{max}}$, δ_{max}, λ_{max}, h_{max}) are necessarily statistically acceptable. They define the limits of the rectangular box $(\phi_s, \delta, \lambda, h)$-space that contains all solutions that are not rejected at the 95% confidence level.

2.5 Summary

For selected regional recordings predictions of fundamental-mode arrival times are calculated and used to isolate regional, dispersive, wavetrains from unwanted signals and noise in the period range 100–20 s. 3-D Earth synthetic seismograms are generated using the CUB model and the MINOS modes calculation program. A grid-search is performed over all D-C solutions and a suitable range of source depths and a least squares misfit calculation is performed in logarithmic amplitude space to identify the source corresponding to the best fitting synthetic amplitude spectra.

A series of weights is applied in the grid-search to account for variations in receiver coverage, confidence in longer-period observations and synthetics and the interference of unwanted signals at the shorter-periods. Estimates of scalar seismic moment are calculated by scaling the unit synthetic amplitude spectra to the observed data. The optimum source mechanism is chosen from four possible candidates using a 100–50 s waveform comparison.

All solutions identified as falling within 95% confidence bounds are retained to place con-

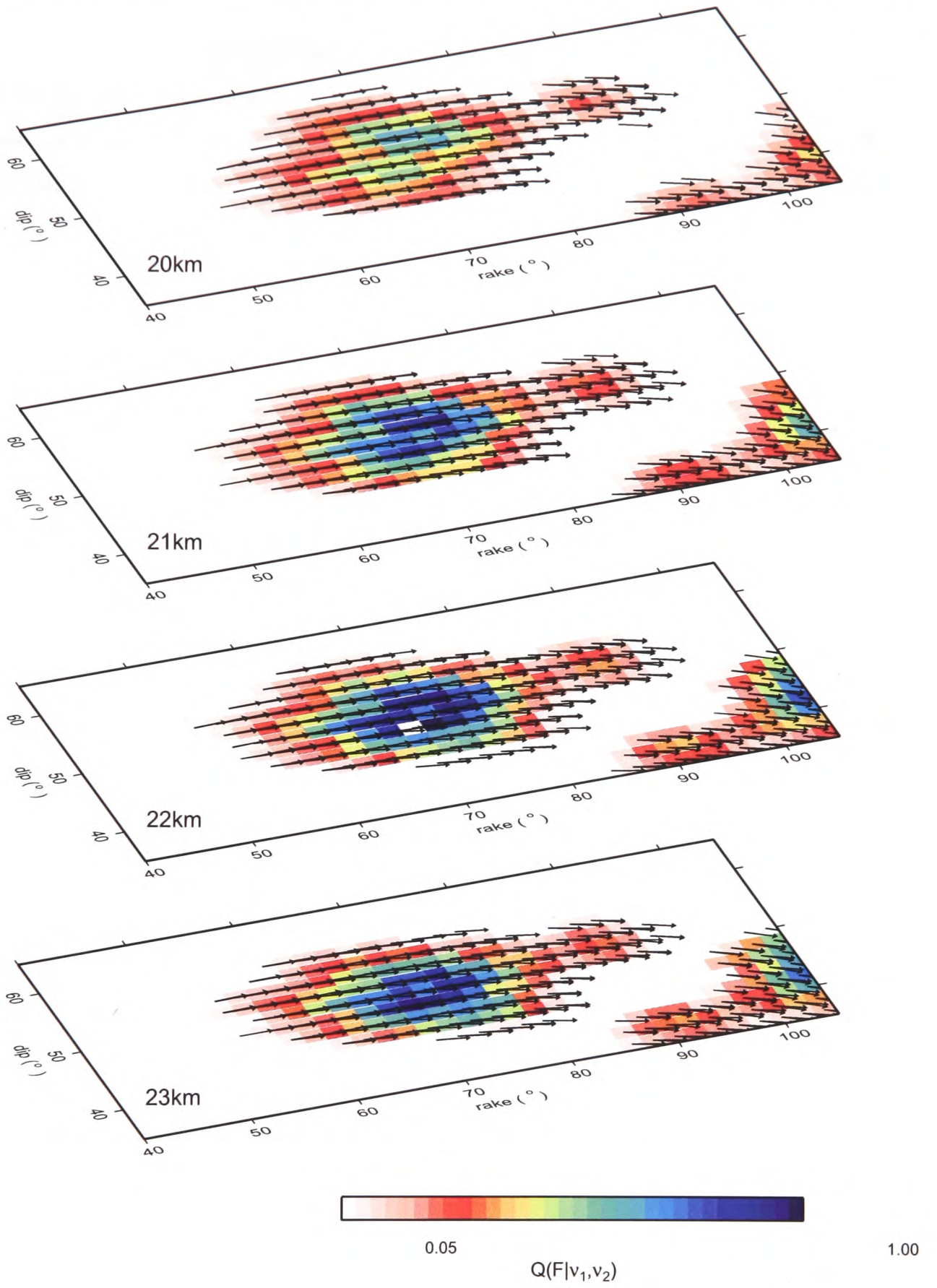


Figure 2.17: Calculated values of $Q(F|\nu_1, \nu_2)$ for event 013099A. Only those solutions with $Q(F|\nu_1, \nu_2) \geq 0.05$ are shown, all other solutions are discarded. Rake-dip planes are plotted at 1 km-incremental depths between 20-23 km. The colour of the grid cell represents the maximum value of $Q(F|\nu_1, \nu_2)$ calculated in that square. The black arrows in each grid square indicate the minimum and maximum strike angles found for a given combination of (λ, δ, h). For clarity, the white square at the centre of the region of highest probabilities at 22 km indicates the location of the statistically optimum mechanism (at δ=48°, λ=70°).

straints on the ranges of the optimum source parameters. The maximum and minimum values of strike, dip, rake, depth and scalar moment existing with the 95% confidence solution space are taken as trustworthy estimates of the statistically acceptable ranges of the respective source parameters.

Chapter 3

Validation

"We all agree that your theory is crazy, but is it crazy enough?"

Niels Bohr (1885–1962)

3.1 Overview

For testing and validation purposes, 14 earthquakes are selected for analysis. The techniques described in Chapter 2 are applied systematically to these events with the aim of developing a procedure that can be routinely used to study a large number of earthquakes in the future. The selected events have magnitudes between $5.4 \leq M_{\mathrm{w}} \leq 6.5$, occur in diverse geographic and tectonic settings and have been studied in detail elsewhere. By comparing the focal mechanisms and centroid depths calculated here with the results of other source determination techniques, it is hoped that the validity of this method can be established. Hypocentral parameters published in the NEIC catalogue for selected events are listed in Table 3.1.

Analysis of the CMT solutions for these events show that five earthquakes represent thrust-faulting, six are normal faulting events and three describe strike-slip faulting. It will be of interest if any types of focal mechanisms are better resolved here than others. Table 3.2 lists the source parameters determined here for each earthquake and the number of Rayleigh and Love wave recordings used in their calculation. best-fitting depths are calculated between 2–39 km, and source mechanisms are found to be in broad agreement with those determined

Date yyyy mm dd	Time hh:mm:ss.s	Lat (°)	Lon (°)	Magnitude M_w	Event code	Location
1993 08 03	12:43:05.4	28.73	34.55	6.0	080393G	Gulf of Aqaba, Egypt
1995 05 13	08:47:12.7	40.15	21.70	6.4	051395B	Grevena, Greece
1995 10 01	15:57:16.2	38.06	30.13	6.0	100195B	Dinar, Turkey
1997 09 21	18:13:22.8	-7.36	30.37	5.9	092197C	Lake Tanganyika, Zaire
1999 01 30	03:51:05.4	41.67	88.46	5.4	013099A	South Xinjiang, China
1999 02 25	18:58:29.4	51.60	104.86	5.9	022599H	Lake Baikal, Siberia
1999 09 07	11:56:49.4	38.12	23.61	5.9	090799C	Athens, Greece
1999 10 22	02:18:58.6	23.45	120.51	5.9	102299A	Chi-Chi, Taiwan
1999 09 13	22:28:29.5	13.04	93.07	6.5	091302C	Andaman Islands
2002 09 14	19:58:37.0	13.06	93.16	5.8	091402B	Andaman Islands
2002 10 31	10:32:58.8	41.79	14.87	5.9	103102B	Molise, Italy
2002 11 01	15:09:00.8	41.73	14.88	5.8	110102F	Molise, Italy
2004 09 28	17:15:24.2	35.82	-120.36	6.0	092804H	Parkfield, Ca, USA
2005 11 27	10:22:19.2	26.77	55.86	5.9	112705I	Qeshm Island, Iran

Table 3.1: NEIC hypocentral parameters of the 14 earthquakes used in the validation of the method presented here. Event codes refer to the corresponding CMT codes, with the exception of event 112705I which occurred on Qeshm Island, Iran after the change by the Global CMT Project in their *mmddyyx* naming conventions where *mm* refer to the month, *dd* refers to the day of the month, *yy* refers to the last two numbers of the year (e.g. 01 for 2001) and x is a single character event identifier.

in other studies.

Selected earthquakes are studied in order of their predominant faulting type. Reverse-faulting earthquakes are presented first with event 013099A (South Xinjiang, western China) studied in detail as a case study, partly due to its proximity to the former Chinese nuclear test site. Events 091302C and 091402B (mainshock and principal aftershock, Andaman Islands) afford an opportunity to study subduction zone setting earthquakes occurring closely in space and time. Normal-faulting events are considered next with analyses of events 051395B (Kozani-Grevena, Greece), 100195B (Dinar, Turkey) and 092197C (Lake Tanganyika, Zaire). The $M_w = 6.4$ Kozani-Grevena earthquake has been well studied using a variety of techniques; the Dinar earthquake is an example of a very shallow source, while the Lake Tanganyika, Zaire earthquake represents a particularly deep continental earthquake. Two similar strike-slip earthquakes (103102B and 110102F) in Italy occurring at $\sim$10 km depth are analysed, followed by the 2004 Parkfield earthquake, one of the most intensely studied earthquake in recent history, which is analysed here as it represents a very shallow strike-slip event. Results of the source parameter determinations performed for events 080393G (Gulf of Aqaba, Egypt), 022599H (Lake Baikal, Siberia), 090799C (Athens, Greece), 102299A (Chi-Chi, Taiwan) and 112705I (Qeshm Island, Iran) can be found in Appendix C.

Event code	Strike (°)	Dip (°)	Rake (°)	Depth (km)	Moment (10^{17} Nm)	LHZ records	LHT records	Mechanism
080393G	357	50	-70	9 (-4/+7)	12.6	17	18	
051395B	245	39	-100	8 (-4/+2)	43.6	24	20	
100195B	128	44	-98	5 (-3/+3)	18.9	33	27	
092197C	326	36	-110	39 (-17/+7)	7.43	23	21	
013099A	100	48	70	22 (-5/+1)	0.954	23	19	
022599H	74	40	-78	8 (-3/+2)	5.06	34	23	
090799C	118	46	-78	9 (-3/+3)	8.14	30	27	
102299A	182	50	64	11 (-2/+5)	6.64	26	20	
091302C	214	52	130	19 (-10/-10)	52.2	35	41	
091402B	208	52	126	17 (-6/+8)	3.77	29	24	
103102B	269	70	-171	12 (-5/+10)	3.63	33	24	
110102F	264	74	-164	11 (-7/+13)	3.01	36	25	
092804H	140	86	136	2 (-1/+11)	11.0	27	17	
112705I	269	53	99	8 (-5/+4)	9.41	24	21	

Table 3.2: Optimum source parameters determined here for the 14 events studied along with the number of LHZ and LHT channel recordings used and the focal mechanism calculated. Errors on the depths estimates indicate the range of statistically acceptable depths determined here.

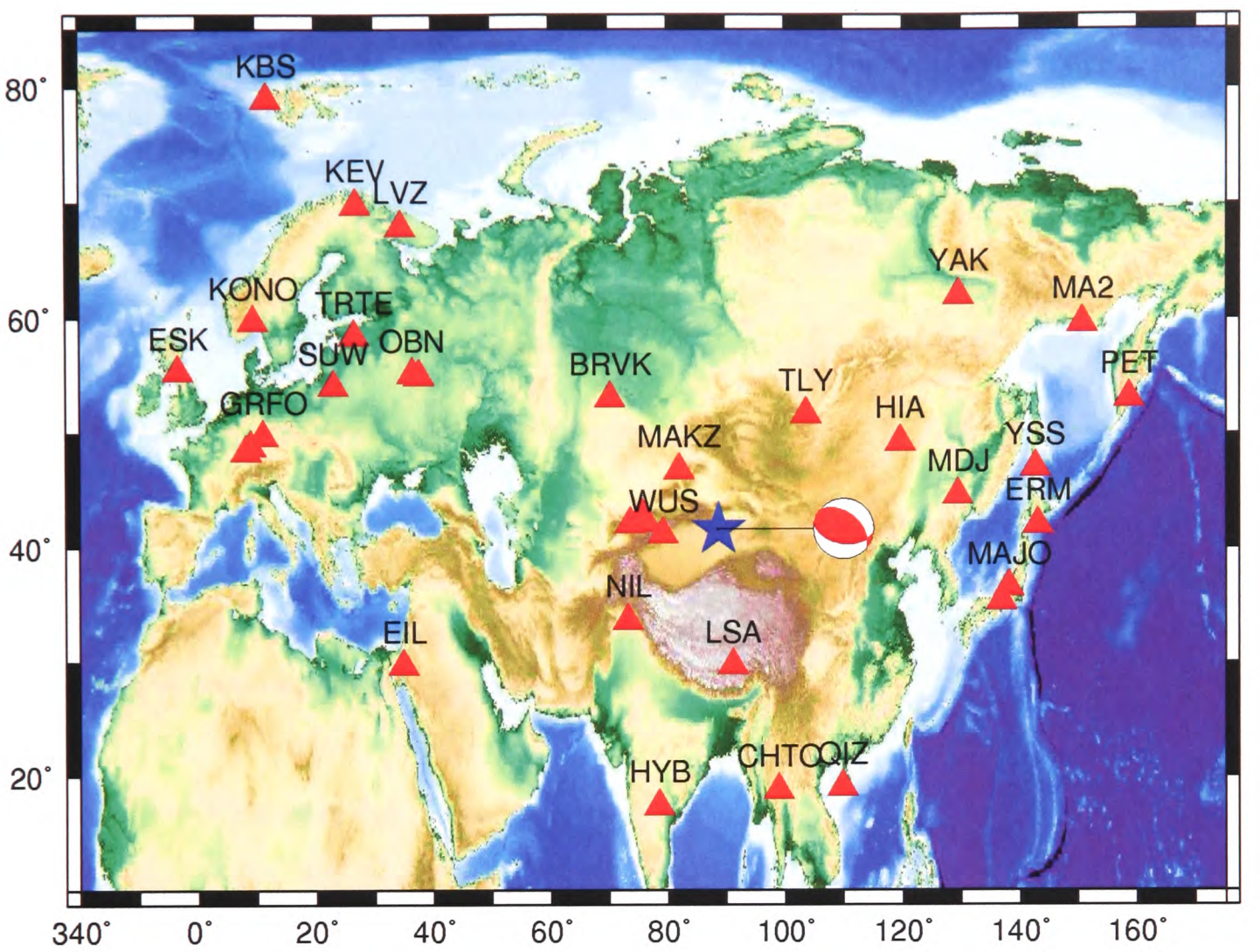


Figure 3.1: Regional map of western China and setting of event 013099A. The site of the former Chinese nuclear test site at Lop Nor is shown by the blue star. The focal mechanism shown is that determined in this study. For clarity some station names have been removed: the receiver stations just south of GRFO are BFO and STU; station MHV is just west of OBN; the stations to the west of WUS are AML, TKM2 and ULHL; and the station south of MAJO is INU.

3.2 1999 South Xinjiang, China, earthquake (013099A)

3.2.1 Introduction

The region around the former Chinese nuclear test site at Lop Nor in South Xinjiang, western China, is an area of particular interest to forensic seismologists. Located to the northeast of the Tarim Basin, seismic events in this region, both earthquakes and explosions, have been rigorously examined. Research in this particular area has focused on the determination of the local Earth structure to aid seismic detection and discrimination studies.

On 31 January 1999, NEIC reported a seismic disturbance close to Lop Nor occurring some

Study	Strike (°)	Dip (°)	Rake (°)	Depth (km)	Moment (10^{17} Nm)	Mechanism
This Study	**100**	**48**	**70**	**22**	**0.954**	
CMT	116	36	99	23.3	1.7	
USGS	90	42	71	17	1.4	
Ammon et al. (2003)	93	56	67	20	1.02	

Table 3.3: Source parameters determined for event 013099A here (bold) and in other studies.

20 km away from the test site and a number of studies have been performed on this earthquake to determine whether it was a naturally-occurring earthquake or a man-made explosion. Figure 3.1 shows the locations of the seismic stations used in the study of this event, the smallest magnitude earthquake examined in this chapter.

3.2.2 Previous Studies

The CMT and USGS Fast Moment Tensor solutions for this earthquake report a predominantly thrusting focal mechanism and centroid depths of 23.3 km and 17 km respectively (see Table 3.3). Ammon et al. (2003), combining surface wave amplitude spectra observations with long-period body waves in a joint inversion, found an optimum focal depth of 20 km and a focal mechanism consistent with the CMT and USGS solutions. Along with these source studies that strongly point to a tectonic faulting mechanism, Hartse et al. (1999) concluded that the Pn/Sn ratio determined from the seismic record at station WMQ was consistent with Pn/Sn ratios calculated for historical earthquakes in this region rather than those determined for nuclear explosions.

3.2.3 Results

D-C solution space was grid-searched in increments of 2° over strike (0–180°), dip (0–90°) and rake (0–180°) and 1 km over depth (between 10–30 km). By virtue of the 180° symmetries in the surface wave radiation patterns in both strike and rake, this grid-search encompasses all possible D-C solutions. The best-fitting mechanism at each depth is shown in Figure

3.2, with the best synthetic amplitude spectra fits to the data calculated at 22 km depth, along with the crustal model used in the calculation of the synthetics. The misfit-depth curve exhibits a strong dependence on the crustal model, with the jump in misfit values below 23 km caused by a velocity discontinuity in the model at below 23 km depth. Changes in the U, V and W eigenfunctions and their radial derivatives ($\dot{U}$, $\dot{V}$ and $\dot{W}$) across this boundary cause perturbations in the calculated excitation kernels over a single, 1 km, increment in depth (see Figure 2.3). As a result, focal mechanisms at depths of 24 km or greater fall out of the range of statistically significant solutions, meaning the deepest depth bound that can be put on this event is 23 km. The location of this model boundary limits depth constraints below 23 km; the strong model dependency seen here highlights the importance of having good crustal models for source studies such as this. In Appendix C.1 best-fitting source solutions are calculated in velocity models where this boundary is perturbed by ± 10 km. These solutions are found to be in variance with the focal mechanisms listed in Table 3.3 and both have an optimum depth of 17 km, shallower than the best-fitting depth calculated in this section. In the case where the model discontinuity is at 13 km, a 17 km deep earthquake is placed in the upper mantle, demonstrating the sensitivity of this method to the local Earth structure used.

Table 3.3 lists, in bold, the best-fitting source parameters determined here, along with a lower hemisphere 'beach ball' plot of the optimum focal mechanism. This earthquake is found to be a reverse-faulting event with focal parameters ($\phi_s = 100°$, $\delta = 48°$, $\lambda = 70°$). Without additional local information about the likely orientation of the source, it is impossible to say if the rupture occurred on this plane, or the auxiliary plane ($\phi_s = 309°$, $\delta = 46°$, $\lambda = 111°$).

If the focal mechanism determined here is rotated by 180° in strike then the same surface wave radiation pattern is generated and this mechanism ($\phi_s = 280°$, $\delta = 48°$, $\lambda = 70°$) has to be considered as an equally likely source. Likewise, the rake angle of these two solutions can also be rotated by 180° and the two resulting normal-faulting mechanisms are considered legitimate sources. A comparison of synthetic waveforms and recorded data (bandpass-filtered between 100–50 s) was performed to resolve this ambiguity, with the preferred mechanism selected here listed in Table 3.3.

The best-fitting synthetic amplitude spectra and bandpass-filtered waveforms are displayed in Figures 3.3 and 3.4 for Rayleigh and Love waves respectively. The best-matching amplitude spectra exhibit good overall agreement with the observed data, as do the calculated waveforms. Frequency dependent-notches in the Rayleigh wave amplitude spectra have been shown to

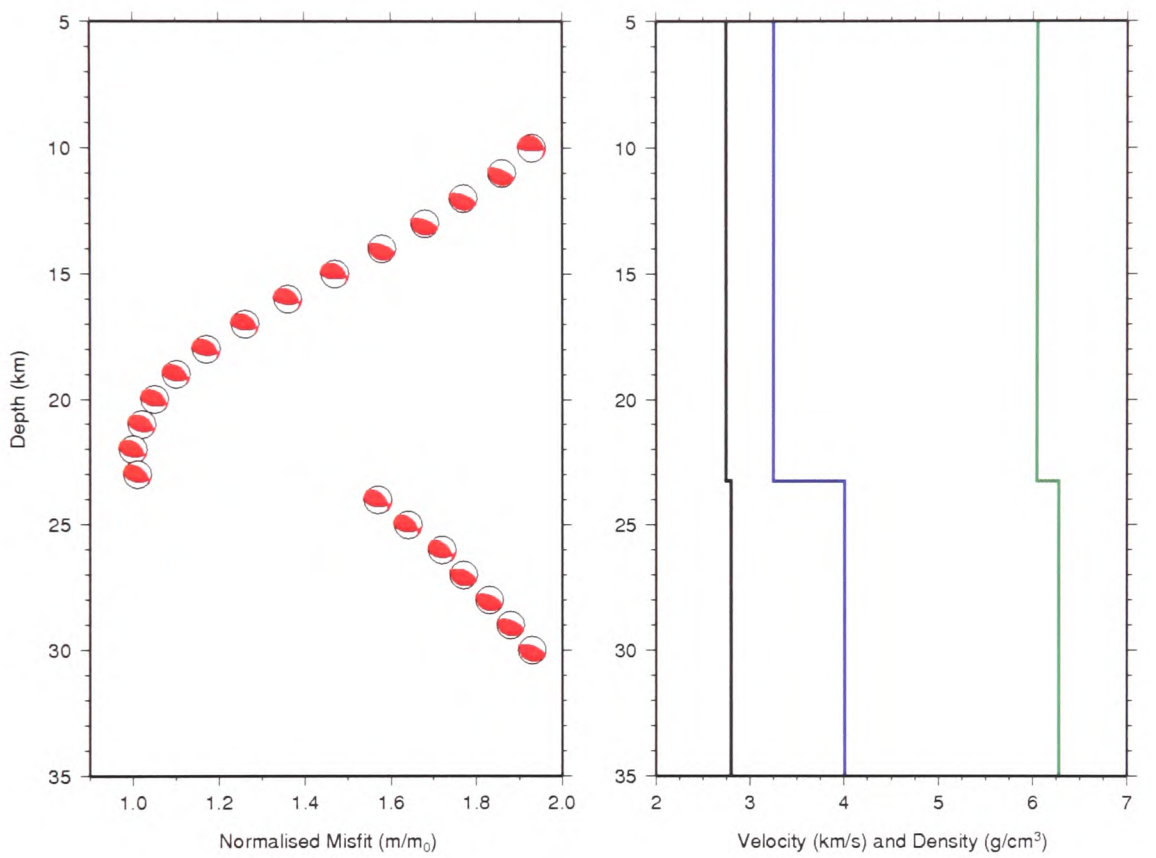


Figure 3.2: LHS: best-fitting mechanisms at each grid-searched depth, plotted as the value of their misfit (m) normalised to the optimum misfit (m_0) for event 013099A. The best-fitting global mechanism is found at a depth of 22 km; the rest of the faulting parameters are listed in Table 3.3). RHS: density (black), and P (green) and S (blue) velocity profile as described in the upper crust by the CUB local model used here (centred on 42°N 88°E). The crust is modelled as isotropic, so $v_{pv} = v_{ph}$ and $v_{sv} = v_{sh}$. The step in normalised misfit after 23 km is clearly attributable to a discontinuity below 23 km where both density and the seismic velocities are subject to a jump across a model boundary.

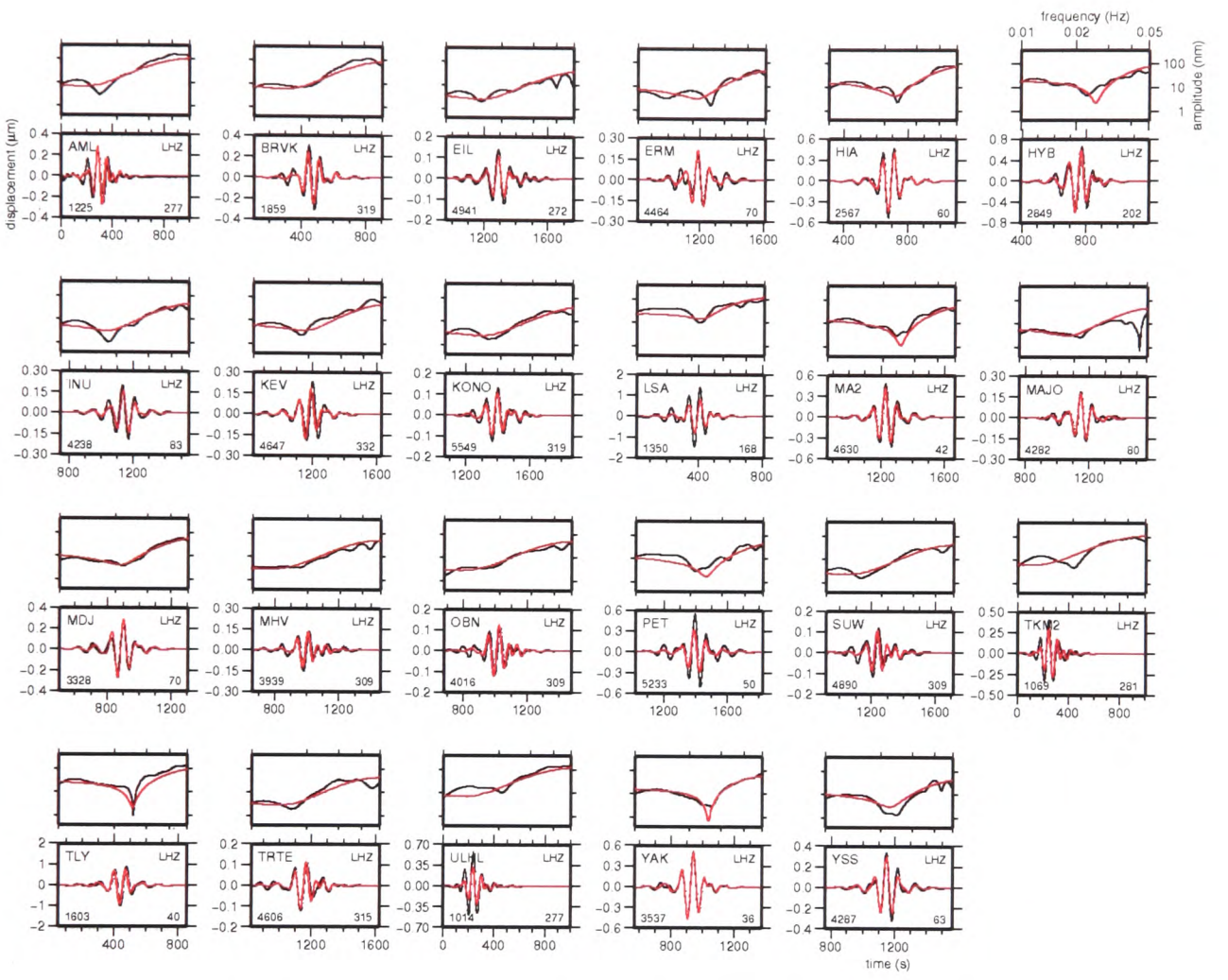


Figure 3.3: best-fitting Rayleigh wave synthetic (red) and data (black) amplitude spectra and filtered waveforms determined here for event 013099A at the 23 stations where LHZ channel recordings were used. For each station the best-matching amplitude spectra are plotted above the 100–50 s bandpass-filtered seismograms, i.e. for the source listed in Table 3.3. Stations are plotted alphabetically by name and the captions accompanying the waveforms refer to (clockwise from top left) station name, channel name, azimuth of receiver from the source (in degrees) and source-receiver distance (in km).

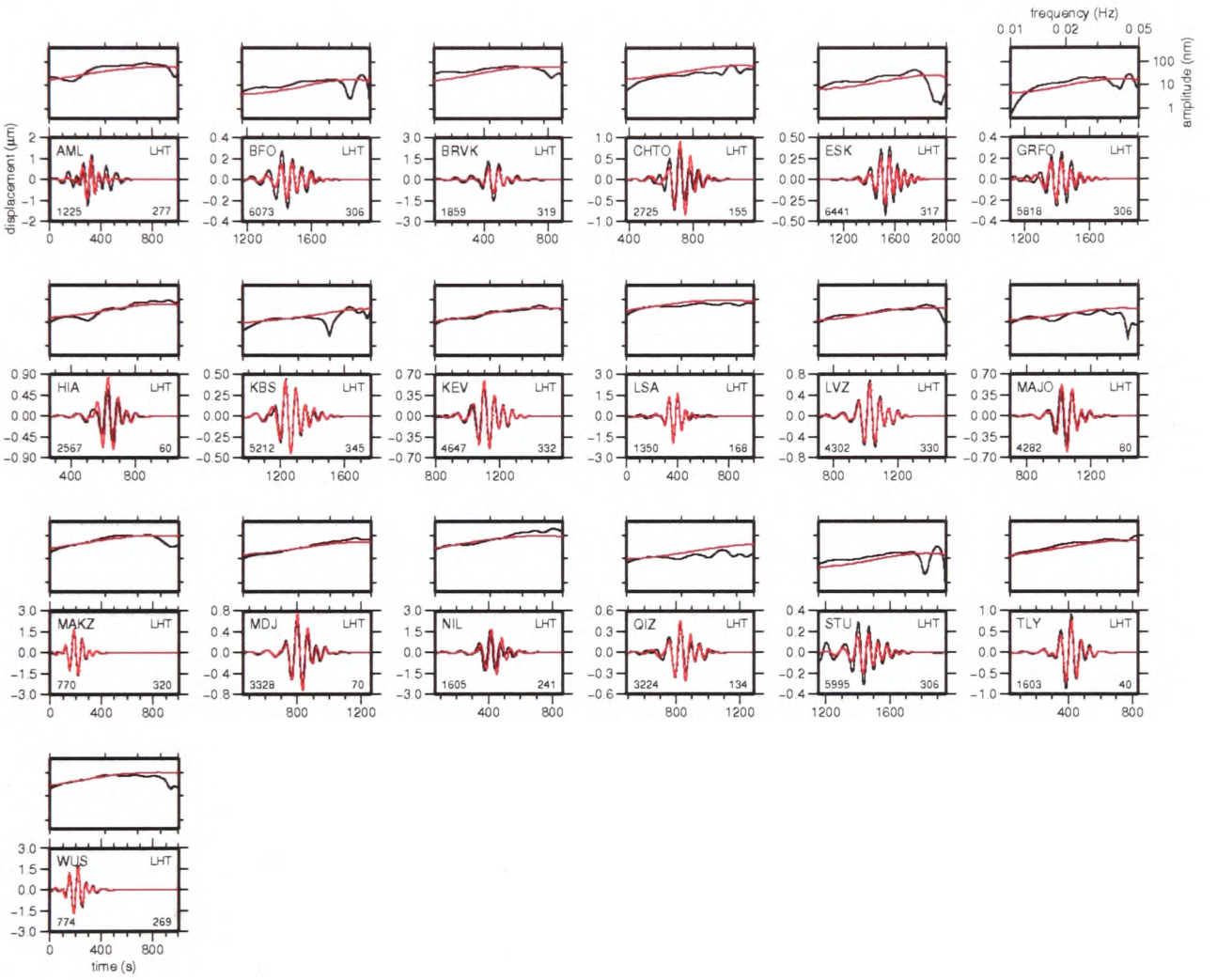


Figure 3.4: As Figure 3.3 but for the 19 Love wave recordings used here.

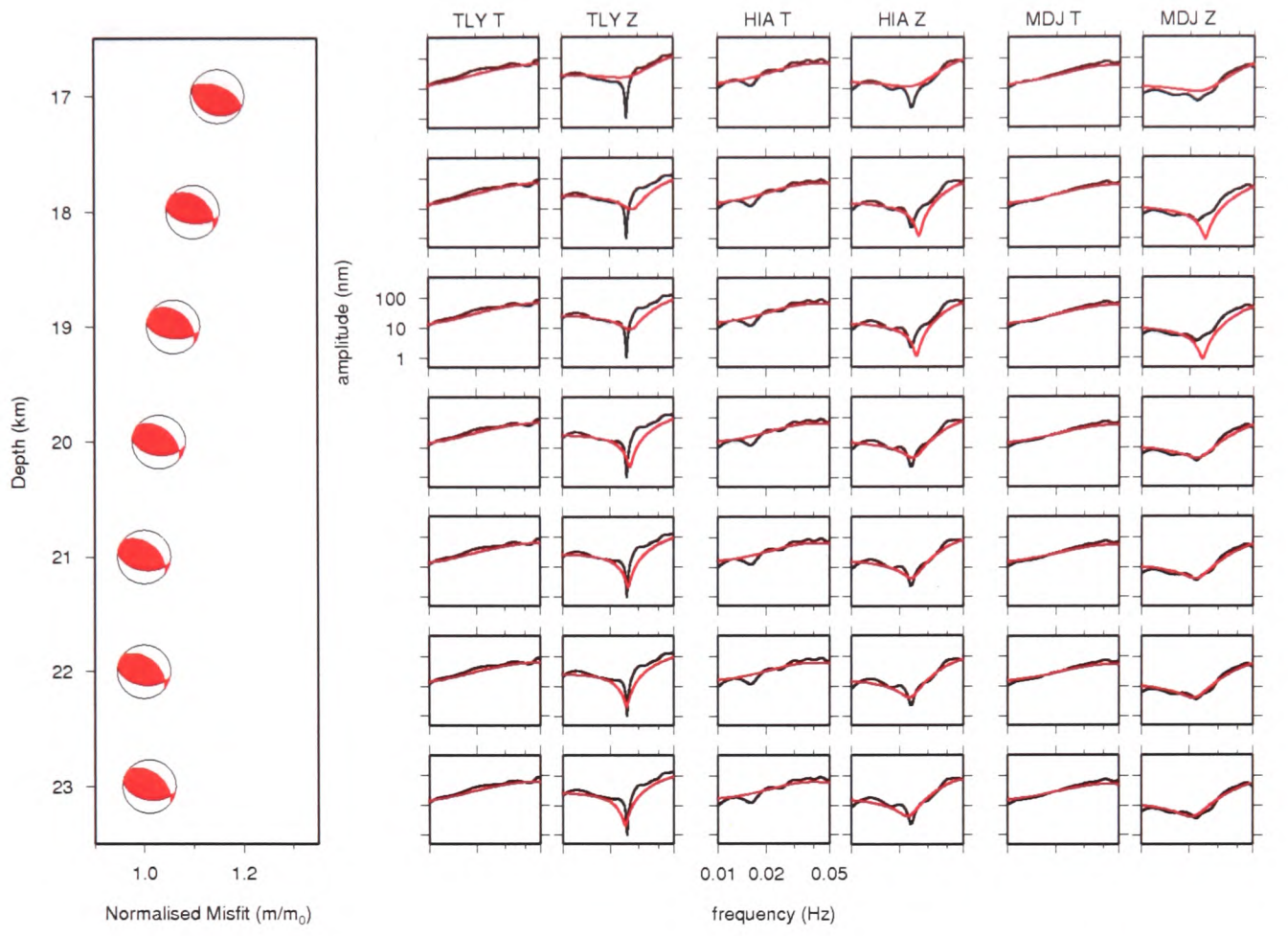


Figure 3.5: Examples of the best-fitting Rayleigh and Love wave amplitude spectra for the seven statistically acceptable depths determined for event 013099A at three stations with increasing azimuth and distance from the source. Synthetic (red) and data (black) LHZ and LHT channel amplitude spectra are shown at stations TLY (azimuth = 40°, distance = 1603 km), HIA (60°, 2567 km) and MDJ (70°, 3328 km). The misfit-depth curve from Figure 3.2 is shown on the left hand side for reference.

provide a tight constraint on centroid depth estimates and a good example of one of these features is shown at station TLY in Figure 3.3. Although the synthetic amplitude spectrum at this station shows a broader notch than the recorded data, both minima occurring at the same frequency (~0.0254 Hz) indicate that 22 km is a good estimate for the centroid depth.

Figure 3.5 shows the best-fitting amplitude spectra at three stations (TLY, HIA, MDJ) for the seven statistically acceptable depths determined here. There is little discernible change in the Love wave amplitude spectra, indicating their insensitivity to source depth. With increasing depth, the position of the null in the synthetic Rayleigh wave amplitude spectrum at station TLY migrates to lower frequencies, and it is clear in the case of this particular station that 22 km is the best-matching depth. Similarly, the closest matching synthetic amplitude spectral notch at station HIA (Hailar, Inner Mongolia, China) occurs at 22 km, though the null here is slightly broader than that in the recorded data. Finally, at shallower

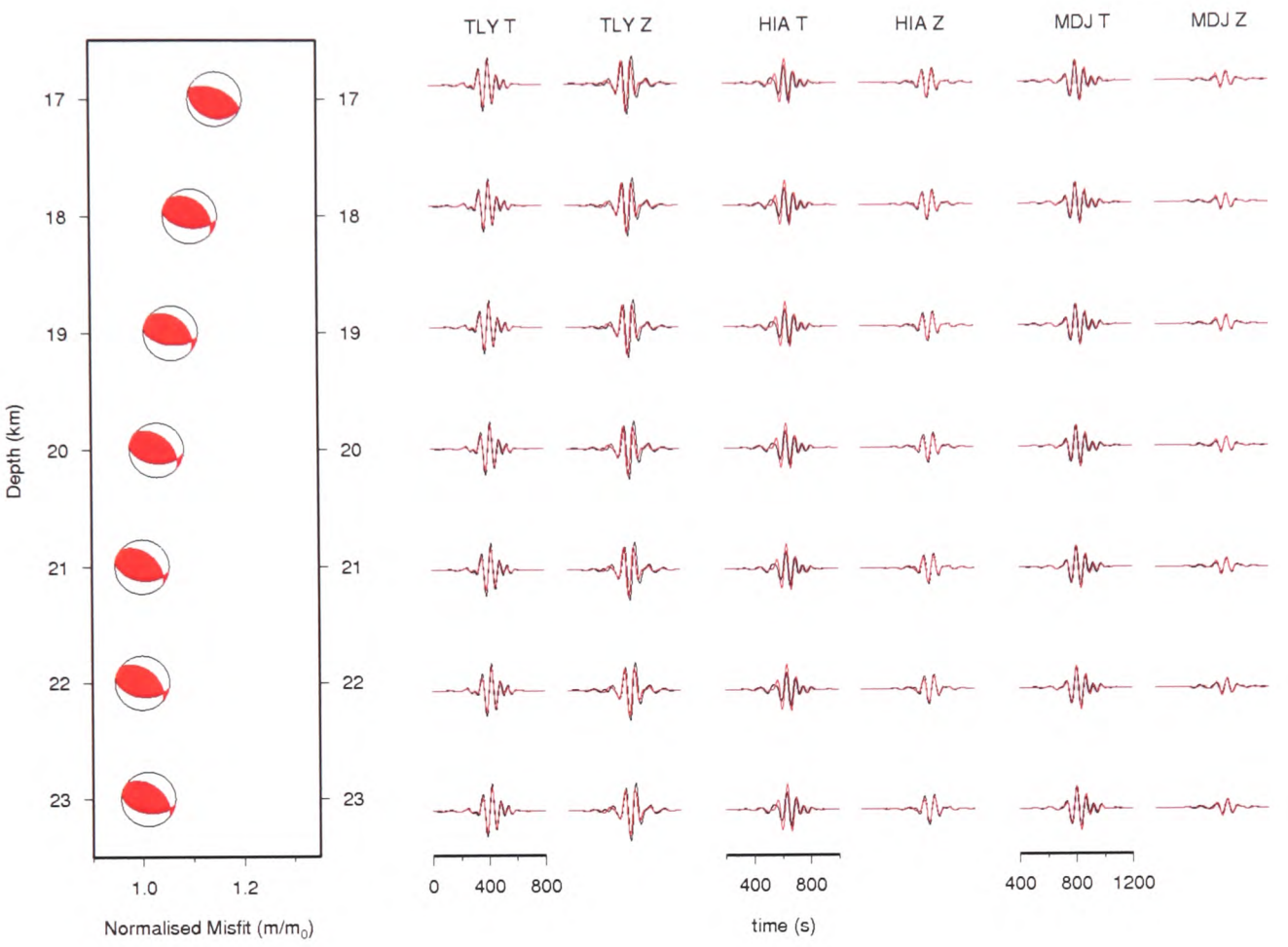


Figure 3.6: Examples of the change in best-fitting Rayleigh and Love 100–50 s waveforms for the seven acceptable depths allowed for event 013099A at three stations with increasing azimuth and distance from the earthquake. In contrast to Figure 3.5, there is little discernible difference between the synthetics over this 7 km depth range; thus displaying the insensitivity of waveform studies to focal depth.

depths (17–21 km) there is a sharp notch in the synthetic Rayleigh wave amplitude spectrum at station MDJ (Mudanjiang, China), which is not in agreement with the data. As the source depth is increased, this null migrates to longer-periods and also broadens out, eventually providing the best match to the data at 22 km. Figure 3.5 promotes confidence that the grid-search algorithm developed here displays a sensitivity to spectral notches when they are present in the data.

Examples of synthetic waveforms calculated using the optimal source parameters at depths between 17–23 km are plotted in Figure 3.6. It is evident from this figure that there is little variation, over a 7 km depth range, in the shape of these seismograms, showing their lack of sensitivity to source depth. Thus, the use of 100–50 s surface waveforms is not recommended for the robust determination of seismic source parameters.

Parameter	Minimum	Optimum	Maximum
Strike (°)	86	100	118
Dip (°)	42	48	62
Rake (°)	52	70	94
Depth (km)	17	22	23
Moment (10^{17} Nm)	0.79	0.95	1.05

Table 3.4: Bounding values of the 95% confidence region of source parameters determined here for event 013099A.

After the optimum source parameters have been determined, a calculation is performed for every grid square to identify the closeness of fit between the calculated misfit for each D-C source (m) and that of the optimum (m_0). Using an F-test calculation and its distribution, all combinations of source parameters that fall outside of 95% confidence limits are discarded and the remaining solutions are used to place bounds on the optimum source parameters as described in 2.4.3.

The distribution of these solutions in 4-D parameter space is shown in Figure 3.7. As well as the cluster of acceptable solutions around the optimum square, another set of solutions with equally high probabilities can be seen in this figure. These source parameters are found clustered around the grid square (δ=46°, λ=111°), which identifies the position of the dip and rake of the auxiliary plane. Solutions in either of these regions can have one of two possible strike orientations as a result of the 180° strike symmetry in the surface wave radiation pattern. In Figure 3.7, the strikes shown are those closest to that of the optimum mechanism (i.e. note that in the case of the auxiliary plane, all of the arrows would be striking 180° away from their plotted orientations).

Where the two distinct regions of best-fitting solutions do not overlap, i.e. they are small in size, source parameters are well constrained (though this is not always the case, e.g. for mechanisms with almost pure reverse or normal-faulting styles on fault planes dipping close to 45°). The range of statistically acceptable parameters is determined by the minimum and maximum values of those source solutions that exist within the space bounded by 95% confidence limits and these are listed in Table 3.4. Conceptually, considering Figure 3.7, the determination of errors on the optimum source parameters involves the identification of the bounds of the 3-D (λ,δ,h) volume, and the global extents of the values of strike and scalar seismic moment within this space.

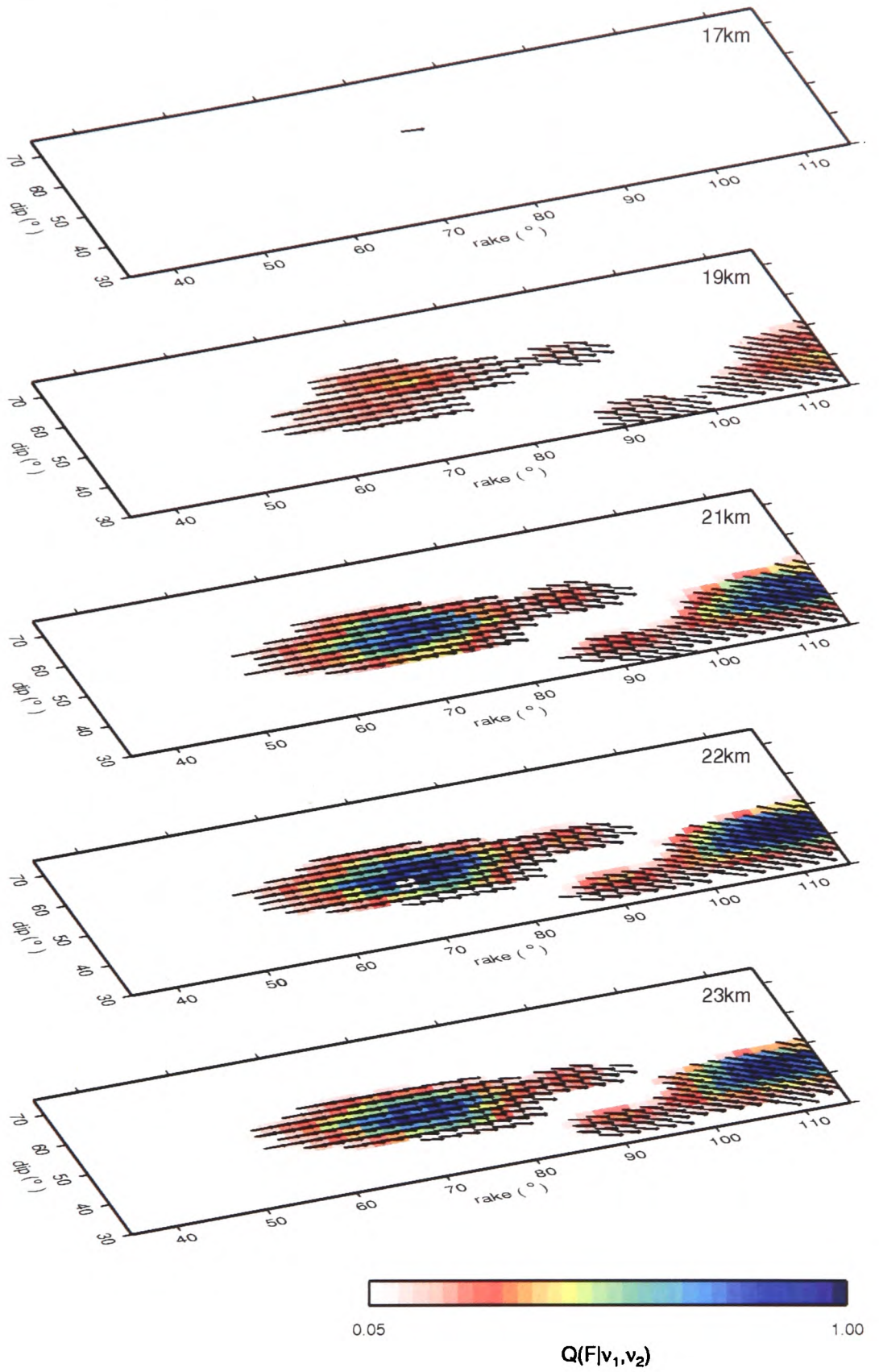


Figure 3.7: Slices through rake-dip-depth space for event 013099A at 17 km (minimum), 19 km, 21 km, 22 km (optimum) and 23 km (maximum) depths. Grid squares are coloured according to values of $Q(F|\nu_1, \nu_2)$, which presents the closeness of fit of the synthetic spectra at a given grid cell to those spectra at the optimum grid cell. White indicates a region that can be discarded with 95% confidence that the spectral misfits are worse than the optimum. The best fits to the data are located in the dark blue regions; for the purpose of clarity the optimum grid cell is coloured white.

The optimum focal mechanism determined here is consistent with previous studies, as is the estimate of 22 km depth. The estimate of seismic moment here (9.54×10^{16} Nm) approximately agrees with that calculated by Ammon et al. (2003) but is almost half the size of the CMT value. It has been noted elsewhere (e.g. Patton, 1998) that CMT seismic moment estimates in central Asia are often greater than regional estimates, in some cases by as much as a factor of 2.

3.3 2002 Andaman Islands earthquakes (091302C & 091402B)

3.3.1 Introduction

An $M_w = 6.5$ earthquake (event 091302C) occurred off the west coast of Digilipur, north Andaman Island on 13 September 2002 and was followed by a series of aftershocks (Rajendran et al., 2003; Kayal et al., 2004), the largest being an $M_w = 5.8$ earthquake (event 091402B) which occurred some 22 hours later. These events were located close to the Andaman Trench, the plate boundary along which the Indian plate is subducting beneath the Burma micro-plate (Fitch, 1970), though the direction of convergence is markedly oblique. Both earthquakes are shown in a regional setting in Figure 3.8 along with the sites of seismic stations used here.

3.3.2 Previous Studies

Source parameters determined for these two earthquakes are listed in Table 3.5. Both the published CMT and USGS focal mechanisms describe predominantly reverse-faulting with a small component of right-lateral strike-slip (assuming a west-dipping fault plane), though the strikes of the CMT and USGS solutions are different (by 21° for the mainshock and by 33° for the aftershock). The mainshock depth is published as 22 km in the CMT catalogue (fixed) and 31 km in the USGS catalogne. Engdahl et al. (2007) calculated a hypocentral depth of 15 km using the EHB method (Engdahl et al., 1998), while the India Meteorology Department (IMD) also published a hypocentral depth, but owing to inaccuracies in their timings and location, it was at 164 km (Rajendran et al., 2003) so is not considered a reliable comparison. For the principal aftershock, CMT and USGS solutions are more consistent with centroid depths of 19 km (fixed) and 21 km respectively; the hypocentre determined by Engdahl et al. (2007) is located at 21 km depth. Engdahl et al. (2007) also report that relocated aftershocks occurring over the following month were found to lie at depths between 15–45 km.

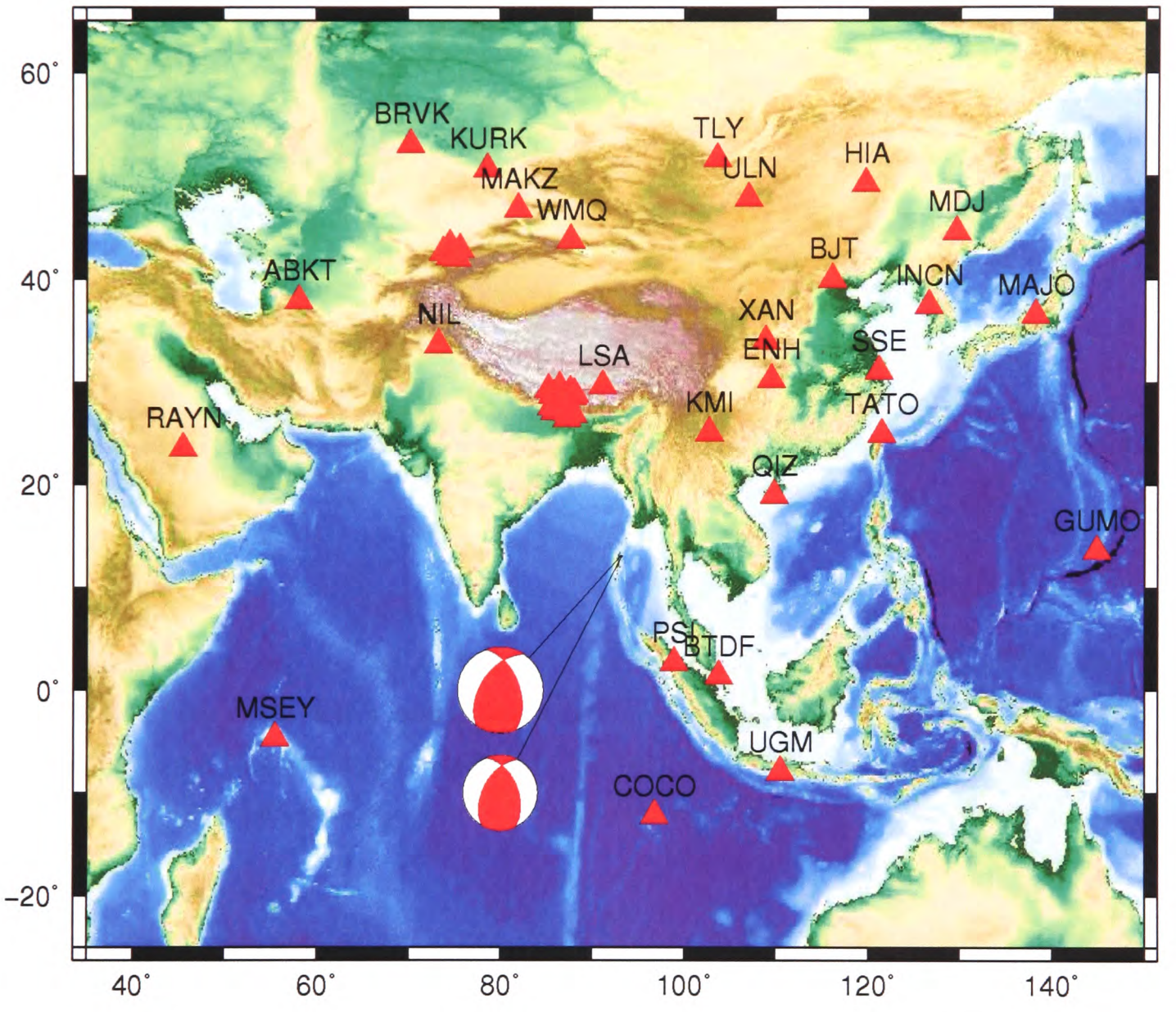


Figure 3.8: Regional map of the September 2002 Andaman Islands mainshock 091302C (top focal mechanism) and its principal aftershock 091402B (bottom focal mechanism) along with the stations used in this study. The cluster of receivers to the west of station LSA are the Himalayan Nepal Tibet Experiment network (YL) stations BIRA, BUNG, HILE, ILAM, LAZE, MAZA, MNBU, NAIL, PHID, RC14, RUMJ, SAGA, SAJA, SIND, SUKT, THAK, TUML and XIXI. Further northwest, the cluster of stations are those in the KN network: EKS2, KBK, KZA, TKM2, UCH and USP.

Study	Strike (°)	Dip (°)	Rake (°)	Depth (km)	Moment (10^{18} Nm)	Mechanism
This Study Mainshock	**214**	**52**	**130**	**19**	**5.22**	
CMT	212	42	137	22*	6.3	
USGS	191	40	137	31	6.0	
Engdahl et al. (2007)				15^{+}	6.5 (M_w)	
This Study Aftershock	**208**	**52**	**126**	**17**	**0.377**	
CMT	206	50	128	19*	0.47	
USGS	173	39	109	21	0.48	
Engdahl et al. (2007)				21^{+}	5.7 (M_w)	

Table 3.5: Source parameters determined for the $M_w = 6.5$ Andaman Islands earthquake (091302C) and its principal aftershock (091402B). * indicates the depth was fixed (in this instance, based on the modelling of broadband P waveforms); $^{+}$ denotes a hypocentre depth.

3.3.3 Results

D-C solution space over the depth range 5–30 km was grid-searched for events 091302C and 091402B and the misfit-depth curves calculated here are shown in Figure 3.9. These earthquakes are found to have similar centroid depths (19 km and 17 km, respectively) and similar focal mechanism solutions dominated by reverse faulting on 52° west-dipping fault planes (see Table 3.5).

The mainshock, though requiring a fault plane dipping 10° steeper than the CMT mechanism to best fit the surface wave data, has values of strike, rake, depth and seismic moment consistent with this solution. The centroid depth estimate of 19 km is also in broad agreement with the Engdahl et al. (2007) hypocentre at 15 km, although is somewhat shallower than the 31 km published by the USGS. The principal aftershock is calculated to have a similar focal mechanism to the mainshock with a centroid depth of 17 km. Both mechanism and depth estimates are in good agreement with the CMT solution and, although the strike is still ~30° away from the optimum determined here, the USGS depth of 21 km is more consistent with this study. The offset in orientations of the CMT and USGS moment tensor solutions is attributed to differences in the data types used, the processing procedures applied and the relative complexity of the subduction zone tectonic setting.

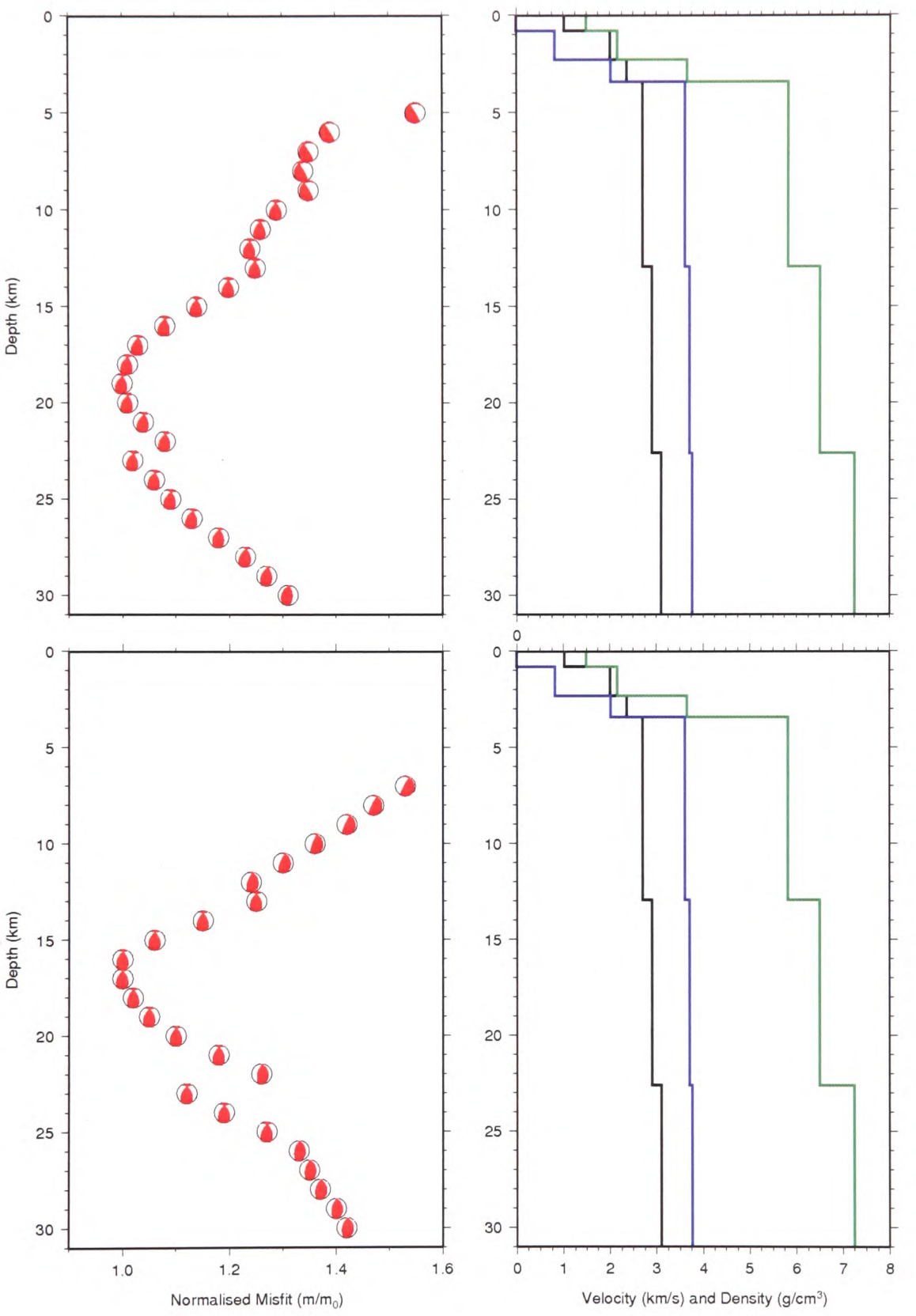


Figure 3.9: LHS: misfit-depth profile for the best-matching source mechanisms at each depth for the Andaman Islands mainshock (091302C, top) and its principal aftershock (091402B, bottom). RHS: local Earth model used, key as described in Figure 3.2.

Parameter	Minimum	Optimum	Maximum
Mainshock			
Strike (°)	198	214	232
Dip (°)	32	52	64
Rake (°)	106	130	154
Depth (km)	10	19	29
Moment (10^{18} Nm)	4.47	5.22	6.64
Aftershock			
Strike (°)	180	208	220
Dip (°)	42	52	72
Rake (°)	84	126	148
Depth (km)	11	17	25
Moment (10^{17} Nm)	3.21	3.77	4.69

Table 3.6: Bounding values of the 95% confidence region of source parameters determined in this study for events 091302C (mainshock) and 091402B (aftershock).

The best-matching synthetic amplitude spectra are plotted in Appendix D, along with the corresponding calculated waveforms; contour plots of the 95% confidence solution space for both the mainshock and aftershock are presented in Appendix E. A summary of these figures is given in Table 3.6. Strike and dip angles, especially, are well constrained; the rake angles less so, and depths span ranges of 19 km and 14 km respectively.

The two sets of source parameters calculated here are similar, indicating a common origin for the mainshock and its principal aftershock. In the absence of a detailed aftershock analysis, of the two possible fault planes preference here is for the steeply-dipping plane to West with its rake angle describing a degree of right-lateral motion in a region dominated by right-lateral plate movements. Both the partially-sinistral rake angle and relatively high dip of the North-striking fault plane are reasons to discount the auxiliary plane as the seismogenic source. Further analysis is required to determine whether these events ruptured in either the over-riding or the subducting plate. It has been previously reported that shallow-depth, reverse-faulting, earthquakes with high dip angles ($\geq 60°$) have been recorded in this area (Dasgupta & Mukhopadhyay, 1993), so they would appear to be somewhat characteristic of the Andaman Sea region.

3.4 1995 Kozani-Grevena, Greece, earthquake (051395B)

3.4.1 Introduction

The Aegean region of the eastern Mediterranean is experiencing significant tectonic extension due to back-arc spreading caused by the subduction of the African plate below the Eurasian plate along the Hellenic Trench. Recent geodetic measurements have shown that southwest Greece is moving south-southwest relative to Eurasia at a rate of ~20 mm/yr (Clarke et al., 1998; McClusky et al., 2000) and this motion causes much of the deformation in Greece to be expressed by extensional tectonics. In northwest Greece, the Aliakmon fault zone is an example of a localised region undergoing extension (Doutsos & Koukouvelas, 1998) and the site of the 5 May 1995 Kozani-Grevena earthquake.

3.4.2 Previous Studies

Source parameters determined for the Kozani-Grevena earthquake are summarised in Table 3.7. All studies estimate consistent focal mechanisms, with the strike of the fault plane reported varies between 242–274°, the dip between 38–47°, and the rake between -79° and -97°. The USGS catalogue quoted the shallowest centroid depth at 7 km, with the deepest reported by Arvidsson & Ekström (1998) at 20 km, using a modified version of the CMT method which incorporates 150–40 s surface waves. Kiratzi & Louvari (2003), using long-period P and SH waveform modelling, identified a 12 km focal depth, whilst Hatzfeld et al. (1997) studied aftershock hypocentres located by a local, temporary, network and found that the main fault was striking 240° west-southwest, dipping between 35–45° northwest and extended from 5–15 km depth. The geodetic study of Clarke et al. (1997), calculated a slip model that allowed rupture to occur between depths of 2.8–13.5 km. Papazachos et al. (1998) analysed aftershocks of the event and found them dipping to the northwest, consistent with the other studies. Resor et al. (2005) combined aftershock locations with geodetic observations and reported a near-west-striking fault dipping north at 43° and extending from 6–15 km in depth. In addition to these seismic, geodetic and InSAR studies, Meyer et al. (1996), using field geological observations, reported unambiguous surface rupture along a segment of a pre-existing fault striking ~250° and dipping ~40° to the northwest.

3.4.3 Results

Study	Strike (°)	Dip (°)	Rake (°)	Depth (km)	Moment (10^{18} Nm)	Mechanism
This Study	**245**	**39**	**-100**	**8**	**4.36**	
CMT	243	47	-97	15*	7.6	
USGS	252	39	-86	7	4.7	
Hatzfeld et al. (1997)	252	41	-87	11	6.2	
Clarke et al. (1997)	253	43	-95	2.8–13.5	16.3	
Arvidsson & Ekström (1998)	259	40	-79	20	8.28	
Kiratzi & Louvari (2003)	242	38	-91	12	4.59	
Rigo et al. (2004)	258	38	-97		6.9	
Resor et al. (2005)	274	43	-90	6–15	13.7	

Table 3.7: Source parameters determined for event 051395B here (bold) and in other studies. The depth ranges reported by Clarke et al. (1997) and Resor et al. (2005) represent the depth of a fault plane which is modelled as having slipped co-seismically. * indicates that the depth was fixed in the CMT inversion.

D-C solution space was grid-searched over the depth range 1–15 km and the optimum source parameters are listed in bold in Table 3.7. The orientation of the normal-faulting focal mechanism determined here is consistent with the results of other studies; while the 8 km optimum source depth here is in agreement with all studies listed in Table 3.7 except Arvidsson & Ekström (1998). Despite both this study and that of Arvidsson & Ekström (1998) using intermediate-period surface wave data, there is a difference in best centroid depth estimates of 12 km. The 8 km depth estimate determined here is more consistent with the other studies, suggesting that the Arvidsson & Ekström (1998) study is in error. It was shown in Figure 3.6 that longer-period waveforms are relatively insensitive to source depth and the use of such data in the work of Arvidsson & Ekström (1998) may explain their inconsistent depth estimate for this earthquake.

Rayleigh and Love wave synthetic amplitude spectra for the optimum source parameters determined in this study are shown, along with synthetic seismograms in Appendix D. The source is confined to be shallow here, between 4–10 km and the strike is well constrained between 230–276°. The bounding values in dip and rake are large for this event, owing to the presence of acceptable solutions corresponding to the other nodal plane; see Figure 3.10.

Parameter	Minimum	Optimum	Maximum
Strike (°)	230	245	276
Dip (°)	20	39	70
Rake (°)	-122	-100	-62
Depth (km)	4	8	10
Moment (10^{18} Nm)	3.34	4.36	6.38

Table 3.8: Bounding values of the 95% confidence region of source parameters determined for event 051395B.

In such a case the 4-D region of acceptable solutions is poorly characterised by the bounding values and leads to overestimations of the parameter bounds.

A summary of Figure 3.10 is given here in Table 3.8 and lists the range of statistically acceptable source parameters for the 1995 Kozani-Grevena earthquake. The close proximity of the fault plane to the auxiliary plane in this figure impairs the identification of rake and dip bounds specific to the fault plane due to the overlap of statistically acceptable solutions e.g. at 4 km especially, and to a lesser extent at 6 and 8 km.

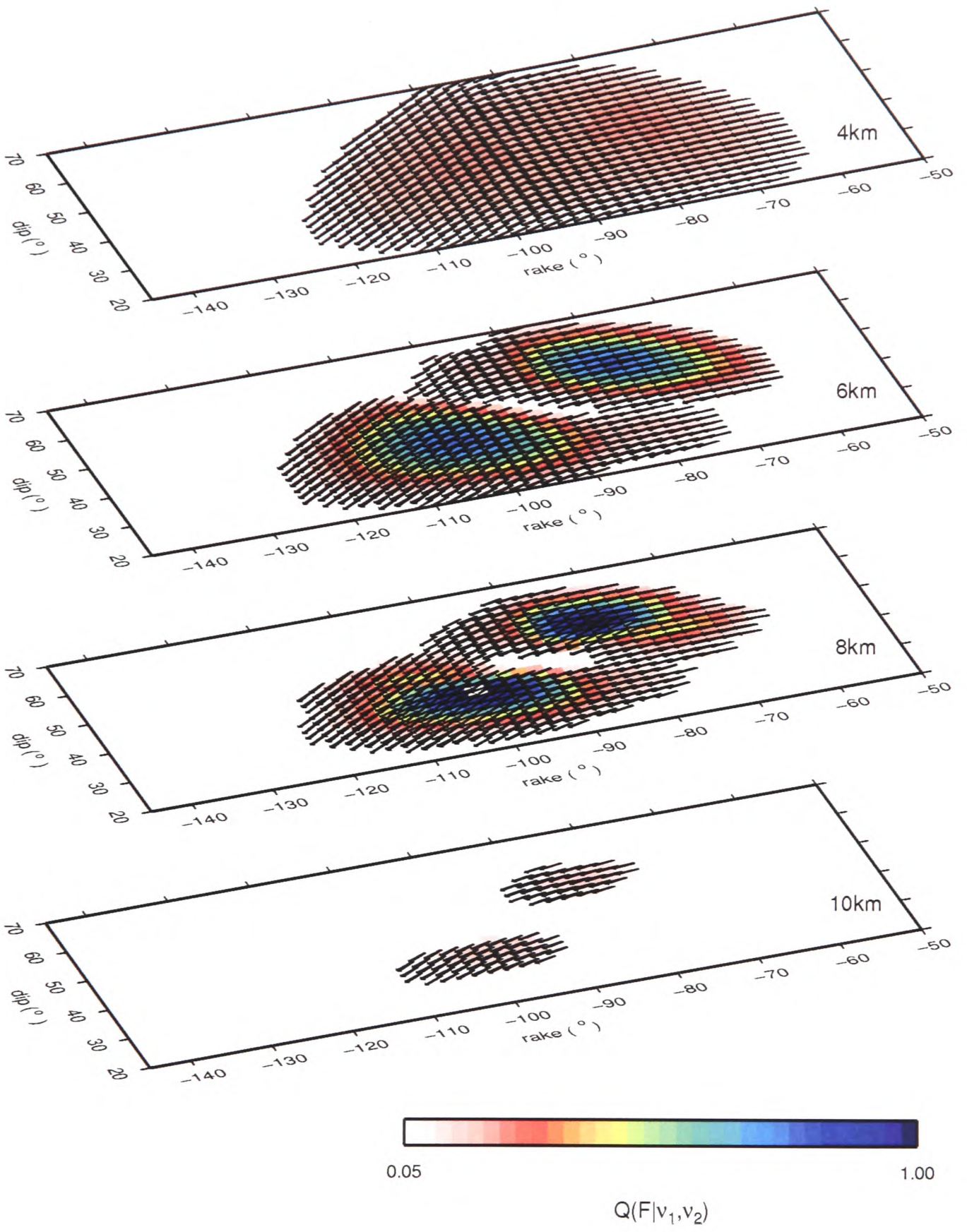


Figure 3.10: Slices through rake-dip-depth space for event 051395B at 4 km (minimum), 6 km, 8 km (optimum) and 10 km (maximum) depths. The optimum grid cell is coloured white. It should be noted that due to the close proximity of the auxiliary plane the bounding values for dip and rake in Table 3.8 do not provide a good measure of the true uncertainties of the source parameters.

3.5 1995 Dinar, Turkey, earthquake (100195B)

3.5.1 Introduction

Southwest Turkey lies in a part of the Aegean extensional domain and geodetic measurements show this region to be undergoing distributed extension of the order of 30 $\pm$ 1mm/yr in a west-southwest direction (McClusky et al., 2000). Extensional earthquake focal mechanisms characterise this region (Taymaz et al., 1991) and normal faults in this area are found generally to be striking northwest-southeast and northeast-southwest (Oncel et al., 1998).

On 1 October 1995 the $M_s = 6.1$ Dinar earthquake ruptured a section of the Dinar-Civril fault some 10 km long (Wright et al., 1999). This normal fault is ~75 km long, striking northwest-southeast and dipping to the southwest between 40–60° (Kocyigit, 1983). This earthquake provides a valuable opportunity to assess the ability of this method to calculate reliable source parameter estimates for a very shallow source.

3.5.2 Previous Studies

Source parameters previously determined for the 1995 Dinar earthquake are summarised in Table 3.9. In addition to the published CMT solution, the Harvard group carried out two further inversions for this event using geodetic and geological information provided in the study of Wright et al. (1999): (i) fixing the dip to be 45° and (ii) fixing the depth at 4 km. Eyidogan & Barka (1996) inverted teleseismic body waveforms after the method of McCaffrey & Nabelek (1987), while Pinar (1998) inverted the same waveforms, but following the inversion scheme of Kikuchi & Kanamori (1991). In both instances the authors chose to model the rupture as two separate sub-events. Wright et al. (1999) used both SAR Interferometry (InSAR) and long-period body-wave modelling to generate source parameters for this event. Utkucu et al. (2002) inverted teleseismic P and SH waveforms to model the co-seismic slip over a fault orientated as described by Pinar (1998).

Table 3.9 lists fault strikes in the range 125–137°, dips of approximately 45°, rake angles between -83° and -139°; all depth estimates reported were shallower than 15 km. The unambiguous determination of the seismogenic fault through the mapping of continuous surface ruptures (Demirtas et al., 1996; Eyidogan & Barka, 1996; Pinar, 1998) has led to the source

parameters of this earthquake being well determined and make the 1995 Dinar earthquake an excellent 'validation' event.

3.5.3 Results

Study	Strike (°)	Dip (°)	Rake (°)	Depth (km)	Moment (10^{18} Nm)	Mechanism
This Study	**128**	**44**	**-98**	**5**	**1.88**	
CMT	125	30	-93	15*	4.7	
CMT (adjusted dip)	125	45*	-93	15*	4.1	
CMT (adjusted depth)	136	45	-90	4*	3.3	
USGS	133	42	-89	8	1.3	
Eyidogan & Barka (1996):						
• 1st sub-event	135*	40	-105	8	0.38	
• 2nd sub-event	135*	62	-139	12	1.64	
Pinar (1998):						
• 1st sub-event	121	34	-99	10	0.5	
• 2nd sub-event	137	40	-83	15	1.6	
Wright et al. (1999)	136	43	-87	4	3.1	
Utkucu et al. (2002)			-102	7.5^{+}	2.8	

Table 3.9: Source parameters determined here (bold) and in other studies for the 1995 Dinar earthquake (event 100195B). * indicates the parameter was held fixed in the inversion. $^{+}$ indicates the depth of rupture initiation modelled by the authors.

D-C solution space in the depth range 1–15 km was grid-searched and best-fitting synthetic surface wave spectra were calculated at a centroid depth of 5 km. The optimum focal mechanism, listed in bold in Table 3.9, describes almost pure normal faulting on a 44° dipping plane striking 128°, in close agreement with that found by other authors. The 5 km depth estimate is consistent with the 4 km found by Wright et al. (1999) and the 8 km USGS solution. The other studies all calculate depths less than 15 km, indicating that this is a shallow event; indeed, the displacements seen at the surface expression of the fault are strong indicators of a very shallow source.

The proximity of the focal plane selected by the algorithm as the best source to the faulting

parameters determined in other studies gives sufficient confidence that this plane was seismogenic and not the auxiliary plane. The addition of 180° to the strike gives a source with identical surface wave amplitude spectra, and for this event it is difficult to choose between the two mechanisms on the basis of a surface waveform comparison. The mechanism chosen here is that which is more consistent with the other source solutions listed in Table 3.9.

Parameter	Minimum	Optimum	Maximum
Strike (°)	114	128	152
Dip (°)	10	44	80
Rake (°)	-122	-98	-58
Depth (km)	2	5	8
Moment (10^{18} Nm)	1.49	1.89	4.35

Table 3.10: Bounding values of the 95% confidence region of source parameters determined here for event 100195B.

Best-fitting waveforms and amplitude spectra for the source parameters calculated here are shown in Appendix D, whilst examples of the solution space confined by 95% confidence bounds are presented in Appendix E. The range of parameters deemed statistically acceptable here are shown in Table 3.10. With the exception of the centroid depth, confined between 2–8 km here, there are wide ranges in the other parameters. Again, this is attributable to the proximity of the fault and auxiliary planes in the solution space, as described for event 051395B. In these cases, the bounding parameter closest to the optimum should be considered representative of the the likely bounds; e.g. 14° in strike, 34° in dip and 24° in rake. At shallow depths especially, the wide range of possible solutions here is a due to the lack of resolution afforded by the f_4 and f_5 components of the seismic moment tensor.

For shallow sources, much of the depth-dependent structure of Rayleigh wave amplitude spectra is at the shorter-periods. It has been demonstrated earlier that frequency-dependent notches that provide depth constraints occur at the higher frequencies for shallower depths. By only using surface waves with periods to 20 s, additional information about the source is not being made available. In order to better constrain the source parameters, shorter-periods will need to be included in the algorithm, and this is considered in Chapter 5.

3.6 1997 Lake Tanganyika, Zaire, earthquake (092197C)

3.6.1 Introduction

Lake Tanganyika lies in part of the Western Rift in Zaire, a region of extension related to the East Africa Rift spreading centre in Ethiopia. The lake is bounded by normal faults striking to the north and northwest (Ebinger, 1989). On 21 September 1997, a $M_w = 5.9$ earthquake occurred beneath Lake Tanganyika, on the western side of the rift. The location of this central African earthquake and the distribution of seismic receivers around the continent make this a desirable event to study in order to assess how well the CUB Earth model represents the seismic properties of the region. In addition, this event occurred in an intra-continental rift, a tectonic setting usually associated with deep continental earthquakes (Doser & Yarwood, 1994).

3.6.2 Previous Studies

Table 3.11 summarises the source parameters published in the CMT and USGS catalogues and the Foster & Jackson (1998) study of large African earthquakes. All results are consistent with the extensional tectonic setting, determining normal-style faulting with a dextral component on a north-west striking, north-east dipping fault. Located to the west of Lake Tanganyika, it is likely that the seismogenic fault plane is one of the rift-bounding normal faults around the lake; if so, then it would be expected that this fault dips towards the east – the orientation of the fault planes reported by these previous studies.

There is close agreement between the depth of the CMT solution (30 km) and the centroid depth of 29 km determined by the teleseismic body-wave inversion of Foster & Jackson (1998), though these differ from the 22 km USGS estimate. The focal mechanisms of these three studies shown in Table 3.11 describe the same style of deformation with strikes varying by 12°, dips by 12° and rake angles by 15°.

3.6.3 Results

A source parameter grid-search was performed at depths between 20–50 km, the misfit-depth curve calculated is shown in Figure 3.11 where the best-fitting depth of 39 km is shown along with the Earth model used. The fault plane is calculated to be dipping to the east, consistent with the expected dip of a normal fault on the western side of an extensional rift.

Study	Strike (°)	Dip (°)	Rake (°)	Depth (km)	Moment (10^{17} Nm)	Mechanism
This Study 39 km	**326**	**36**	**-110**	**39**	**9.04**	
CMT	315	36	-133	30	8.3	
USGS	320	24	-124	22	7.0	
Foster & Jackson (1998)	327	36	-118	29	6.2	

Table 3.11: Source parameters determined here (bold) and in other studies for the 1997 Lake Tanganyika earthquake (event 092197C).

The 39 km centroid depth is greater than any other depths determined in this chapter, but is not uncharacteristic for this area. Nyblade & Langston (1995) reported focal depths in the region between 24–34 km and inferred that the continental crust, in places, was at least 40 km thick. Analysis of Figure 3.11 shows that this event is best located below a major velocity discontinuity in the local Earth model (the Moho) between 37–38 km depth.

At shallower depths than 39 km a local minimum is calculated at 33 km, close to the estimates of Foster & Jackson (1998) and the CMT solution. This solution can be rejected with 35% confidence that it is not the optimum, so the earthquake cannot be entirely discarded as a potential lower crustal event. A waveform comparison between sets of synthetics for these two sources and the data indicates that the 33 km source provides better fits to the recorded seismograms by 1.1%. Between 32–42 km, the optimum source mechanism parameters are determined to be the same (ϕ_s=326°, δ=36°, λ=−110°) indicating that the mechanism is being robustly constrained by this analysis of the surface waves, regardless of the modelled source depth.

The method is sensitive to the Earth model used for this study and the determination of a 39 km source depth is strongly influenced by the nature of the local velocity structure. If this

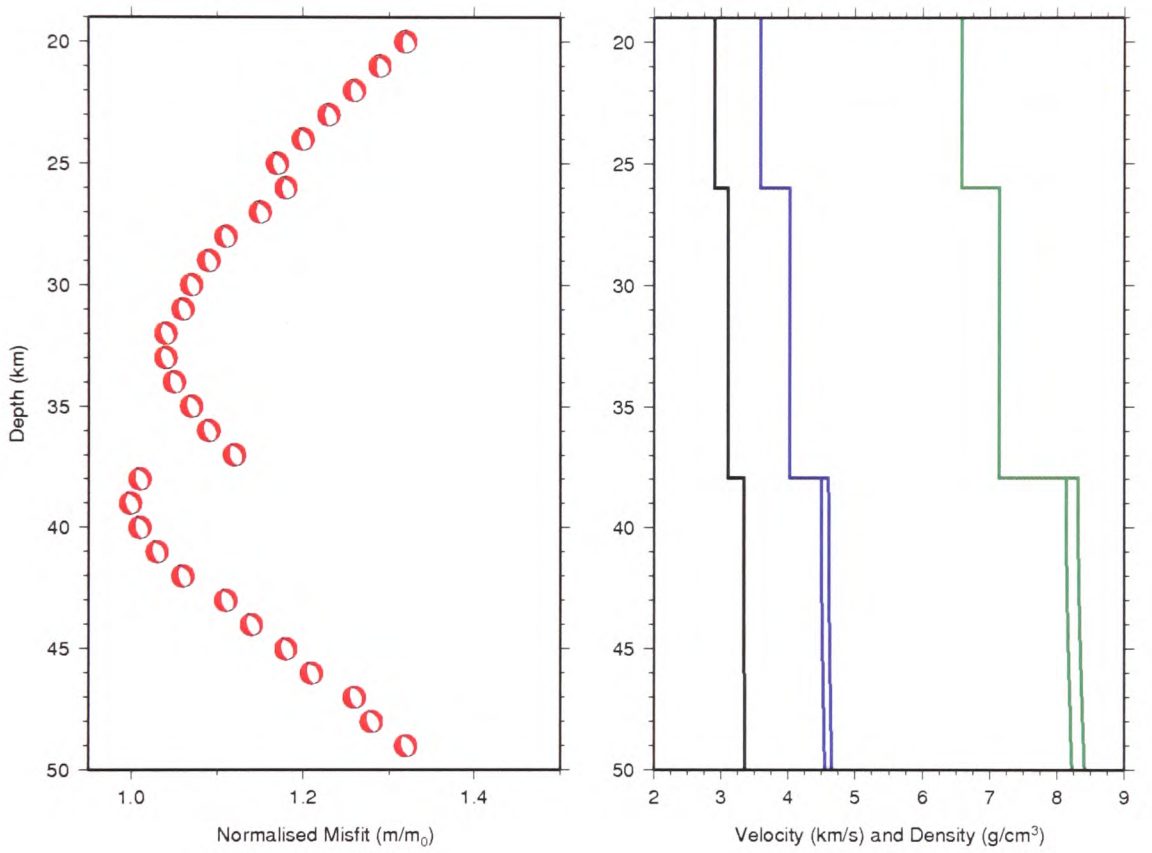


Figure 3.11: LHS: misfit-depth profile for the best-matching source mechanisms at each depth for the 1997 Lake Tanganyika earthquake (event 092197C). RHS: local Earth model used, key as described in Figure 3.2.

structure is accurate and the Moho in this region is shallower than 39 km (no conclusive evidence of the Moho depth around Lake Tanganyika has been found in the literature) then this event is a candidate for further study owing to its importance for the theory that earthquakes do not occur in the continental mantle.

Parameter	Minimum	Optimum	Maximum
Strike (°)	306	326	340
Dip (°)	28	36	44
Rake (°)	-140	-110	-94
Depth (km)	22	39	46
Moment (10^{17} Nm)	5.80	9.04	9.77

Table 3.12: Bounding values of the 95% confidence region of source parameters determined here for event 092197C in Lake Tanganyika, Zaire.

Synthetic amplitude spectra and waveforms for the optimum mechanism at 39 km and for comparison, the 33 km source, are shown in Appendix D; the statistically acceptable solution space is depicted in Appendix E. This is summarised in Table 3.12 and it is shown that the strike, dip and rake of the fault plane selected here are well constrained by 34°, 16° and 46° ranges respectively. Source solutions within the 95% confidence bounds are determined to have centroid depths between 22–46 km, a larger range than previously seen in this chapter and considered to be caused by the lack of depth-sensitive structures in some of the signals used (especially the LHT channel) due to the approximate exponential decay of surface wave excitation with depth.

3.7 2002 Molise, Italy, earthquakes (103102B & 110102F)

3.7.1 Introduction

The Molise region of southeast Italy is situated to the northeast of the Southern Apennine mountain range; the stress regime in this area is complex and open to debate (Di Luccio et al., 2005). The lack of historical or instrumentally-detected earthquakes makes the determination of the dominant style of deformation here difficult. Generally, the southern Apennine region is characterised by normal-faulting, with strike-slip faulting the chief mechanism of deformation in the foreland region (Frepoli & Amato, 2000).

On October 31 2002, a $M_w = 5.7$ earthquake (event 103102B) occurred in this foreland region, near Molise, and it was followed a day later by a second, similarly-sized, earthquake (event 110102F). NEIC located the epicentres of these events at 41.79°N 14.87°E and 41.73°N 14.88°E respectively, some 7 km apart. Figure 3.12 shows the locations of these two earthquakes along with the stations used in this source study.

3.7.2 Previous Studies

Source parameters previously determined for the Molise earthquakes are listed in Table 3.13 and describe strike-slip faulting with depths ranging between 10–20 km. Di Luccio et al. (2005) inverted broadband waveforms, reporting almost pure dextral strike-slip motion on near-vertical, approximately East-West striking fault planes and centroid depths of 14 km (103102B) and 11 km (110102F). The most prominent fault in the area (the Mattinata Fault) was identified as the likely source of these earthquakes, the present-day motion on this steeply-dipping fault is considered to be right-lateral, consistent with both calculated fault plane solutions.

Using teleseismic body waves, Vallee & Luccio (2005) modelled slip distributions and both earthquakes were estimated to have similar focal mechanisms (right-lateral strike-slip, on steeply dipping fault planes) with hypocentral depths of 16 km (103102B) and 18 km (110102F); rupture was estimated to have occurred between depths of 6–20 km and 9–18.5 km respectively.

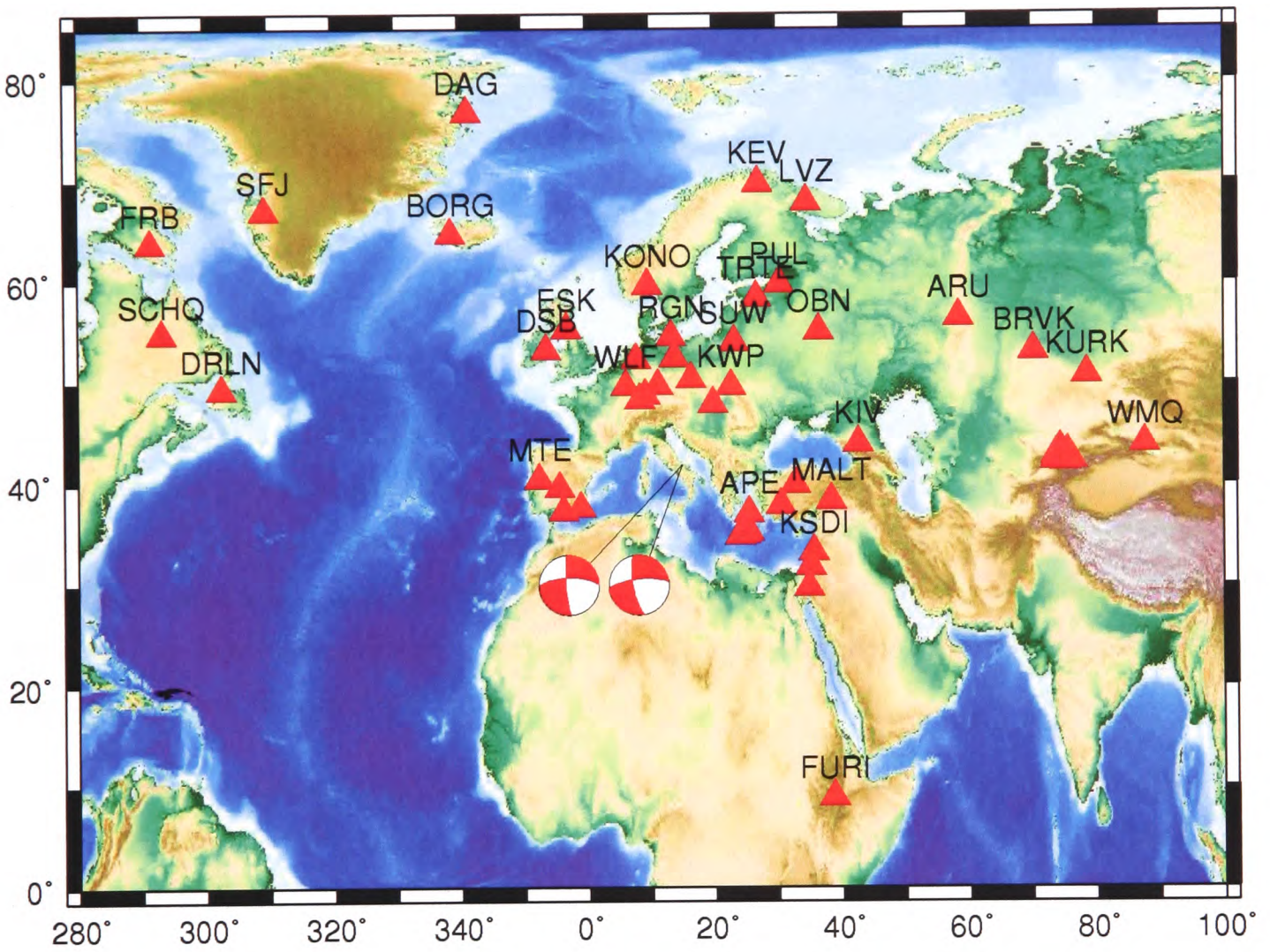


Figure 3.12: Regional map showing the location of the 2002 Molise earthquakes, events 103102B (left focal mechanism) and 110102F (right focal mechanism), and the stations used in this study. The stations to the south of MTE are PAB, CART and SELV; those stations between WLF and KWP are IBBN, BFO, STU, GRFO, RUE, DPC and PSZ; the stations south of APE are FODE, KRIS, APEZ and GVD; between APE and MALT are ISP and ANTO; to the south of KSDI are JER and EIL; and the stations west of WMQ are AAK, AML, CHM, EKS2, KBK, KZA, UCH, ULHL and USP.

Chiarabba et al. (2005) studied the mainshocks and aftershocks in the sequence using a temporary network and determined that both main earthquakes ruptured the same east-west trending fault. In addition, the aftershock locations indicated that event 103102B ruptured along a fault plane dipping almost vertically (with aftershocks located between 8–20 km depth), while event 110102F ruptured a segment of the fault with a ~75° N-directed dip, with aftershocks occurring between 10–20 km.

The CMT and USGS catalogues list both earthquakes as being of predominately dextral strike-slip style. The CMT depth is fixed at 15 km for both events and the USGS report centroid depths of 11 and 10 km.

3.7.3 Results

All D-C sources in the depth range 1–30 km were grid-searched with the best-fitting synthetic amplitude spectra identifying optimum centroid depths at 12 km (103102B) and 11 km (110102F) as listed in bold in Table 3.13. These depths closely match the USGS estimates of centroid depths and also those published by Di Luccio et al. (2005); in studies where distributed slip has been modelled, these estimates fall within the depth ranges over which slip has been allowed to have occurred.

The fault plane solution listed for event 103102B describes almost pure right-lateral strike-slip motion on a steep (70°), north-dipping fault plane; consistent with the focal mechanism of Chiarabba et al. (2005) and similar to those determined by Vallee & Luccio (2005) and the USGS. A waveform comparison demonstrates that mechanism 1 provided better waveform fits to the data than a 180° strike rotation of that source; for the second event, such a comparison does not categorically identify the best oriented source so both mechanism 2 and 3 are listed in Table 3.13. Of the 61 surface wave recordings used in the waveform analysis of event 110102F, 31 favoured mechanism 2 with 30 favouring mechanism 3. Preference here is made for mechanism 3, a dextral strike-slip focal mechanism with a small normal faulting component, occurring on a fault plane striking 264° and dipping northwards at 74°. This source is consistent with both mechanism 1 and the pattern of aftershocks reported by Chiarabba et al. (2005).

Plots of the best-fitting surface wave amplitude spectra and waveforms for both of these

Study	Strike (°)	Dip (°)	Rake (°)	Depth (km)	Moment (10^{17} Nm)	Mechanism
This Study 1	**269**	**70**	**-171**	**12**	**3.63**	
CMT	180	79	11	15*	4.6	
USGS	1	88	1	11	7.3	
Di Luccio et al. (2005)	83	80	-170	14	6.2	
Vallee & Luccio (2005)	276	84	-177	6-20	5.46	
Chiarabba et al. (2005)	178	80	-10	8-20	5.7 (M_w)	
This Study 2	**84**	**74**	**-164**	**11**	**3.01**	
This Study 3	**264**	**74**	**-164**	**11**	**3.01**	
CMT	171	66	-5	15*	4.6	
USGS	357	85	5	10	6.4	
Di Luccio et al. (2005)	81	85	-164	11	4.99	
Vallee & Luccio (2005)	273	76	-178	9-18	3.58	
Chiarabba et al. (2005)	165	76	-29	10-20	5.7 (M_w)	

Table 3.13: Source parameters determined for the Molise, Italy, earthquakes, 103102B (top, 1) and 110102F (bottom, 2 and 3) here (bold) and in other studies. The fault plane solutions reported by Chiarabba et al. (2005) are taken from the Harvard European-Mediterranean Regional Centroid-Moment Tensors Project. The depth ranges determined by Vallee & Luccio (2005) are the minimum and maximum extents of the fault planes on which rupture was modelled. The depth ranges published by Chiarabba et al. (2005) represent the minimum and maximum depths of aftershock activity.

earthquakes are shown in Appendix D; contour plots of solutions falling within 95% confidence bounds are presented in Appendix E and summarised in Table 3.14. The optimum strike, dip and rake angles are calculated to lie in statistically acceptable ranges of size 12°, 30°, and 34°; and 12°, 58°, and 52°, for events 103102B and 110102F respectively. The ranges of acceptable depths for these events, 7–22 km and 4–24 km, are larger than have been found for other similar-sized earthquakes at these depths with non-strike-slip focal mechanisms.

Parameter	Minimum	Optimum	Maximum
Event 103102B			
Strike (°)	262	269	274
Dip (°)	50	70	80
Rake (°)	-192	-171	-158
Depth (km)	7	12	22
Moment (10^{17} Nm)	3.21	3.63	4.37
Event 110102F			
Strike (°)	258	264	270
Dip (°)	32	74	90
Rake (°)	-188	-164	-136
Depth (km)	4	11	24
Moment (10^{17} Nm)	2.49	3.01	4.40

Table 3.14: Bounding values of the 95% confidence region of source parameters determined here for the 2002 Molise earthquakes.

3.8 2004 Parkfield, California, USA, earthquake (092804H)

3.8.1 Introduction

The San Andreas Fault (SAF) is the primary fault accommodating the predominantly dextral motion between the Pacific plate and the North American Plate. The Parkfield region of the SAF marks the transition between a seismically locked zone to the south east and a region of creep to the northwest (Custodio et al., 2005). The locked portion of this fault is responsible for the generation of moderate to large earthquakes spaced ~150 years apart (Sieh, 1978); Bakun & McEvilly (1984) suggested that a significant earthquake could be expected in Parkfield between 1983 and 1993, leading to the creation of the Parkfield Prediction Experiment (Bakun & Lindh, 1985) and resulted in the 28 September 2004 earthquake (event 092804H) being extensively recorded in the near-source region.

Situated on the west coast of North America, the majority of the surface wave recordings used in this study are from stations located to the north and east of the earthquake, leading to a distinctly non-uniform azimuthal coverage. The analysis of this earthquake will indicate how well intermediate-period surface waves can constrain the source parameters of a shallow, strike-slip faulting event. In addition, this study allows an assessment of the quality of the CUB Earth model in this region to be made, it being the only event studied in this thesis with a source on the North American continent.

3.8.2 Previous Studies

Much of the published literature concerning this event focuses on the modelling of the distribution of fault slip, treating the earthquake as a finite source rather than a point source. Many studies make use of local seismic networks and strong-motion data to calculate 'ground truth' estimates with which the results of this study can be compared.

Table 3.15 summarises the source parameters published for the 2004 Parkfield earthquake. Both CMT and USGS catalogues quote almost pure dextral strike-slip mechanisms on a fault trending southeast-northwest, with centroid depths of 12 km (fixed) and 8 km respectively. These two solutions differ in their direction of dip, with the former indicating a northeast-dipping fault plane, whilst the latter describes rupture on a southwest-dipping fault.

Study	Strike (°)	Dip (°)	Rake (°)	Depth (km)	Moment (10^{17} Nm)	Mechanism
This Study	**140**	**86**	**136**	**2**	**11.0**	
CMT	321	72	-178	12*	11	
USGS	147	83	-175	8	9.8	
SCEC	140	83	170	18 (5.5^{+})	12.6	
SLUEC	140	85	-155	6	5.9 (M_w)	
Langbein et al. (2005)	140	77	-172	8	9.97	

Table 3.15: Source parameters determined for the 2004 Parkfield earthquake here (bold) and in other studies.

The Southern California Earthquake Center (SCEC)[1] calculated a real-time hypocentre depth of 5.5 km and published a reviewed moment tensor solution with a similar mechanism to that of the USGS but with a greater depth of 18 km. The Saint Louis University Earthquake Center (SLUEC) calculated a centroid depth of 6 km using surface wave spectral amplitude observations between 200–10 s periods. Predominantly right-lateral strike-slip motion is determined, although a rake angle of -155° describes a significant normal faulting component. The optimum centroid depth of 6 km is similar to the 8 km reported by the USGS, although upon closer inspection of the depth-fit curve published[2], there is little difference in the fit at depths between 4–25 km.

Langbein et al. (2005) calculated source parameters using an automated, complete waveform method described by Pasyanos et al. (1996), which fitted 50–20 s period three-component waveforms at five local stations. An analysis of the locations of aftershocks identified a southwest dipping fault plane and they reported a similar mechanism to that of the USGS and exactly the same focal depth of 8 km.

Custodio et al. (2005) inverted near-source ground motion and modelled rupture on a fault striking 141° and dipping 89° to the southwest, consistent with the orientation determined by Langbein et al. (2005). The hypocentre was found to be at 8.1 km depth and the fault was allowed to rupture between the surface and 15 km depth. The highest regions of slip were found to be around the hypocentre, with another area at shallower depths ($\sim$ 2 km).

[1] http://www.data.scec.org/mtarchive/solution.jsp?eventid=14094992
[2] http://www.eas.slu.edu/Earthquake_Center/MECH.NA/20040928171524/index.html

A rupture model using solely seismic data calculated by C. Ji[3] described peak slip occurring between 5–7 km; a model using only geodetic data calculated peak slip between 6–8 km, with significant slip as shallow as 2 km depth (R. Murry[4]). A combined seismic and geodetic slip model presented by D. Dreger[5] calculated two distinct areas of peak slip; one centred around 5 km depth and another around 2 km.

3.8.3 Results

D-C solution space was searched between 1–15 km and the best-fitting solutions at each depth are shown in Figure 3.13. The observed surface wave spectra are best matched by synthetics generated at a 2 km centroid depth with a focal mechanism as listed in bold in Table 3.15. The fault plane solution calculated here describes faulting on a plane striking 140° and dipping 86° to the southwest, in close agreement with the other source studies and the aftershock study of Langbein et al. (2005). However the calculated angle of rake is somewhat different to the other studies; at 136° it describes a style of deformation partitioned almost equally between dextral strike-slip and reverse faulting. The 2 km best-fitting centroid depth is somewhat shallower than centroids determined in other studies; but is consistent with shallow patches of high slip found in some of the rupture models. In places, observations of discontinuous surface ruptures over some 32 km (Rymer et al., 2006) indicate the occurrence of slip at shallow depths, although the calculated rupture models suggest the maximum displacements took place at around 6 km depth.

The 2004 Parkfield earthquake was a predominantly dextral strike-slip event, so the determination of a faulting style with a significant reverse-faulting component is somewhat unexpected. Table 3.16 lists the results of a source parameter search for a fixed strike of 140° where the fault dip angle was systematically shallowed at 5° intervals between 90° and 60°. It can be seen that as the fault angle shallows, the rake angle gets closer to describing pure dextral strike-slip. Indeed, there are some source solutions listed in Table 3.15 that appear to support this finding (e.g. Langbein et al., 2005); for instance, with the exception of this study, the focal mechanism with the steepest dipping angle has the rake angle that deviates most from pure right-lateral strike-slip.

[3] http://www.tectonics.caltech.edu/slip_history/2004_ca/parkfield1.html
[4] http://www.cisn.org/special/evt.04.09.28/finite.jmurray.html
[5] http://www.cisn.org/special/evt.04.09.28/finite.dreger.html

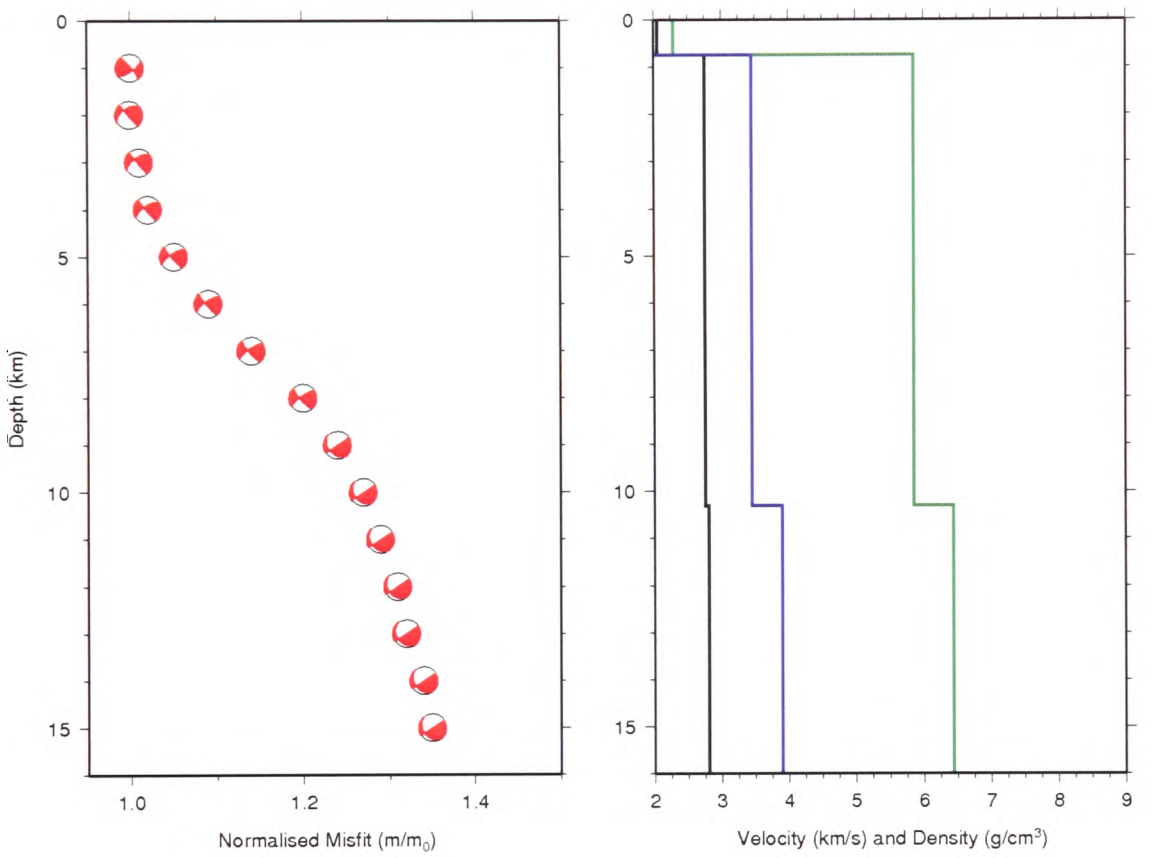


Figure 3.13: LHS: misfit-depth profile for the best-matching source mechanisms at each depth for the 2004 Parkfield, California, earthquake. RHS: local Earth model used here, key as described in Figure 3.2.

Strike (°)	Dip (°)	Rake (°)	Depth (km)	Moment (10^{17} Nm)	Mechanism
140	90	130	3	12.4	
140	85	142	2	10.1	
140	80	158	2	8.70	
140	75	164	2	8.56	
140	70	168	2	8.64	
140	65	170	2	8.90	
140	60	172	1	8.99	

Table 3.16: The results of source parameter search when the strike is fixed at 140° and the dip of the fault plane is systematically altered between 90° and 60°.

This relationship is clear to see in the contour plots in Figure 3.14. Here solutions falling within 95% confidence bounds are described on depth slices through (λ,δ,h) space. The trade-off between dip and rake presented in Table 3.16 is clearly displayed in this figure too, especially at the shallow depths, with the region of best fits (i.e. highest values of $Q(F|\nu_1, \nu_2)$) indicating that by shallowing the fault dip the data is best matched by increasing the rake angle.

A waveform comparison indicates that a source representative of a 180° rotation of the focal mechanism determined here ($\phi_s = 326°$, $\delta = 86°$, $\lambda = 136°$) produces synthetic seismograms which match the observed data equally well causing a source ambiguity. However, this alternative source mechanism is rejected because the orientation of the fault described is in contrast to the orientation of the SAF observed in the Parkfield region.

Parameter	Minimum	Optimum	Maximum
Strike (°)	134	140	146
Dip (°)	4	86	90
Rake (°)	94	136	178
Depth (km)	1	2	12
Moment (10^{18} Nm)	0.76	1.10	10.4

Table 3.17: Bounding values of the 95% confidence region of source parameters determined here for the 2004 Parkfield, California, earthquake.

Comparisons with other work suggest that the strike of the fault plane of the 2004 Parkfield

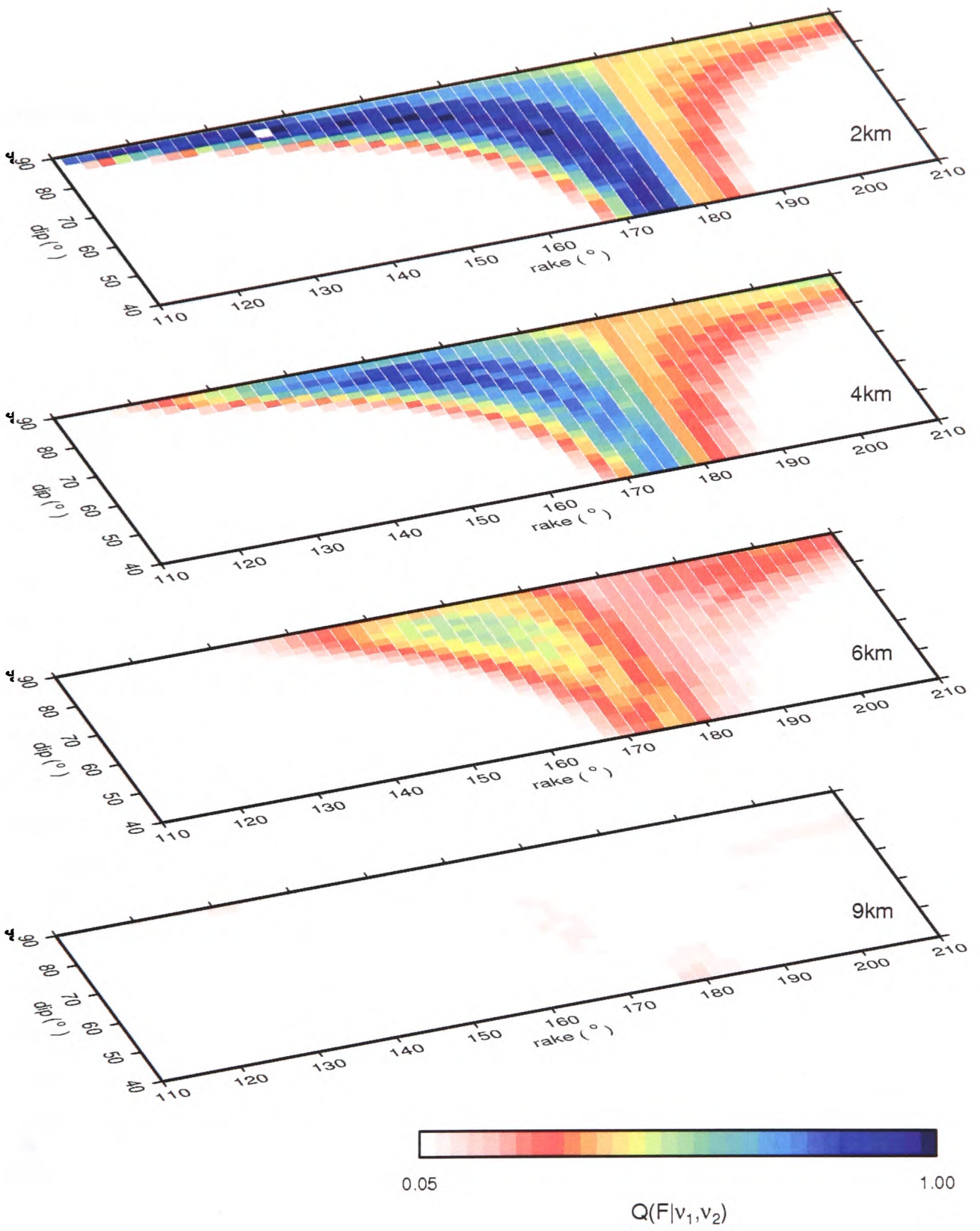


Figure 3.14: Plots of calculated values of $Q(F|\nu_1, \nu_2)$ for a fixed strike of 140° at 2 km, 4 km, 6 km and 9 km depths. The best-fitting dip-rake combination ($\delta = 86°$, $\lambda = 136°$) is signified by the white square on the 2 km plane.

earthquake is well determined here, along with a steeply southwest-dipping angle of faulting. However, the very shallow calculated centroid depth, along with a rake angle describing ~50% strike-slip motion on perhaps the world's most famous dextral strike-slip fault, is of concern. The best-fitting surface wave amplitude spectra and waveforms generated here are shown in Appendix D, whilst the range of statistically acceptable solutions bounded by 95% confidence bounds are shown in Appendix E. The range of source parameters allowed by these solutions are summarised in Table 3.17. Of these parameters, the strike is constrained to within $\pm 6°$ of the 140° optimum; and whilst the centroid depth is certainly confined to be 'shallow' (≤ 12 km), some solutions falling within 95% confidence bounds require dips as low as 4° and rakes as small as 94° (describing almost pure thrust-faulting). With reference to Figure 3.14 it can be seen that these shallow dips correspond to almost pure dextral strike-slip rakes, whilst at high angles, the synthetic surface wave amplitude spectra require low rake angles to best describe the data. The lack of constraints placed on the dip and rake angles here is believed to be caused by the poor resolution of the f_4 and f_5 components of the moment tensor at shallow depths.

Due to the shallow nature of the source, it is highly likely that there is additional information in shorter-period surface waves that is being excluded from this study. The shape of the misfit-depth profile in Figure 3.13 is a clear indication that there is not sufficient resolution in 100–20 s period surface waves to satisfactorily identify and constrain optimum source parameters for very shallow strike-slip faults.

Analysis of the 2004 Parkfield earthquake also suffers from a strongly non-uniform distribution of seismic stations over regional distances due to its location on the west coast of North America. It might be considered that the unsatisfactory identification of source parameters here could partly be due to the poor constraint of the surface wave radiation patterns. Along with the inclusion of shorter-period data, this matter of receiver distribution is addressed in Chapter 5.

3.9 Summary

The method of analysis outlined in Chapter 2 has been systematically applied to a representative set of 14 shallow, well studied earthquakes. Comparisons with other source studies indicate that this method yields reliable determinations of focal mechanisms and source depths across a range of tectonic regimes from subduction environments (events 091302C and 091402B) to intra-continental rift zones (events 092197C and 022599H).

With the exception of the 2004 Parkfield earthquake, source parameters are in good agreement with those determined in other studies; in the case of the Parkfield event, further work is required to assess the effects that the azimuthal station coverage, the 100–20 s spectral period range and the very shallow strike-slip source have on the ability of surface waves to constrain the faulting parameters.

Source depths are calculated in this chapter between 2–39 km. The optimum depth of 39 km calculated for the 1997 Zaire earthquake lies below the Moho in the local Earth model used. Additional study is required to assess whether this event really lies in the upper mantle; this would require better knowledge of the local velocity structure, especially the location of the Moho in this region. It is likely that this result is influenced by changes in the local eigenfunctions and their radial derivatives across the Moho, though this is a computational artefact and would be expected with any model containing such velocity discontinuities.

In the cases of the Andaman and Molise earthquakes, where two significant seismic events occurred in close proximity in both space and time, it may be assumed that both sets of events ruptured similar portions of their respective seismogenic faults. That consistent source parameters were determined in both studies gives confidence in the reliability of these techniques.

This method is shown to generate good matches between synthetic and data amplitude spectra and synthetic and data seismograms (see Appendix D). Not only does this prove the worth of the synthetic seismogram generation code and provide confidence in the determined source parameters, but it also justifies the use of the CUB Earth model. While the majority of these earthquakes occurred and were recorded on the Eurasian continent, the 1997 Zaire and 2004 Parkfield earthquakes afford an opportunity to asses the performance of the Earth model on both Africa and North America. In both cases 100–50 s synthetic waveforms are seen to match recorded seismograms and show that, although the model is expected to be best determined

across Eurasia (see Shapiro & Ritzwoller, 2002), it does contain sufficient detail to allow the accurate synthesis of realistic Earth synthetics on these other continents.

These earthquakes vary in magnitude between $5.4 \leq M_{\mathrm{w}} \leq 6.5$ and at both ends of the scale it has been demonstrated that the method gives trustworthy estimates of source parameters. Papazachos et al. (1998) modelled the $M_{\mathrm{w}} = 6.4$ Kozani-Grevena earthquake as a rupture some 30 km in length; the shortest period of the surface waves used here (20 s) corresponds to wavelengths of the order of 70 km. The modelling of this relatively large event as a point source is justified given that the length of the waves used is somewhat larger than the likely spatial extent of the source. It is unlikely that for events much larger than $M_{\mathrm{w}} = 6.4$ that the point-source approximation is realistic, although given favourable signal-to-noise ratios it is anticipated that earthquakes smaller than $M_{\mathrm{w}} = 5.4$ can be studied with confidence; indeed this theme is continued in the following chapter.

In some cases it was found that source parameters (especially dip and rake) could not be tightly constrained. As a result of imposing a D-C constraint on the source, in cases where both planes of a focal mechanism have similar dip and rake angles, the full 4-D distribution of solutions acceptable at the 95% confidence level is not well characterised by considering only the bounding values. In such cases, faulting parameters are often over-estimated and should be treated accordingly. This D-C constraint does not affect the estimates of source depth determined in this chapter, which have been demonstrated to be trustworthy and generally well constrained.

Chapter 4

Sumatra Aftershocks 2004–2005

"There are no facts, only interpretations."

Friedrich Nietzsche (1844–1900)

4.1 Overview

Source parameters are determined for 16 aftershocks ($4.8 \leq M_{\mathrm{w}} \leq 6.0$) of the 2004 great Sumatra earthquake. Three distinct regimes of seismicity are identified with focal depths ranging from 3–61 km. Despite the relatively complex tectonic setting, trustworthy source parameters are determined which include the relocation of one earthquake some 27 km deeper than the depth published in the CMT catalogue, to a location more consistent with neighbouring events.

4.2 Introduction to Sumatra

The $M_{\mathrm{w}} = 9.15$ Sumatra earthquake which occurred on 26 December 2004 was the largest seismic event of the past 40 years. The aftershock sequence of this earthquake occurred along a ~1300 km-long portion of the curved plate boundary between the Indo-Australian plate and the southern section of the Eurasian plate (Lay et al., 2005; Ni et al., 2005; Ishii et al., 2005; Ammon et al., 2005; Tsai et al., 2005). On 28 March 2005, some three months later,

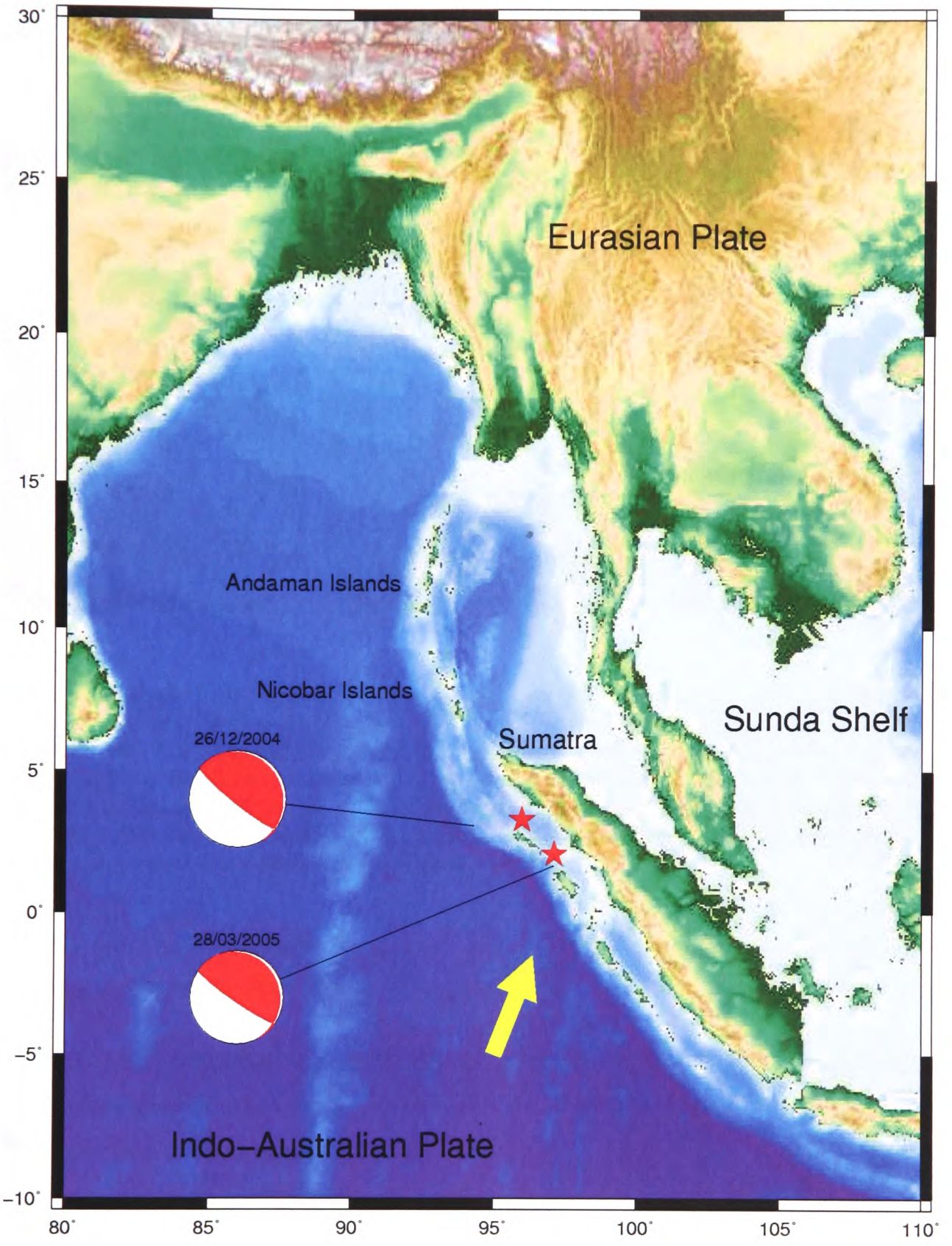


Figure 4.1: Regional map showing the boundary between the subducting Indo-Australian plate and the over-riding Sunda Shelf (part of the Eurasian plate). The angle of convergence becomes increasingly oblique northwards, the yellow arrow denotes the 20° collision angle at 5°S 95°E. CMT best double-couple fault plane solutions are shown for both the 26 December 2004 and 28 March 2005 earthquakes; the red stars denote the positions of the epicentres as reported by NEIC.

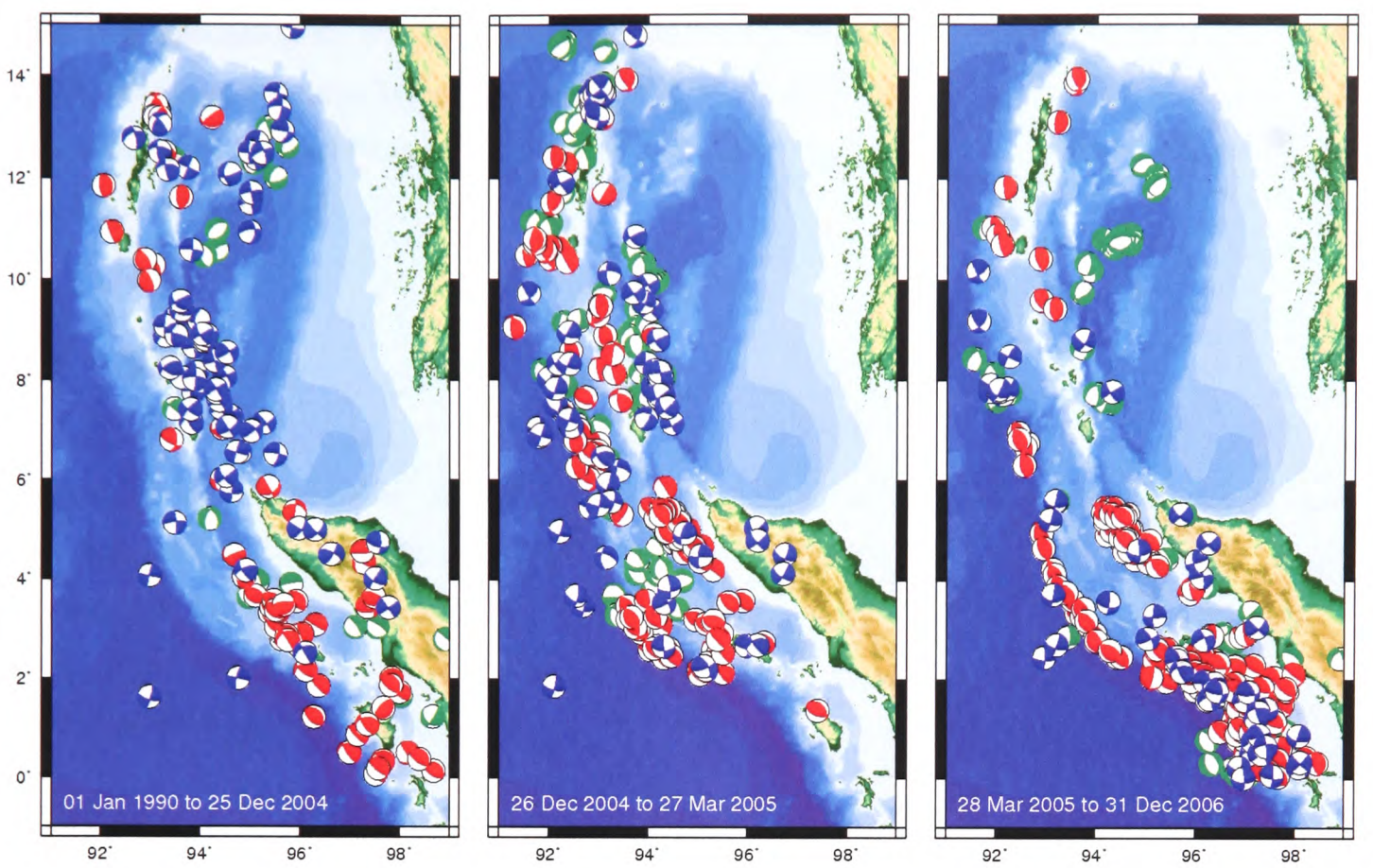


Figure 4.2: Published CMT mechanisms located in the Sumatra-Andaman region over three distinct time periods: 1 January 1990 to 25 December 2004 (left); 25 December 2004 to 28 March 2005 (centre) and 28 March 2005 to 31 December 2006 (right). Many of the events occurring between the two great earthquakes are considered to be aftershocks of the December 2004 mainshock. Red focal mechanisms represent thrust faulting ($45° \leq \lambda \leq 135°$); green focal mechanisms indicate extensional faulting ($-45° \leq \lambda \leq -135°$) and blue mechanisms describe strike-slip faulting (all other rake angles). Focal mechanism size plotted is not scaled to event magnitude.

a $M_w = 8.7$ earthquake ruptured an adjacent ~300 km portion of the plate boundary to the south in the region of the Nias Islands (Bilham, 2005).

Both earthquakes occurred along the Sunda Trench; where the Indian and Australian plates, moving northeastwards, are subducting beneath the Sunda Shelf (the southern most part of the Eurasian plate in this region). In the epicentral region of the 2004 mainshock, the oblique plate convergence takes place at some 40 mm/yr (Bettinelli et al., 2006; Socquet et al., 2006). Figure 4.1 gives a generalised overview of the regional tectonic setting along with NEIC locations of the epicentres of both the 2004 and 2005 mainshocks and the corresponding CMT mechanisms and centroid locations.

All CMT solutions determined in this region between 1 January 1990 and 31 December 2006 are plotted in Figure 4.2 coloured according to their predominant faulting type. As an indi-

cation of how energetic the 2004 and 2005 aftershock sequences were, 159 earthquakes with CMT solutions occurred between 1 January 1990 and 25 December 2004; 399 occurred between the 2004 and 2005 mainshocks and a further 352 occurred between the 2005 mainshock and 31 December 2006.

4.3 Transect

Guided by the central plot in Figure 4.2 a transect is selected between the Sunda Trench and the northwest coast of Sumatra and aftershocks are identified for study. As part of the most significant aftershock sequence in recent times, the range of available earthquake sizes, styles and depths make this area worthy of study. The hypocentral parameters of 16 chosen earthquakes, along with their corresponding CMT solutions are listed in Table 4.1.

Date	Time hh:mm:ss.s	Lat (°)	Lon (°)	Depth (km)	Magnitude (M_w)	Event Code	Mechanism
2004 12 27	00:24:30.8	4.47	93.81	12	5.2	122704A	
2004 12 27	10:05:05.4	4.72	95.11	53	5.7	122704T	
2004 12 28	21:09:05.4	3.71	94.61	12	5.1	122804R	
2004 12 30	01:04:51.8	4.23	94.22	19	5.2	123004A	
2004 12 30	01:43:05.4	4.22	94.26	25	4.8	123004C	
2004 12 31	17:48:05.7	4.73	95.14	24	5.9	123104M	
2005 01 04	18:26:44.7	4.92	94.79	49	5.2	010405A	
2005 01 05	05:32:38.5	3.53	93.65	12	5.1	010505A	
2005 01 06	00:56:29.9	5.32	94.83	54	5.6	010605A	
2005 01 09	17:16:46.0	3.32	94.28	12	5.2	010905A	
2005 01 14	21:38:16.7	3.13	93.92	12	5.6	011405A	
2005 01 29	06:10:43.8	3.33	93.70	12	5.5	012905A	
2005 02 09	13:27:25.3	4.80	95.12	47	6.0	020905A	
2005 02 13	01:22:09.3	5.08	94.79	51	5.3	021305A	
2005 02 17	05:31:28.1	4.70	95.16	50	5.6	021705A	
2005 03 17	23:20:49.4	4.86	95.09	45	5.7	031705A	

Table 4.1: NEIC epicentral parameters for the 16 events chosen for study. Depth, magnitude and focal mechanism estimates are those from the CMT catalogue.

Analysis of the CMT solutions for these events identifies three distinct styles of seismicity. There are three high-angle, thrust-faulting earthquakes with depths all fixed at 12 km located close to the trench axis (events 010505A, 011405A and 012905A). Landward of the Sunda Trench are four normal-faulting earthquakes (events 122704A, 123004A, 123004C and 010905A), underlying a strike-slip event (event 122804R); the remaining earthquakes are located 250–300 km from the trench, in the so-called 'Offshore Banda Aceh' region (after Dewey et al., 2007) and are all low-angle, reverse-faulting events. Of this final cluster of aftershocks, event 123104M is somewhat of an anomaly as it describes very-low angle (3° dip) thrust faulting and has a calculated CMT depth of 24 km, much shallower than nearby earthquakes which are located between 45–54 km depths.

4.4 Results

Intermediate-period regional surface wave recordings from 32 different seismic stations are used in this study, and the distribution of these receivers is shown in Figure 4.3. Regional coverage is best to the north, across much of the southeastern part of the Eurasian landmass, but the availability of recordings from stations across Australia and the Indian Ocean means that there is suitable coverage to the south.

Source parameters are determined for the 16 selected aftershocks and listed in Table 4.2. Focal mechanisms are found to be in general agreement with those generated by the CMT method (see Figure 4.1) and best fitting depths are calculated between 3–61 km, with scalar seismic moment estimates over the range 0.16–10.8 $\times$ 10^{17} Nm.

These solutions are shown in map and cross-section view in Figure 4.4; the corresponding CMT solutions are plotted in the cross-section for comparison. The shallow-depth resolution afforded by this method is clear, with the identification of four earthquakes less than 10 km deep. The broad alignment of the eight intermediate-depth earthquakes in the Offshore Banda Aceh region seen in Figure 4.4 indicates that the depths of these events are well resolved. The determination of source parameters for event 123004C, the smallest earthquake studied here, should be highlighted as a success of the method. Occurring in spatial and temporal proximity to event 123004A, consistent depth and focal mechanism estimates are calculated for both these events.

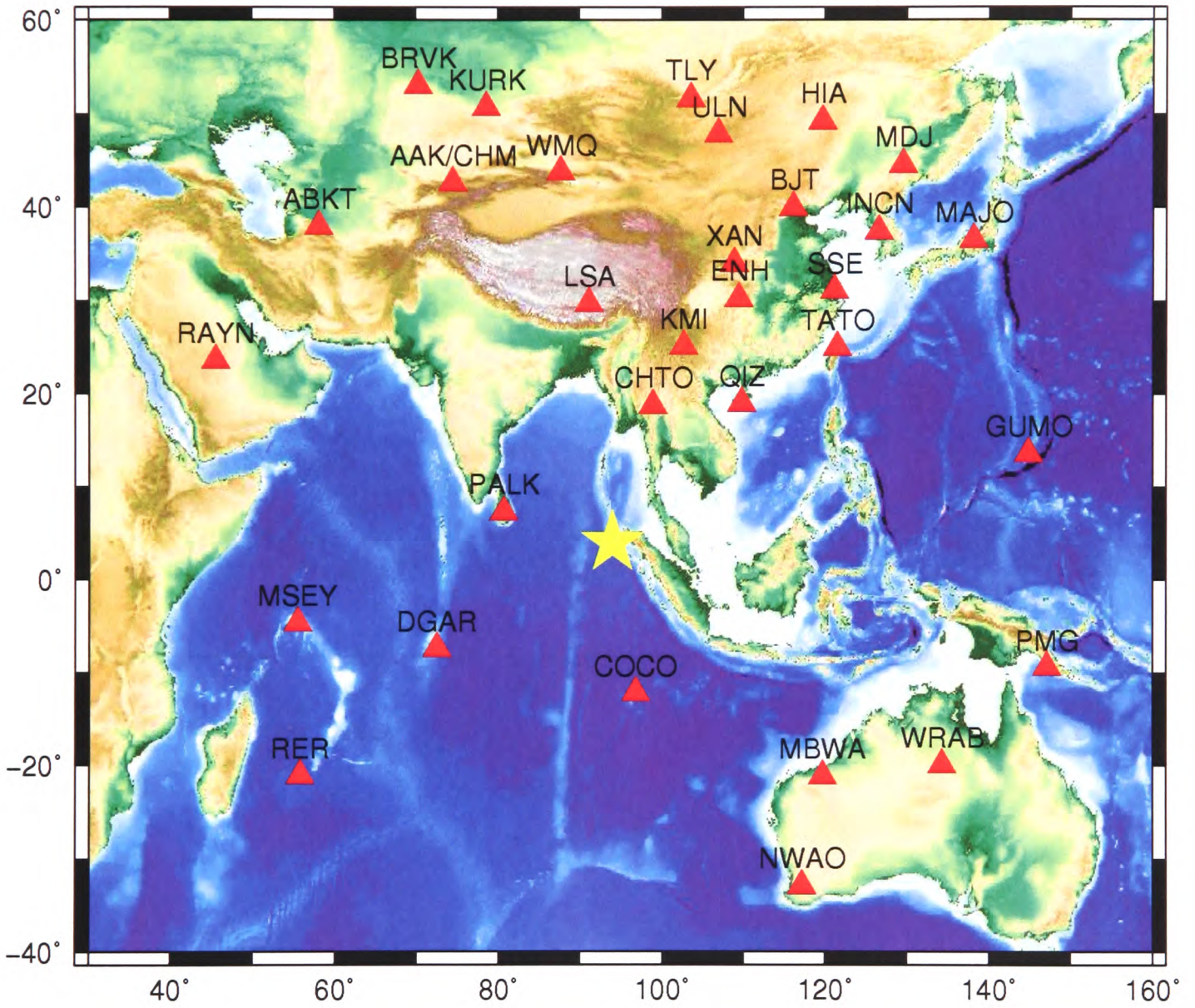


Figure 4.3: The 32 stations used to determine the source parameters of selected Sumatra aftershocks. The yellow star indicates the position of the earthquakes in their regional setting.

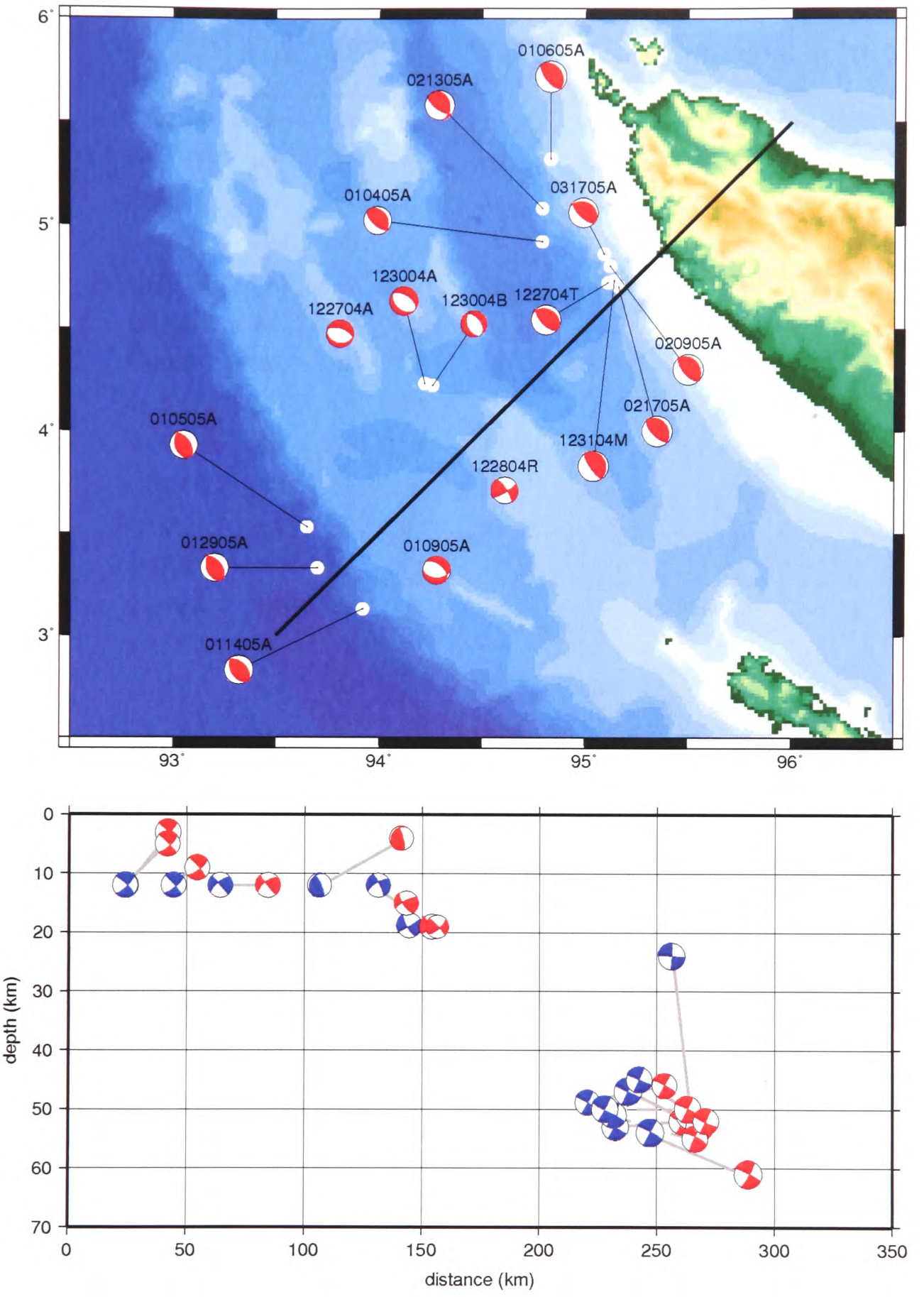


Figure 4.4: Map view (top) of the focal mechanisms determined in this study (red) as listed in Table 4.2. Latitudes and longitudes are as listed by the NEIC (Table 4.1). The cross-section (bottom) shows the depth profile along the transect, with fault plane solution beach balls shown as they would appear side-on, viewed from the southeast; those determined here are coloured red, and the corresponding CMT solutions are shown in blue. Grey lines attach solutions for the same events.

Event	Strike (°)	Dip (°)	Rake (°)	Depth (km)	Moment (10^{17} Nm)	Mechanism
122704A	288	58	-86	15	0.70	
122704T	298	28	74	52	5.11	
122804R	326	76	168	4	0.39	
123004A	300	54	-98	19	0.67	
123004C	320	46	-104	19	0.16	
123104M	342	16	106	51	4.43	
010405A	325	29	101	46	0.85	
010505A	324	50	78	9	0.46	
010601A	326	28	94	61	4.02	
010905A	308	52	-66	12	0.77	
011405A	314	45	80	3	1.70	
012905A	320	46	76	5	1.57	
020905A	320	26	90	53	10.8	
021305A	345	30	125	48	1.17	
021705A	326	26	100	50	3.58	
031705A	296	26	74	52	5.04	

Table 4.2: Source parameters determined in this study for the 16 events off the north-west coast of Sumatra. Best fitting waveforms and amplitude spectra for these aftershocks can be found in Appendix F.

Focal mechanisms for the shallow, near-trench aftershocks (events 010505A, 011405A and 012905A) are consistent with those listed in the CMT catalogue, describing predominantly reverse faulting occurring on planes dipping at 50°, 45° and 46° respectively. However, though the CMT centroid depths were all fixed at 12 km, here depths of 9 km, 3 km and 5 km, respectively, are calculated.

Events 122704A, 123004A, 123004C and 010905A are all calculated to be normal-faulting earthquakes on planes dipping between 46–58° with centroid depths between 12–19 km. The strike-slip earthquake in this region (122804R), with a 4 km centroid depth, is found to lie shallower. This pattern of shallow strike-slip faulting, underlain by extensional tectonics has been identified previously for this off-shore region (Engdahl et al., 2007).

The eight low-angle thrusting aftershocks occurring in the Offshore Banda Aceh region (events 122704T, 123104M, 010405A, 010601A, 020905A, 021305A, 021705A and 031705A) between 46–61 km generally increase in depth landwards along the transect (see Figure 4.4 cross-section), indicating a common source orientation. The average dip of the focal planes determined for these earthquakes is 26°, consistent with the 27° average dip of Engdahl et al. (2007), which was inferred from CMT solutions. The overall increase in aftershock depths across this region, from 46–61 km, can allow estimates to be made of the subduction zone dip.

An example of the success of applying this method to the Sumatra aftershocks can be seen in the study of event 123104M. This earthquake has a CMT solution with a thrusting mechanism on a 3° dipping fault. Not only is this solution significantly shallower in depth (24 km) than the surrounding aftershocks, but it describes a much lower-dipping fault plane. In this study, a steeper angle of dip (16°) and greater depth (51 km) are determined for this aftershock, consistent with the other neighbouring Offshore Banda Aceh events. Figure 4.5 shows a comparison of the Rayleigh wave amplitude spectra and waveforms generated for event 123104M using both the CMT source and that determined here.

It is clear from Figure 4.5 that the scalar seismic moment from the CMT solution is somewhat over-estimated, resulting in greater predictions of waveform amplitudes than are seen in the data; most amplitude spectra plot significantly higher than either the synthetics determined in this chapter or the observed data. Were this value of scalar seismic moment reduced then better fits could be provided for both amplitude spectra and seismograms; however, the observations at stations MBWA, especially, and TLY still indicate that the CMT focal mechanism is not optimal for these data. It is expected that the method developed here provides better estimates of source parameters compared to those of the CMT solution due to the use of (i) local models for source excitations, (ii) more accurate phase corrections from a detailed phase velocity model.

4.5 Summary

Source parameters have been determined for 16 aftershocks occurring between the trench axis and the Offshore Banda Aceh region of Sumatra following the 26 December 2004 megathrust earthquake. Focal depths were determined between 3–61 km and estimates of scalar seismic

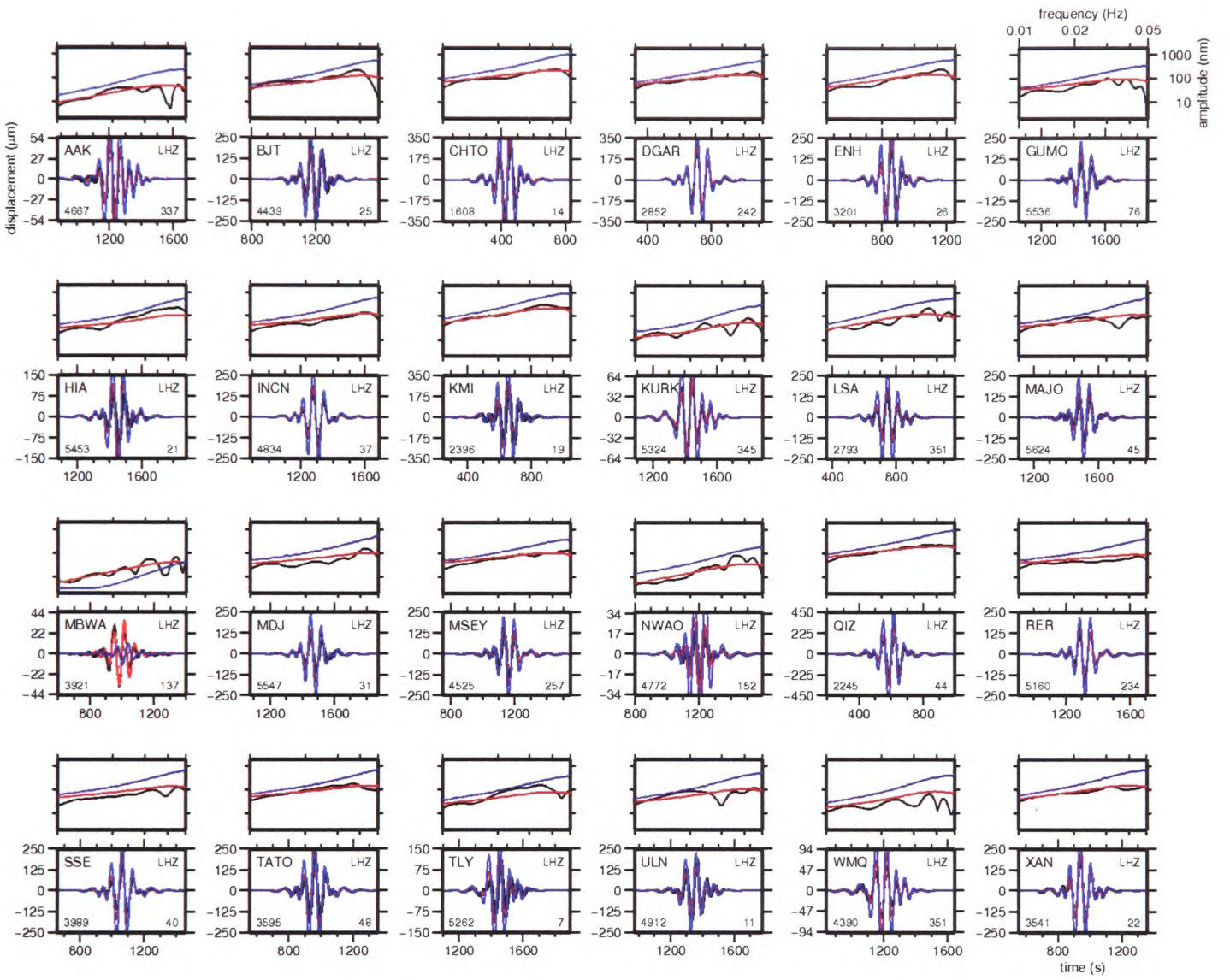


Figure 4.5: Comparison of the synthetic Rayleigh wave amplitude spectra and waveforms produced for the mechanism and depth listed in the CMT catalogue (blue) using the CUB Earth model and the optimum source parameters derived here (red) for event 123104M at a selection of stations. The black traces are the recorded seismograms.

moment ranged between 0.16–10.8 $\times$ 10^{17} Nm. Three distinct styles of tectonic deformation were identified along a transect oriented landward from the trench:

- shallow-depth (3–9 km), high-angle (45–50°) reverse-faulting close to the trench axis
- shallow-depth (4 km), strike-slip faulting underlain by deeper (12–19 km), high-angle (46–58°) extensional faulting
- intermediate-depth (46–61 km) low-angle (~26°) thrust-faulting

The identification of source parameters for event 123004C, shows that the method is capable of producing robust results for events where $M_w < 5.0$. The application of this method also allowed the identification of a poorly resolved CMT solution. The centroid depth of event 123104M is recalculated from 24 km to 51 km and its dip angle is increased from 3° to 16°. These changes to the source parameters produce estimations of the depth and style of faulting more consistent with the other Offshore Banda Aceh aftershocks in this area.

Comparisons of the amplitude spectra and waveforms in Figure 4.5 show this method to generate synthetics which closely match recorded data in this region. That these matches are achieved when propagation paths occur across complex tectonic settings such as the Himalayas and Tibet, the Pacific Ocean and south east Asia (see Figure 4.3), further highlights the benefit of applying this method. Given the complexity of the structure of the source and path regions, it can be inferred from these findings that the main control on intermediate-period surface wave amplitudes to be the source.

4.6 Interpretations

The results of this aftershock study may be used to draw interpretations about the nature of both the Sumatra tectonic setting and the mainshock rupture. Although many of the inferences made in this section are open to conjecture they nonetheless highlight the uses of well constrained aftershock source parameters.

The shallow, high-angle thrust faults, found close to the trench axis, probably lie in the over-riding plate above regions of that interface that did not rupture significantly during the

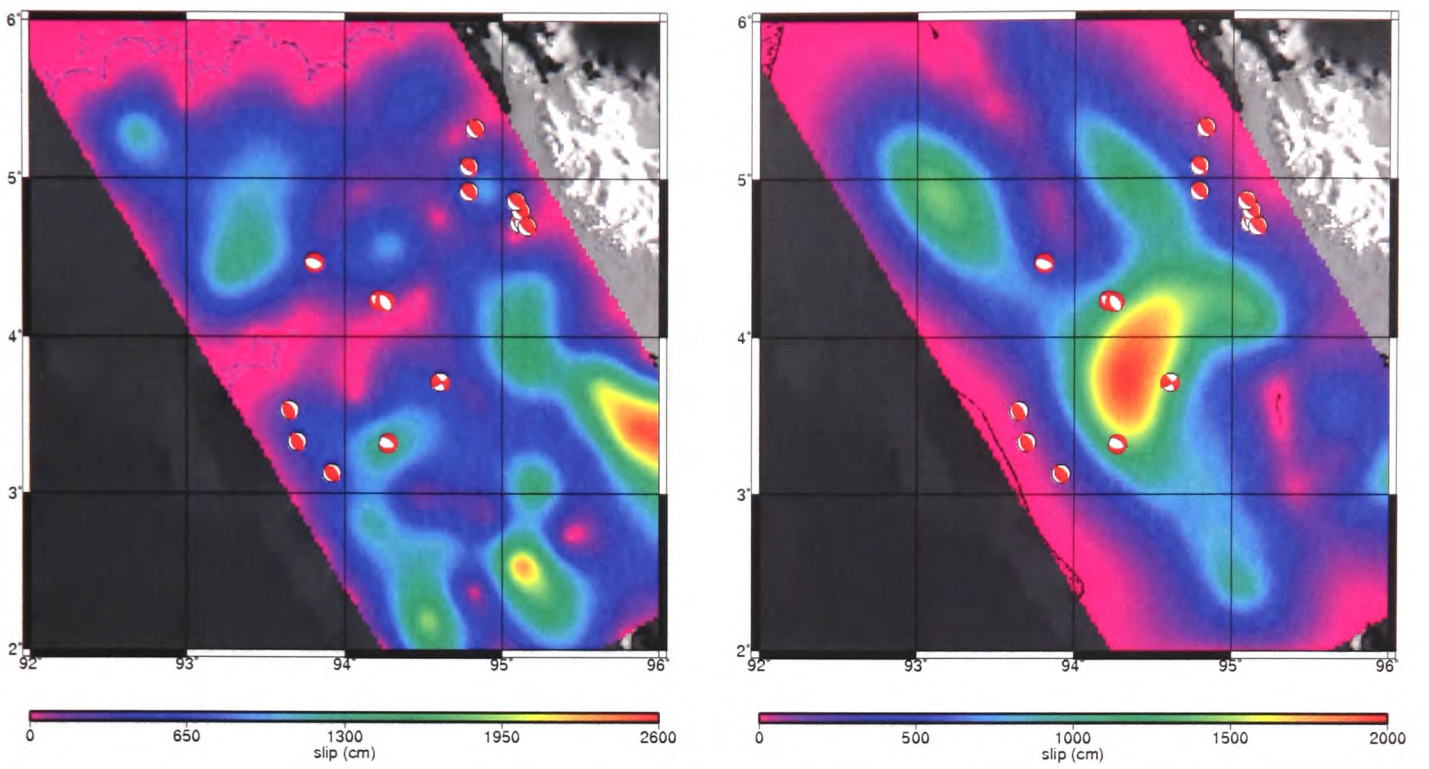


Figure 4.6: Comparisons of two rupture models of the 2004 Sumatra megathrust earthquake and the distribution of the aftershocks studied here. The LHS model is kindly supplied by Robinson (2007, pers. comm.) and shows part of the calculated slip occurring in the first 168 s estimated from *SH* waveforms; the RHS model (downloaded from the USGS website at http://neic.usgs.gov/neis/eq_depot/2004/eq_041226/neic_slav_ff.html) shows the slip distribution calculated using teleseismic body waves (200–5 s), intermediate-period regional waves (500–50 s) and long-period teleseismic waves (2000–250 s). There is some correlation with the deeper events coinciding with regions of the fault that did not slip significantly during the 2004 rupture.

mainshock. It is thought that the resultant change in stress conditions following the rupture caused brittle failure along a series of faults dipping ~45° away from the trench. Seismic reflection profiles along the Nankai Trough subduction zone have imaged steeply landward-dipping splay faults in areas previously ruptured by large megathrust earthquakes (Park et al., 2002), providing direct observations of the structures required to generate the focal mechanisms determined here.

The intermediate-depth events may be considered representative of faulting occurring at the subduction interface; improved depth locations allow the estimation of a 22°-dipping plate boundary (see Appendix G for details of these calculations), though associated depth errors mean this is not well constrained.

A detailed aftershock study in this area may identify patterns between aftershock locations and modelled fault rupture. A comparison of preliminary versions of two slip models presented by Ammon et al. (2005) is shown in Figure 4.6 and there appears to be some correlation

between the locations of the Offshore Band Aceh aftershocks and regions of the plate boundary where little or no slip is modelled to have occurred at depth. If such aftershock locations are taken to identify regions where little slip occurred, then it is possible to place constraints on the maximum down-dip depth of the mainshock rupture. The depth estimates determined by this study suggest that it is unlikely that significant slip took place at depths greater than 46 km in the Offshore Banda Aceh region.

Event 010601A is calculated to have the greatest depth (61 km) of all the low-angle thrusting aftershocks; located furthest from the trench, this earthquake may represent the maximum down-dip extent of faulting on the subduction interface. No earthquakes were identified further landward with mechanisms similar to those found in the Offshore Banda Aceh regions, so it is believed that at greater depths temperatures are sufficiently high to cause deformation to occur aseismically (by plastic flow) as opposed to seismically (by brittle fracture).

The identification of this boundary is of great interest as it can be used to indicate the end of the seismogenic region of a subduction zone and the extent of the fault interface which may be considered to be seismically-coupled (Tichelaar & Ruff, 1991, 1993). The seismic identification of this boundary can be used to place temperature-depth constraints on a region and allow the estimation of shear stresses (e.g. Molnar & England, 1990; von Herzen et al., 2001; Fox, 2001). These latter calculations are beyond the scope of this work, but comparisons with previous estimates of the depth of this transition can be made. Tichelaar & Ruff (1993) argued that the depth at which unstable sliding changes to stable sliding occurs globally at $\sim$40 km $\pm$ 5 km. They also reported exceptions to this global trend, most notably at the Hokkaido trench junction, where the Japan Trench and the Kuril Trench intersect, here interplate seismicity has been observed as deep at 55 km.

Chapter 5

Discussion

"In mathematics you don't understand things. You just get used to them."

Johann von Neumann (1903–1957)

5.1 Overview

In this chapter assessments of both the methodology developed here and the CUB Earth model are made. Comparisons between predictions and observations of group arrival time provide part of a model critique. Perturbations are applied to the method to investigate how robustly source parameters are determined. The effects of source-receiver distances, azimuthal receiver coverage and source location are considered, along with the relative contributions of the Rayleigh and Love wave data subsets.

Synthetic waveforms are calculated with cut-off periods between 50–20 s and are compared with the recorded seismograms. The amplitude spectral cut-off period of 20 s is varied to assess the importance of shorter-period observations. In particular, the 2004 Parkfield earthquake is revisited, to assess whether the inclusion of surface wave observations between 20–15 s can better constrain the estimates of both focal mechanism and depth.

5.2 The CUB Earth Model

By comparing predictions of group velocity arrival times with those measured from recorded seismograms using the MFT, it is possible to analyse how well the dispersive characteristics described by the model match those of the real earth. For the 14 validation earthquakes and 16 Sumatran aftershocks studied here, the differences between the predicted and observed dispersion are plotted to give a visual representation of the accuracy of the velocity model globally. This analysis is constrained by the locations of the earthquakes studied and the heterogeneous receiver distribution imposed by the pattern of continents and oceans.

Figures 5.1 and 5.2 show the discrepancies between calculated and observed Rayleigh and Love group velocity arrival times (δt) for the 14 validation events presented in Chapter 3 at 50 s, 33 s and 20 s periods. In these figure δt at any given frequency is calculated by:

$$\delta t = t_o - t_p, \tag{5.1}$$

where t_o is the observed group arrival time and t_p is the group arrival time predicted by the Earth model. It follows that positive values of δt indicate that the recorded data arrives after it is predicted, that is to say that the model predictions of group velocity are over-estimated; negative values of δt identify the model as under-estimating group velocities.

At the longer-periods, e.g. 50 s in Figures 5.1 and 5.2, recorded group arrival times are well predicted by the model. While significant discrepancies are generally rare, they typically occur at the shorter-periods (e.g. at 20 s) where surface wave paths are expected to be complex and the dispersive characteristics are poorly predicted by the model. In Figure 5.1, at 20 s, a difference between group velocity perturbations on the continents and oceans is evident from recordings made of the 2004 Parkfield earthquake. Group velocities are overestimated by the model across the Pacific Ocean and underestimated across the North American continent.

Data coverage in the model is best at the intermediate-periods rather than the very-short or very-long periods (Shapiro & Ritzwoller, 2002) which explains the observations made here. The Love wave group discrepancies in Figure 5.2 are typically greater at shorter-periods than those of the Rayleigh waves; this is partly explained by the greater number of Rayleigh wave recordings used in the construction of this model compared to Love waves.

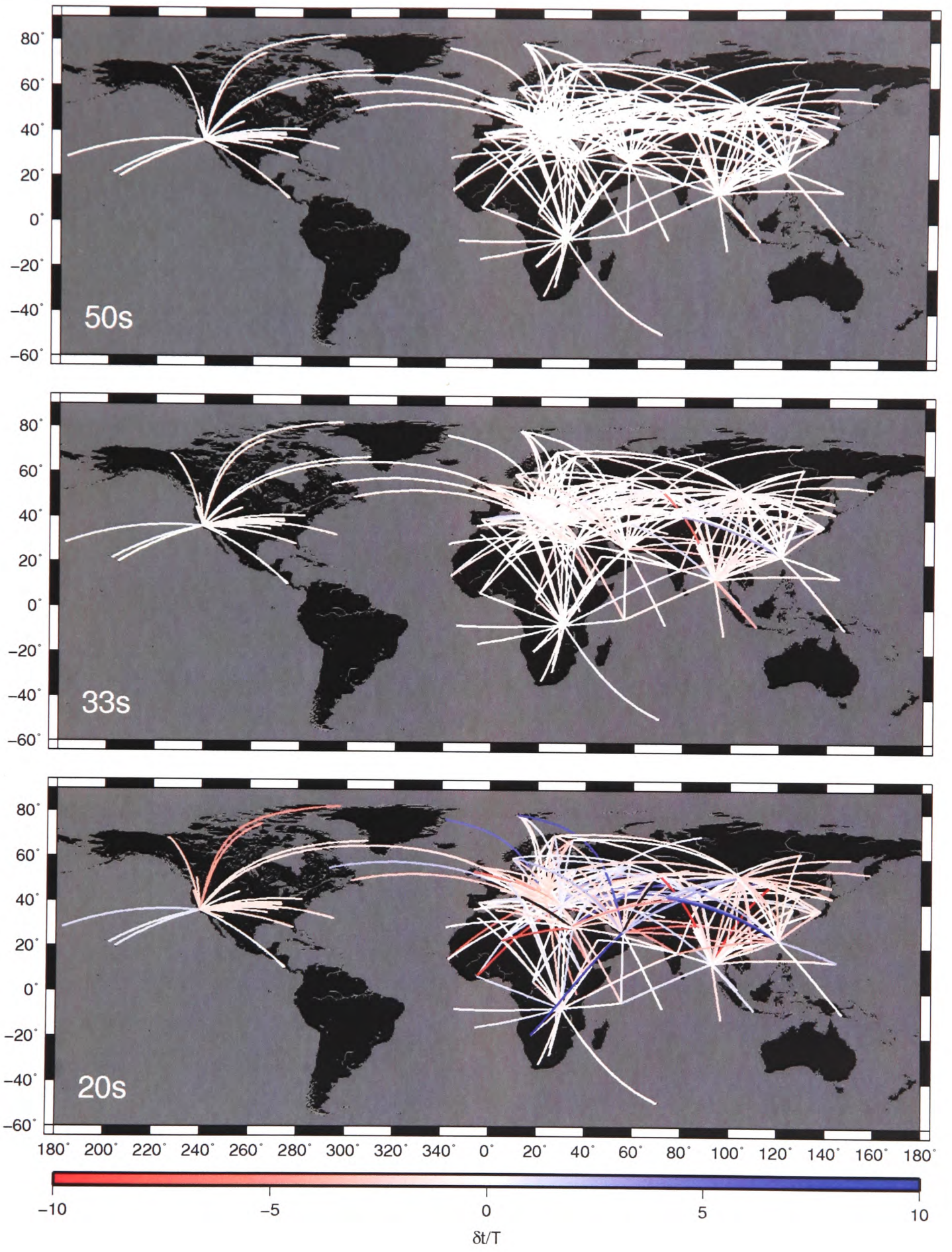


Figure 5.1: Discrepancies (δt) in predicted and measured Rayleigh wave group velocity arrival times normalised by their period (T) which are calculated for recordings of the 14 validation events at 50, 33 and 20 s. Positive values of $\delta t/T$ (blue) indicate that the model predicts faster velocities than are observed, whilst negative values (red) show the model describing slower velocities than are observed.

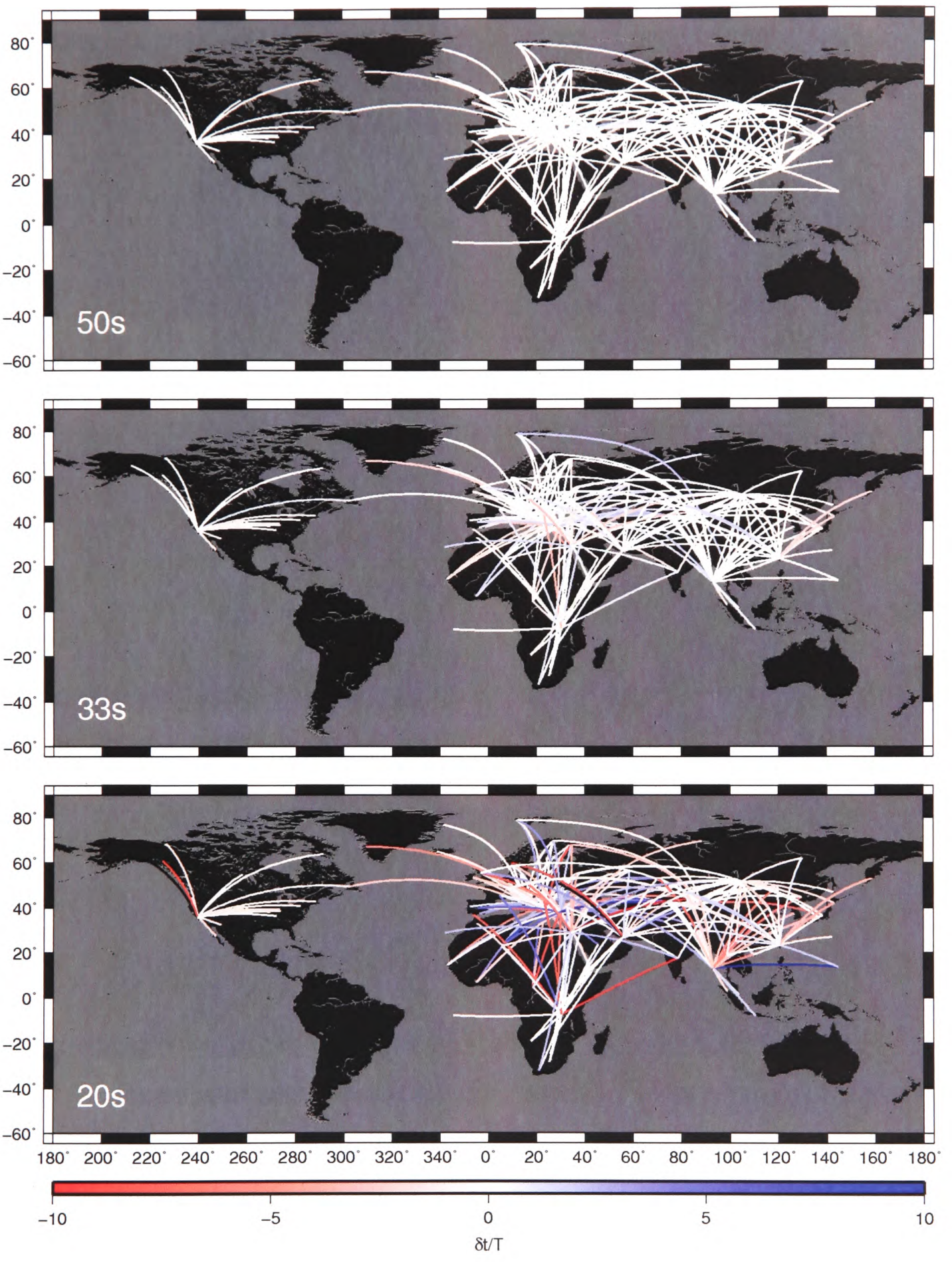


Figure 5.2: As Figure 5.1 but for Love waves.

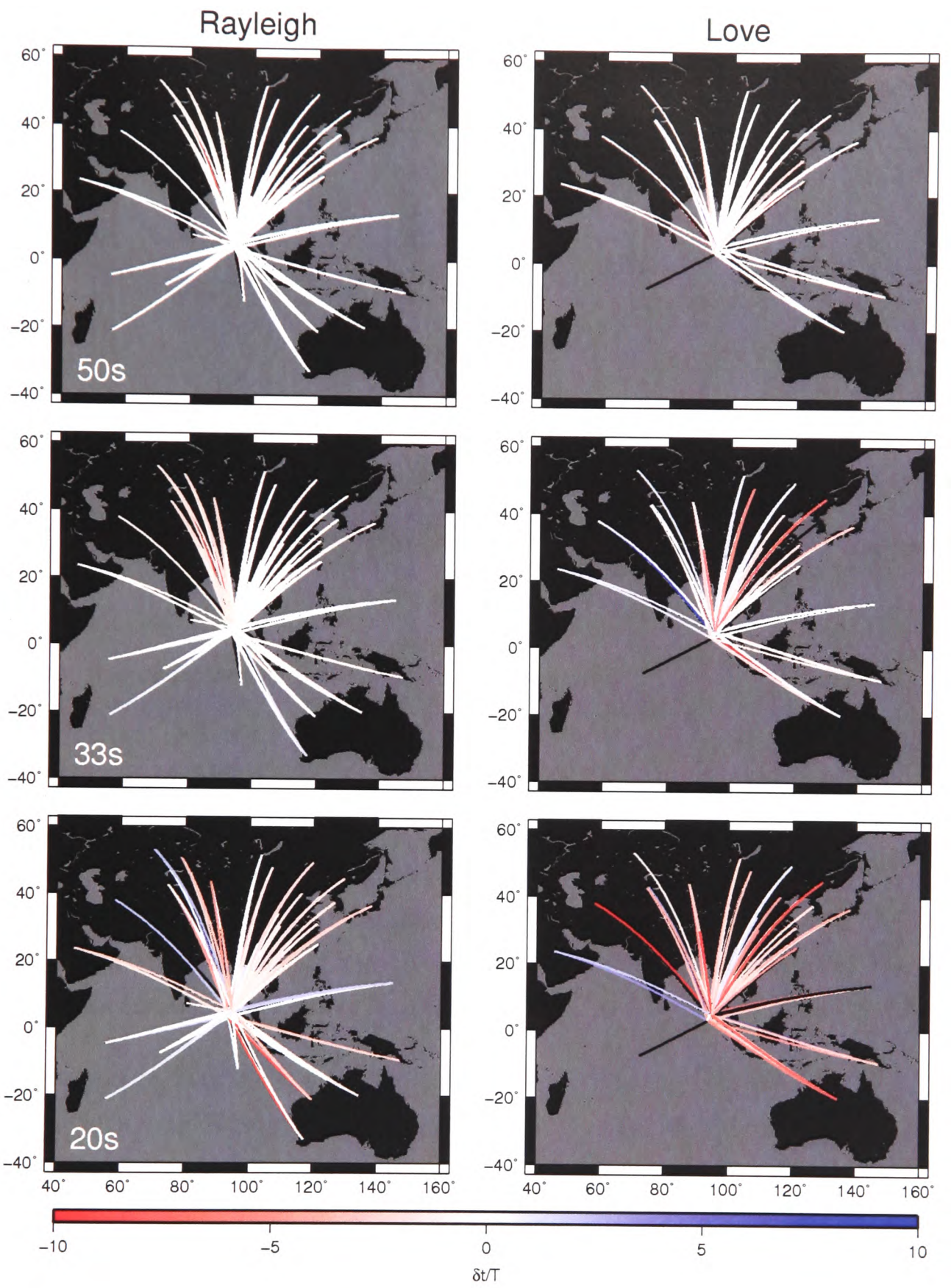


Figure 5.3: As Figures 5.1 and 5.2, but for Rayleigh (left) and Love (right) wave recordings of the 16 aftershocks of the 2004 Great Sumatra earthquake. Black lines indicate significant discrepancies related to additional seismic noise, not errors in the velocity model and these traces are downweighted in the source parameter determinations.

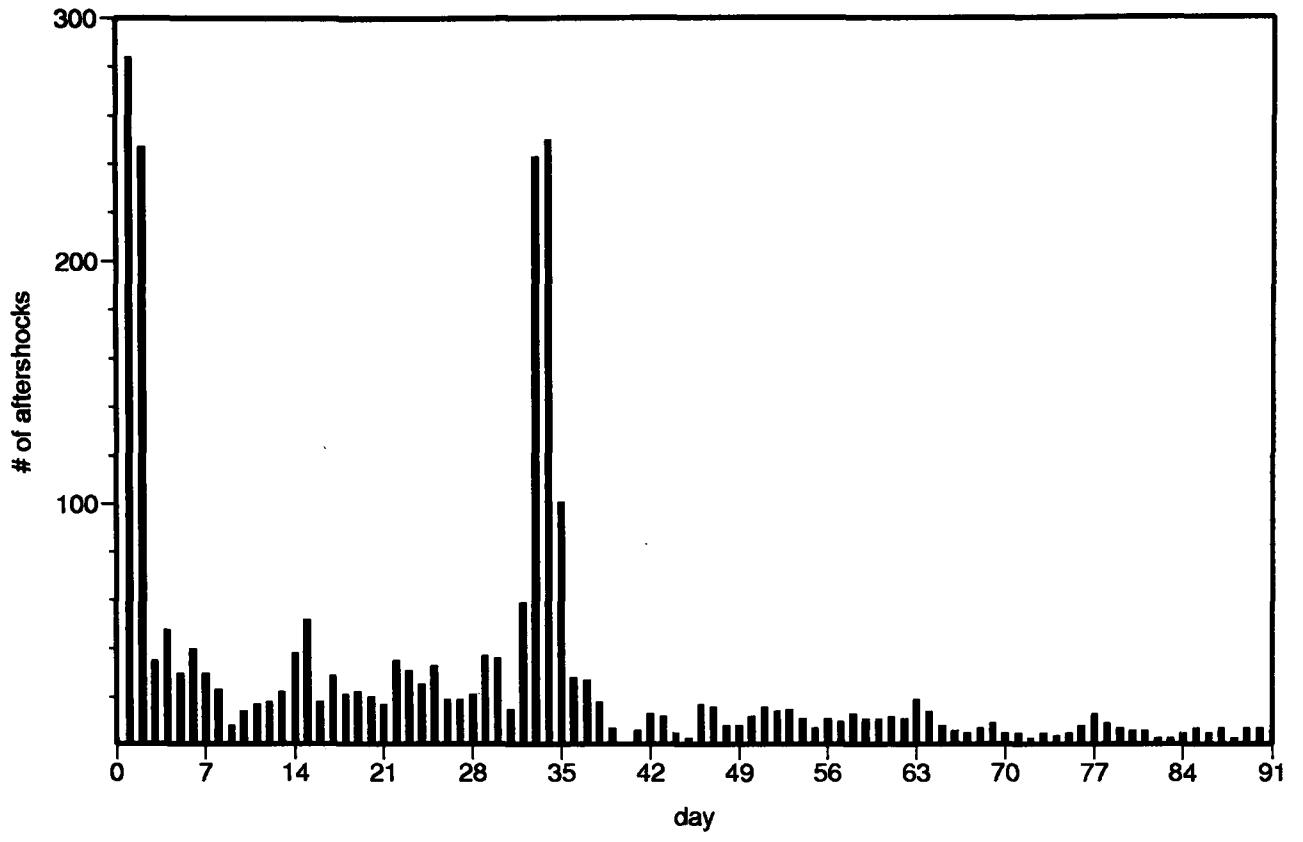


Figure 5.4: Histogram showing the daily number of aftershocks of the 2004 Sumatra earthquake for 91 days after the mainshock (where day 1 is the 26 December 2004).

Figure 5.3 presents discrepancies in the group arrival times for the 16 aftershocks studied in Chapter 4. When compared with Figures 5.1 and 5.2, it is clear that there are larger differences between the measured and predicted dispersion (this is especially true for events 122704A and 122704T). Such discrepancies are not necessarily due to errors in the velocity model. The presence of seismic noise from other events occurring in the aftershock sequence can cause inaccuracies in the determination of the peak group arrival times for a given event.

The histogram in Figure 5.4 shows the number of earthquakes identified by NEIC in the Sumatra region for 91 days after the mainshock occurred. It is seen that during the first two days there is intense seismic activity with some 284 separate events occurring on 26 December and a further 247 a day later. As mentioned in Chapter 4, there were no earthquakes found that were suitable for study on the day of the mainshock, and on 27 December the effects of additional earthquake activity makes identification of peak group arrivals difficult, leading at times to large discrepancies from model predictions. After 27 December, with the exception of some intense seismic activity occurring on the major strike-slip fault to the north, in the Andaman Sea, in late January 2005 (Dewey et al., 2007; Engdahl et al., 2007), the number of daily aftershocks reduces significantly, resulting in improved dispersion measurements.

Although there are exceptions (e.g. event 123004C, which occurred in close temporal and spatial proximity to event 123004A), discrepancies in the group arrival times are generally small, especially for the Rayleigh waves. In particular, the majority of recordings made at stations to the north and north east are found to have their dispersive characteristics well predicted by the CUB model. A noticeable absence from Figure 5.3 are Love wave recordings made at stations located between the southwest of the Sumatran aftershock sources. This is not just attributable to the heterogeneous coverage of receivers in this region as there are examples of useful Rayleigh wave recordings made in the Indian Ocean. The low signal-to-noise ratios of the LHT channel compared to the LHZ channel on oceanic islands is likely to be due to the presence of background seismic noise caused by oceanic gravity waves, long known to affect coastal horizontal recordings (Longuet-Higgins, 1950). This view is also consistent with analysis of data from the Parkfield earthquake (see Figures 5.1 and 5.2). Here robust measurements at seismic stations to the west, whilst restricted in number by the Pacific Ocean, are available in the LHZ channel at POHA (Pohakuloa, Hawaii), KIP (Kipapa, Hawaii) and MIDW (Midway); but analysis of the corresponding Love wave amplitude spectra results in their rejection due to high signal-to-noise-ratios.

5.3 Source-Receiver Distance

Rayleigh and Love wave dispersion discrepancies, plotted as a function of source-receiver distance, are presented in Figure 5.5. For both surface wave types there are few significant differences between observed and predicted group arrival times at the periods of 33 s and longer. At the shorter periods, these discrepancies are greater and there is a very weak correlation with distance which is more evident in the Rayleigh wave data than in the Love. Where significant discrepancies do occur, recordings are downweighted accordingly (see 2.4.2), but these plots demonstrate that generally the Earth model predicts group arrival times accurately for stations in the 10–60° epicentral range.

Figure 5.6 shows the values of individual station amplitude spectral misfits calculated for the optimum source for each validation event. Here these spectral misfits at the j'th station, m_j,

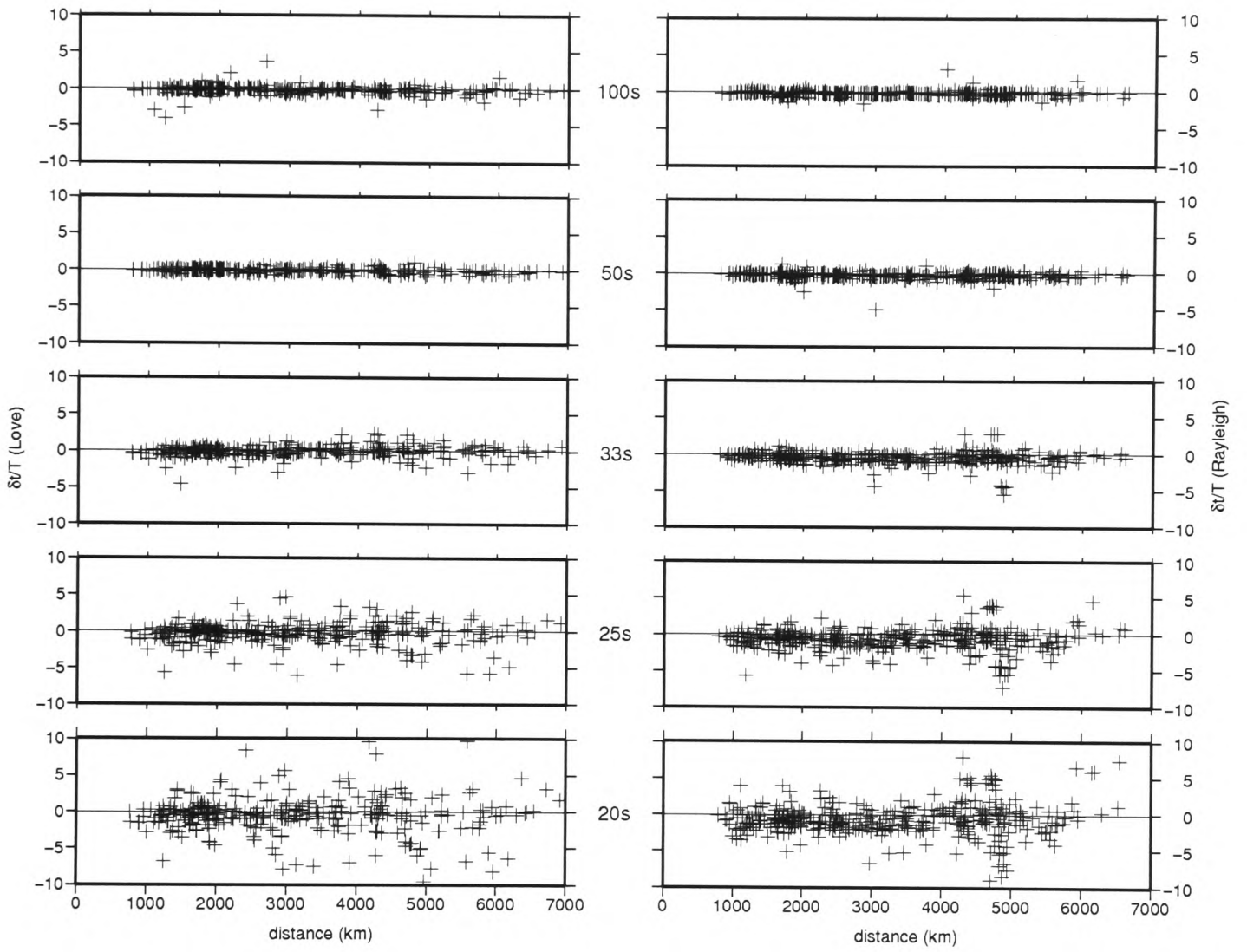


Figure 5.5: Discrepancies in predicted and recorded Love (left) and Rayleigh (right) group arrival times ($\delta t/T$); plotted by source-receiver distance for all validation events at 100, 50, 33, 25 and 20 s. Positive discrepancies indicate that the model predicts faster velocities than are observed.

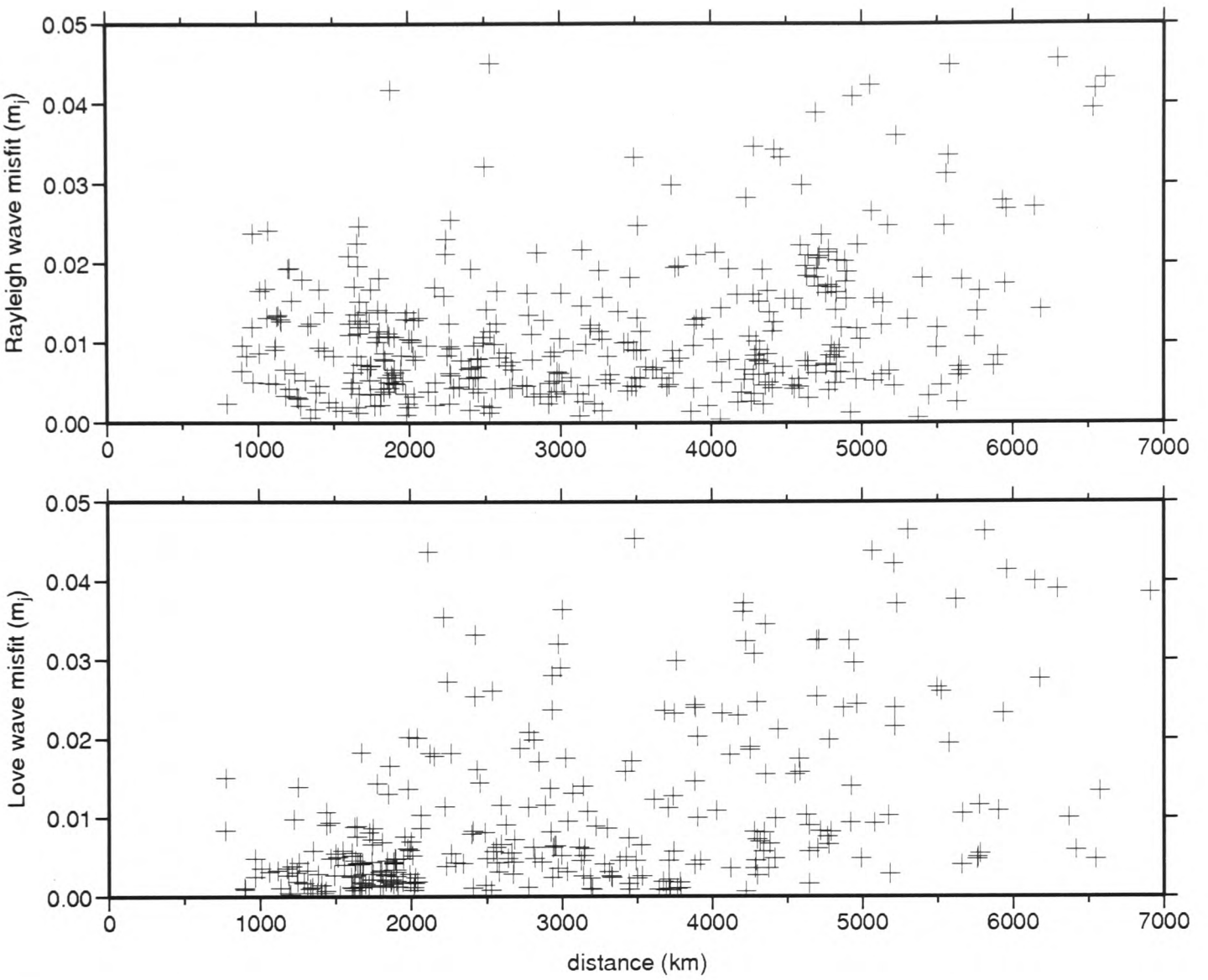


Figure 5.6: Individual station misfits (m_j) for the optimum Rayleigh (top) and Love (bottom) wave synthetic amplitude spectra as determined for events in Chapter 3.

are calculated as follows:

$$m_j = \frac{\sum_{i=1}^{N} (\log d_{ij} - \log s_{ij})^2 \Psi_{ij}}{\sum_{i=1}^{N} (\log d_{ij})^2 \Psi_{ij}}, \tag{5.2}$$

where d_{ij} and s_{ij} represent the amplitude spectra of data and synthetic traces respectively, N is the number of discrete frequencies in the amplitude spectra and Ψ_{ij} is the combination of applied weights (as defined in 2.4.2) for a given trace and frequency interval. Equation 5.2 is the same as Equation (2.33), but with the summation over total traces removed from both numerator and denominator.

It is seen in Figure 5.6 that there is no clear trend between distance and individual station amplitude spectral matches. Although the larger misfits are generally found at the greater distances, the number of low misfits found further than 5000 km indicate that there is no need to weight stations according to the length of the source-receiver path. In cases where the total number of available stations is low, it may be advantageous to select more distant stations and Figure 5.6 shows that such stations may provide fits to the data comparable with those made much closer. Where larger amplitude misfits do exist at distant stations, they are probably due to inaccuracies in the PREM attenuation model used.

5.4 Azimuthal Receiver Coverage

It has been shown in Chapter 3 that selecting stations in the epicentral distance range 10–60° can impose irregular receiver distributions. This is particularly clear on the west coast of North America, where resolution of the surface wave radiation patterns of the 2004 Parkfield earthquake is impaired by the paucity of stations to the West. The effect of the distribution of receivers on the ability of this method to identify optimum seismic source parameters is investigated using the 1995 Dinar, Turkey, earthquake as a case study.

Figure 5.7 shows the location of the Dinar earthquake along with the receivers used in Chapter 3. Here source parameters are calculated by only using recordings from the 25 northerly (red) stations and then only using the 9 southerly (black) stations. The results are shown in Table 5.1 and tests were re-run with the removal of the azimuthal weightings defined in 2.4.2 and those results are listed in brackets.

Stations	Strike (°)	Dip (°)	Rake (°)	Depth (km)	Moment (10^{17} Nm)	LHZ records	LHT records	Mechanism
Red	126 (131)	47 (46)	-100 (-92)	5 (4)	20.0 (19.3)	25	19	
Black	132 (133)	48 (48)	-94 (-94)	5 (5)	15.6 (15.8)	8	8	
All	128 (128)	44 (48)	-98 (-98)	5 (5)	18.9 (18.8)	33	27	

Table 5.1: Optimum source parameters for event 100195B determined using the stations shown in Figure 5.7. The values in brackets refer to the corresponding source parameters calculated when the azimuthal weights are removed. The final three columns show the numbers of LHZ and LHT channel recordings used and the mechanism calculated with azimuthal weightings applied.

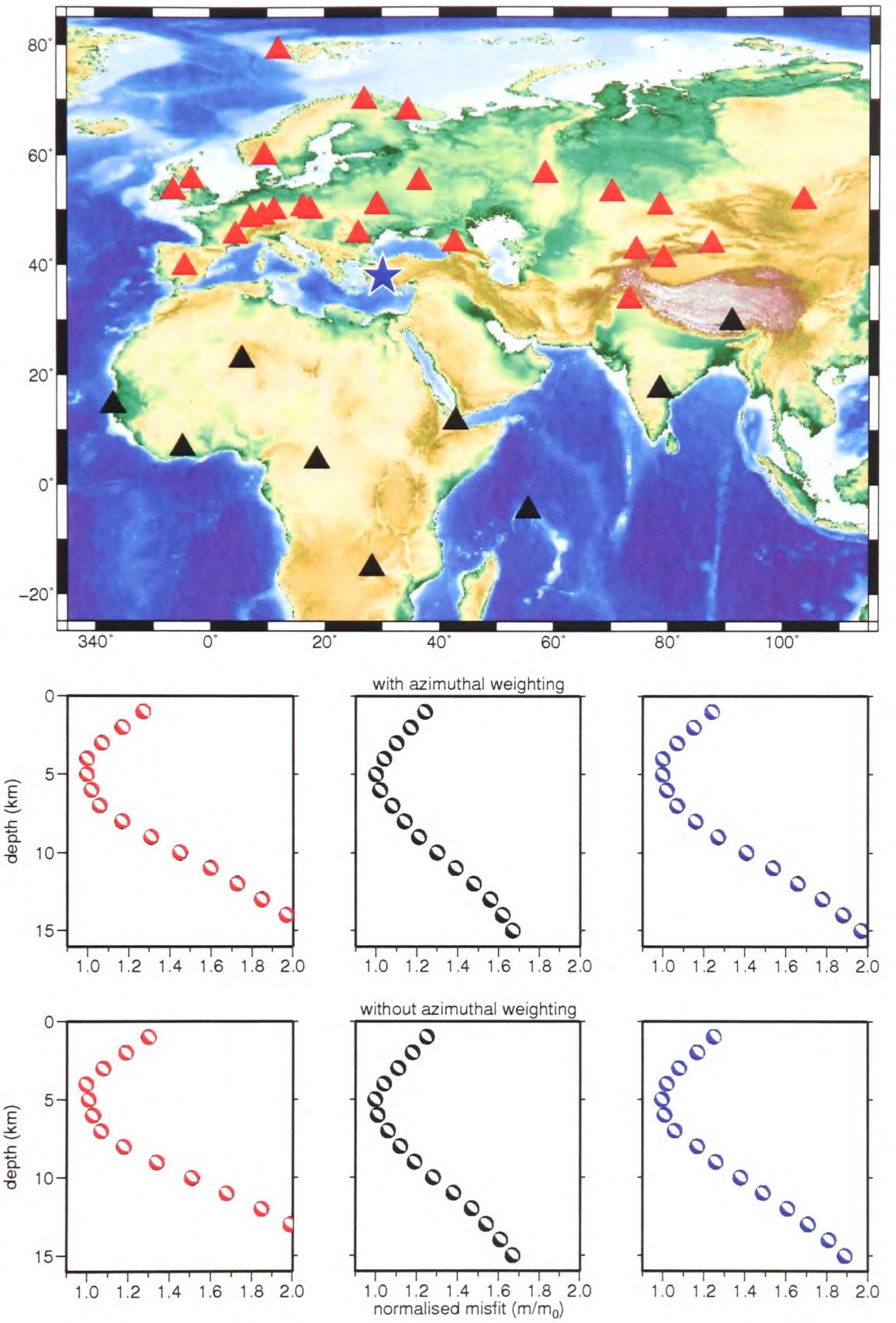


Figure 5.7: Map of the location of the 1995 Dinar, Turkey, earthquake (event 100195B, blue star) and the stations used in the determination of best fitting source parameters. The algorithm is run using only recordings at the red stations, then only recordings from the black stations and, finally, all the stations together (blue). The misfit-depth profiles below are colour-coded so (left to right) they represent the results of using just the red stations, just the black stations and then all the stations. The top sets of profiles are run with azimuthal weighting imposed, whilst the bottom set are not.

Just considering the black stations (small in number and poorly distributed), it is possible to derive a set of source parameters consistent with those determined in 3.5.1 (listed as 'All' in Table 5.1). The determination of source parameters using 16 recordings only, all located within 180° azimuth of each other demonstrates the robustness of this method in cases where data coverage is not ideal.

Two sets of misfit-depth profiles are shown in Figure 5.7; one for source parameters calculated enforcing an azimuthal weighting system, and one without. When the weighting system is removed, each recording is considered an individual data source, independent from all the other observations. As can be seen from these profiles and Table 5.1 there is only instance of a change in optimum centroid depth and generally, variations in the other source parameters are small.

5.5 Rayleigh Waves vs Love Waves

So far, source parameters have been determined using both Rayleigh and Love wave data sets. It might be expected that by using both types of surface waves more constrained source parameters can be calculated. To test the respective contributions of both types of surface waves, source parameters are determined for all the validation events using solely Rayleigh wave recordings and then using solely Love wave recordings.

When just Rayleigh waves are considered, source parameters are determined, and their variance from the parameters listed in Table 3.2 are presented in Table 5.2. In some cases the effect of removing the Love wave contributions is small, for instance event 013099A, where the best fitting source parameters vary only by 2° (i.e. one grid cell) in strike and rake only. In this case, the frequency-dependent notches in the Rayleigh wave spectra provide strong constraints on the source parameters, and therefore it is not unexpected that the exclusion of Love wave amplitude spectra has little effect on the best-selected source parameters.

Elsewhere, considerable variations are seen, such as in the source parameters determined for event 112705I on Qeshm Island, Iran. As discussed in Appendix C and considered later in this chapter, this earthquake is one of the least well constrained events. Although the variations in strike, dip and rake are relatively large, the optimum depth changes by only 1 km, indicating that the depth determination for this event is robust.

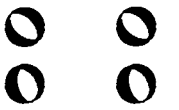
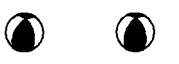
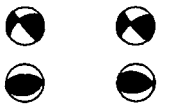
Event code	Strike (°)	Dip (°)	Rake (°)	Depth (km)	Moment (10^{17} Nm)	% Rayleigh Stations	M1	M2
080393G	2	2	0	1 (-4)	3.3	49		
051395B	5	-1	2	0 (-1)	10.0	55		
100195B	-9	1	-4	2 (-3)	12.0	55		
092197C	-2	-2	-6	-2 (4)	-0.39	52		
013099A	2	0	2	0 (-1)	0.08	55		
022599H	-5	3	-1	0 (-1)	0.56	60		
090799C	6	0	2	1 (-3)	2.44	53		
102299A	-2	0	-2	0 (-1)	0.66	57		
091302C	-1	0	1	0 (-2)	4.1	46		
091402B	2	0	-2	0 (0)	0.51	55		
103102B	1	4	1	3 (-2)	1.4	58		
110102F	1	2	-2	1 (-1)	0.66	59		
092804H	-2	-8	20	2 (4)	-0.3	61		
112705I	20	-7	14	1 (-1)	1.32	53		

Table 5.2: Perturbations from the source parameters listed in Table 3.2 when just Rayleigh wave amplitude spectra are used. A positive value in this table means the parameter is determined to be greater than before. The numbers in brackets in the depth column are the perturbations in depth ranges, negative numbers indicates better constrained depths. The % contribution of Rayleigh waves are also listed. The focal mechanisms represent the original solutions (from Table 3.2, M1) and those determined in this section (M2).

The exclusion of Love wave data from Table 5.2 is not seen to significantly affect the bounds placed on depth constraints. Generally, depth ranges are found to be smaller here than when Love waves are used, although typically only by a few kilometres. Indeed the maximum perturbation of the depth bounds calculated is only ± 4 km.

It was not possible to produce a corresponding table for the source parameters generated using solely Love wave data. In each of the 14 cases, the grid-search failed to conclusively calculate optimum source parameters or determine any suitable constraints; this lack of source sensitivity, especially to depth, has long been known (e.g. Tsai & Aki, 1970, 1971). The lack of structures in the Love wave amplitude spectra and their insensitivity to source depth over the ranges searched resulted in a wide variety of solutions being found to generate statistically similar synthetics.

Nonetheless, Love wave observations provide some control on the identification of source parameters here (if they did not, then there would be no variations in the optimum source parameters determined here), but only when guided by the greater sensitivities to source mechanism and depth afforded by the Rayleigh wave data. The inclusion of Love wave recordings in the method presented here ensures that the information contained in both surface wave radiation patterns is brought to bear, although it is clear that the Rayleigh wave sensitivity to the source dominates in the grid-search. In most instances where Love wave recordings are not readily available, reliable source parameter estimates can be determined using solely Rayleigh waves.

5.6 Spectral Notches

It has been demonstrated in this thesis that in cases where Rayleigh wave amplitude spectral contain notches that they can be modelled as attributable to the seismic source (e.g. event 013099A in 3.2). However for certain mechanisms and focal depths notches from the source are not found in the recorded data. Although good matches to the data are provided by the method presented here, in the absence of clear spectral notches it may be unclear where the depth sensitivity comes from.

Figures 5.8 and 5.9 show best fitting Rayleigh and Love wave amplitude spectra calculated in Chapter C for event 022599H in Lake Baikal. Synthetics are shown for the optimum depth (8 km) and two depths outside acceptable depth range (2 km and 14 km). The lack of depth sensitivity in the Love wave spectra is evident whereas there is a large variation in the shapes of the Rayleigh wave spectra over the 12 km depth range shown. In the case of the spectra at MA2 in Figure 5.8 it is clear where the depth resolution comes from, with the best fitting amplitude spectra at 14 km producing a pronounced null that is not found in the data and this depth is rejected as a plausible source depth. Less obvious, but still identifiable in Figure 5.8 are the mismatches provided by the very shallow, 2 km, source depth (a depth also rejected by the algorithm). At each station these shallow source spectra are found to be smaller in amplitude at the longer-periods and higher in amplitude at the shorter-periods than the data. The range of best fitting patterns of synthetics in this figure demonstrates that there is still sufficient structure in the Rayleigh wave amplitude spectra in the absence of distinct nulls, to provide tight depth constraints at shallow depths.

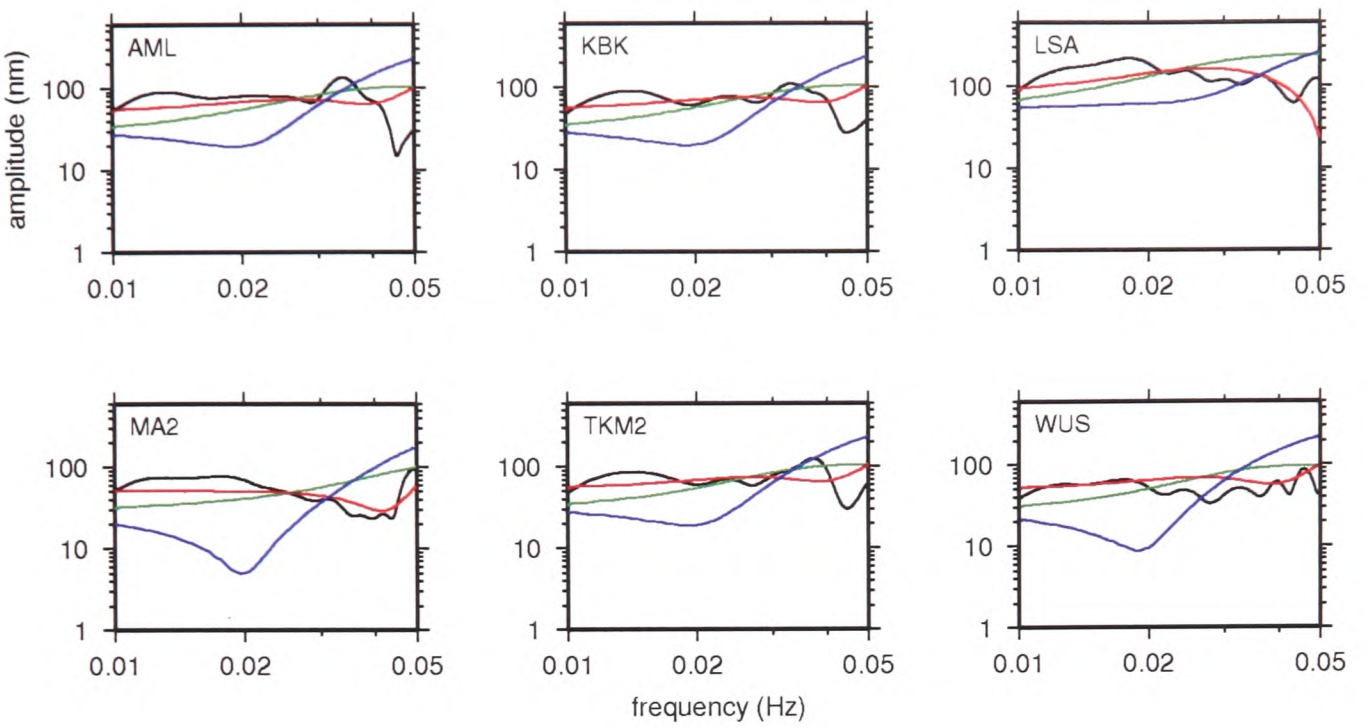


Figure 5.8: Variations in the best fitting Rayleigh wave amplitude spectra calculated in Chapter C for event 022599H. Best fitting spectra are shown for six selected stations at depths of 2 km (green), 8 km (optimum depth, red), and 14 km (blue). Data amplitude spectra are plotted in black.

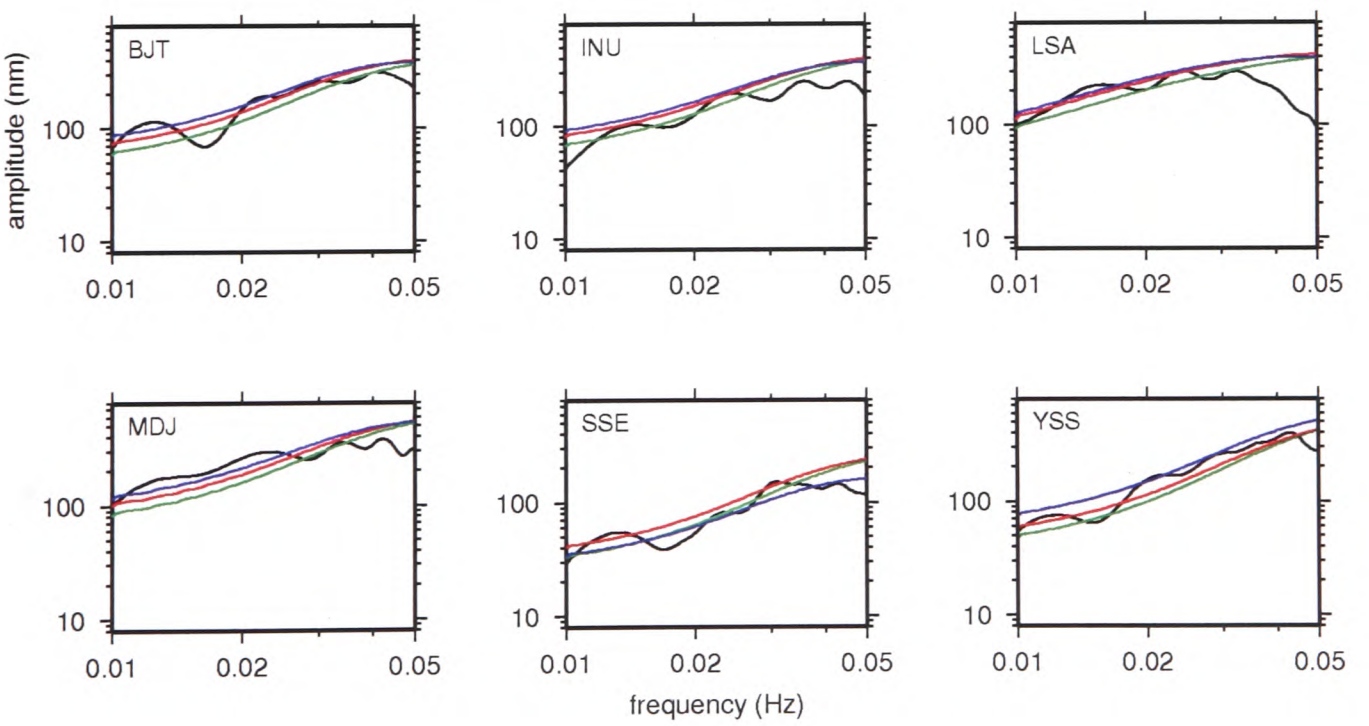


Figure 5.9: As Figure 5.8 but for Love wave amplitude spectra at six selected stations.

There are examples of data amplitude spectra in Appendix D that contain nulls which are not replicated in the best fitting synthetics. In these examples the notches are considered to be due to path effects (multipathing, focussing and defocussing). The use of multiple stations to find the best fitting surface wave radiation patterns prevents these these features from being reproduced in the best matching synthetics. As discussed in Chapter 1, Tsai (1969) matched nulls in the Rayleigh wave amplitude spectra of mid-ocean ridge earthquakes and concluded that source depths could be identified as deep as 65 km. Weidner & Aki (1973) analysed the same events and concluded that the spectral nulls were not indicative of the seismic source and were actually propagation effects (e.g. interference due to multipathing) and demonstrated that these earthquakes occurred at depths shallower than 10 km. If a small number of traces are used then it is possible that features not related to the source could be modelled. However when many recordings are used to constrain the surface wave radiation patterns, the effect of the presence of these nulls is seen to be negligible.

5.7 Scalar Seismic Moment Estimates

The scalar seismic moment was not included as an independent variable in the grid-search algorithm. Instead, estimates were determined independently for each combination of $(\phi_s,\delta,\lambda,h)$ by scaling the unit synthetic amplitude spectra generated for a given source to the corresponding data. As much as this decision was motivated by the desire to optimise the selection of source parameters, it was also influenced by the need to reduce computational run-times by limiting the number of grid-search parameters.

Unlike strike, dip and rake, and to a lesser extent, depth, sensible selections of minimum moment, maximum moment and increments of moment are often not trivial and open to interpretation. It is important to avoid scenarios where, following lengthy run times, it is discovered that poor choices of these moment parameters were made at the outset; especially given the desire for quick, robust source parameter determinations.

In order to validate the decision to scale unit synthetics and establish the scalar seismic moment estimate as defined in Equation (2.32), comparisons are run for three events between the method presented here and an alternate version where seismic moment is included in the grid-search. In all cases a suitably large range of seismic moments are searched over, guided

Event code	Strike (°)	Dip (°)	Rake (°)	Depth (km)	Moment (10^{17} Nm)
092197C					
• GS	326	36	-110	39	7.00
• SC	326	36	-110	39	7.43
091402B					
• GS	208	52	126	17	3.50
• SC	208	52	126	17	3.77
112705I					
• GS	269	53	99	8	9.00
• SC	269	53	99	8	9.41

Table 5.3: Examples of the optimum source parameters determined for three earthquakes, when the scalar seismic moment is calculated by either grid-searching (GS) or scaling the synthetic amplitude spectra to fit the data (SC).

by previous results here and those published elsewhere; clearly there is a trade off between the size of the increments grid-searched (i.e. the resolution afforded by the technique) and the time taken for the grid-search algorithm to run.

Here increments seismic moment of 5×10^{16} Nm are chosen, resulting in run-times of over two days for events 092197C and 091402B, where some 30 different depths were searched. This kind of run-time is clearly unacceptable, especially when considering the results in Table 5.3. In all cases the same set of optimum source parameters are found by the algorithm, though it is observed that the actual misfits were always slightly smaller for the grid-searched sources. Given these results, it is difficult to conclude that grid-searching for scalar seismic moment is preferable to the current scaling approach.

5.8 $Q(F|\nu_1, \nu_2)$ Confidence Levels

The choice of $Q(F|\nu_1, \nu_2) = 0.05$ is such that every solution kept and used to determine error bounds on the optimum source parameters, is done so with a 95% confidence. If this boundary was lowered to 68%, then the corresponding cutoff value of $Q(F|\nu_1, \nu_2)$ rises to 0.32 (relating to the red-orange transition seen in the figures in Appendix E). The application of this solution filter leads to a reduction in the number of solutions used to bound the source parameters, and also in reduced intervals derived for individual source parameters within this solution

space. For the 14 validation events, Table 5.4 lists the ranges of source parameters existing within a solution set bounded by 68% confidence limits. For comparison, the corresponding ranges are listed (in brackets) for the $Q(F|\nu_1, \nu_2) = 0.05$ (95%) cut-off figure.

Event code	Strikes (°)	Dips (°)	Rakes (°)	Depths (km)	Moments (10^{17} Nm)
080393G	54 (62)	32 (46)	78 (96)	7 (11)	4.60 (6.27)
051395B	20 (46)	24 (50)	22 (60)	4 (6)	11.0 (30.4)
100195B	30 (38)	54 (70)	46 (64)	4 (6)	12.2 (28.6)
092197C	16 (34)	10 (16)	18 (46)	13 (24)	2.70 (3.97)
013099A	24 (32)	14 (20)	36 (42)	4 (6)	0.19 (0.26)
022599H	30 (38)	30 (38)	44 (56)	4 (5)	0.96 (1.33)
090799C	40 (50)	30 (42)	58 (74)	4 (6)	2.24 (3.41)
102299A	18 (28)	16 (26)	24 (38)	4 (7)	1.16 (1.57)
091302C	22 (34)	16 (32)	32 (48)	11 (19)	12.5 (21.7)
091402B	18 (40)	16 (30)	28 (60)	8 (14)	0.80 (1.48)
103102B	6 (10)	18 (22)	20 (30)	8 (14)	0.73 (1.16)
110102F	6 (12)	32 (58)	28 (52)	11 (18)	0.84 (1.91)
092804H	8 (12)	86 (86)	82 (84)	6 (11)	94.4 (96.4)
112705I	42 (54)	58 (70)	64 (78)	5 (9)	6.63 (13.1)

Table 5.4: The range of acceptable source parameters when a cut-off value of $Q(F|\nu_1, \nu_2) = 0.32$ is applied to bound the acceptable sets of source solutions. Values in brackets refer to the ranges defined by $Q(F|\nu_1, \nu_2) = 0.05$.

The reduction in confidence from 95% to 68% decreases the number of solutions used to define the range of 'acceptable' values; however this does not result in a significant 'improvement' in the constraints placed on the optimum source parameters. Examples of this come from some events that were originally well constrained (e.g. event 022599H) and some that were poorly confined (e.g. events 080393G and 112705I). Events where this reduction in confidence significantly reduces the inferred range of parameter estimates include 110102F, where the 68% confidence estimates are of the order of half those made using 95% confidence.

A graphical representation of the number of solutions found for each validation event for decreasing values of $Q(F|\nu_1, \nu_2)$ from 1.0–0.05 is shown in Figure 5.10. There is only ever one solution where $Q(F|\nu_1, \nu_2) = 1.0$, and then the numbers of solutions grow as $Q(F|\nu_1, \nu_2)$ decreases.

There is variation in the number of acceptable source solutions found for each earthquake, from 4,465 for event 102299A in Taiwan, to 51,510 for event 112705I earthquake on Qeshm Island, Iran. Whilst these might appear large numbers it is worth considering that, respectively,

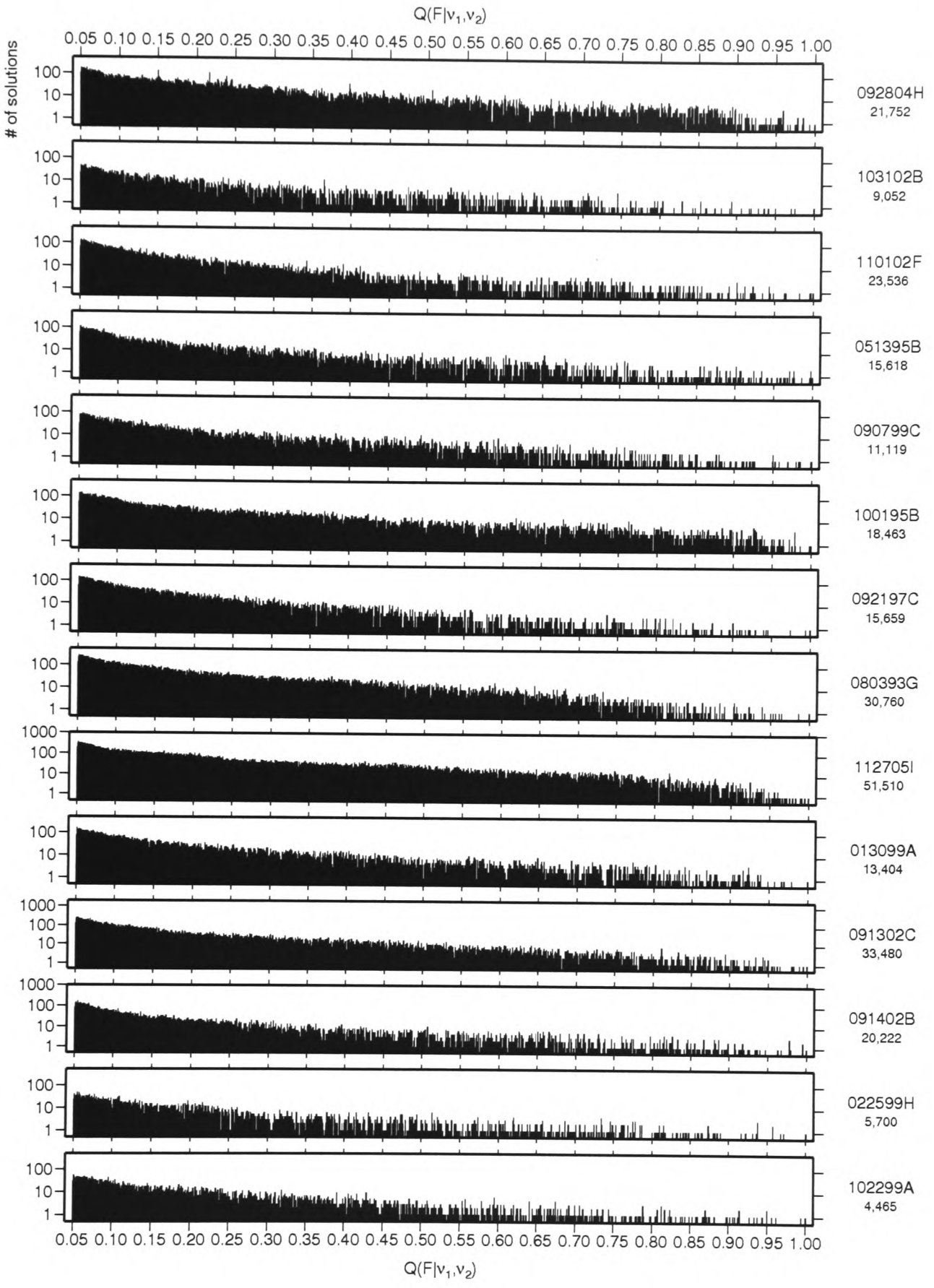


Figure 5.10: Histograms of number of solutions plotted as a function of their calculated $Q(F|\nu_1, \nu_2)$ for the validation events of Chapter 3. Events are listed in increasing longitude order with the total number of solutions shown in the histograms listed below.

some 2,551,500 and 3,280,500 D-C solutions were analysed, and the solution spaces used to place constraints on the source parameters only represent 0.17% and 1.57% of the total global solution space.

There are explanations for the larger number of statistically acceptable solutions seen in Figure 5.10 for events such as the 2004 Parkfield earthquake (event 092804H). It has previously been shown that, for a steeply dipping fault plane, significant dip-rake trade-offs can occur, over a range of depths, which contribute to give similar synthetic amplitude spectra, making identification of the optimum and the bounds difficult. There are also cases where events with rake angles close to either 90° or -90° and dips of the order of 45° have 180°-strike-rotated auxiliary planes closely positioned in the solution space, an unfortunate effect of constraining a D-C source leading to a single source being considered twice. In these cases both the focal plane and auxiliary plane are considered as likely rupture sources, despite representing the same mechanism. This leads to the situation, noted earlier, in which simple bounds on the acceptable range of fault parameters do not adequately reflect the statistical distribution of the 4-D solution space; it should be noted, however, that this does not affect the bounds placed on depth estimates.

Clearly, the reduction in confidence levels in the solution set from 95% to 68% decreases the ranges defined by the bounds placed on source parameters, but at the same time it also lowers the trust that can be placed in those constraints. With few exceptions the reduction in these source estimates are not significantly affected by this change (see Table 5.4) and it can be inferred that the variation in source parameters falling within the bounds $0.05 \leq Q(F|\nu_1, \nu_2) \leq 0.32$ are not as significant as those falling within $Q(F|\nu_1, \nu_2) \geq 0.32$.

5.9 Amplitude Spectra: Above 20 s

The 20 s cut-off period is increased in this section to investigate how much information provided in the 100–20 s amplitude spectra is required to allow trustworthy estimations of seismic source parameters to be made. Focal mechanisms and centroid depths were calculated for four of the validation events using intermediate-period surface wave amplitude spectra with cut-off periods of 50 s, 40 s, 30 s, and 25 s, as well as 20 s. The events selected range in centroid depth from 5 km (100195B) to 39 km (092197C). The same depth ranges were searched over

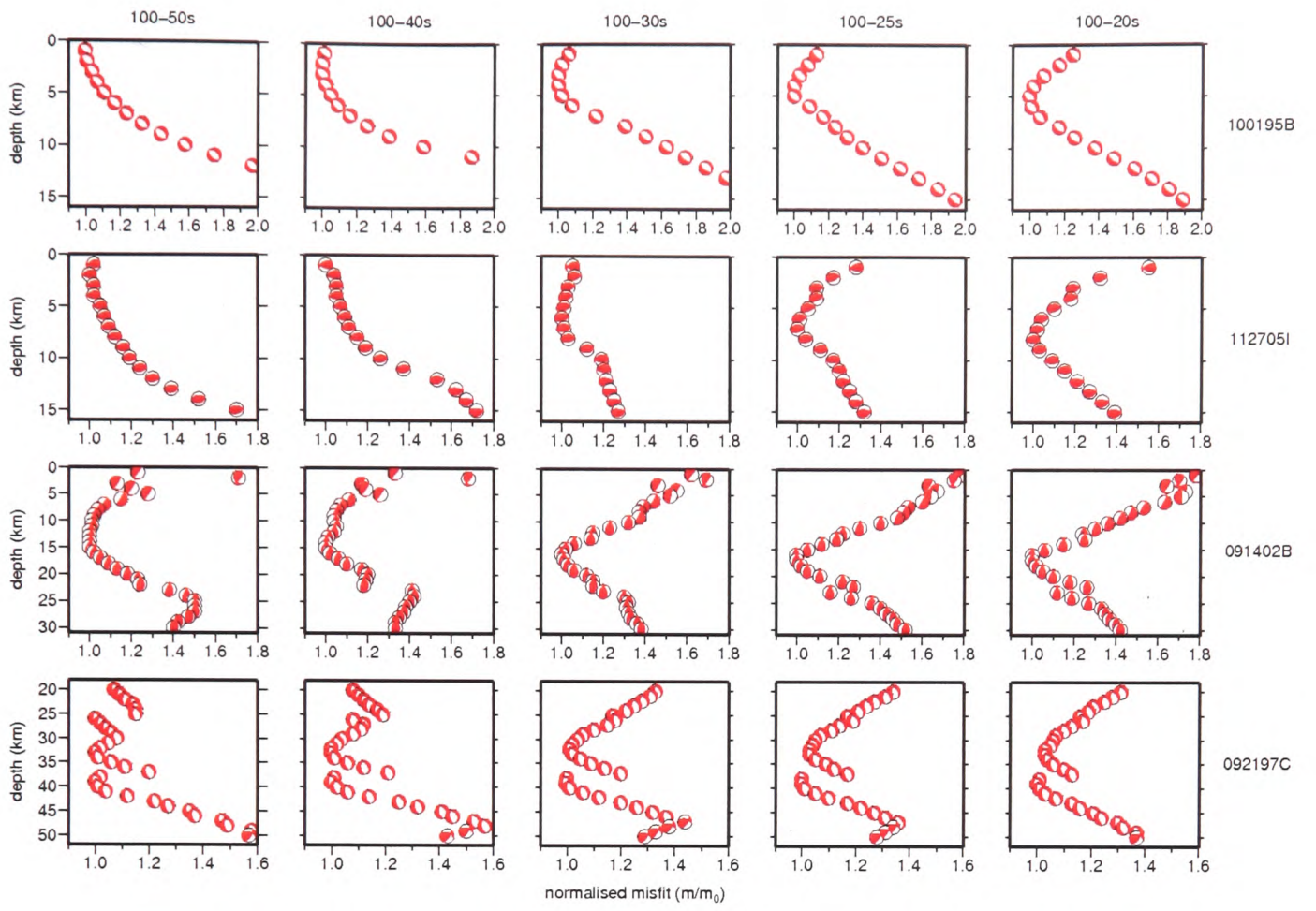


Figure 5.11: Misfit-depth profiles for four events using surface wave amplitude spectra ranging from 100 s to cut-off periods of 50 s, 40 s, 30 s, 25 s and 20 s.

as in Chapter 3 and the calculated misfit-depth curves are shown in Figure 5.11.

Considering these earthquakes in decreasing depth, there is little difference between the misfit-depth curves of the 1997 Zaire earthquake (event 092197C) when the cut-off period is varied from 30–20 s. This is perhaps expected, because information about the relatively deep source depth is found at longer periods than 20 s.

The optimum source depth for the 2002 Andaman aftershock (event 091402B) only becomes clear in the misfit depth curves below 30 s periods. Indeed, the minimum in these curves becomes more pronounced at the shorter-periods, an indication that the source depth is becoming increasingly well constrained with the additional information provided by the higher frequency surface waves. For the 2005 Qeshm Island, Iran, earthquake, (event 112705I) it would be difficult to have any confidence in the optimum depths determined by the algorithm at the longer periods until the introduction of 20 s period surface waves. This demonstrates that the shorter periods are needed to provide source information about shallow earthquakes

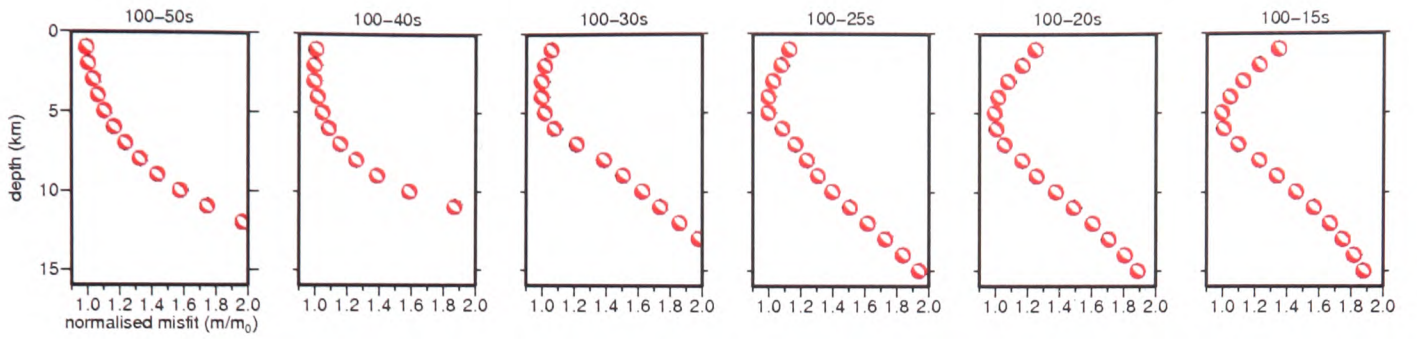


Figure 5.12: As Figure 5.11 but just for event 100195B in Dinar, Turkey, with the addition of the misfit-depth profile relating to amplitude spectra in the period range 100–15 s.

that is not available in the longer period spectra.

Of all the misfit-depth curves in Figure 5.11 the most revealing are those associated with the 1995 Dinar, Turkey, earthquake (event 100195B). It is demonstrated that, using 50 s or 40 s cut-off period waves, the only conclusion that can be drawn about the source depth is that it is highly likely to be shallow. As the cut-off periods decrease through 30 s and 25 s to 20 s, the additional source information provided by the shorter-period surface wave amplitude spectra result in the optimum centroid depth of 5 km becoming increasingly evident. Indeed, it might be expected that were even shorter periods used, then this depth would become better identified and more robustly constrained.

5.10 Amplitude Spectra: Below 20 s

Motivated by the results of the previous section, Figure 5.12 shows the same information as Figure 5.11 for the 1995 Dinar earthquake alone but with the addition of an extra misfit-depth curve. This extra profile shows the resolution afforded by comparing synthetic and data amplitude spectra down to a 15 s cut-off period.

The best fitting source parameters in Figure 5.12 are summarised in Table 5.5 and the shorter period determinations compare favourably with the results of other studies (listed in Table 3.9). The resolution of depth provided by the reduction in cut-off period is clearly demonstrated in Table 5.6 with the range of statistically acceptable depths halving from 8 km to 4 km.

The misfit-depth profile calculated for the 2004 Parkfield earthquake presented in Figure

Study	Strike (°)	Dip (°)	Rake (°)	Depth (km)	Moment (10^{18} Nm)	Mechanism
50 s	134	70	-89	1	3.76	
40 s	132	60	-91	2	2.71	
30 s	135	50	-88	4	2.25	
25 s	135	50	-88	4	2.02	
20 s	128	44	-98	5	1.88	
15 s	126	47	-100	5	1.72	

Table 5.5: Optimum source parameters for event 100195B calculated here using cut-off periods between 50–15 s.

Cut-off Period (s)	$h_{\min}$ (km)	h_0 (km)	$h_{\max}$ (km)	Δh (km)
50	1	1	9	8
40	1	2	8	7
30	1	3	7	6
25	1	4	8	7
20	2	5	8	6
15	3	5	7	4

Table 5.6: Estimates of minimum ($h_{\min}$), optimum (h_0) and maximum ($h_{\max}$) acceptable depths for event 100195B, along with the range of depths (Δh) constrained by each cut-off period. Surface wave amplitude spectra with 15 s cut-off are shown to provide the tightest depth estimates.

3.13 shows similarities with the longer-period curves shown in Figure 5.12 presented here. Given that the introduction of shorter-period surface wave observations has led to a more trustworthy solution for event 100195B, it must be worth considering whether 15 s surface wave amplitude spectra can help better constrain the source parameters of the Parkfield earthquake?

5.11 Parkfield Revisited

A failing of this work thus far has been the inability to calculate an optimum source for the 2004 Parkfield earthquake consistent with the co-seismic faulting determined by local and field studies. The determination in section 3.8 of a strike and dip consistent with the

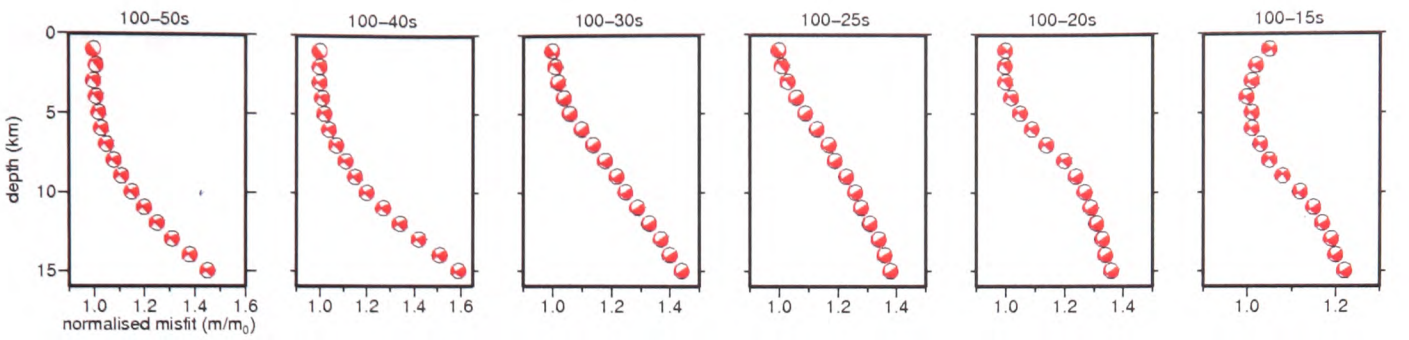


Figure 5.13: As Figure 5.12 but for the 2004 Parkfield earthquake; the additional depth resolution provided by the shorter-periods is clearly shown here.

orientation of the SAF in the Parkfield region is certainly of merit, but the calculation of a rake angle describing dextral strike-slip (expected) combined with reverse-faulting (not expected) is inconsistent with other determinations. A number of possible explanations were put forward to explain this erroneous result, including the poor receiver coverage imposed by the Pacific Ocean to the west and the consideration that shorter-period surface wave observations were required.

As demonstrated in 5.4, the algorithm has shown that it is capable of identifying reliable source parameters where there are limited stations and azimuthal coverage, so this is discarded as a possible explanation for the failings of the Parkfield study. Based on the findings of the previous section, the Parkfield earthquake is now studied using surface wave amplitude spectra in the range 100–15 s.

Cut-off Period	Strike (°)	Dip (°)	Rake (°)	Depth (km)	Moment (10^{18} Nm)	Mechanism
50 s	140	90	94	1	1.17	
40 s	140	86	138	2	1.16	
30 s	140	86	138	1	1.13	
25 s	140	88	118	1	1.74	
20 s	140	86	136	2	1.10	
15 s	140	70	172	4	0.78	

Table 5.7: Optimum source parameters for event 092804H calculated here using cut-off periods ranging from 50–15 s.

Misfit-depth profiles corresponding to cut-off periods of 50 s, 40 s, 30 s, 25 s, 20 s and 15 s are

shown in Figure 5.13 and the optimum source parameters are summarised in Table 5.7. It can clearly be seen that only for the cut-off value of 15 s does the source mechanism closely resemble those previously determined (see Table 5.8) and it also more accurately describes the style of faulting expected on the SAF.

Study	Strike (°)	Dip (°)	Rake (°)	Depth (km)	Moment (10^{17} Nm)	Mechanism
This Study 20 s	**140**	**86**	**136**	**2**	**11.0**	
This Study 15 s	**144**	**78**	**176**	**4**	**7.83**	
CMT	321	72	-178	12*	11	
USGS	147	83	-175	8	9.8	
SCEC	140	83	170	18 (5.5^{+})	12.6	
SLUEC	140	85	-155	6	5.89 (M_w)	
Langbein et al. (2005)	140	77	-172	8	9.97	

Table 5.8: As Table 3.15 but with the addition of the 15 s solution determined here.

Best fitting amplitude spectra and 50 s seismograms are plotted for both Rayleigh and Love waves in Figures 5.14 and 5.15 respectively. Synthetic waveforms generated for the source parameters determined here provide good fits to the data and, though there are cases where the recorded short-period amplitude spectra are seen to behave abnormally due to propagation effects, they are appropriately downweighted in the grid-search. The addition of these shorter-periods provides 35 additional frequency comparisons to be used in the amplitude spectral comparisons. There are cases where this additional data is not of use and is discarded, e.g. in the LHZ channel recording at JTS, but there are examples elsewhere (e.g. in many of the LHT channel recordings) where a close data-synthetic match is seen.

5.12 Synthetic Seismograms: Below 50 s

Throughout this work, waveform comparisons have been performed between 100–50 s. At these relatively long-periods, the synthetic seismograms generated for optimum source parameters have often closely matched the data (see Appendix D). Such observations promote confidence in the synthetics generation program and the Earth model used. Synthetic wave-

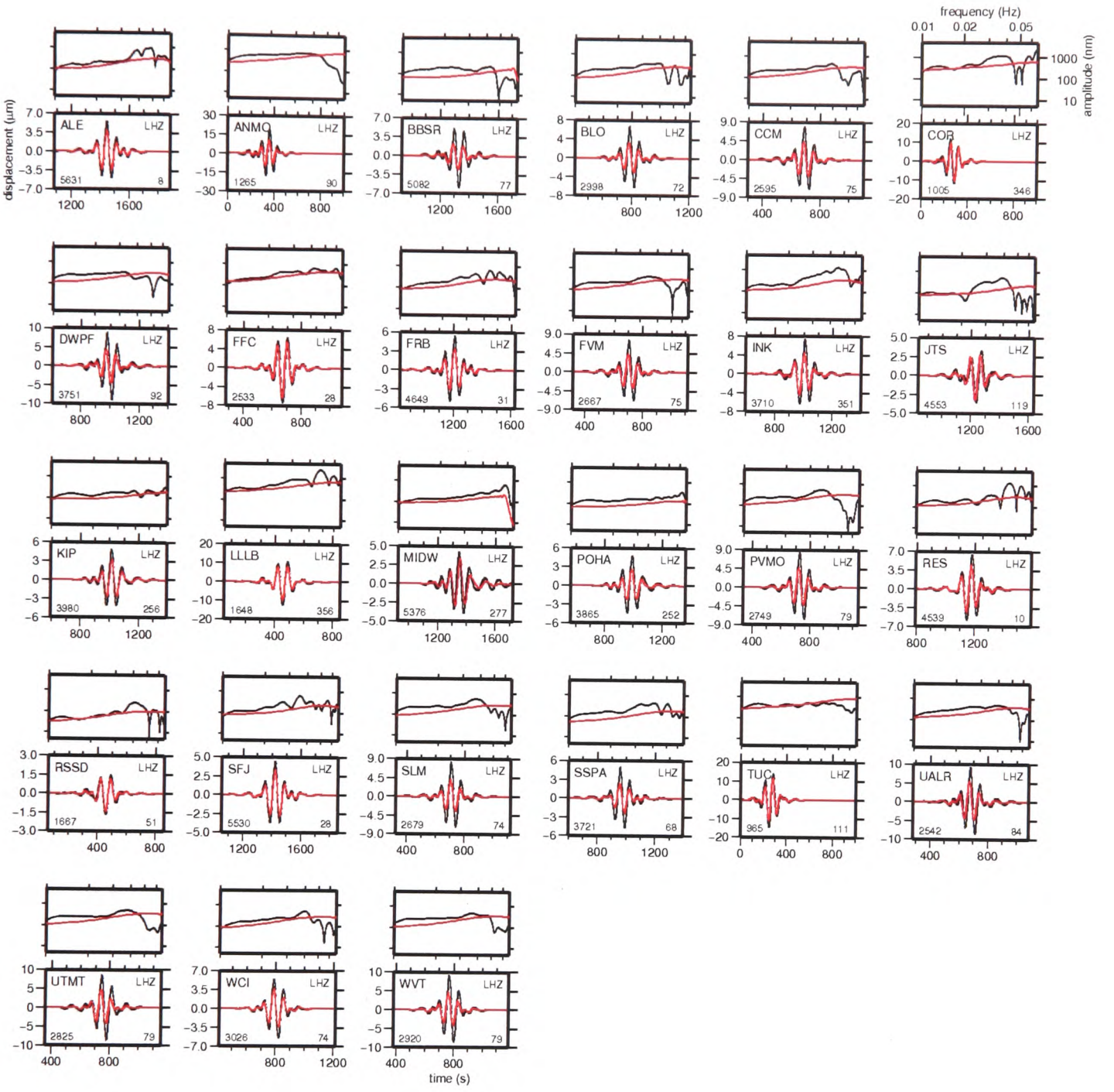


Figure 5.14: Best fitting Rayleigh wave synthetic (red) and data (black) amplitude spectra and filtered waveforms determined here for event 092804H using surface waves to 15 s cut-off period. In contrast to previous figures of this type, the amplitude spectra are plotted from 0.01–0.067 Hz, to show the additional information provided at the shorter periods.

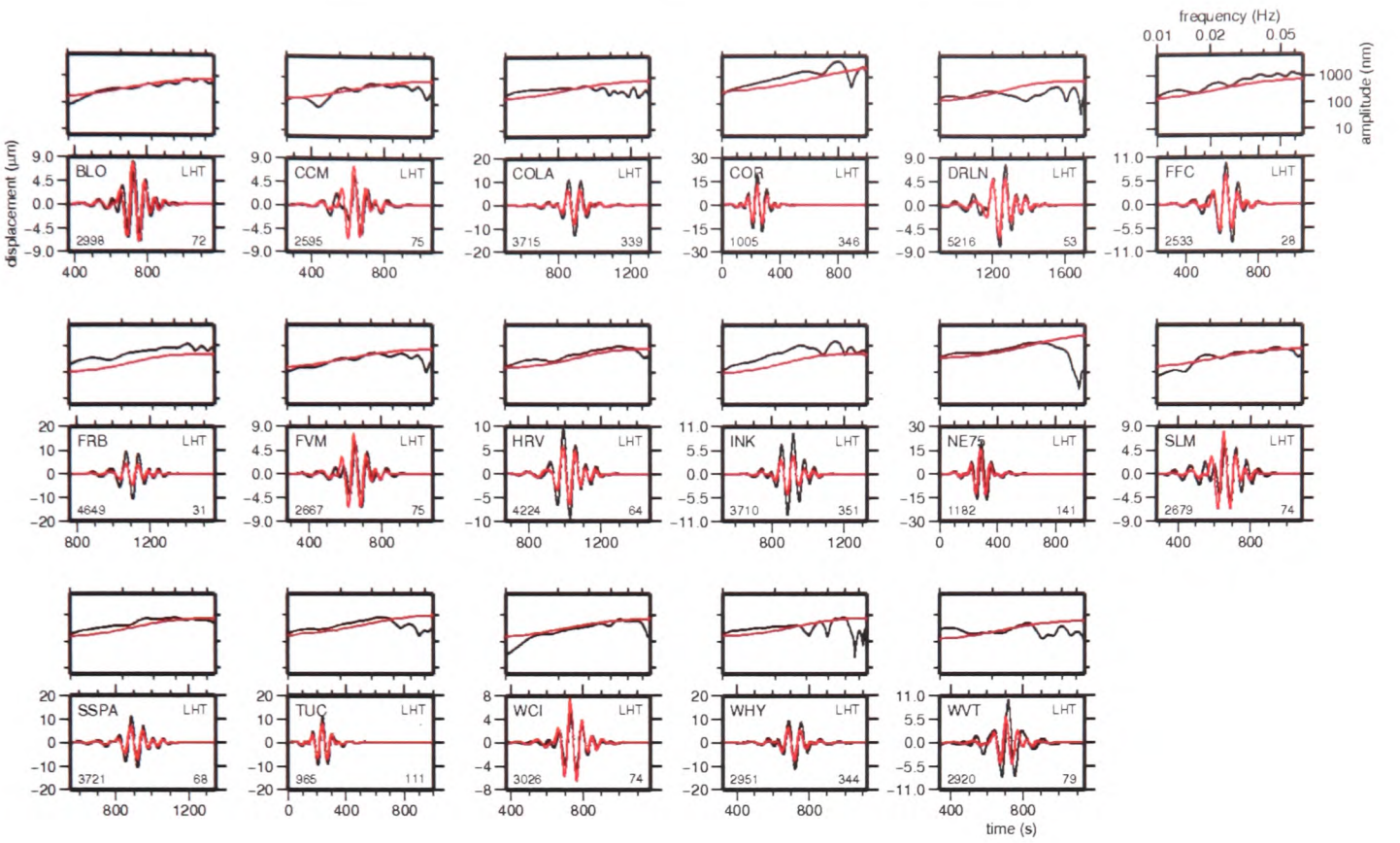


Figure 5.15: As Figure 5.14 but for Love waves.

forms are now generated at shorter-periods in order to examine how closely they match the recorded data, and whether the waveform comparisons used in this work could be performed at these shorter-periods with increased accuracy. Because of the success in matching synthetic and data amplitude spectra at the short-periods it should be expected that the corresponding waveforms would also be similar, and this provides another opportunity to analyse how well the phase and amplitude predictions of the Earth model match those of recorded data.

Figure 5.16 show Rayleigh and Love wave best synthetic and data seismograms generated for the 1993 Gulf of Aqaba earthquake in Egypt (event 080393G) with a range of cut-off periods between 50–20 s. Accurate Rayleigh wave seismogram matches are seen at 50 s periods and shorter especially at stations HYB, BNG and TAM to a cut-off period of at least 30 s. The Love wave fits are less good, but still approximately match the data at periods as low as 30 s. The shapes of some of the 20 s waveforms are caused by the underestimation of attenuation in the model.

For a given set of synthetic amplitude spectra, there are four corresponding source mechanisms. A comparison of 50 s cut-off period waveforms has been performed to help select the

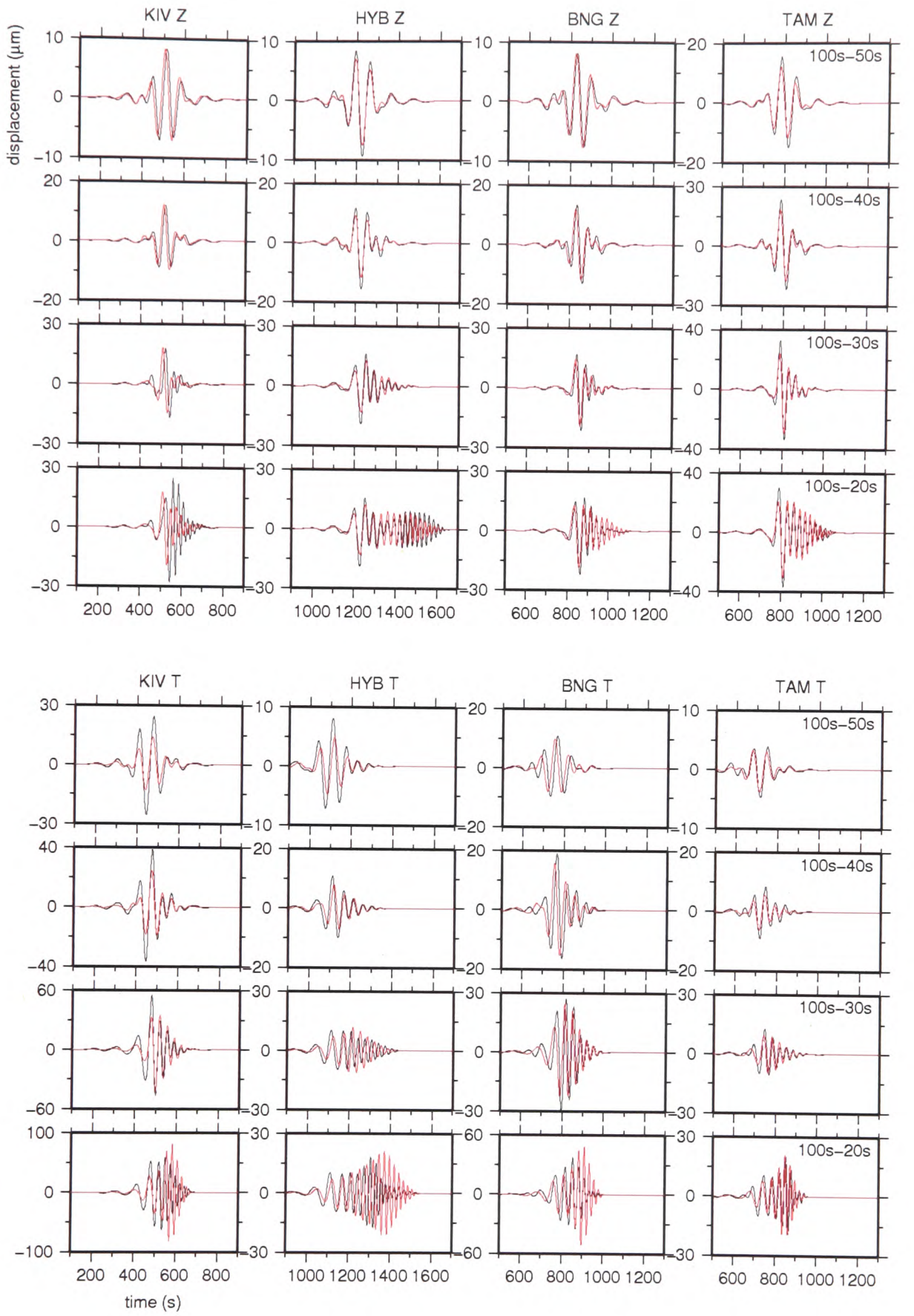


Figure 5.16: Rayleigh (top) and Love (bottom) wave data (black) and calculated synthetic (red) waveforms plotted at cut-off periods of 50 s, 40 s, 30 s and 20 s for event 080393G in the Gulf of Aqaba, Egypt. Stations shown in increasing azimuth from north are: KIV (Kislovodsk, Russia, azimuth = 21°, distance = 1838 km) HYB, (Hyderabad, India, 95°, 4648 km), BNG (Bangui, Central African Republic, 215°, 3173 km) and TAM (Tamanrasset, Algeria, 263°, 2975 km).

best set of source parameters (though it was proved that at times this was extremely difficult, especially for shallow sources), and in the cases where the cut-off periods were reduced to 40 s, 30 s and 20 s, exactly the same selections were made. Indeed where ambiguities were found at 50 s and had to be aided by external, independent, information they remained at the shorter-periods too, caused by poor excitation of the e_4 and e_5 elementary seismograms. As such, there is no clear evidence that using waveforms with periods shorter than 50 s improves this study.

In a final (re)visit to the 2004 Parkfield earthquake, Figure 5.17 shows recorded waveforms with cut-off periods varying between 50–20 s and two sets of synthetic seismograms. One set of these synthetics are generated for the source determined using 100–20 s amplitude spectra (in 3.8) and the other set were generated using the source found in this chapter using 100–15 s amplitude spectra. There are small differences between the two sets of synthetic waveforms, those that are apparent correspond to the greater seismic moment calculated for the shallower source. A comparison of the waveform misfits (m_w) between the two sets of synthetics and data shows a preference for the 4 km source (e.g. that identified using 15 s surface waves), at both 50 s and 20 s, but these misfit values only vary from those corresponding to the 2 km source by 1.7% and 1.0% respectively.

5.13 Source Locations and Origin Times

The epicentral coordinates and origin times of the sources studied in this work are taken from the hypocentre locations quoted by NEIC. A comparison is presented here of two sources for the 1999 Athens earthquake (event 090799C), one defined by the NEIC hypocentral parameters and one defined by the CMT centroid location and origin time; these locations are listed in Table 5.9.

Also shown in Table 5.9 are source parameters determined for these two locations and they exhibit little variation if the source is moved from the NEIC hypocentre to the CMT centroid epicentre. Indeed, only a 2° change in strike and rake occurs, with no changes in dip, depth or seismic moment. Synthetic seismograms are generated for a range of cut-off periods from 50–20 s and are plotted for both Rayleigh and Love waves in Figure 5.18. It can be seen that broadly there is little difference between the waveforms and the data, especially at the

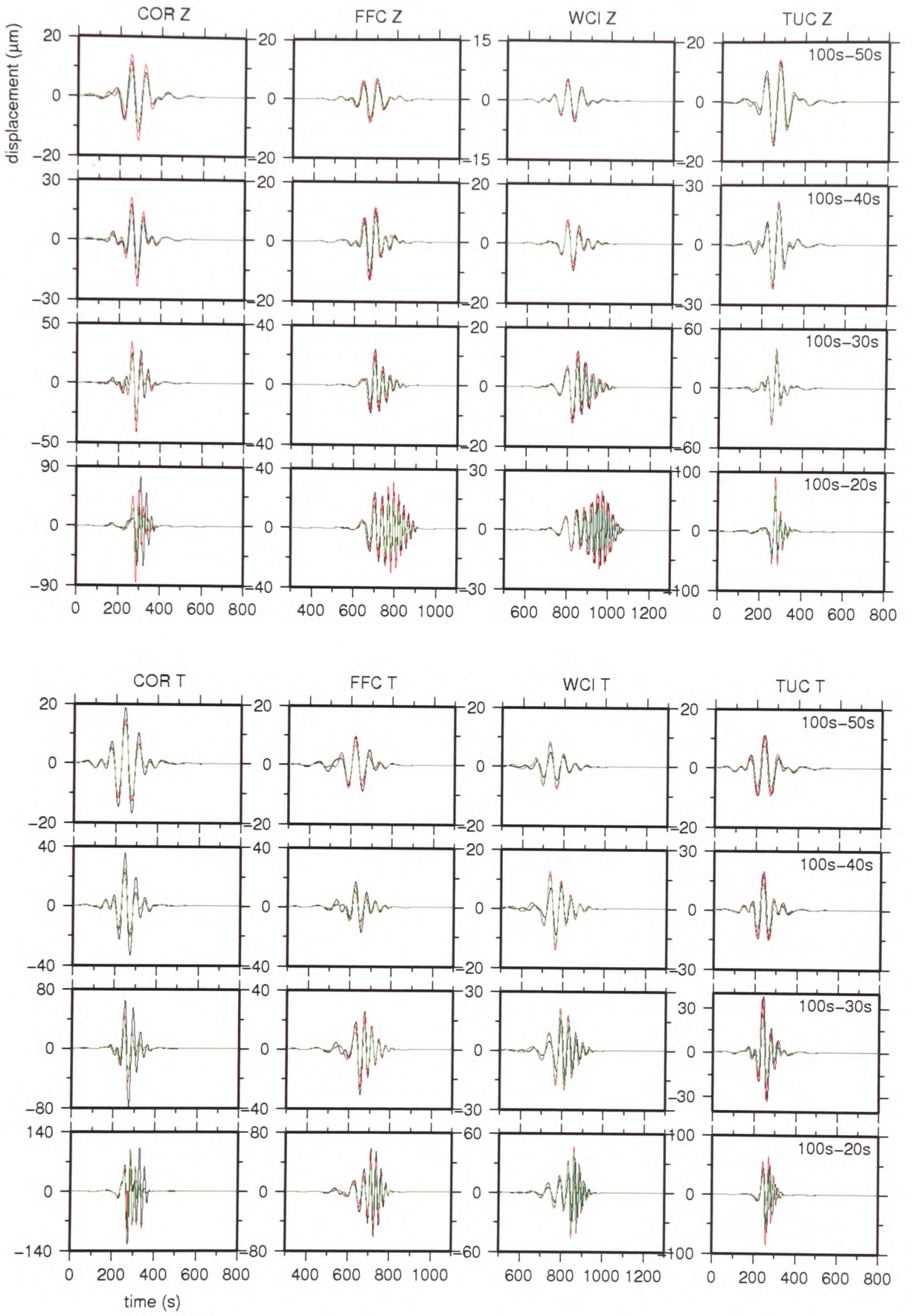


Figure 5.17: As Figure 5.16 but for the 2004 Parkfield earthquake (event 092804H). Waveforms are shown for the stations COR (Corvallis, Oregon, 346°, 1005 km) FFC (Flin Flon, Canada, 28°, 2533 km) WCI (Wyandotte Cave, Indiana, 74°, 3026 km) and TUC (Tucson, Arizona, 111°, 965 km). Red synthetics are those generated by the optimum source using amplitude spectral observations down to 20 s, whilst green waveforms are those generated for the 15 s cut-off period source (see Table 5.8).

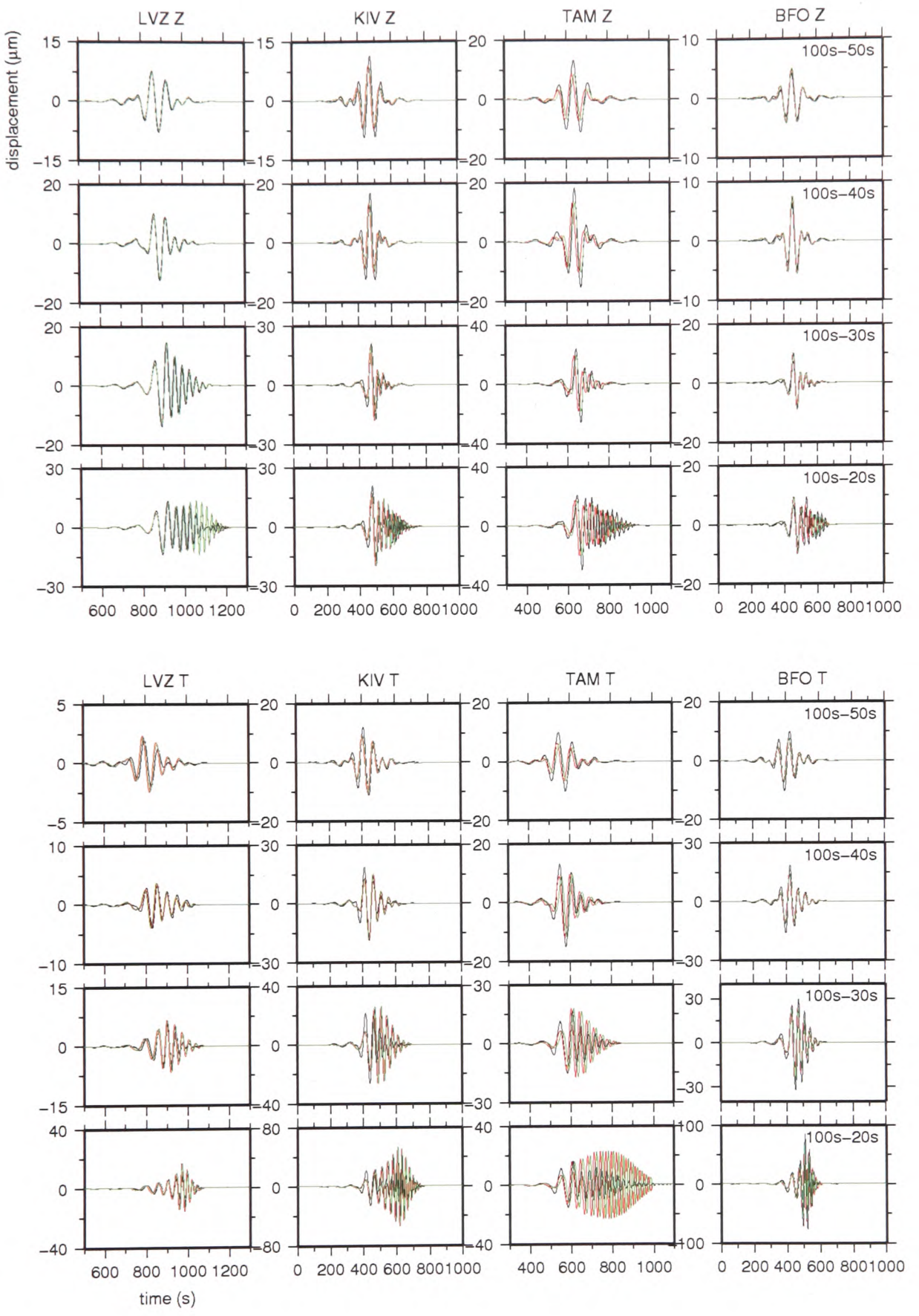


Figure 5.18: Comparisons of data (black) and synthetic seismograms generated for sources with epicentral coordinates given by NEIC (green) and CMT (red) at 50 s, 40 s, 30 s and 20 s cut-off periods for event 090799C. Waveforms are shown at stations LVZ (Lovozero, Russia, 8°, 3386 km), KIV (Kislovodsk, Russia, 61°, 1720 km), TAM (Tamanrasset, Algeria, 230°, 2425 km) and BFO (Black Forest Observatory, Germany, 317°, 1680 km).

Origin Time hh:mm:ss.s	Lat (°)	Lon (°)	Strike (°)	Dip (°)	Rake (°)	Depth (km)	Moment (10^{17} Nm)	Mechanism
11:56:49.4	38.12	23.61	118	46	-78	9	8.14	
11:56:56.5	37.87	23.64	120	46	-76	9	8.14	

Table 5.9: Epicentral coordinates and origin times, along with calculated source parameters for both NEIC (top) hypocentral and CMT (bottom) centroid locations.

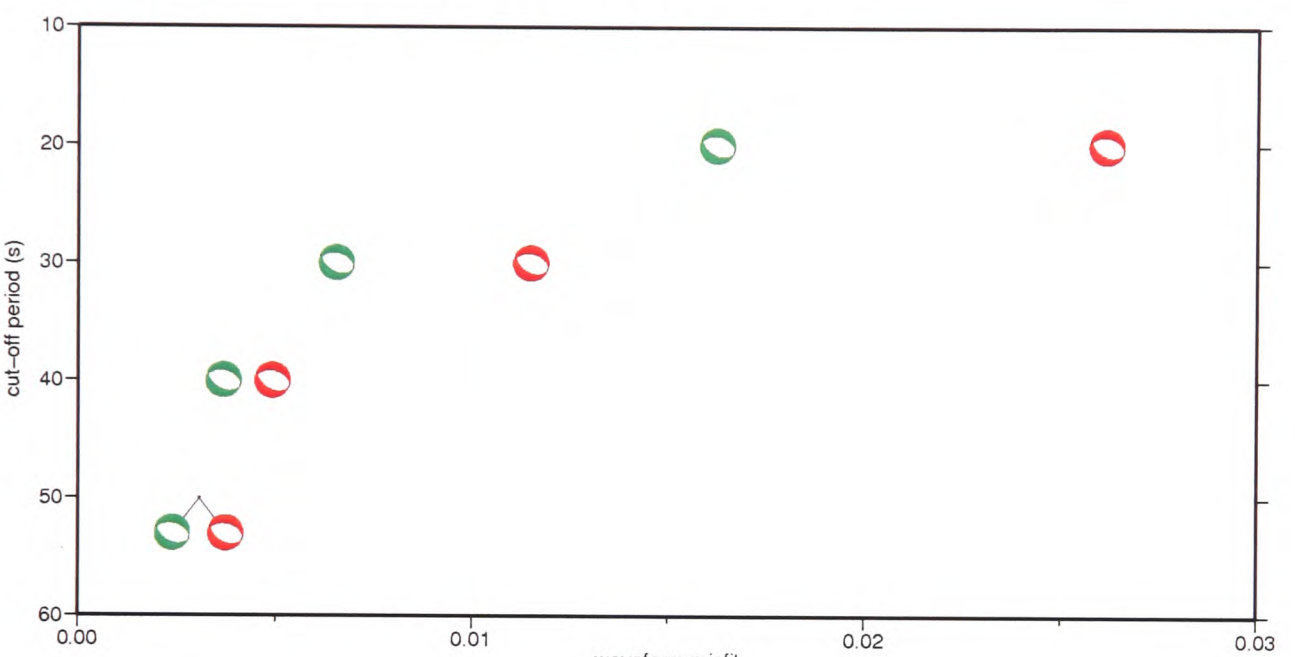


Figure 5.19: A comparison of the waveform misfit (m_w) values between 50–20 s for NEIC (green) and CMT (red) source locations of the 1999 Athens earthquake.

longer-periods. The difference in location equates to a distance of about 28 km, much smaller than the approximate wavelength of a 100 s surface wave (~350 km).

In order to quantify Figure 5.18, waveform misfit (m_w) values are plotted in Figure 5.19. The misfits are calculated between 50–20 s for both sources and clearly shows that, with the exception of the 50 s cut-off waves, preference is made for the NEIC synthetics. Observations such as these support the initial decision to use NEIC epicentral coordinates over those listed in the CMT catalogue for the corresponding centroid. In addition, the fact that the waveform misfits are similar at 50 s shows that the seismic source can be moved without unduly affecting the fits to the data; as the CMT algorithm typically uses waves of longer-periods than this, it is clear why the centroid location is not always well determined.

5.14 Summary

The CUB model and synthetic calculation program have generated accurate 3-D Earth seismograms for receivers in the 10–60° epicentral range and comparisons of predicted and recorded dispersion show that discrepancies are mainly limited to the shorter-periods. Synthetic waveforms are calculated that provide close matches to the data to at least 30 s period.

Seismic moment estimates produced by scaling synthetic amplitude spectra to the observed data are seen to be robust and not significantly less accurate than those derived from grid-searching. Whilst a good azimuthal distribution of stations is expected to tightly constrain source parameters, in cases where coverage is poor, trustworthy estimates have still been calculated. Reliable source parameters have been determined here using only Rayleigh wave recordings, though the sole use of Love wave observations precludes the determination of reliable focal mechanism and depth estimates.

For earthquakes at depths of 20 km and greater, amplitude spectral observations to cut-off periods of 30 s allow the robust determination of source parameters. However, the importance of shorter period surface waves for constraining very shallow sources (< 15 km, say) is emphasised here. In the study of the 1995 Dinar and 2004 Parkfield earthquakes, source estimates using longer-period data identifies these events as 'shallow'; trustworthy estimates of their likely centroid depth can only be made through the analysis of surface waves with periods of 20 s and less.

Chapter 6

Conclusions

"There are only two ways to live your life. One is as though nothing is a miracle. The other is as though everything is a miracle."

Albert Einstein (1879–1955)

6.1 Summary

A method is presented to calculate seismic source parameters using 100–20 s period surface wave observations. 3-D Earth synthetic Rayleigh and Love wave amplitude spectra are compared with data recordings in a grid-search algorithm and best fitting focal solutions and depth estimates are determined.

Source parameters determined for 14 global $5.4 \leq M_{\mathrm{w}} \leq 6.5$ earthquakes occurring at shallow (4–39 km) depths are used to test and validate the techniques developed. The results presented here are consistent with those determined in other studies and the close waveform and amplitude spectral matches seen here promotes confidence in the synthetic seismogram generation program, the 3-D Earth model and the source parameter search algorithm.

Shallow sources are better constrained by this method than those at greater depth due to the approximate exponential decay of the surface wave excitation with depth at intermediate-periods. As a result, the estimated depth of the 1997 Zaire earthquake (39 km) is the least well resolved of the validation events. This earthquake is found to lie beneath the Moho in

the local Earth model used and the influence of this velocity discontinuity on the misfit-depth profile for this event is significant. This earthquake merits further analysis to better determine whether it occurred in the lower crust or the upper mantle owing to its importance for the theory that earthquakes do not occur in the continental mantle.

Source parameters calculated for the shallow 2004 Parkfield earthquake are poorly constrained using surface wave observations between 100–20 s periods. The orientation of the San Andreas Fault in the near-source region is well determined here, but the style of faulting calculated is not consistent with the observed co-seismic slip. With the use of shorter-period surface wave data (20–15 s) more trustworthy estimate of both rake angle and source depth are calculated. These results, combined with the tighter depth constraints placed on the 1999 Dinar earthquake using shorter-period surface waves, highlight the importance of these data in improving the resolution of shallow source studies.

Focal mechanism and depth estimates are calculated for 16 aftershocks ($4.8 \leq M_{\mathrm{w}} \leq 6.0$) of the great 2004 Sumatra earthquake and used to identify the depth distribution of seismicity in the region. Source depths are found between 3–61 km and three distinct tectonic regimes are identified. Eight aftershocks, furthest from the trench in the Offshore Banda Aceh region, are determined to broadly align suggesting a common origin. The relocation of one of these events identifies the CMT depth estimate to be in error by 27 km and results in the calculation of a focal mechanism more consistent with neighbouring earthquakes.

In a series of tests of the method, the Earth model and synthetic calculation program generate accurate waveforms for recordings made in the 10–60° epicentral range and cut-off periods as short as 30 s. While a good azimuthal distribution of stations is expected to tightly constrain the surface wave radiation patterns, in cases where coverage is poor trustworthy estimates of optimum sources can still be made using this method. Reliable source parameters have been determined here using solely Rayleigh wave recordings, though the sole use of Love wave observations is found to preclude the identification of reliable focal mechanism and depth estimates.

The calculation of robust source parameters for shallow earthquakes with $4.8 \leq M_{\mathrm{w}} \leq 6.5$ shows the benefit of applying this method to suites of earthquakes in order to characterise the nature of the depth distribution of earthquakes in the crust. One advantage of this method is that, unlike other source parameter studies, it allows the reliable determination of focal

mechanisms for relatively small magnitude events due to the source information contained in the intermediate-period surface waves used. Previously, before the advent of accurate upper mantle and crustal models, such determinations were only possible with dense, local, networks which, themselves, are not extensively distributed and extremely localised. The extensive application of this method, therefore, can allow the identification of local tectonic patterns using earthquakes previously too small in size to warrant study. Local tectonic patterns can then be analysed and used to draw conclusions about the overall style of deformation on regional scales, which may only be revealed through analysis of larger-magnitude, less-frequent, earthquakes. That smaller earthquakes are more common than larger earthquakes also means regional and local seismo-tectonic assessments can be made over much shorter time periods, which could have great implications in seismic hazard studies, for instance.

6.2 Future Work

The application of trustworthy depth estimates is of great interest in explosion discrimination studies. The determination of a focal mechanism representing shear dislocation for a seismic event occurring in the upper-crust is not sufficient proof that the event is not an explosion. Instead, if a suspect seismic signal can be reliably calculated to have been excited deeper than 10 km, say, then it can be considered to have been produced by an earthquake and not an explosion. In instances where depths shallower than 10 km are calculated events can be flagged for further screening.

In this study it has been shown that shallow seismic source depths can be well constrained using surface wave amplitude spectra. The 9 October 2006 nuclear test in North Korea highlighted the scientific and political need for accurate seismic discrimination techniques, of which this method can be considered an example. It is anticipated that the method developed here can be applied to large man-made explosions to see if reliable source parameters can be calculated. Currently sources are constrained to be solely D-C; the analysis of appropriate source parameters for predominantly explosive sources will require a modification allowing the calculation the six moment tensor components without the application of the D-C constraint. It would be hoped that in the case of man-made explosions, their shallow source depth would be identified using this method, but additional techniques would be required to positively identify the event as an explosion. The analysis of smaller-magnitude events will require the

use of recordings made closer to the source than 10°, as the detection and identification of seismic signals become more difficult as source-receiver distances increase.

The method presented in this study is developed to allow flexibility in the choice and application of global Earth models. With the development of increasingly accurate Earth velocity models, using more data at periods shorter than 20 s, it is hoped that source parameter determinations can be performed routinely with cut-off periods as low as 15 s. The use of these waves has been unambiguously demonstrated to provide better source constraints and should be considered imperative in the study of very shallow sources.

Surface wave radiation patterns and amplitudes have been shown to be tightly controlled by seismic source parameters. Indeed, observations of the synthetic-data matches provided by this method indicate that the source term significantly dominates over path and receiver effects. More accurate source information can be applied to update current Earth models; knowledge of reliable source constraints on the surface wave radiation patterns can be used to better identify the nature of velocity and attenuation variations in the crust and upper mantle.

The insensitivity of the f_4 and f_5 components of the seismic moment tensor close to the Earth's surface mean that waveform comparisons cannot definitively select between two of the four source mechanisms that generate identical surface wave radiation patterns. A possible enhancement to the current methodology would be the inclusion of short-period body wave data in the grid-search algorithm to guide this choice.

Currently, surface wave recordings are manually selected based on a visual analysis of the signal-to-noise ratio. The procedure can be automated to either reject stations before source parameters are determined, or remove stations for which poor synthetic-data misfits are found during the grid-search itself.

After such automation, this method can be routinely applied to regions of interest, an example of which is the Hellenic Arc region of the Mediterranean. This region is characterised by abundant, low-magnitude, seismicity; but the nature of the plate boundary between northern Africa and southern Europe is not especially well known. The determination of robust focal mechanisms, combined with reliable depth estimates, may provide insights into the character of this particular region that were not previously possible using other techniques.

Appendix A

3-D CUB Earth Model

A laterally heterogeneous crust and upper mantle shear velocity model, recently made available by the Center for Imaging the Earth's Interior (CIEI) at the University of Colorado at Boulder (Shapiro & Ritzwoller, 2002) is used in this study. This 3-D Earth model incorporates group velocity measurements determined by frequency-time analysis (FTAN, Levshin et al., 1989) and phase velocity maps described by Trampert & Woodhouse (1995) and Ekström et al. (1997). The group velocity measurements cover the period range 200–16 s, whilst the phase velocity maps used are described between 150–40 s. Data coverage is generally better for Rayleigh waves than Love waves and intermediate-periods rather than either very-short or very-long periods.

The heterogeneous data coverage is imposed by the distribution of seismic stations and sources, and is best on the Eurasian continent. The CUB model was generated using a Monte-Carlo inversion, starting with an initial model generated from a variety of sources of global information. These include the global sediment model of Laske & Masters (1997), the CRUST5.1 model of Mooney et al. (1998) and the S20A shear-wave upper mantle velocity model of Ekström & Dziewonski (1998).

A water layer is included where appropriate, as is topography on the solid surface and the Moho along with 3-D variations in compressional and shear velocities in the sediments and crystalline crust. The final database describes the distribution of shear velocities on a global $2° \times 2°$ geographic grid from 0° to 360° in longitude and 88° to -88° in latitude (poles are not included) and therefore consists of some 16,020 individual velocity models centred on the even latitudes and longitudes.

The global range of topography and bathymetry in the CUB model is shown in Figure A.1. The elevation, relative to a radius 6371 km, is plotted for each $2° \times 2°$ grid square. Highest elevations are found in Tibet, with average grid heights in excess of 5 km being found in the middle of the plateau. In contrast, the greatest average sea floor depths are described in the West Pacific, off the south east coast of Japan, with water column depths exceeding 6.5 km in places, consistent with the subduction of very old (~180Ma) oceanic crust (Muller et al., 1997).

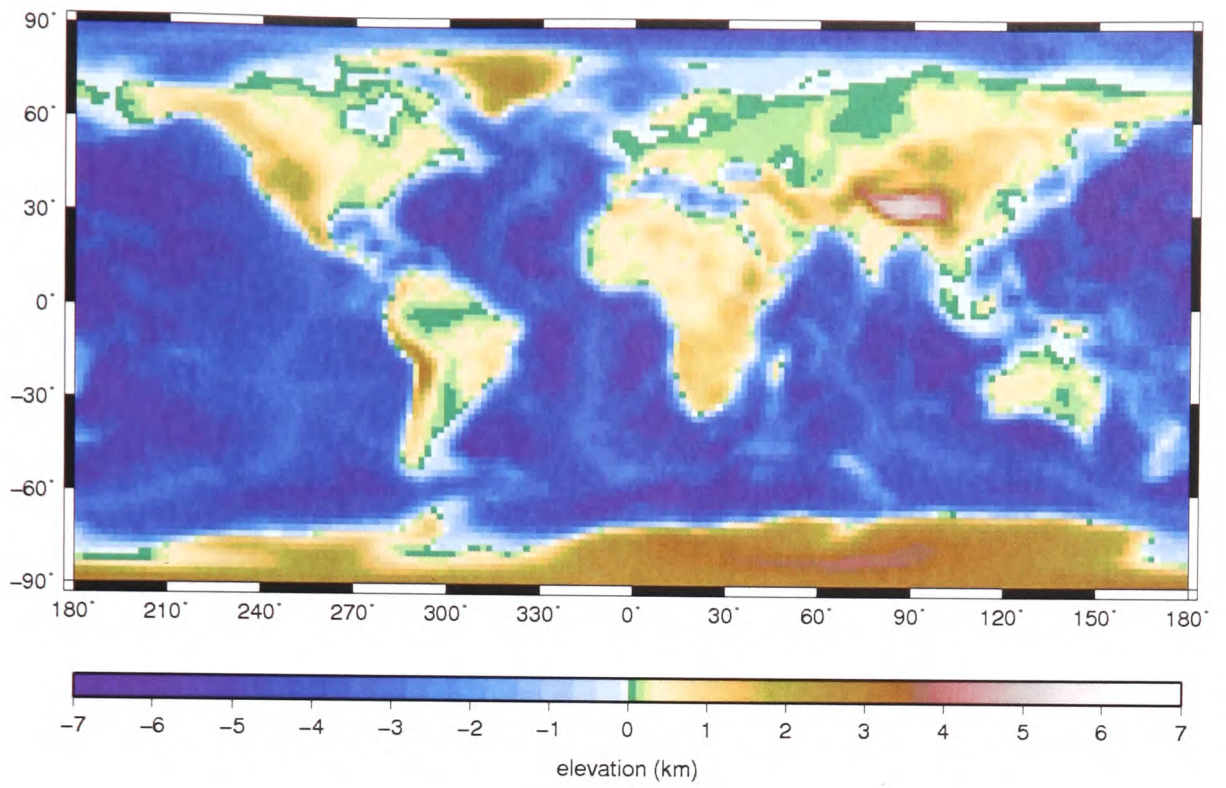


Figure A.1: Global elevation relative to mean sea level (at radius 6371 km) described in the 3-D CUB Earth model. The greatest elevations, up to 5.44 km, are associated with the Himalayas and the Tibetan Plateau region; whilst the most depressed regions extend to depths of 6.77 km, along the Japan Trench, to the south east of Japan.

Figure A.2 shows the range of crustal thickness described in the CUB model. Globally, the range is found to be between 80 km (beneath Tibet consistent with numerous studies of the region, e.g. Royden et al., 1997) and 3 km, close to the spreading ridges in the central Pacific and Atlantic oceans.

The CUB model describes the velocity structure of the upper Earth from the surface down to a depth corresponding to a radius of 5971 km (i.e. 400 km below 6371 km). As such, this model contains no information about the Earth's velocity structure below this point. In order to generate dispersion curves, eigenfunctions relating to the Earth's discrete modes of oscillation and, ultimately, synthetic seismograms, a model representative of the entire Earth from core to crust is required.

The laterally homogeneous one-dimensional (1-D) Preliminary Reference Earth Model (PREM, Dziewonski & Anderson, 1981), constructed using a dataset including free-oscillations, long-period surface wave and body wave observations has long been recognised as describing the seismic properties of the Earth accurately at long-periods (> 100 s). Full, core-to-crust Earth models are generated by combining the PREM model with the CUB crust and upper mantle model at the 5971 km boundary. In the resulting model, above this boundary the velocity and density structure of the Earth are described by the CUB model, with the structure below given by PREM. Surface waves in the period range 100–20 s do not exhibit any significant sensitivity to structure below 400 km depth.

The attenuation profile in the final model used here is that described by PREM throughout

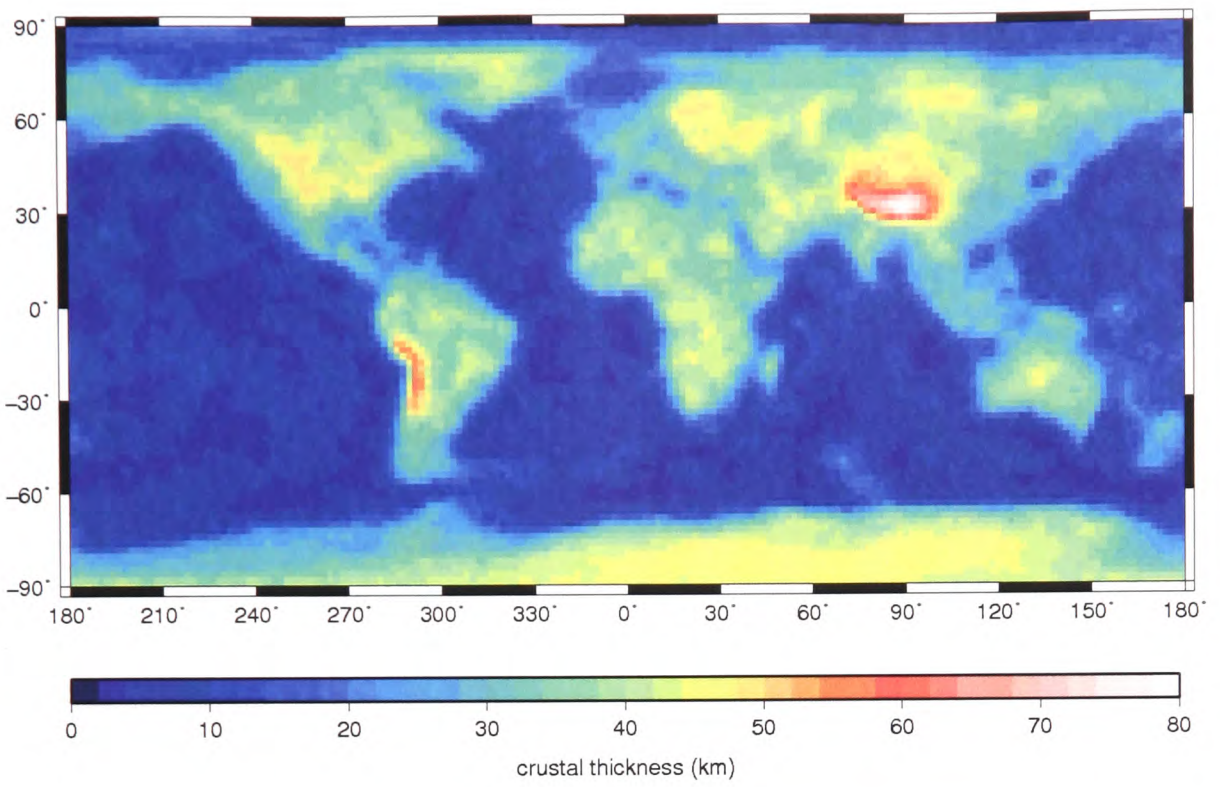


Figure A.2: Global crustal thickness described by the CUB Earth model. The thickest crust is found beneath the Himalaya-Tibet region of central Eurasia and the Andes in South America, whilst the oceanic regions are characterised by thin (< 20 km) crustal thickness.

the Earth. The bulk and shear quality factors, $Q_\kappa(\omega)$ and $Q_\mu(\omega)$, have been observed to be approximately constant over the band of seismic frequencies studied in this thesis (Kanamori & Anderson, 1977; Liu et al., 1976) so no frequency-dependency is assumed here.

The generation of 16,020 local velocity models allows the calculation of global phase and group velocity maps. Dispersion curves are generated for every $2° \times 2°$ square and as a result the phase and group velocities corresponding to selected periods can be plotted globally and interpreted as required.

Figure A.3 shows the 50 s, 100 s and 150 s phase and group velocity maps calculated here plotted alongside those generated from another crust and upper mantle model for comparison. These maps shown were calculated by Ferreira (2005) using a hybrid model (referred to as the S20 model) composed of the S20RTS upper mantle model (Ritsema et al., 1999) and the crustal model CRUST2.0 (Bassin et al., 2000). There is broad agreement between the maps at all periods shown, especially at 50 s, which is to be expected due to the common nature of parts of the datasets used in their construction. The S20 model has been shown to successfully generate 3-D Earth synthetic seismograms at long-periods (Ferreira, 2005) but lacks resolution at shorter-periods ($T < 40$ s) due to the absence of phase or group velocity measurements in the dataset used to generate the model. The use of group velocity measurements as short as 16 s in the CUB model would suggest that realistic earth-like synthetic seismograms can be generated down to periods of at least 20 s.

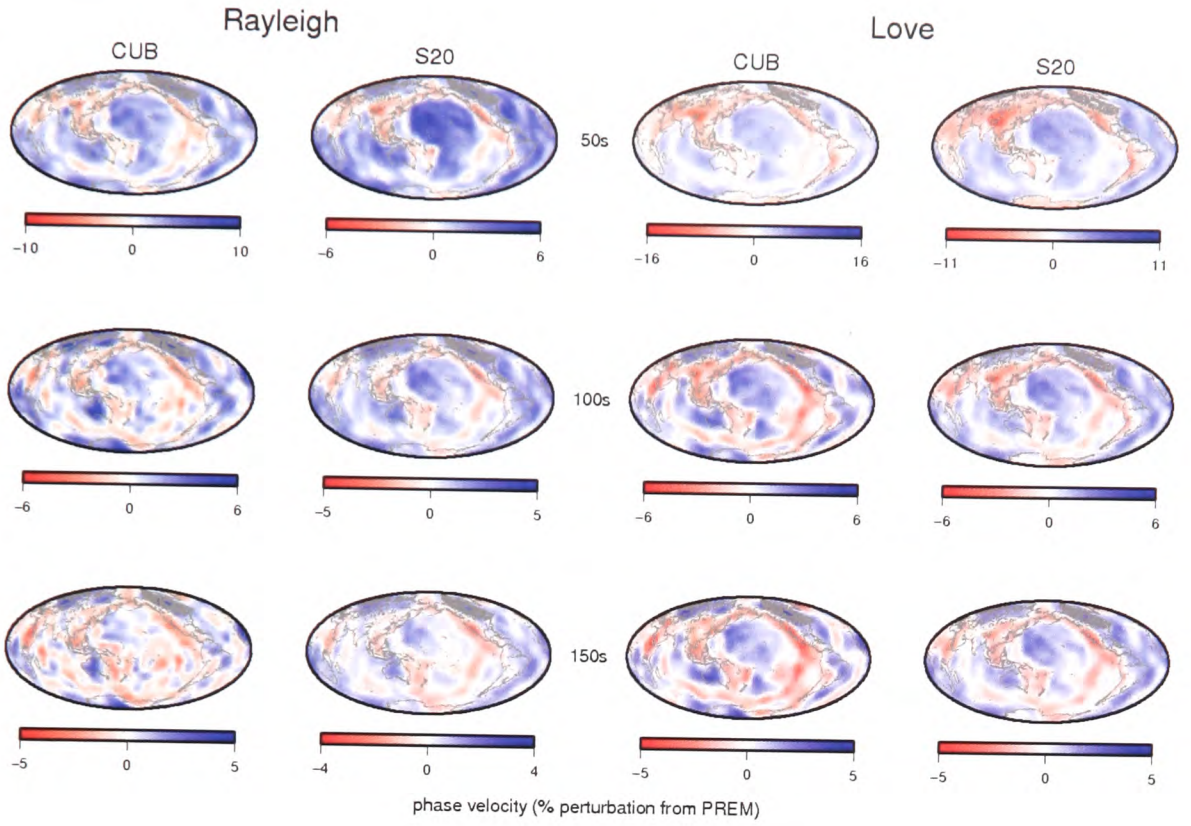


Figure A.3: Rayleigh and Love wave phase (top) and group (bottom) velocity maps calculated for 50 s, 100 s and 150 s period surface waves for the CUB and S20 Earth models.

Appendix B

Isolating the Fundamental Mode

B.1 Multiple Filter Technique

A wavetrain is passed through many filters centred on a range of frequencies, with the result being a contour plot of intensity of the wavetrain content resolved in frequency and time. The technical details of the choice of filter parameters are described by Inston et al. (1971) and Cara (1973). The chosen filter ($H_n(\omega)$) has the form:

$$H_n(\omega) = exp \left[-\left(\alpha \frac{\omega - \omega_n}{\omega_n} \right)^2 \right], \tag{B.1}$$

centred on the frequency ω_n, multiplied by a rectangular window having upper and lower limit frequencies:

$$\omega_{un} = \omega_n[1 + \gamma], \tag{B.2}$$

and

$$\omega_{ln} = \omega_n[1 - \gamma]. \tag{B.3}$$

If a parameter β is defined as the natural logarithm (ln) of the ratio of the peak value of H_n to its value at the cut-off frequency, thus:

$$\beta = ln \left[\frac{H_n(\omega_n)}{H_n(\omega_{ln})} \right], \tag{B.4}$$

then the following relationship then exists:

$$\alpha(\gamma)^2 = \beta. \tag{B.5}$$

The code used to perform this filter-domain filtering was kindly provided by Selby (2004, pers. comm.) In this study values of $\gamma = 0.5$ and $\beta = 5$ are empirically chosen.

Figure B.1 shows the LHT and LHZ channel recordings of the 28 September 2004 Parkfield, California, earthquake at station INK (Inuvik, Northwest Territories, Canada). Beneath the

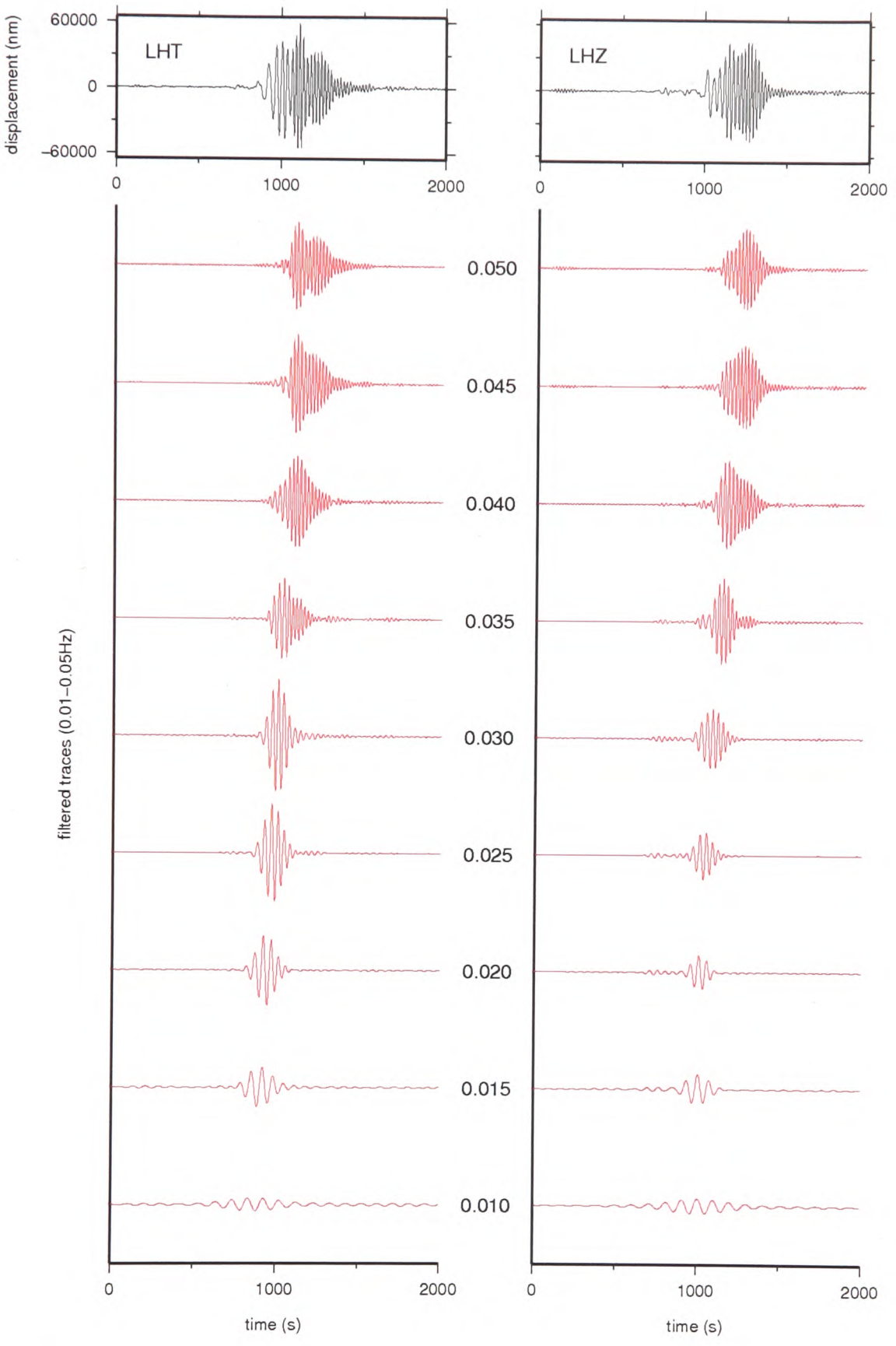


Figure B.1: LHT (left) and LHZ (right) channel bandpass-filtered (100–20 s) seismograms of the 28 September 2004 Parkfield, California, earthquake (event 092804H) recorded at station INK (Inuvik, Northwest Territories, Canada). Filtered traces (red) are bandpass-filtered between 0.01–0.05 Hz in 0.005 Hz increments and a common amplitude scale is used. The dispersive nature of this signal is clear as the longer-period waves arrive earlier than the shorter-periods.

recorded seismograms are narrow bandpass-filtered waveforms, where the filters have been centred on frequencies between 0.01–0.05 Hz. The dispersive nature of both seismograms is clearly shown here, with the peak arrivals at longer-periods arriving earlier than those at the shorter-periods. An envelope function is also calculated that describes the absolute amplitudes of the filtered waveform and the position of the peak height of the envelope function is taken to signify the time of the maximum energy arrival, i.e. the peak group arrival time.

The summation of a series of these calculated envelope functions across the frequency range leads to the generation of a FTAN contour plot, an example of which is shown in Figure 2.10. Here the LHZ recording of event 013099A in western China at station MA2 (Magadan, Russia) is shown along with the calculated filtered traces and associated envelope functions. In addition to the clear fundamental-mode surface arrivals, the non-dispersive body wave arrivals are also evident. The highest amplitude arrivals can be seen to occur between 0.04 Hz and 0.05 Hz; because the waveforms are cosine-filtered between 20–17.5 s there is little signal at periods shorter than 20 s. This cut-off is selected because at periods below 20 s it become increasingly difficult to distinguish the fundamental-mode from other arrivals (e.g. overtones and late arriving body waves).

B.2 Time Variable Filtering

Time Variable Filtering (TVF) can be used to remove unwanted signals and noise from recorded seismograms. First applied to dispersive surface waves by Pilant & Knopoff (1964), TVF allows a single mode of dispersion to be removed from a seismic signal given a suitable estimation of the dispersive characteristics of the mode of interest. Following the methodology of Landisman et al. (1969) and using code kindly provided by Patton (2006, pers. comm.), TVF uses group velocity curves calculated from the CUB model to isolate the fundamental-mode arrivals in a recorded wavetrain. Filtering occurs in the frequency domain, with a Fast Fourier Transform (FFT, after Cooley & Tukey, 1965) algorithm converting the original time series into a set of sine and cosine co-efficients. Each frequency component within the overall passband is reconstructed as a temporarily windowed harmonic function. Finally the filtered seismograms are obtained by the linear superposition of these harmonic signals.

In practice the reconstructed harmonic functions are windowed by the operator

$$W(t) = \begin{pmatrix} 0 & t < t_a \\ \cos\left(\frac{\pi\left[t - \frac{D}{C(t)}\right]}{t_b - t_a} \right) & t_a \leq t \leq t_b \\ 0 & t > t_b \end{pmatrix}, \tag{B.6}$$

where

$$t_a = \frac{D}{C(T)} - T\left[\alpha + \beta \left| \frac{dC(t)}{d(t)} \right|\right], \tag{B.7}$$

and

$$t_a = \frac{D}{C(T)} + T\left[\alpha + \beta \left| \frac{dC(t)}{d(t)} \right|\right], \tag{B.8}$$

where D is the source-receiver distance (km) and $C(T)$, the group velocity arrival times (as a function of period, T), are those from the dispersion curves calculated from the CUB model. It should be noted that the parameters α and β presented here are not the same as those used in the MFT.

Landisman et al. (1969) reported that they found that values of $\alpha = 3.5$ and $\beta = 80$ led to the most satisfactory results for the fundamental-oceanic mode. In practice, this study requires that both continental and oceanic modes be considered. The selection of $\alpha = 3.5$ is guided by Patton (2006, pers. comm.), with the β parameter estimated as:

$$\beta = \left[\frac{\frac{D}{10}+0.5}{10} \right]. \tag{B.9}$$

Plots of the variation of the parameter α for a fixed $\beta = 35.4$ are shown in Figure B.2. α varies between 1.5–5.5 in 1.0 increments and $\alpha = 3.5$ is selected as best isolating the fundamental-mode from the signal. A value of $\alpha = 1.5$ precludes parts of the low frequency ($\omega = 0.01$ Hz) arrivals from being captured, and those at higher frequencies (ω=0.05 Hz) are also inadequately captured. In contrast, higher values of α (e.g. $\alpha = 4.5$ and $\alpha = 5.5$) are rejected as they include too much of the long-period signal, capturing parts of the earlier body-wave arrivals and also contain unwanted information at shorter-periods where a significant contribution from overtones and noise can be included.

B.3 Phase-Matched Filtering

Phase velocity curves for a given source-receiver path are calculated using the CUB model and then used to predict the arrival times of the fundamental-mode surface waves. Once a phase velocity curve is derived for a given seismogram it is used to effectively remove the dispersion from the waveform, collapsing it about the centre of the time window (see Equations 2.18, 2.19, 2.20). Once compressed, it is possible to simply window out additional noise and unwanted signals from the collapsed signal. By calculating the amplitude spectrum of the resultant waveform in a narrow time window it is possible for the amplitude spectrum to be extracted from the part of a seismic signal representative of the fundamental-mode arrival. This Phase-Matched Filtering (PMF) technique (Herrin & Goforth, 1977) is commonly used, described in Chapter 2.3.3 and well documented elsewhere (e.g. Levshin & Ritzwoller, 2001; Stevens & McLaughlin, 2001).

Once the dispersion is removed from a surface wave recording, a simple cosine bell window is applied around the compressed seismogram to window out unwanted signals and noise. This time-domain filter is described by a maximum width, t_{win}, and a parameter, p, which corresponds to the fraction of the window that is cosine tapered. For example a window 100 s wide with $p = 0.1$ would have cosine tapers of width 10 s at each end. As such the parameter p can take any value between 0, where no tapers are applied (i.e. a boxcar), and 0.5, where the window is of the form of two, back-to-back, cosine tapers.

Figure B.3 shows the shape of the windowing functions and the effects that variations in

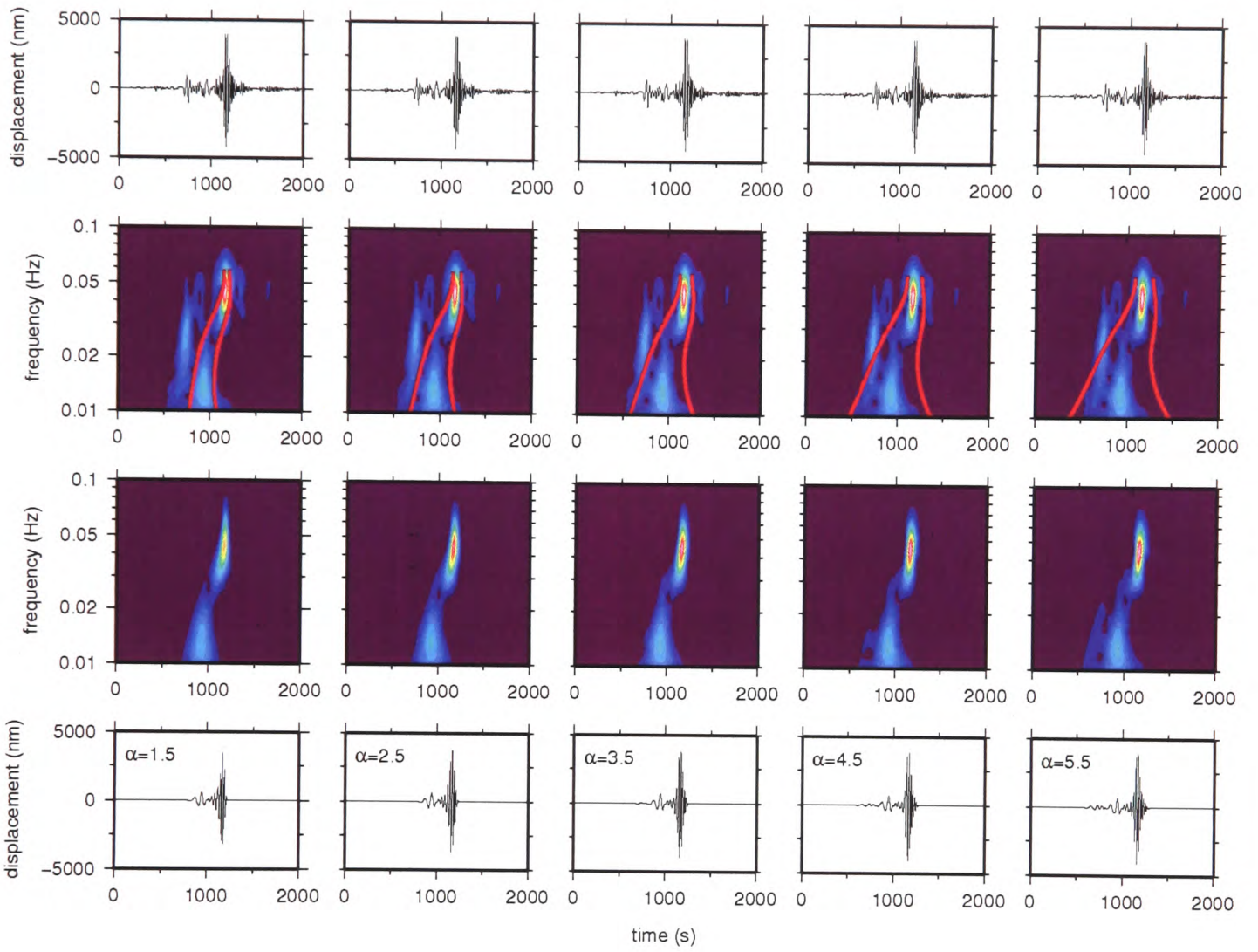


Figure B.2: Example of the application of TVF to the LHZ channel recording of event 013099A, western China at station YAK (Yakutsk, Russia, epicentral distance = 3537 km). The α parameter is varied between 1.5–5.5 in 1.0 increments for a fixed value of $\beta = 35.4$. Original recordings are shown at the top, with the corresponding FTAN contour plots below showing the extents, in time-frequency space, of the calculated windowing function (red lines). The application of the time-variable filtering results in the processed FTAN contour plots beneath, with the seismograms at the bottom show the final, processed waveforms. The value of the α parameter is shown in the upper left corner of the lower seismograms.

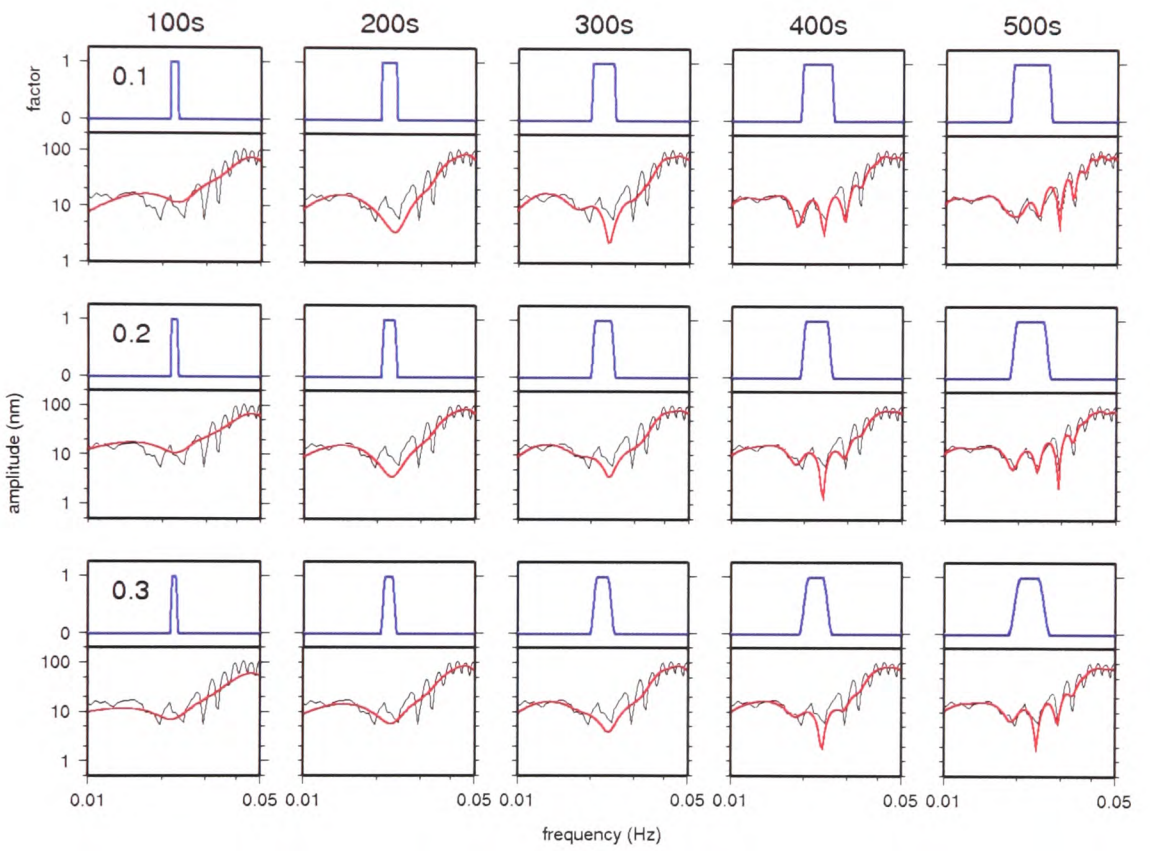


Figure B.3: Plots of the shape of the windowing function and the effect on the amplitude spectra of the vertical processed signals from event 013099A at station HIA (Hailar, Inner Mongolia). The width of the windows (t_{win}) varies horizontally across the figure from 100 s on the left to 500 s on the right. Values of the parameter p of 0.1, 0.2 and 0.3, from top to bottom are shown. The original, raw, amplitude spectrum is shown in black, with the processed spectra plotted in red.

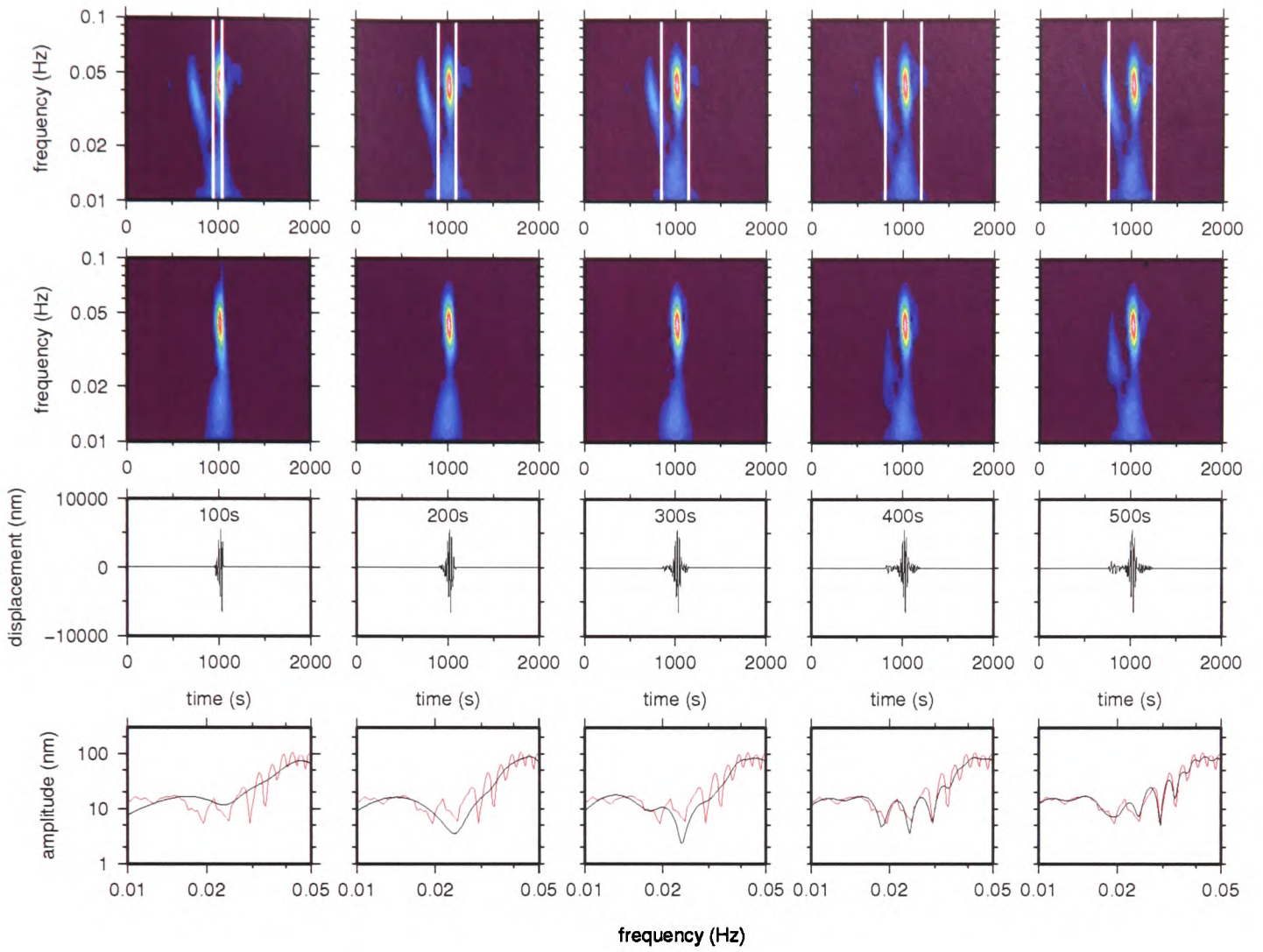


Figure B.4: Examples of the effect of changes in the parameter t_{win} for $p = 0.1$ on the vertical recording of event 013099A at HIA. Values of t_{win} ranging from 100 s to 500 s are shown, left to right. The top FTAN contour plots show the compressed signal (see Figure 2.11) along with the position in time-frequency space of the window, shown by white lines. Below these are the corresponding FTAN contour plots after windowing along with the windowed seismograms and processed amplitude spectra.

t_{win} and p have on the retrieved amplitude spectra. At $t_{win} = 100$ s the window is not wide enough to capture all the energy from the fundamental-mode arrivals. This is especially clear at longer-periods where the group arrival wavelengths are of the order of the width of the window. Conversely, a window with t_{win}=500 s captures too much unwanted signal and noise, especially at the higher frequencies. In these cases, as expected, there is little discernible difference between the raw and processed amplitude spectra.

Further examples of the effect of t_{win} are shown in Figure B.4. Windowing functions where $p = 0.1$ are shown with values of t_{win} ranging from 100–500 s. The effects of changes in t_{win} are made clearer by the use of FTAN contour plots. At 100 s too little of the fundamental-mode signal is captured, whilst at 500 s contributions to the amplitude spectra from the S-wave arrival are included. The effect of reducing the total number of points in the windowed seismogram is clearly seen here, as the narrower windows generate smoother amplitude spectra than the wider ones, which follows from Equation (2.26).

Changes in the values of p are more subtle and numerous windowing functions over many traces were analysed before optimum parameters of $t_{win} = 300\,\mathrm{s}$ and $p = 0.1$ were selected to be used in this study. Figure B.5 show further examples of changes in the windowing parameters for four signals recorded from event 013099A; with the raw and processed amplitude spectra at stations TLY, AAK, YSS and LSA presented. Analysis of the variations shown in the recorded and processed amplitude spectra at station TLY especially guided the selection of values of t_{win} and p. In the raw data there is a clear frequency-dependent notch between 0.02–0.03 Hz here and it is imperative that the window chosen best capture both the frequency and the depth of this notch. The 100 s and 200 s time windows produce notches at frequencies slightly higher than is seen in the raw data so must be rejected, with the 400 s and 500 s windows rejected as they incorporate more than just the fundamental-mode signal. The 300 s is observed to best preserve the notch whilst a window of this width would filter out much of the unwanted signal in more complicated recordings. As p increases from 0.1 to 0.3 there is also a migration in the frequency of the notch to slightly higher-periods, so preference is for the lowest value of 0.1.

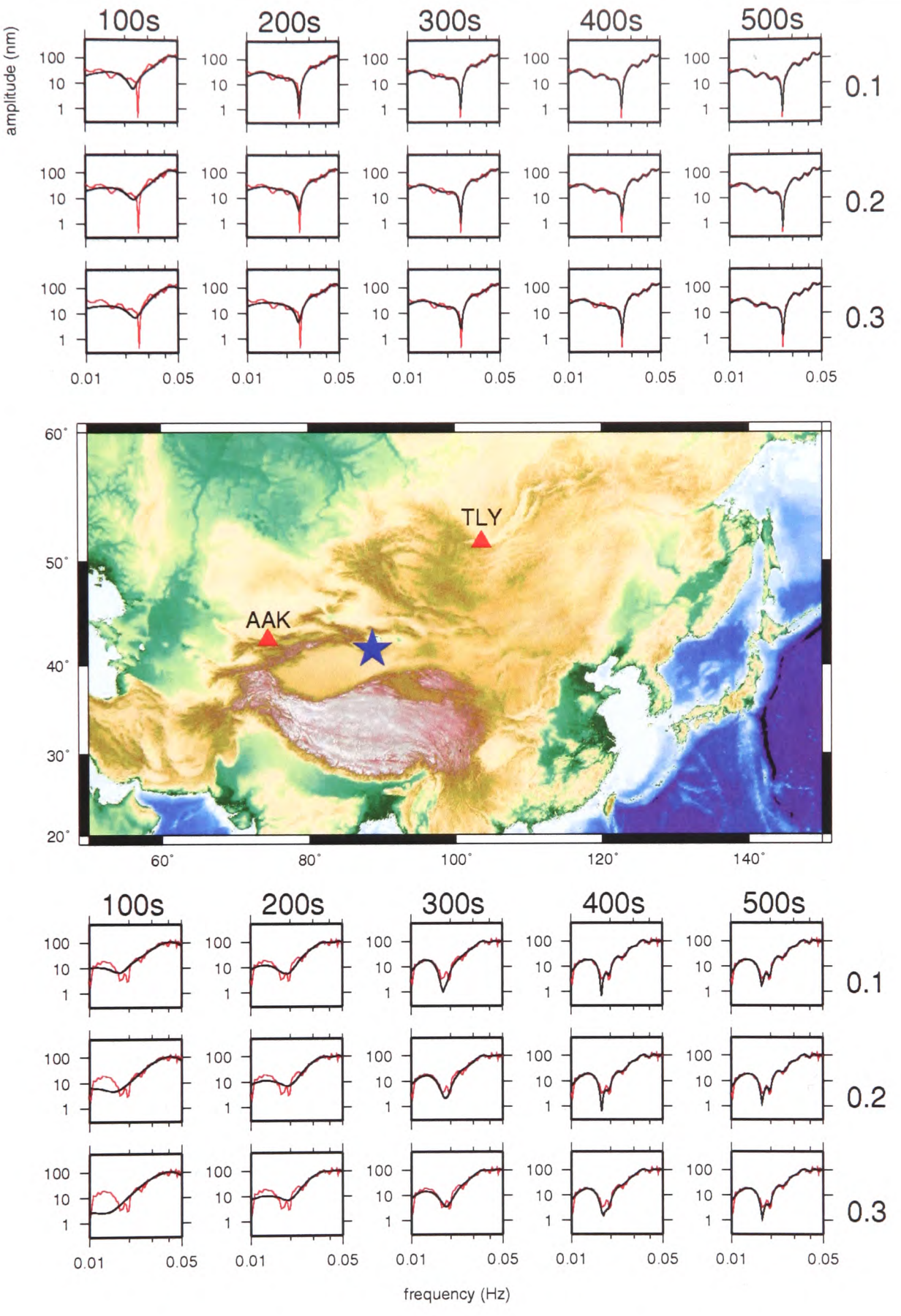


Figure B.5: Effects of altering the shape of the windowing function around an undispersed seismogram for event 013099A. Raw (red) and processed (black) LHZ channel amplitude spectra from recordings at stations TLY (top) and AAK (bottom) are shown. Values of t_{win} ranging from 100–500 s are shown horizontally, whilst changes in the parameter p are shown from 0.1–0.3 vertically. Optimum values of t_{win}=300 s and p=0.1 are selected as a result of comparisons with recorded data, but guided, especially, by observations at TLY.

Appendix C

Source Determinations for Chapter 3 Earthquakes

C.1 1999 South Xinjiang, China, earthquake (013099A)

In this section the effects of moving the model discontinuity observed in section 3.2 are analysed. The velocity and density boundary at 23.23 km is moved 10 km shallower and 10 km deeper and full grid searches are performed for the best fitting source solutions. The misfit-depth profile and adjusted Earth model for a discontinuity at 13.23 km are shown in Figure C.1. The best fitting source is listed in Table C.1, along with the corresponding solutions for models with discontinuities at 23.23 km and 33.23 km. Figure C.2 shows the same information as Figure C.1, but for a model where the velocity and density boundary is moved some 10 km deeper, to 33.23 km.

Study	Strike (°)	Dip (°)	Rake (°)	Depth (km)	Moment (10^{17} Nm)	Mechanism
This Study (13.23km)	**114**	**28**	**90**	**17**	**1.23**	
This Study (23.23km)	**100**	**48**	**70**	**22**	**0.954**	
This Study (33.23km)	**114**	**32**	**90**	**17**	**0.820**	

Table C.1: Source parameters determined here (bold) for event 013099A using three different velocity models. The depths in brackets denote the position of the major discontinuity in each model.

It can be seen that in the cases where the model boundary is moved by 10 km, that the best fitting solutions are in variance with that obtained in section 3.2. In both cases a shallower (17 km) depth is found to best fit the data, with a pure-thrusting mechanism on a much shallower fault plane (28–32°). The misfit (m) values of these optimum solutions are greater than that calculated with the original Earth model, indicating that they provide a worse

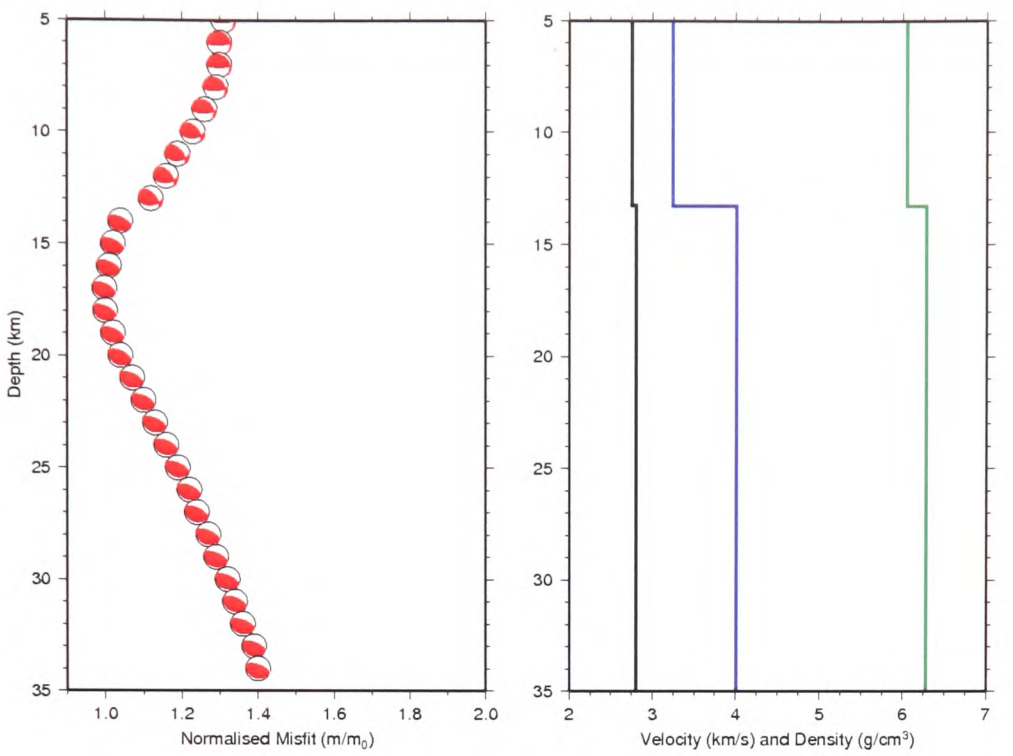


Figure C.1: LHS: normalised misfit plotted against depth for the best mechanism found at each depth for event 013099A. RHS: the Earth model used - in contrast to Figure 3.2, the model discontinuity at 23.23 km is moved to 13.23 km. The best global mechanism is found at a depth of 17 km (the rest of the faulting parameters are listed in Table C.1). The key for this plot is that described in Figure 3.2.

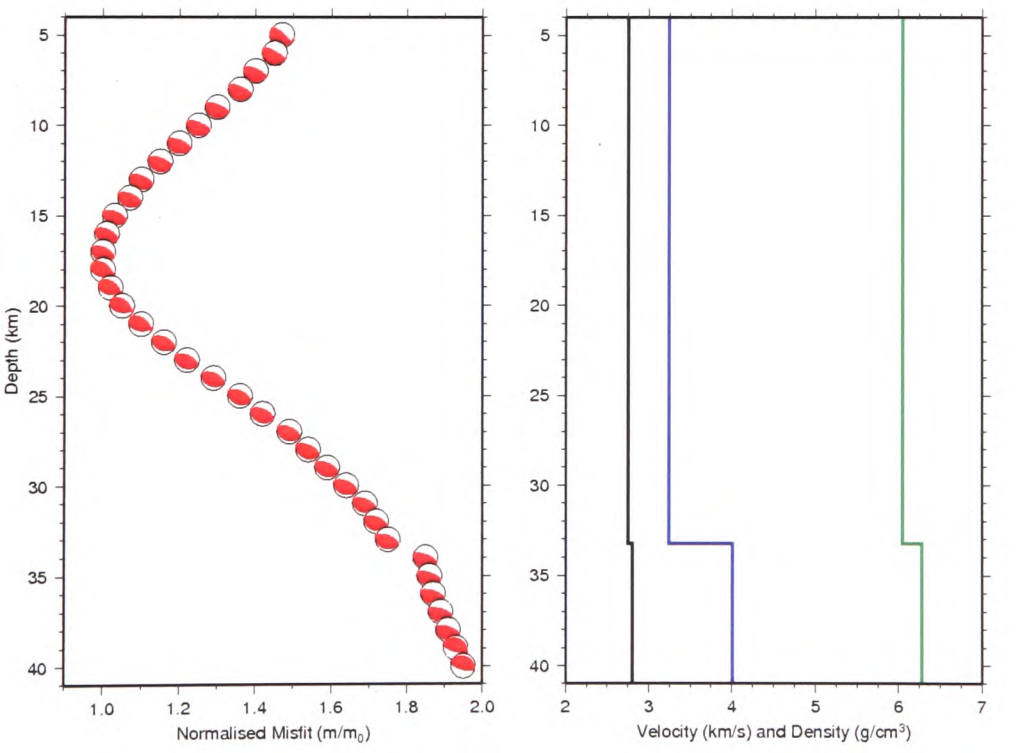


Figure C.2: LHS: normalised misfit plotted against depth for the best mechanism found at each depth for event 013099A. RHS: the Earth model used - in contrast to Figure 3.2, the model discontinuity at 23.23 km is moved to 33.23 km. The best global mechanism is found at a depth of 17 km (the rest of the faulting parameters are listed in Table C.1). The key for this plot is that described in Figure 3.2.

fit to the observed data. In addition these two new solutions are less consistent with other published results for this earthquake (see Table 3.3).

C.2 1999 Chi-Chi, Taiwan, earthquake (102299A)

All D-C source mechanisms in the depth range 5–20 km were grid-searched, an optimum depth of faulting at 11 km was calculated (see Figure C.3) and optimum faulting parameters are listed in Table C.2. The effect of boundaries in the local model are seen in Figure C.3, with a small jump in the misfit-depth profile between 12–13km. This offset in misfit across the discontinuity is not significant as it does not affect the selection of 11 km as the optimum depth. Best-fitting synthetic amplitude spectra and waveforms for this event are plotted in Appendix D.

Study	Strike (°)	Dip (°)	Rake (°)	Depth (km)	Moment (10^{17} Nm)	Mechanism
This Study	**182**	**50**	**64**	**11**	**6.64**	
CMT	178	49	54	15*	6.9	
USGS	26	55	103	7	6.9	
Kao & Chen (2000)	33	57	117	18	5.6 (M_w)	
Kao & Angelier (2001)	171	42	56	18	5.64 (M_w)	
Shin & Teng (2001)				16.6^+	6.40 (M_L)	
Chi & Dreger (2004)	20	75	90	16	17	

Table C.2: Source parameters determined here (bold) and by other studies for event 102299A in Taiwan.

Plots of slices through the solution space for this earthquake are shown in Appendix E and the calculated ranges of the determined source parameters are listed in Table C.3. The 'bullseye' pattern shown in Appendix E indicates a tightly constrained source mechanism and a range of source depths of just 7km. With only a few mechanisms deemed acceptable at 16km, it seems unlikely that the centroid for this aftershock is that deep, or any deeper for that matter. Whilst studies previous to Chi & Dreger (2004) concluded that the earthquake occurred on the east dipping fault plane, these authors contend that recent evidence (unpublished relocations of the aftershocks in this region) is more consistent with a west-dipping fault. In this case their calculated centroid depth shallows from 16 km to about 8km; a depth which, whilst just outside the identified depth range determined here, is nonetheless closer to the 11 km centroid depth determined by this study.

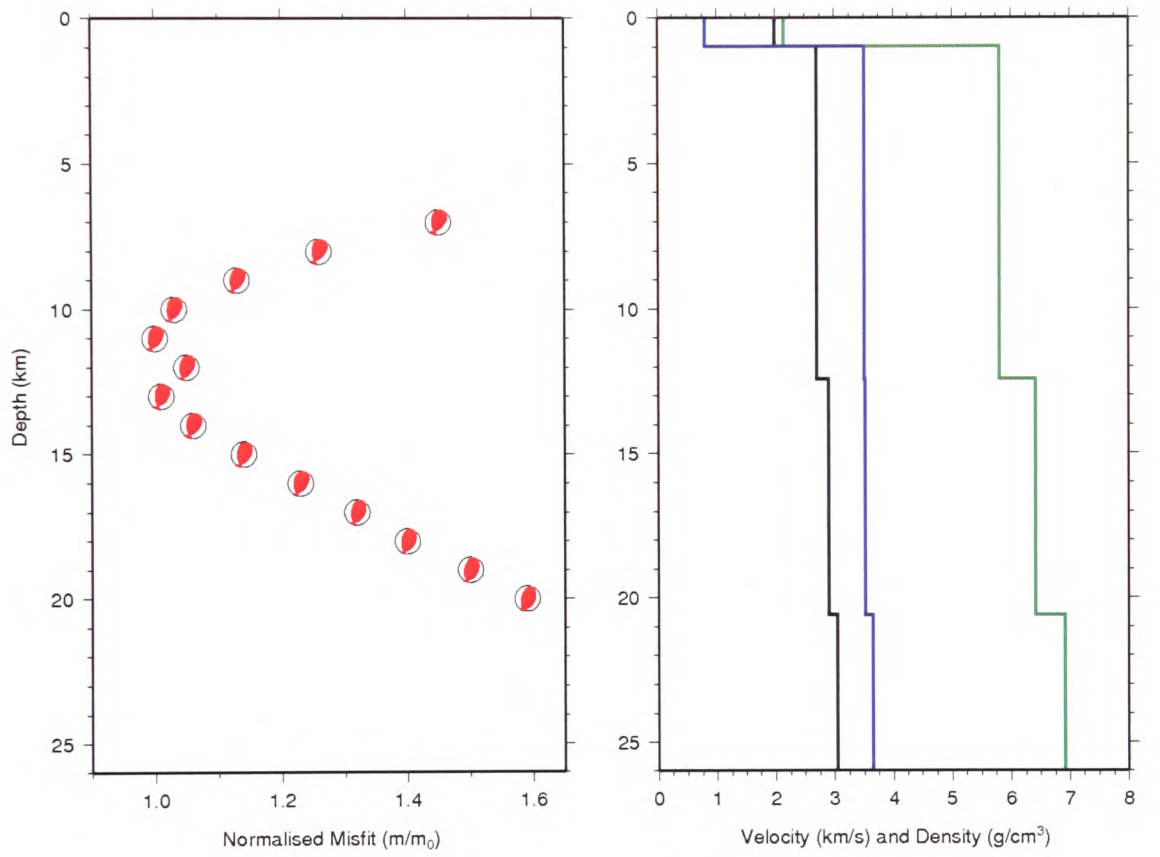


Figure C.3: LHS: normalised misfit plotted against depth for the best mechanism found at each depth. The best global mechanism is found at a depth of 11 km (the rest of the faulting parameters are listed in Table C.2). The effect of discontinuities in the Earth model is evident here, with the local CUB model used (centred on 24°N 120°E) shown on the RHS. The change in seismic velocities and densities at the boundary between 12–13 km are clearly responsible for the jump in the misfit-depth profile between these two depths. The key for this plot is that described in Figure 3.2.

Parameter	Minimum	Optimum	Maximum
Strike (°)	168	182	196
Dip (°)	38	50	64
Rake (°)	42	64	80
Depth (km)	9	11	16
Moment (10^{17} Nm)	5.71	6.64	7.28

Table C.3: The statistically acceptable range of faulting parameters determined by this study for event 102299A. The numbers in the brackets show the range of focal parameters at the optimum depth, 11km.

C.3 2005 Qeshm Island, Iran, earthquake, (112705I)

All D-C source solutions in the depth range 1–15 km were grid-searched and the optimal centroid depth was found to be 8 km (see Figure C.4). The best-fitting set of surface wave amplitude spectra relate to four possible focal mechanisms: the optimum mechanism found (mechanism 1, listed as '**This Study 1**' in Table C.4), the 180° rotation of the optimum mechanism (mechanism 2, listed as '**This Study 2**' in Table C.4), and these two mechanisms with a 180° change in the direction of rake angle (i.e. describing normal-faulting deformation instead of reverse-faulting). Both mechanisms 1 and 2 are listed in Table C.4 because a waveform comparison between the two and the data does not conclusively select one over the other. For the seismograms used in this study, the two values of misfit (m_w) calculated only differed by their 3rd significant figure, so a definitive selection cannot be made based on the data used here.

Study	Strike (°)	Dip (°)	Rake (°)	Depth (km)	Moment (10^{17} Nm)	Mechanism
This Study 1	**254**	**38**	**78**	**8**	**9.41**	
This Study 2	**269**	**53**	**99**	**8**	**9.41**	
CMT	257	39	83	12*	10.3	
USGS	249	45	91	10	7.3	
Nissen et al. (2007):						
• InSAR	267	49	105	3.9–8.1	12.7	
• Body wave (A)	259	50	95	9	7.1	
• Body wave (B)	250	50	91	6*	9.9	

Table C.4: Source parameters determined for event 112705I here (bold) and those published in other studies. The depths listed for the InSAR parameters refer to the top and bottom depths of the fault plane on which uniform slip was modelled.

The similarity in these two sets of synthetic waveforms arises from the two components of the moment tensor that vanish at the free surface. At shallow depths, the contributions of the f_4 and f_5 components diminish such that certain changes to the moment tensor result in no significant differences in the calculated waveforms. Adding 180° to the strike of a given mechanism results in a change in sign of the f_4 and f_5 components with all of the others remaining the same. When the f_4 and f_5 components are small (by at least an order of magnitude compared to the other components) then the mechanism is dominated by the other contributions (e.g. f_1, f_2, f_3 and f_6). As these remain the same for both mechanism 1 and 2, whilst the very small components f_4 and f_5 change sign, the calculated waveforms do not exhibit sufficient variation for a waveform comparison to conclusively select between them.

In such cases, it is necessary to resolve this ambiguity by the addition of extra information

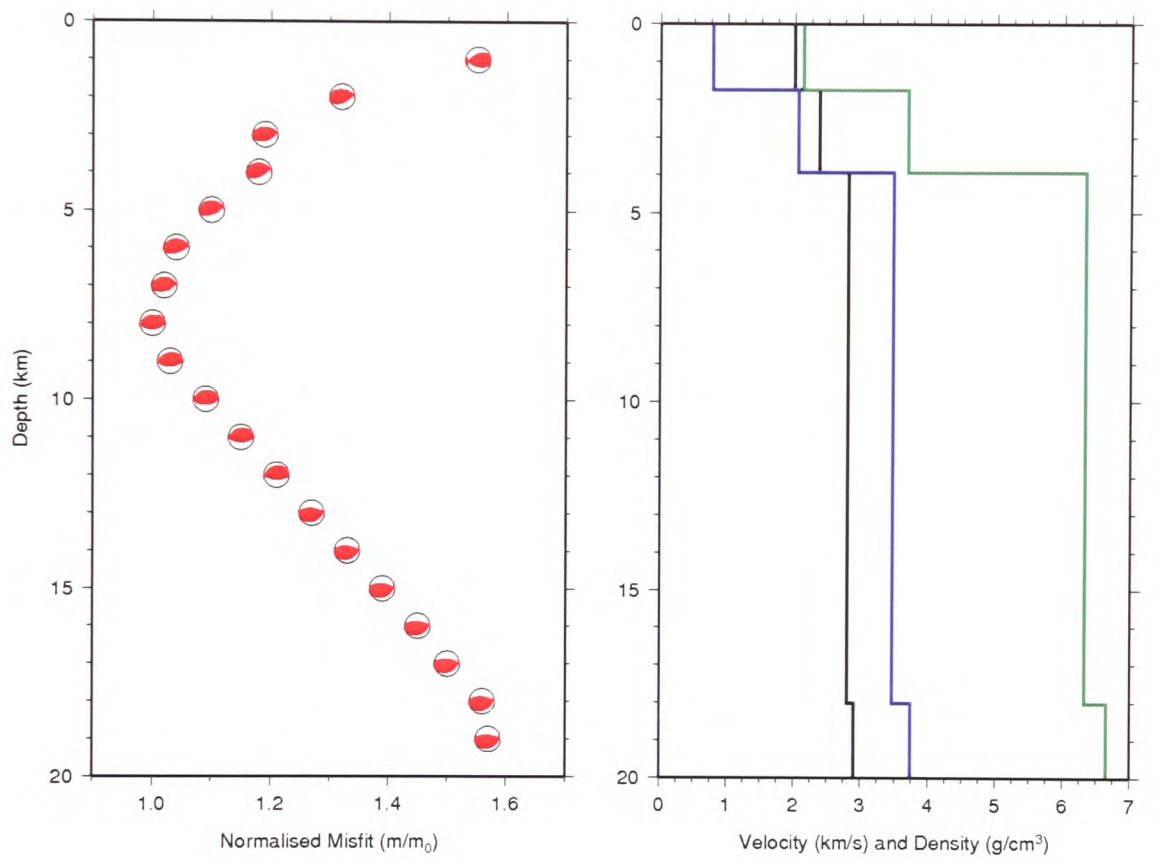


Figure C.4: LHS: misfit-depth profile for the best-matching source mechanisms at each depth for the Qeshm Island earthquake (event 112705I). RHS: local Earth model used, key as described in Figure 3.2.

such as independent geological observations (e.g. surface ruptures or fault orientations), other seismological studies (i.e. those using InSAR or short-period body waves) or relocated aftershocks. Here preference is for mechanism 2 based on the higher angle of dip and the rake angle being more consistent with the work of Nissen et al. (2007). A rotation of 180° of the CMT solution would produce a beachball more in keeping with the others listed in Table C.4 and gives a focal mechanism of ($\phi_s = 266°$, $\delta = 51°$, $\lambda = 91°$).

Debates about the selection of mechanism aside, the optimum centroid depth (8 km) is consistent with the other studies. Although slightly shallower than both the fixed CMT, USGS and long-period body wave (A) study, 8 km the depth lies at the deepest part of the slip model used in the InSar model of Nissen et al. (2007): This model allowed uniform slip of 0.88m across a fault 8.4 km in length, between depths of 3.9–8.1 km, putting the centroid depth found here at its deepest bound. Further InSAR studies modelling distributed slip may show concentrated regions of rupture on the fault. Should this be the case, then the results of this study would suggest they would be found at the deeper bounds of the fault.

Best-fitting Rayleigh and Love wave amplitude spectra are presented in Appendix D; in addition a contour plot of the solution space's 95% confidence bounds for this earthquake is shown in Appendix E. A summary of the range of statistically acceptable source parameters is listed in Table C.5. The shallow centroid depth is confined to lie between 3–12 km, and whilst the strike is fairly well bounded, the dip angle has a total minimum-maximum range of 70° and the rake angle varies between 50–128°. The reason for these large ranges is that both nodal planes lie sufficiently close in rake-dip space ($\delta = 38°$, $\lambda = 78°$ and $\delta = 53°$, $\lambda = 99°$) that the regions of acceptable solutions combine and it is impossible to identify the outer bounds of one, without interference from the other. As such, the only option is to describe this 'hybrid' space, with the provision that these errors bounds are almost certainly over-estimated.

Parameter	Minimum	Optimum	Maximum
Strike (°)	236	269	290
Dip (°)	10	53	80
Rake (°)	50	99	128
Depth (km)	3	8	12
Moment (10^{17} Nm)	6.61	9.41	19.7

Table C.5: Bounding values of the 95% confidence region of source parameters determined by this study for event 112705I.

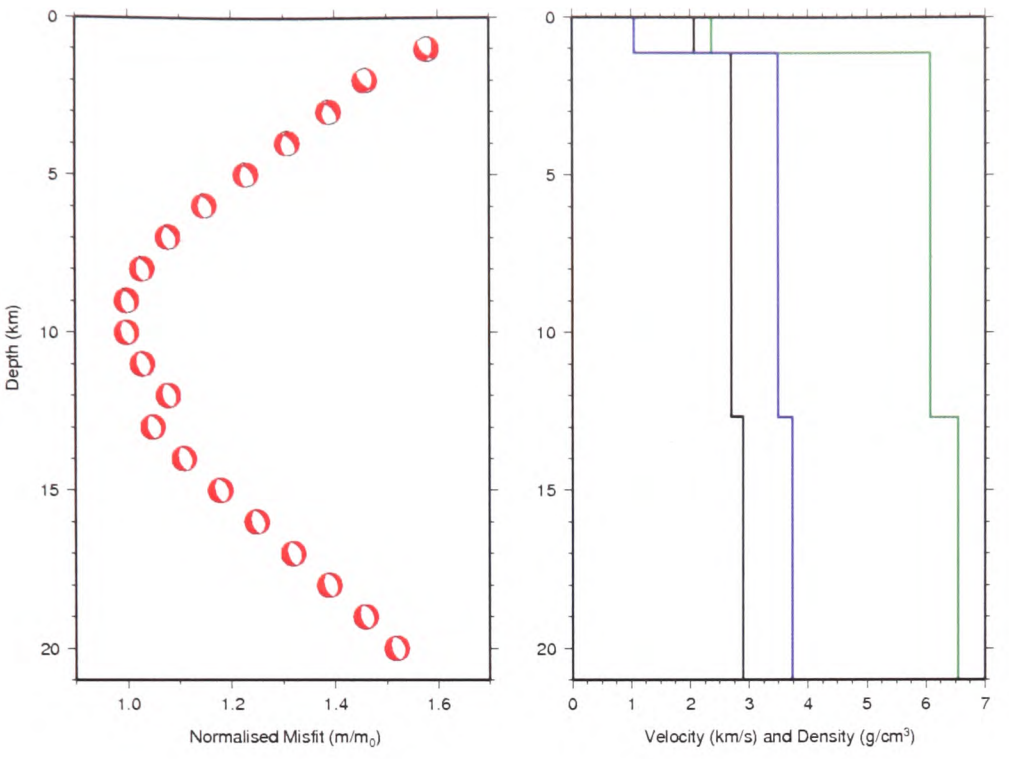


Figure C.5: LHS: misfit-depth profile for the best-matching source mechanisms at each depth for the Gulf of Aqaba earthquake (event 080393G). RHS: local Earth model used, key as described in Figure 3.2.

C.4 1993 Gulf of Aqaba, Egypt, earthquake (080393G)

All D-C source mechanisms were grid-searched between 1–20 km depths and Figure C.5 shows the misfit-depth profile for the best solutions calculated here at each depth. The source parameters for the optimum solutions at 9 km depth, are listed in Table C.6 and describe deformation similar to the Foster & Jackson (1998) study, namely normal-faulting with a small sinistral component on a north-striking fault plane.

Study	Strike (°)	Dip (°)	Rake (°)	Depth (km)	Moment (10^{18} Nm)	Mechanism
This Study	**357**	**50**	**-70**	**9**	**1.26**	
CMT	357	60	-69	15*	1.8	
USGS	7	62	-49	17	1.3	
Pinar & Turkelli (1997)	328	57	-113	10	1.4	
Foster & Jackson (1998)	354	57	-69	8	1.97	

Table C.6: Source parameters for the 1993 Gulf of Aqaba earthquake (event 080393G).

The synthetic amplitude spectra and waveforms are presented in Appendix D. A contour plot of solutions falling within 95% confidence bounds can be found in Appendix E, a summary

Parameter	Minimum	Optimum	Maximum
Strike (°)	312	357	14
Dip (°)	24	50	70
Rake (°)	-140	-70	-64
Depth (km)	5	9	16
Moment (10^{18} Nm)	0.973	1.26	1.60

Table C.7: Bounding values of the 95% confidence region of source parameters determined by this study for event 080393G.

of that Figure is given in Table C.7. As is the case with event 112705I, the close proximity of the focal plane and the 180° strike-rotated auxiliary plane in rake-dip space mean that the range of acceptable source parameters are over-estimated here.

The calculation of a 9 km centroid depth is consistent with the other studies. It lies between the two results using teleseismic body waves, and the 15 km fixed CMT depth suggests a centroid shallower than 15 km. The USGS focal depth is somewhat deeper than the other studies, but has a seismic moment similar to that estimated here and that reported by Pinar & Turkelli (1997).

C.5 1999 Lake Baikal, Siberia, earthquake (022599H)

D-C source parameter solution space was searched between 1–15 km depths and the best-fitting mechanisms at each centroid depth are shown in Figure C.6. An optimum centroid depth of 8 km is found here, along with a focal mechanism describing almost pure-normal faulting on a northeast-southwest trending fault plane (see Table C.8). Analysis of the synthetic waveforms show that the 180° rotation in strike of this mechanism fits the data less well so that mechanism is rejected as a likely source. The auxiliary plane for this source ($\phi_s = 238°$, $\delta = 51°$, $\lambda = -100°$) is chosen as the rupture plane, given that it represents a northwest-dipping fault plane, consistent with the aftershock study of Radziminovitch et al. (2005).

Study	Strike (°)	Dip (°)	Rake (°)	Depth (km)	Moment (10^{17} Nm)	Mechanism
This Study	**74**	**40**	**-78**	**8**	**5.06**	
CMT	66	36	-86	21*	8.9	
USGS	50	26	-120	4	8.5	
Peacock & Douglas (2007):						
• 1st event	252	72	-90	15	1.26	
• 2nd event	252	72	-90	15	7.24	
CSEM	172	55	-31	10	11	
OBN	50	20	-104	10	11	
CEME	18	26	-134	33	10	
IEC	60	20	-101	12	-	

Table C.8: Source parameters determined for event 022599H here (bold) and in other studies. The sources CSEM (European-Mediterranean Seismological Centre) and OBN (Russian National Seismological Center, Obninsk, Russia) were obtained through the USGS Source parameter SEARCH WEBSITE; whilst CEME (Central Experimental Methodical Expedition, Obninsk, Russia) and IEC (Institute of the Earth's Crust, Irkutsk, Russia) were taken from Radziminovitch et al. (2005).

Best-fitting Rayleigh and Love wave amplitude spectra are shown in Appendix D; with contour plots taken through the set of solutions lying within 95% confidence bounds plotted in Appendix E. A summary of the bounds of this solution space is shown in Table C.9. All source parameters determined here are tightly constrained with errors bounds of 38° on strike and dip, and rake of 56°; with the centroid depth confined to lie between 5–10 km. The small range of shallow depths also constrains the range of scalar seismic moment between 0.429–0.562 $\times$ 10^{18} Nm.

There is little doubt that the 1999 Lake Baikal earthquake was a complex seismic event, with the range of published focal mechanisms and, especially, depths testament to this. In contrast to those source studies that have focused on modelling local depth phases with little

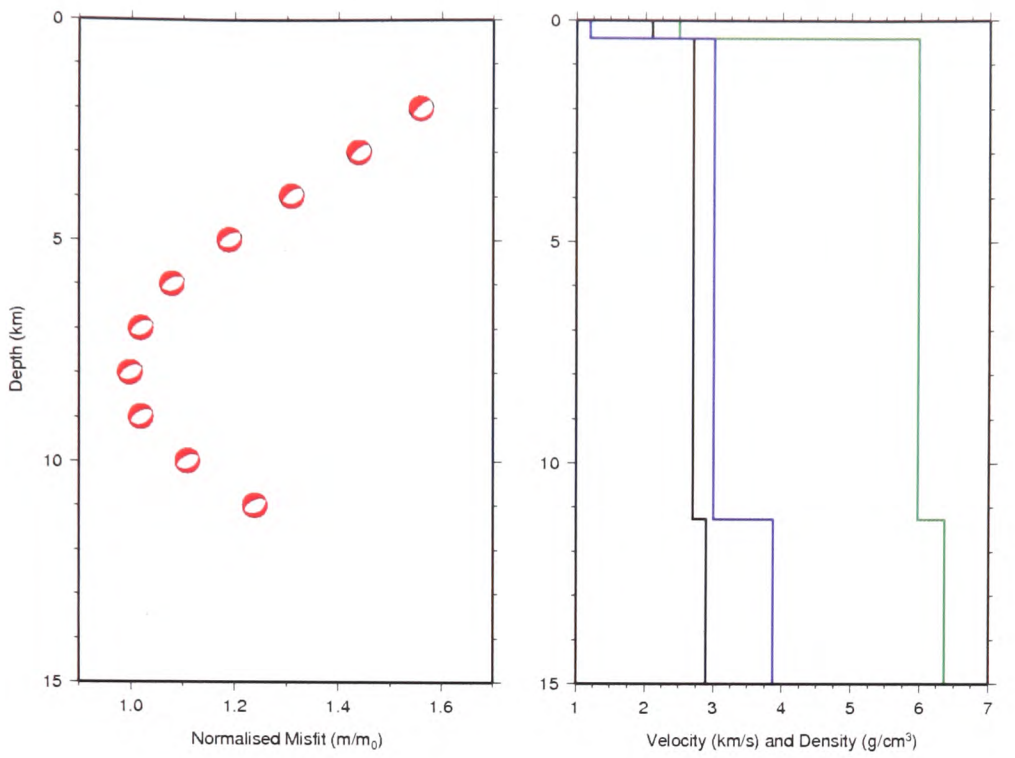


Figure C.6: LHS: misfit-depth profile for the best-matching source mechanisms at each depth for the 1999 Lake Baikal, Siberia, earthquake (event 022599H). RHS: local Earth model used, key as described in Figure 3.2.

Parameter	Minimum	Optimum	Maximum
Strike (°)	48	74	86
Dip (°)	26	40	64
Rake (°)	244	282	300
Depth (km)	5	8	10
Moment (10^{18} Nm)	0.429	0.506	0.562

Table C.9: Bounding values of the 95% confidence region of source parameters determined here for event 022599H in Lake Baikal.

success, a well constrained set of source parameters are determined here. The complexity of the waveforms prevented Emmerson et al. (2006) from performing a long-period body wave modelling study; yet this earthquake proved to be one of the best-constrained earthquakes studied here, with a calculated source mechanism consistent with the overall tectonics of the Lake Baikal Rift Zone.

C.6 1999 Athens, Greece, earthquake (090799C)

Synthetic surface wave amplitude spectra were generated for all D-C solutions between 1–15 km depths and compared with recorded data to identify the best-fitting set of faulting parameters. The results are shown in Figure C.7 and listed in Table C.10. The optimum centroid depth was calculated to be at 9 km, with statistically acceptable solutions between 3–12 km. The focal mechanism determined here describes normal faulting with a small sinistral component on a fault striking 118° and dipping 46° to the southwest. Whilst both the fault strike and rake are in close agreement with those parameters determined in previous studies, with the exception of the CMT and Papadopoulos et al. (2000) results, the angle of fault dip is somewhat shallower than is described in other published solutions.

Study	Strike (°)	Dip (°)	Rake (°)	Depth (km)	Moment (10^{17} Nm)	Mechanism
This Study	**118**	**46**	**-78**	**9**	**8.14**	
CMT	116	39	-81	15*	11.0	
USGS	123	55	-84	9.0	7.8	
Caltech	122	60	-80	-	-	
Papadopoulos et al. (2000)	113	39	-90	16.8^{+}	11.2	
Tselentis & Zahradnik (2000)	117	52		10		
Louvari & Kiratzi (2001)	115	57	-80	11.0	7.56	
Papadimitriou et al. (2002)	105	55	-80	8.0	10.1	
Sargeant et al. (2002)	115	60	-80	10.0	6.01	
Hutchings et al. (2007)				12		

Table C.10: Source parameters calculated for the 1999 Athens earthquake (event 090799C) here (bold) and in other studies. The Caltech solution is quoted from Pavlides et al. (2002).

A 180° rotation in strike of the auxiliary plane ($\phi_s = 101°$, $\delta = 45°$, $\lambda = -102°$) can also be considered a likely source here. However this is rejected after a waveform comparison with the recorded data. In addition, the strike of this plane is less consistent with the results of other studies, as is the rake angle, describing a small component of dextral strike-slip motion on the fault, as opposed to the small sinistral component determined here originally and elsewhere.

A further source parameter search was performed for a fixed dip angle of 60°. The optimum centroid depth was still found to be 9 km, with values of $\phi_s = 114°$ and $\lambda = -84°$ calculated. Both amplitude spectra (m) and waveform (m_w) misfits were worse for this steeper dipping plane, indicating that an increase in fault dip of 15° didn't lead to an improved the fit to the surface wave data. The calculation, too, of a 9 km centroid depth would suggests that this parameter is well constrained and is not significantly affected by alterations to the dip angle.

Rayleigh and Love wave synthetic amplitude spectra and seismograms generated here for the

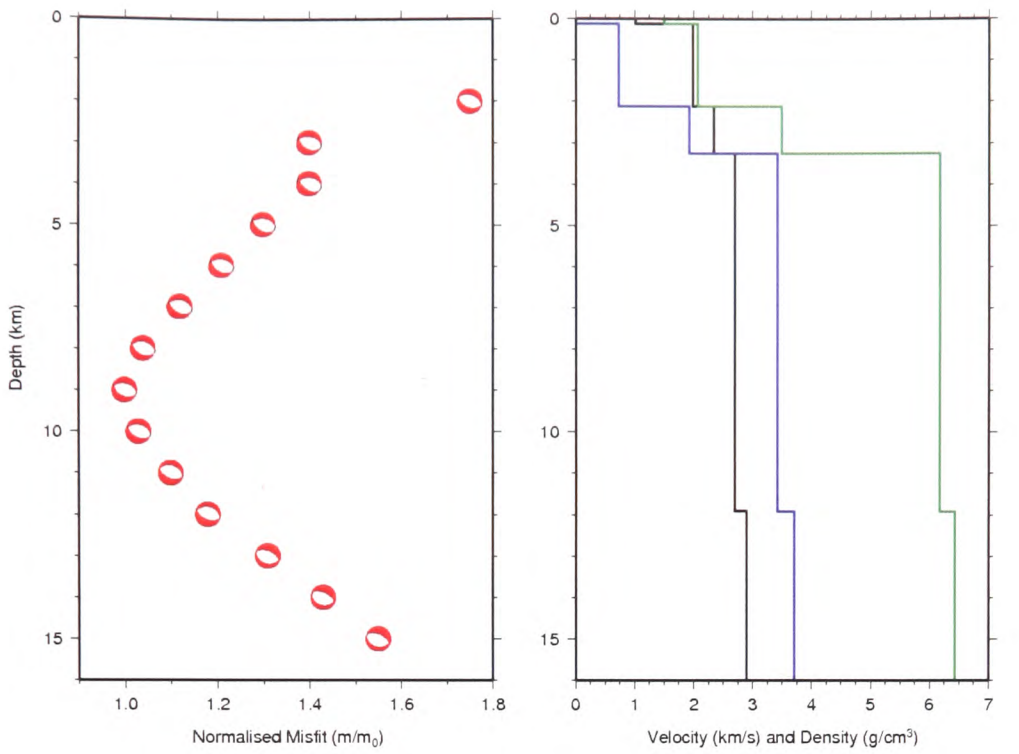


Figure C.7: LHS: misfit-depth profile for the best-matching source mechanisms at each depth for the 1999 Athens, Greece, earthquake (event 090799C). RHS: local Earth model used, key as described in Figure 3.2.

Parameter	Minimum	Optimum	Maximum	Difference
Strike (°)	86	118	136	
Dip (°)	24	46	66	
Rake (°)	-128	-78	-54	
Depth (km)	6	9	12	
Moment (10^{17} Nm)	6.48	8.14	9.89	

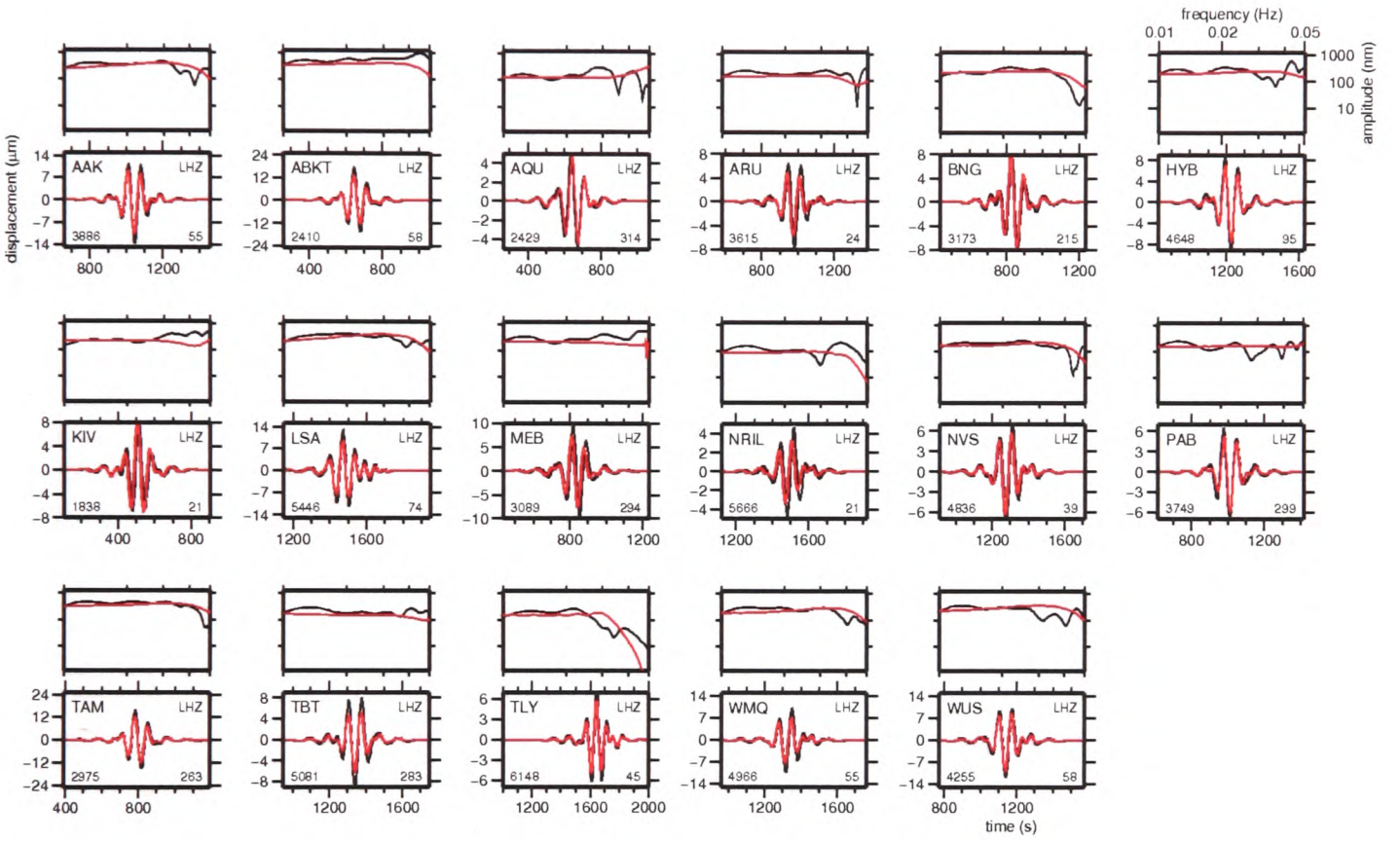
Table C.11: Bounding values of the 95% confidence region of source parameters determined in this study for event 090799C.

optimum mechanism can be found in Appendix D. Table C.11 summarises the contour plot in Appendix E which displays the range of source solutions falling within 95% confidence bounds imposed here. Because of the proximity and overlap in solution space of symmetrical sources, the ranges of acceptable strikes and rakes are over-estimated somewhat for this event. Whilst these parameters have maximum bounds of 136° and -54° respectively, their minimum bounds should be considered to be greater than the 86° and -128° figures presented. The fault dip is constrained to lie between 24° and 66°, in agreement, especially at the upper end, with estimates of dip determined in other studies. Acceptable source solutions are found at depths as shallow as 6 km, the optimum depth is calculated at 9 km whilst a maximum centroid depth of 12 km is determined. These bounds, particularly the maximum are in strong agreement with the solutions listed in Table C.10, as all centroid depths (with the exception of the fixed CMT depth) lie between 8–12 km.

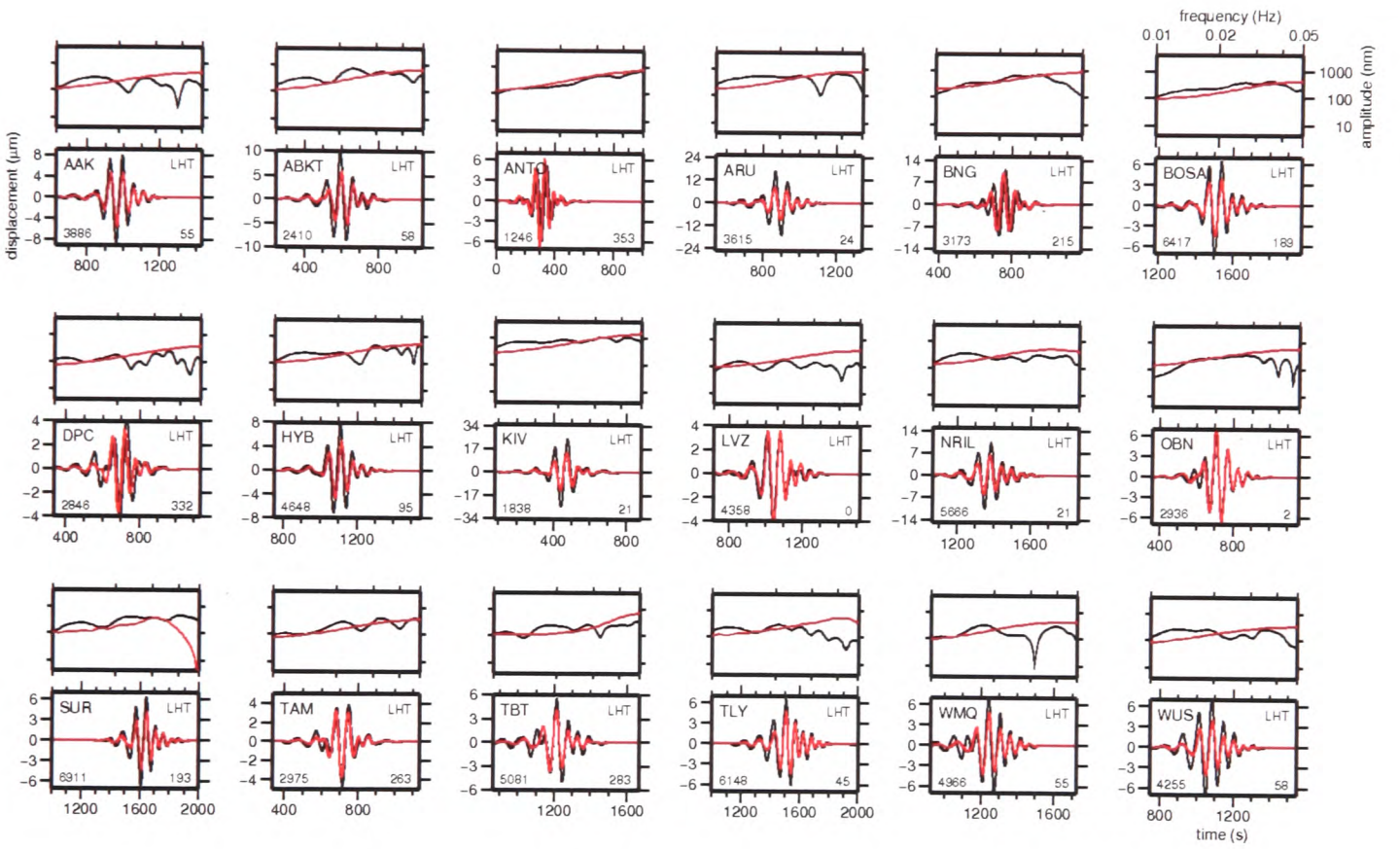
Appendix D

Spectra and Waveforms for Earthquakes in Chapter 3

APPENDIX D. SPECTRA AND WAVEFORMS FOR EARTHQUAKES IN CHAPTER 3

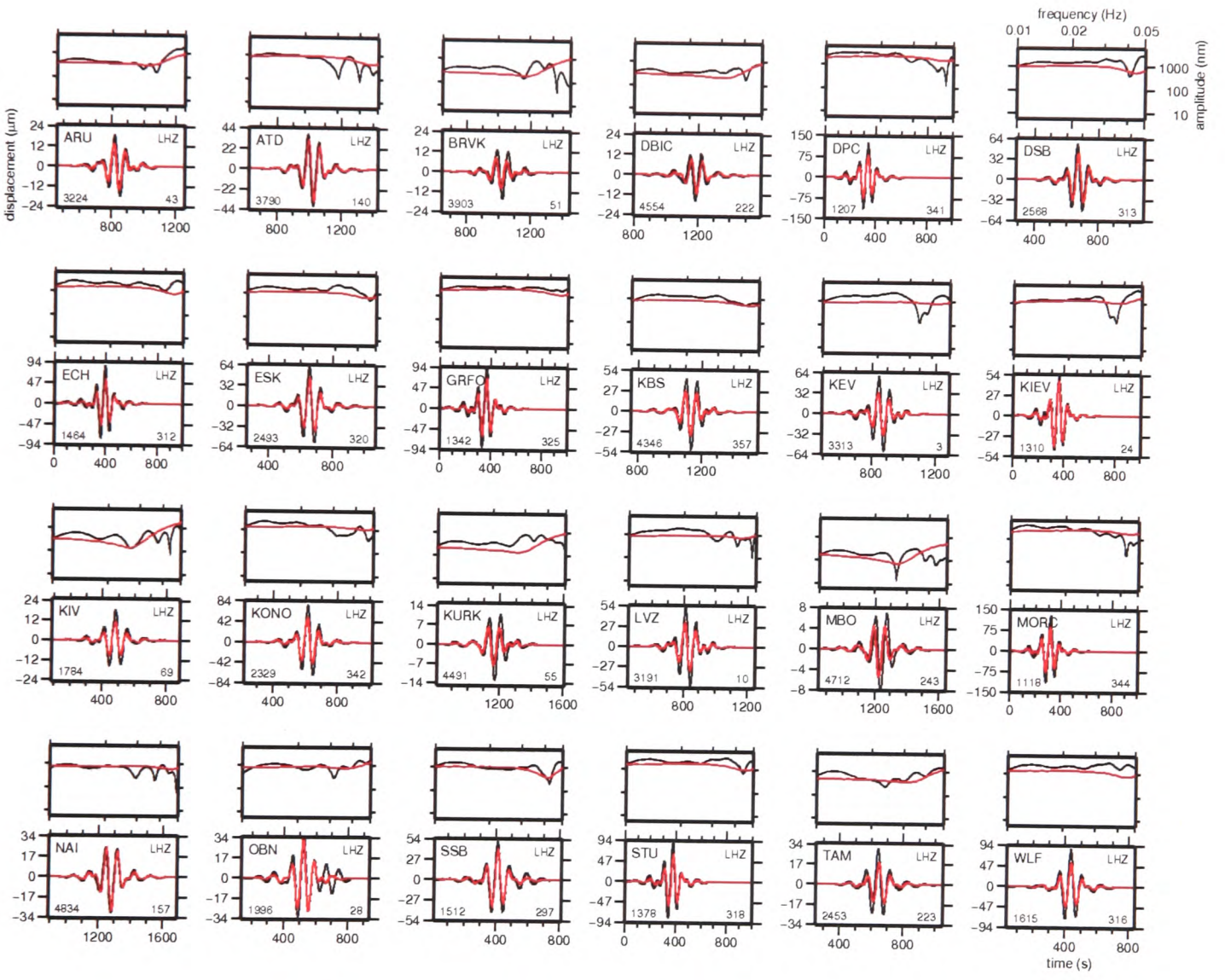


Synthetic (red) and data (black) amplitude spectra (top) and bandpass-filtered seismograms (bottom) for each station where the LHZ channel recording was used in the determination of source parameters for event 080393G.

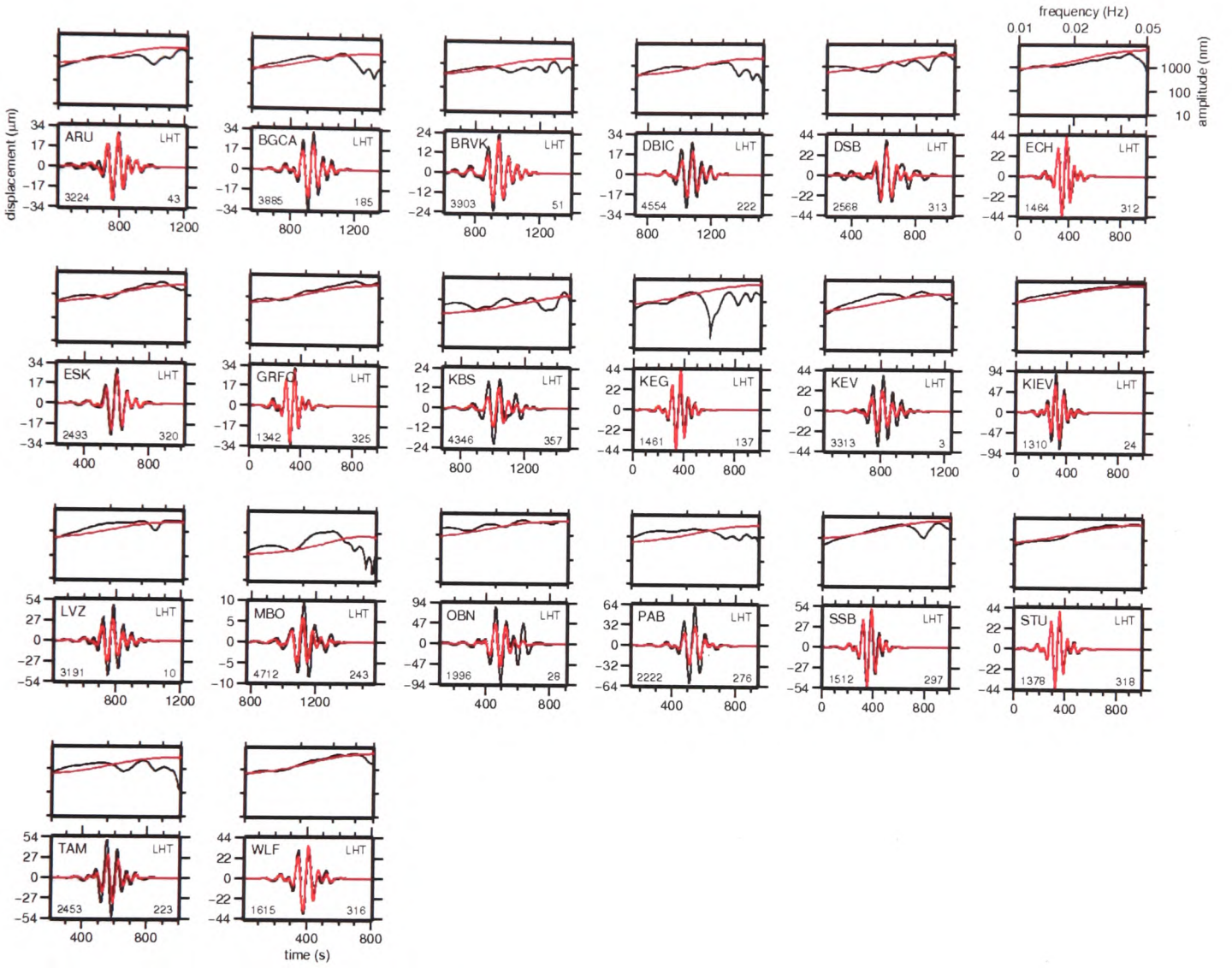


As previous figure but for LHT channel recordings.

APPENDIX D. SPECTRA AND WAVEFORMS FOR EARTHQUAKES IN CHAPTER 3

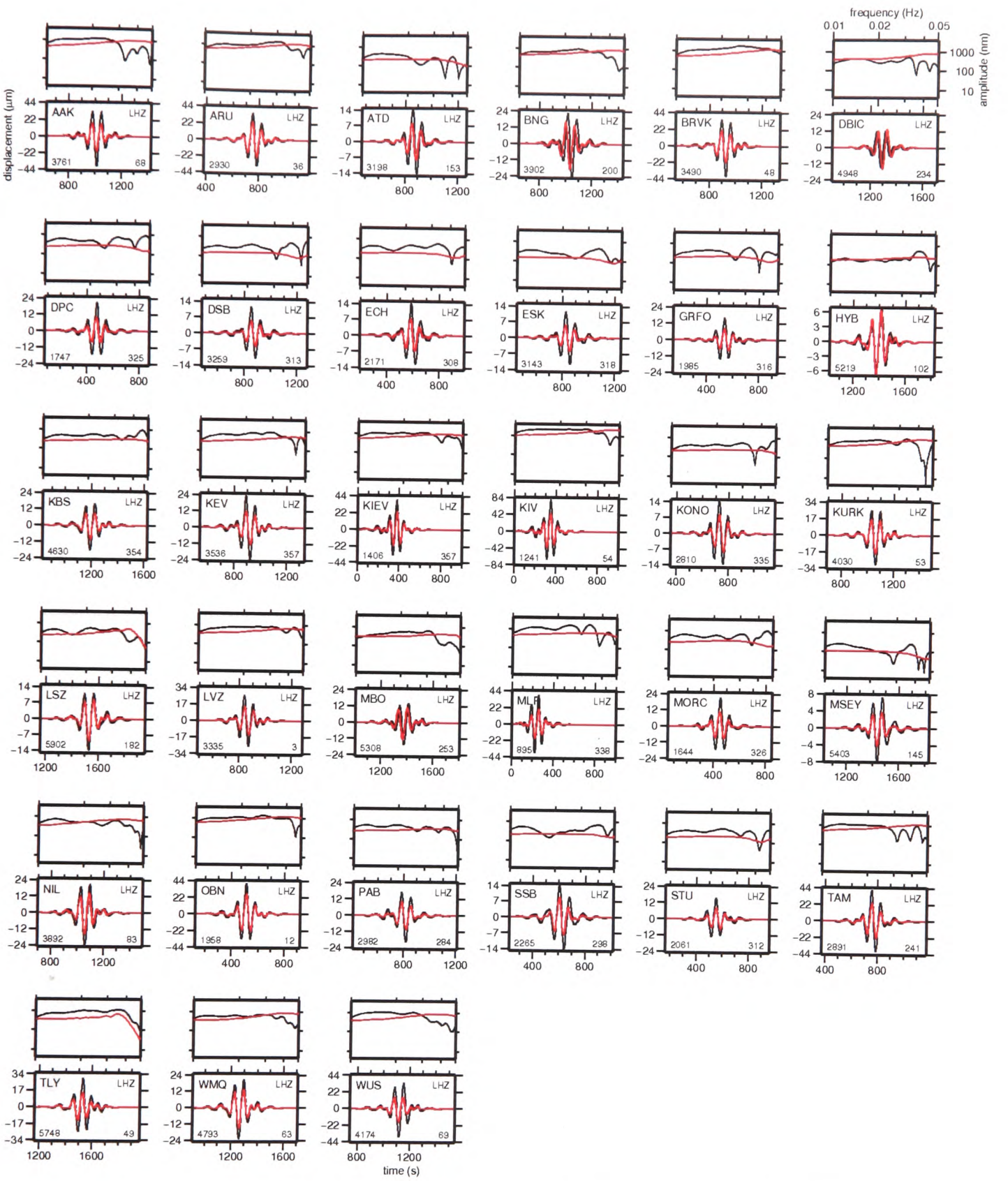


Synthetic (red) and data (black) amplitude spectra (top) and bandpass-filtered seismograms (bottom) for each station where the LHZ channel recording was used in the determination of source parameters for event 051395B.

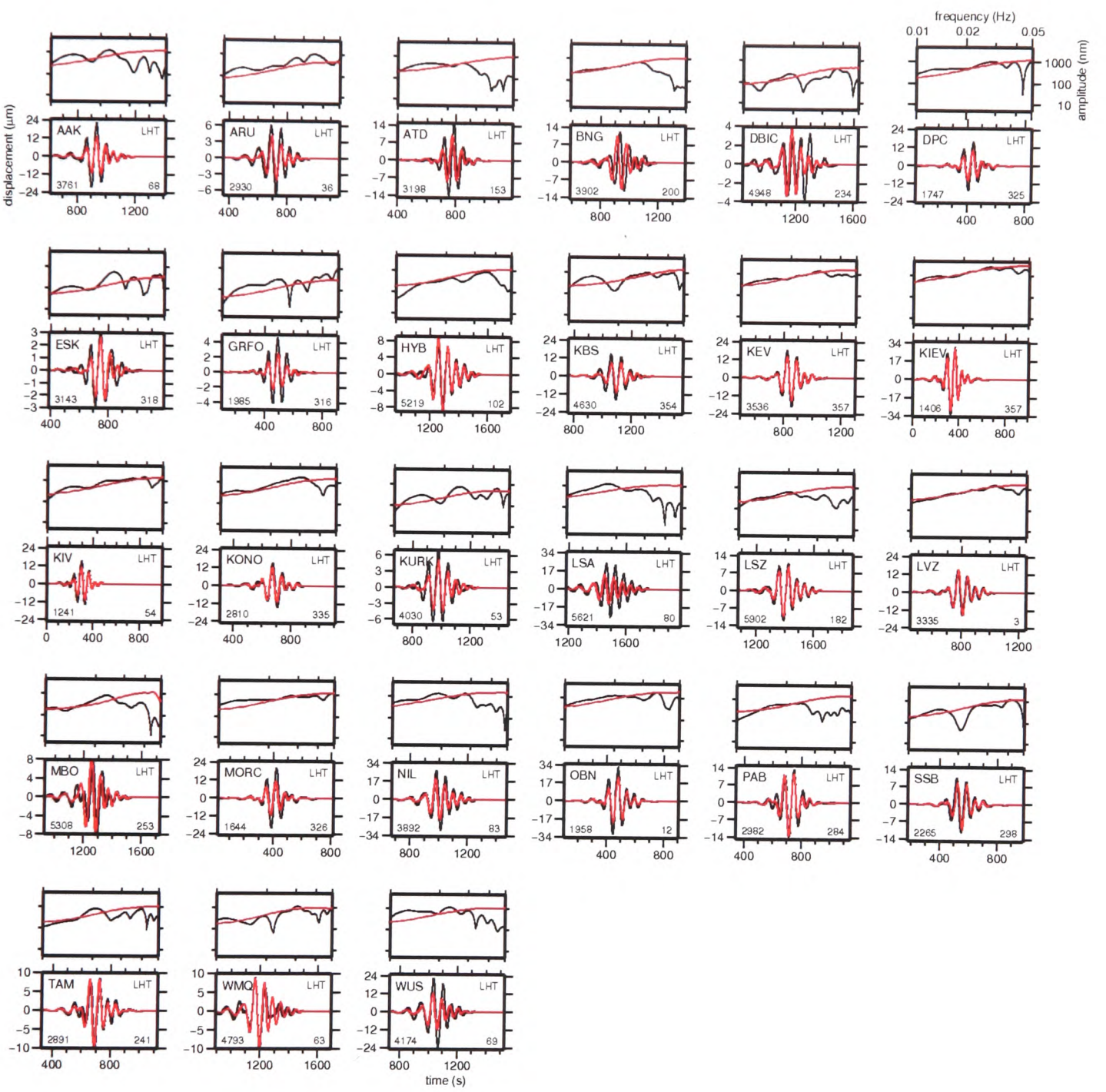


As previous figure but for LHT channel recordings.

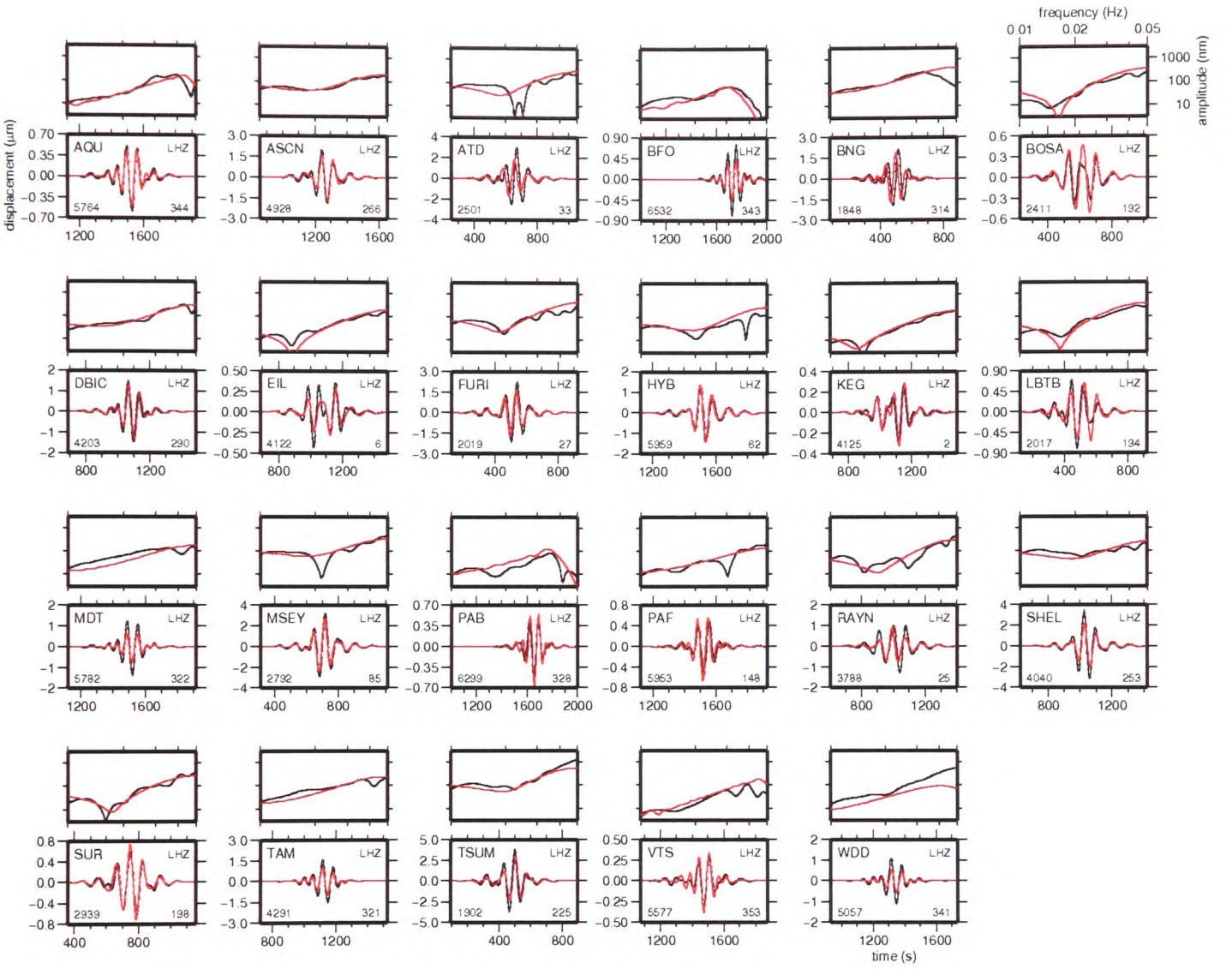
APPENDIX D. SPECTRA AND WAVEFORMS FOR EARTHQUAKES IN CHAPTER 3



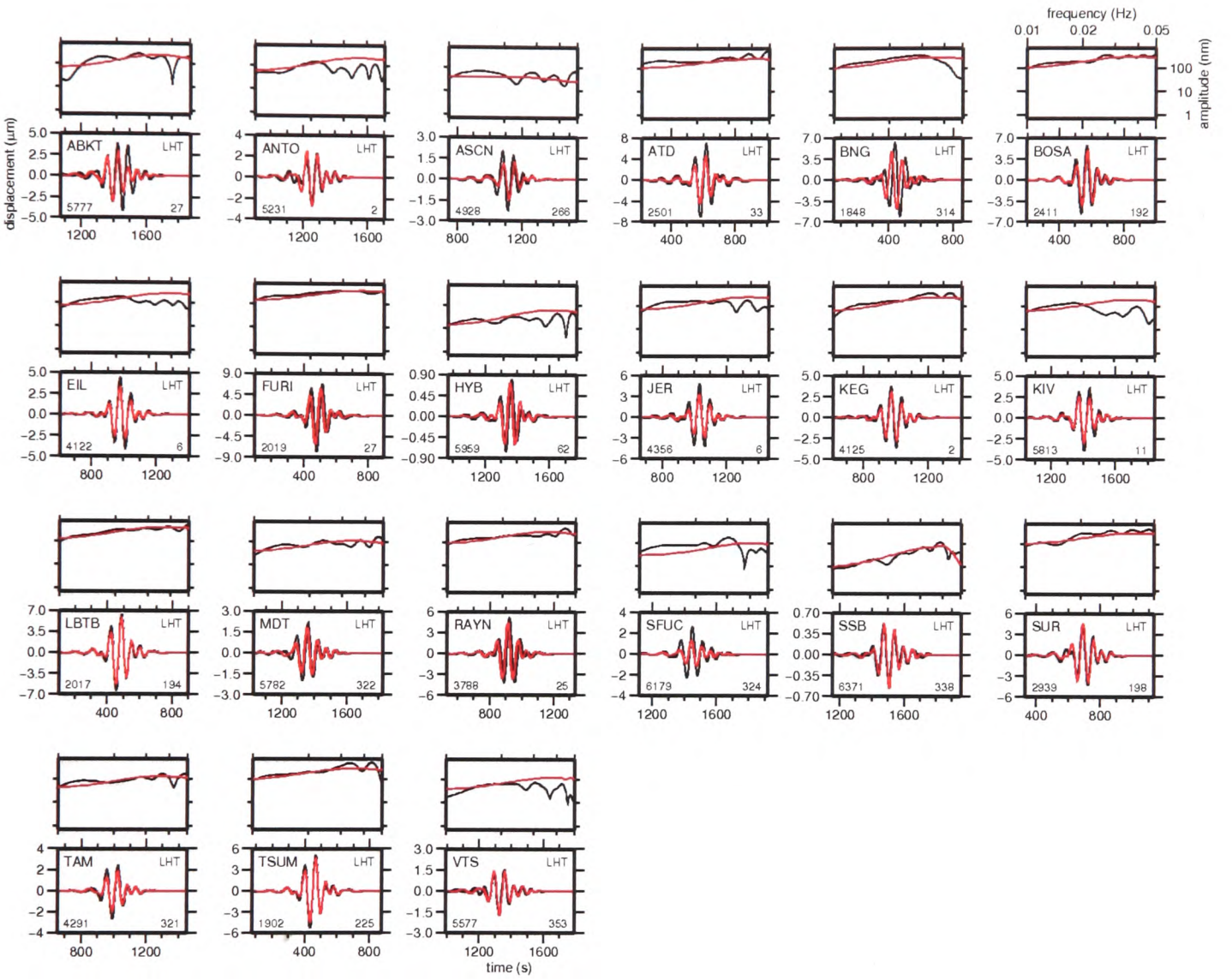
Synthetic (red) and data (black) amplitude spectra (top) and bandpass-filtered seismograms (bottom) for each station where the LHZ channel recording was used in the determination of source parameters for event 100195B.



As previous figure but for LHT channel recordings.

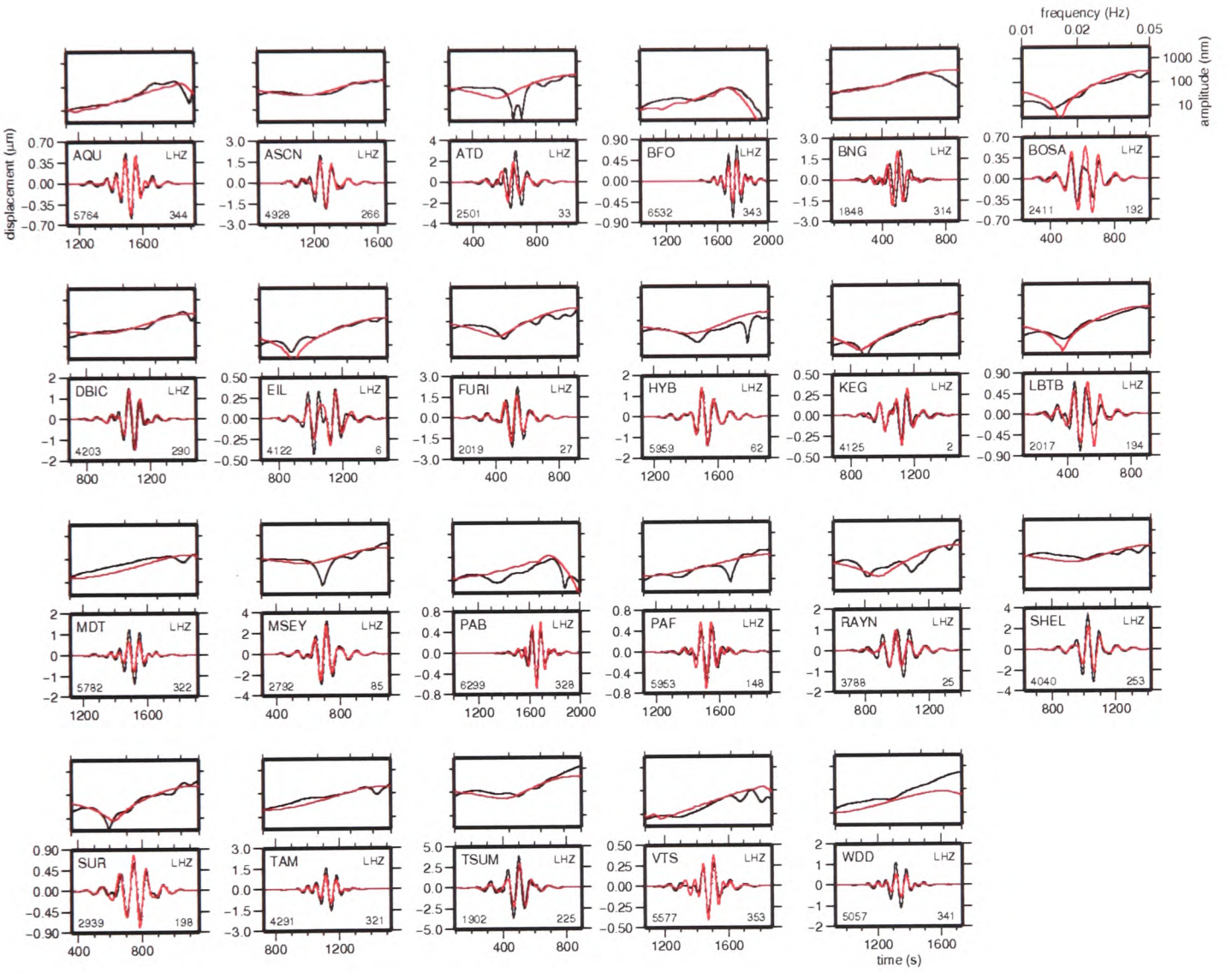


Synthetic (red) and data (black) amplitude spectra (top) and bandpass-filtered seismograms (bottom) for each station where the LHZ channel recording was used in the determination of source parameters for event 092197C. Synthetics are plotted for a source depth of 33 km.

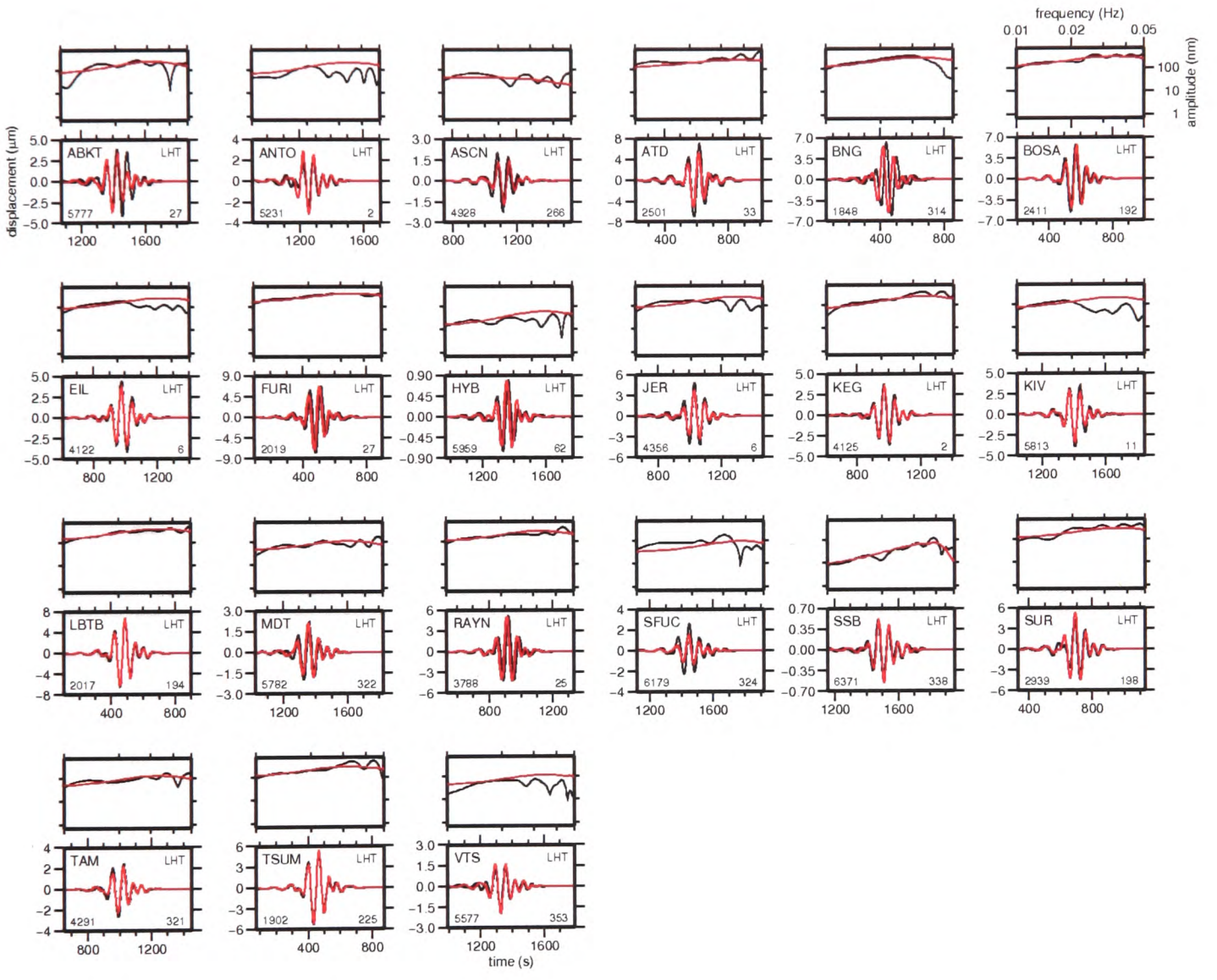


As previous figure but for LHT channel recordings.

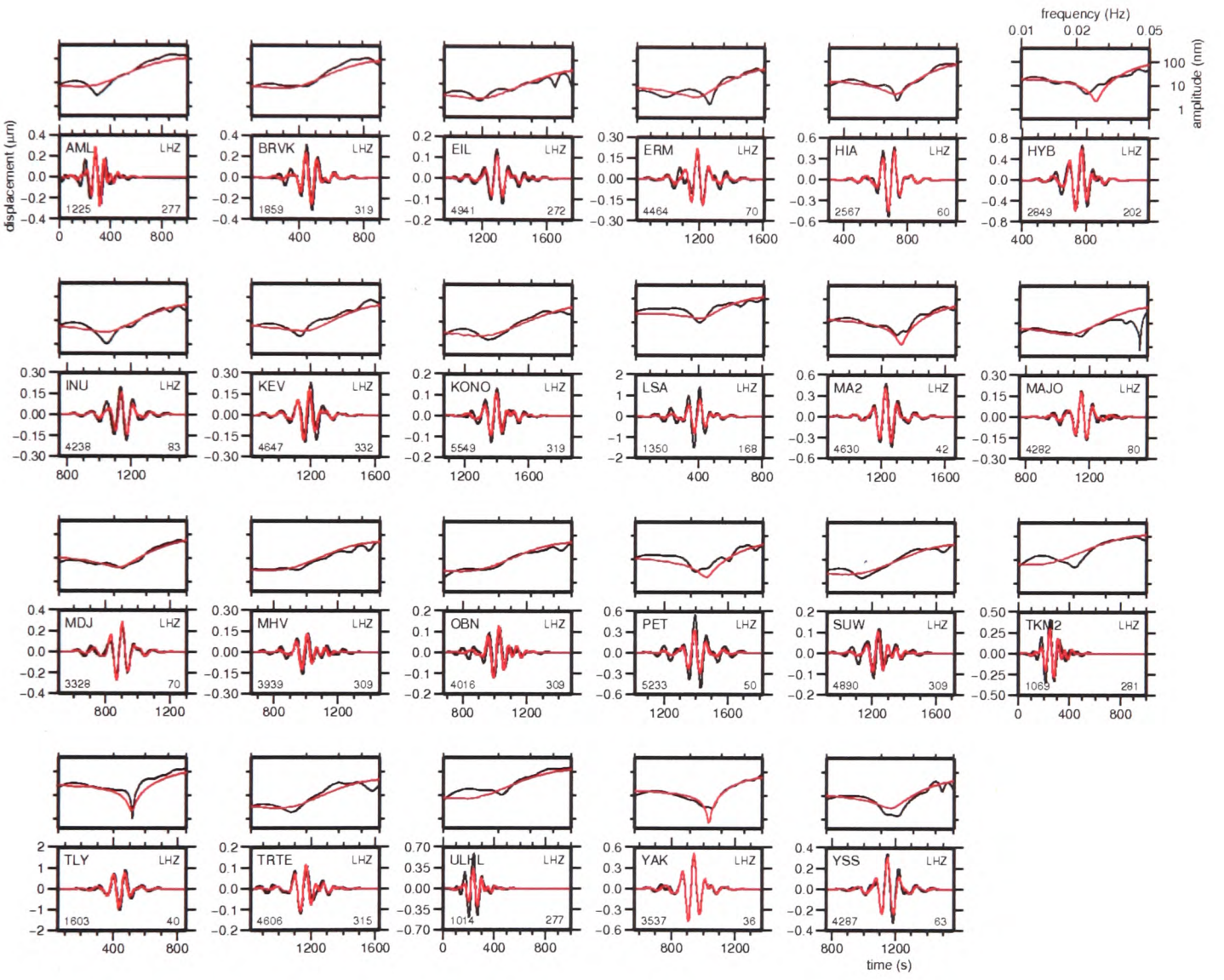
APPENDIX D. SPECTRA AND WAVEFORMS FOR EARTHQUAKES IN CHAPTER 3



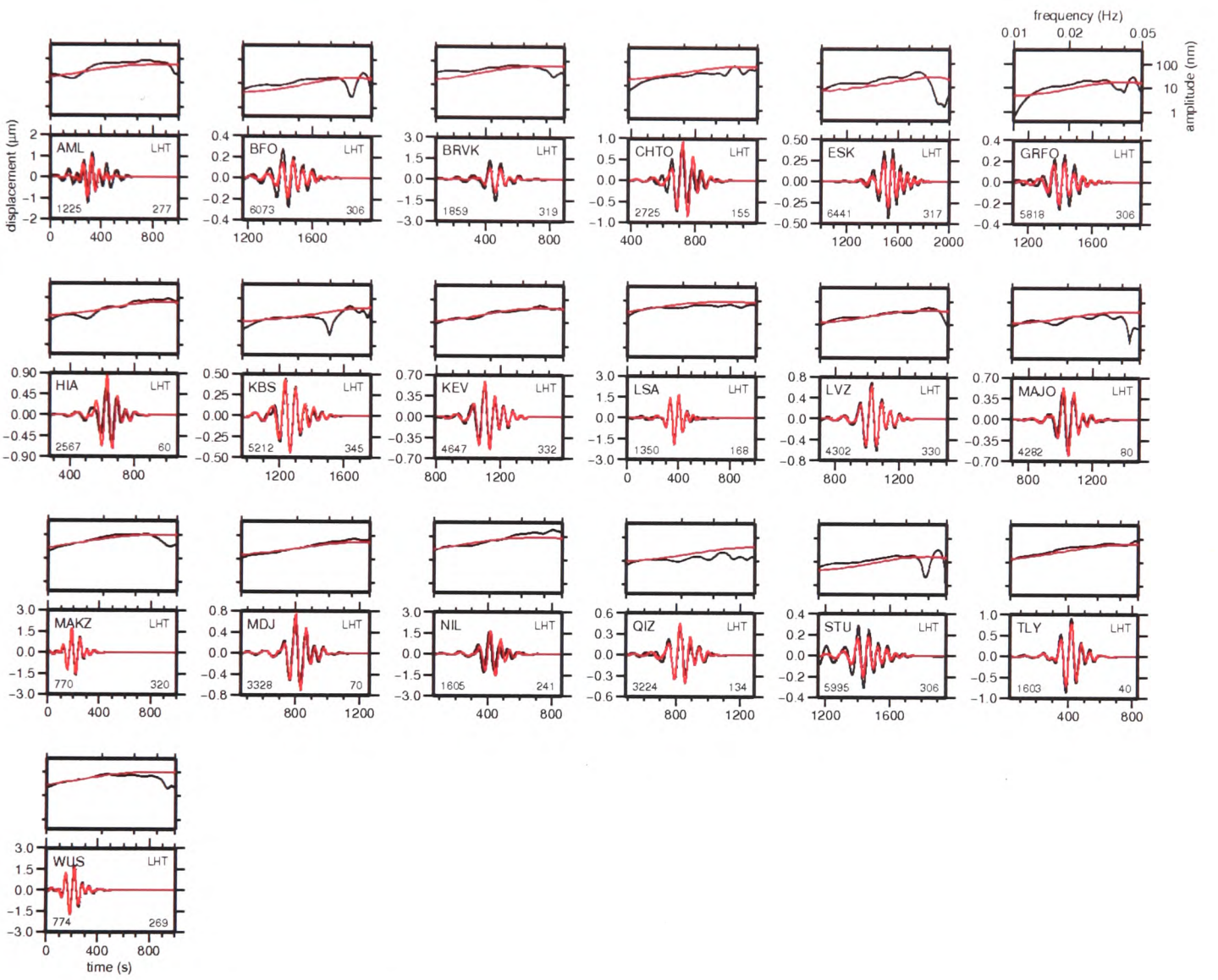
Synthetic (red) and data (black) amplitude spectra (top) and bandpass-filtered seismograms (bottom) for each station where the LHZ channel recording was used in the determination of source parameters for event 092197C. Synthetics are plotted for a source depth of 39 km.



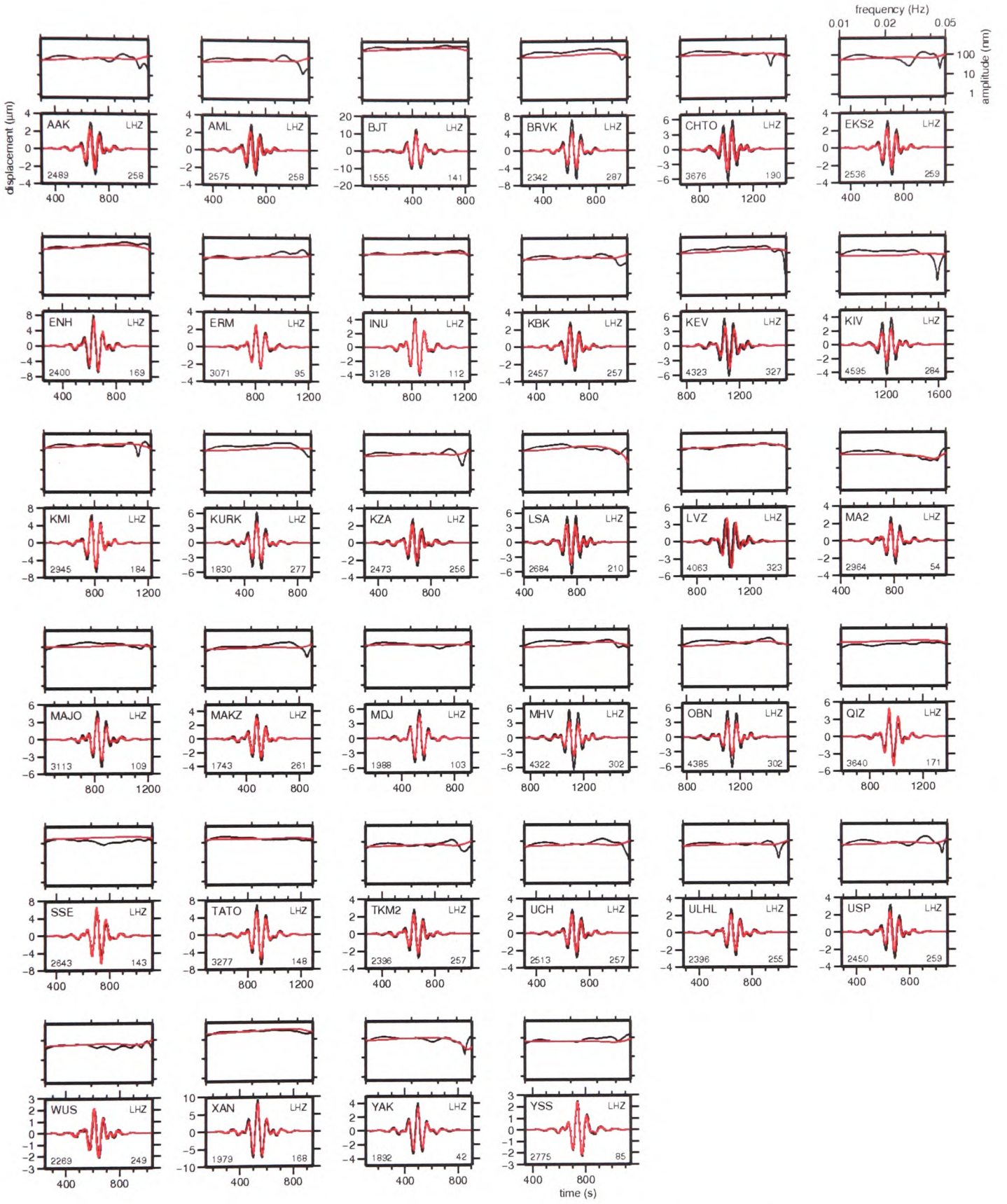
As previous figure but for LHT channel recordings.



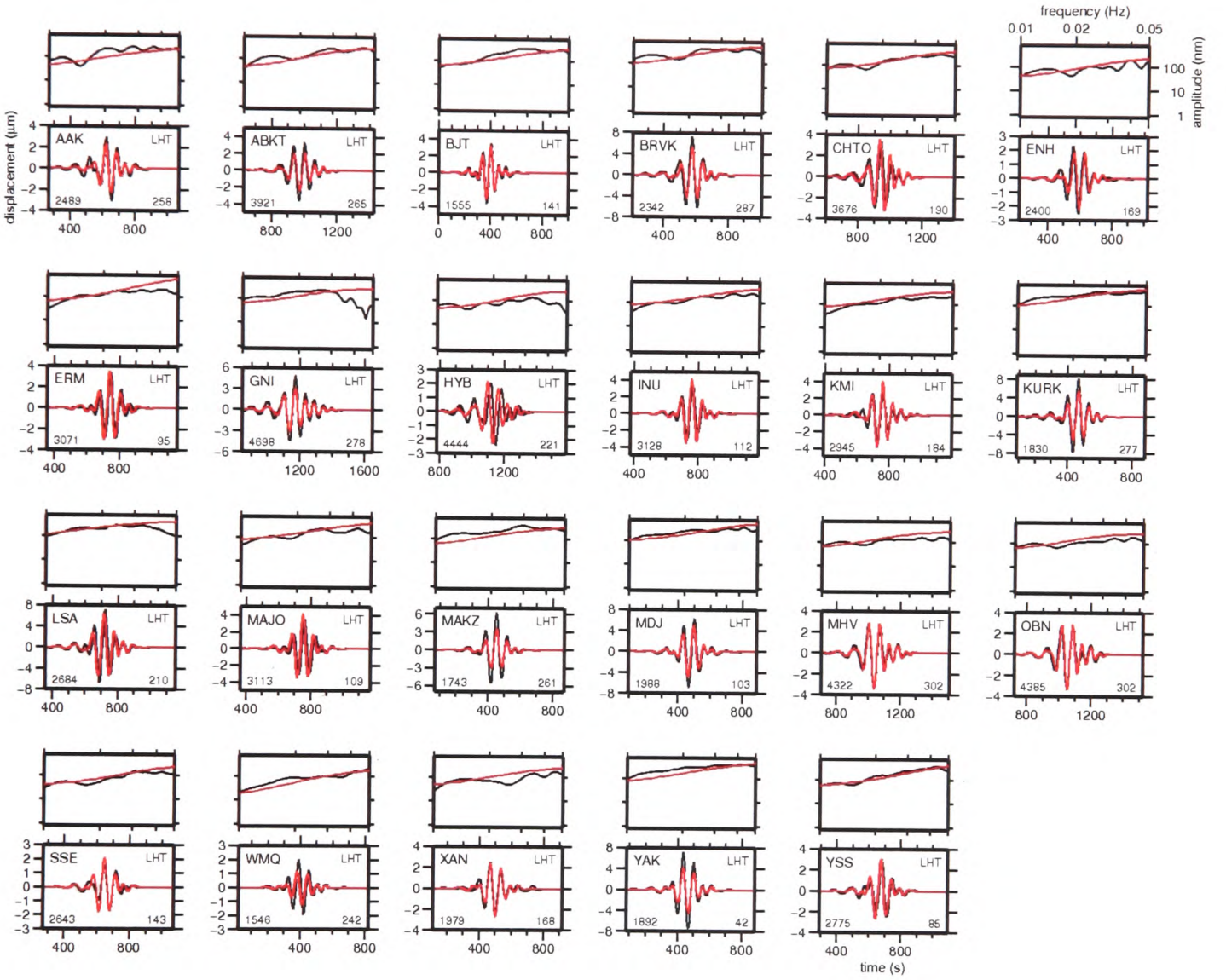
Synthetic (red) and data (black) amplitude spectra (top) and bandpass-filtered seismograms (bottom) for each station where the LHZ channel recording was used in the determination of source parameters for event 013099A.



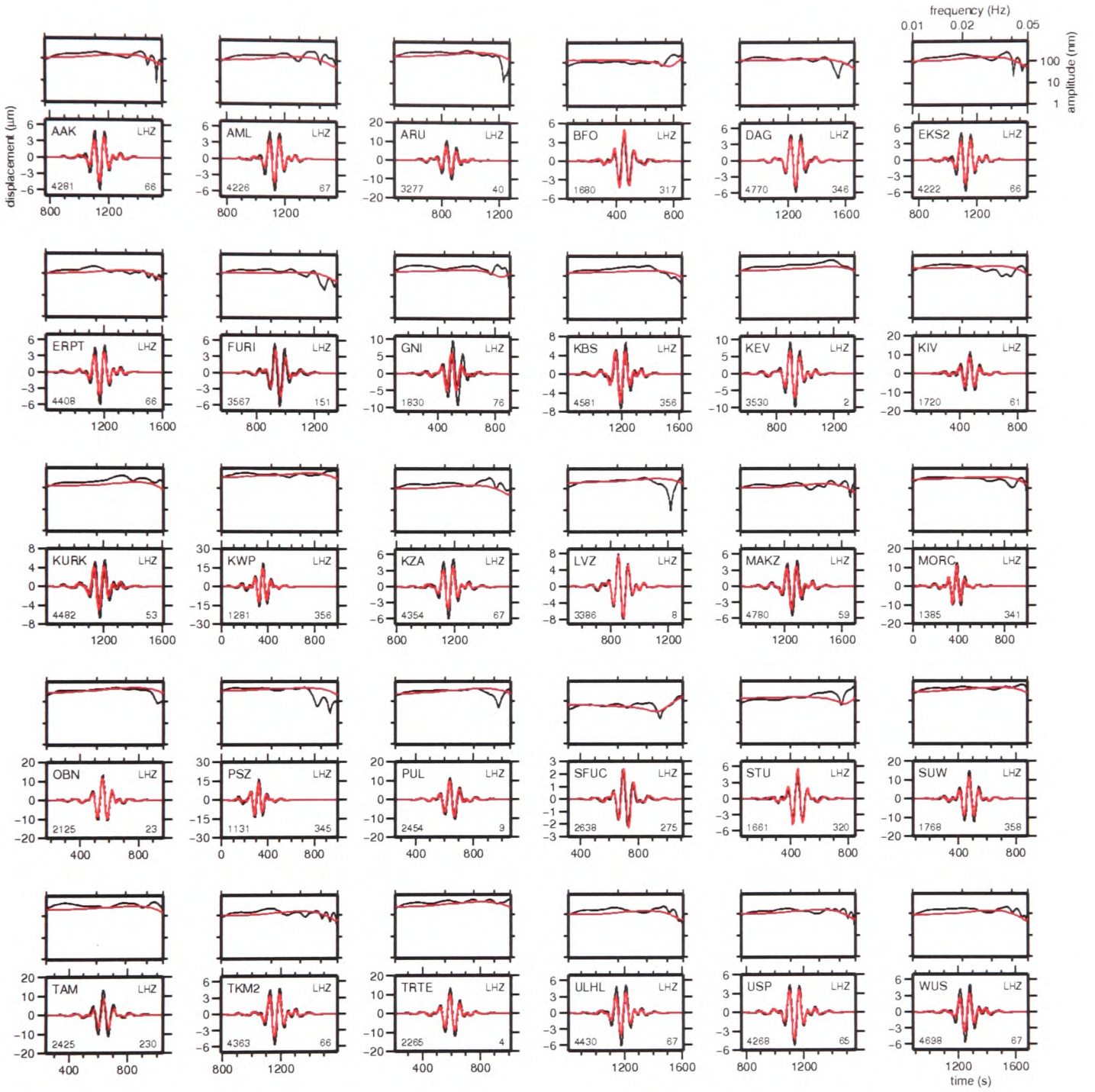
As previous figure but for LHT channel recordings.



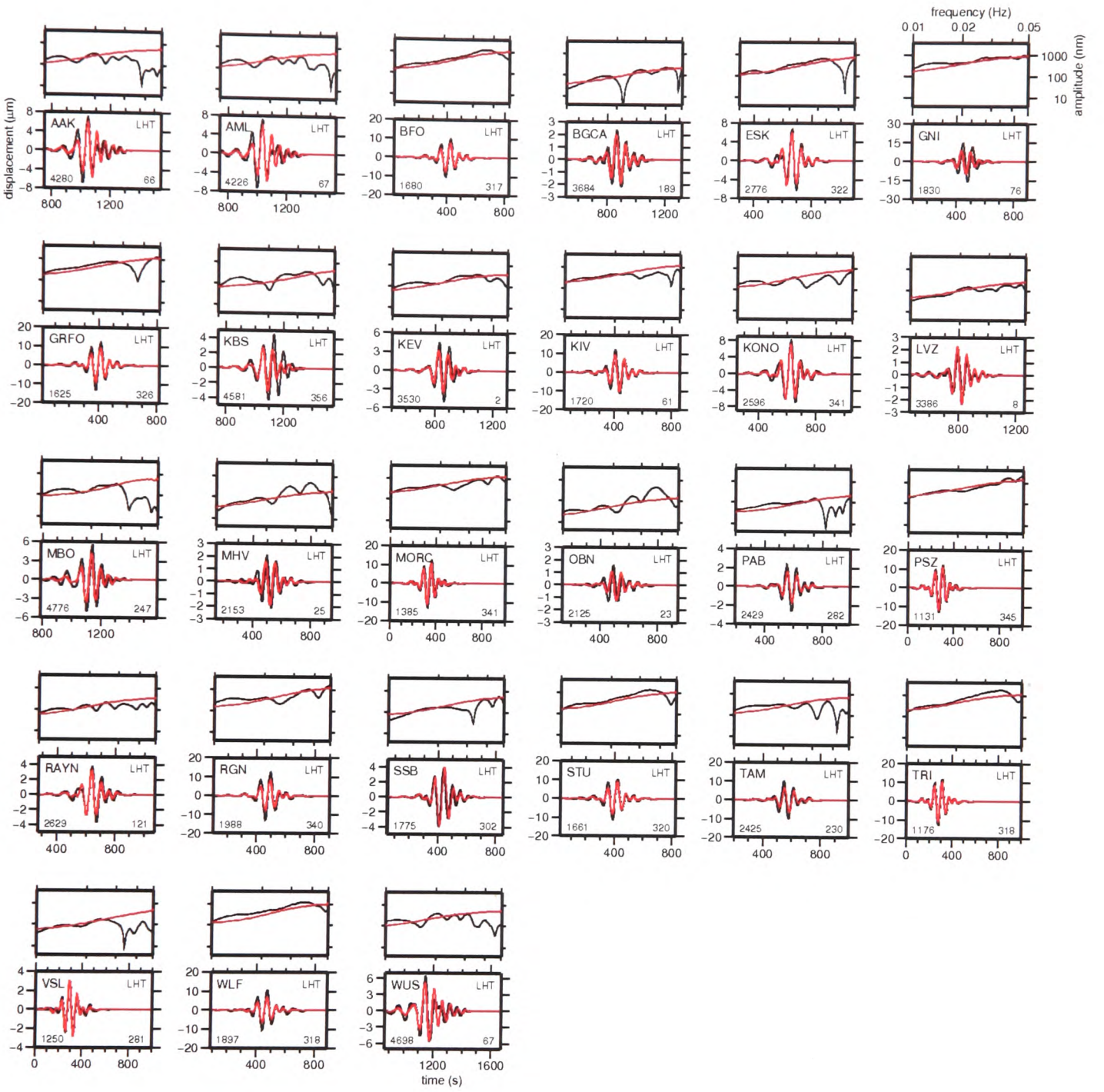
Synthetic (red) and data (black) amplitude spectra (top) and bandpass-filtered seismograms (bottom) for each station where the LHZ channel recording was used in the determination of source parameters for event 022599H.



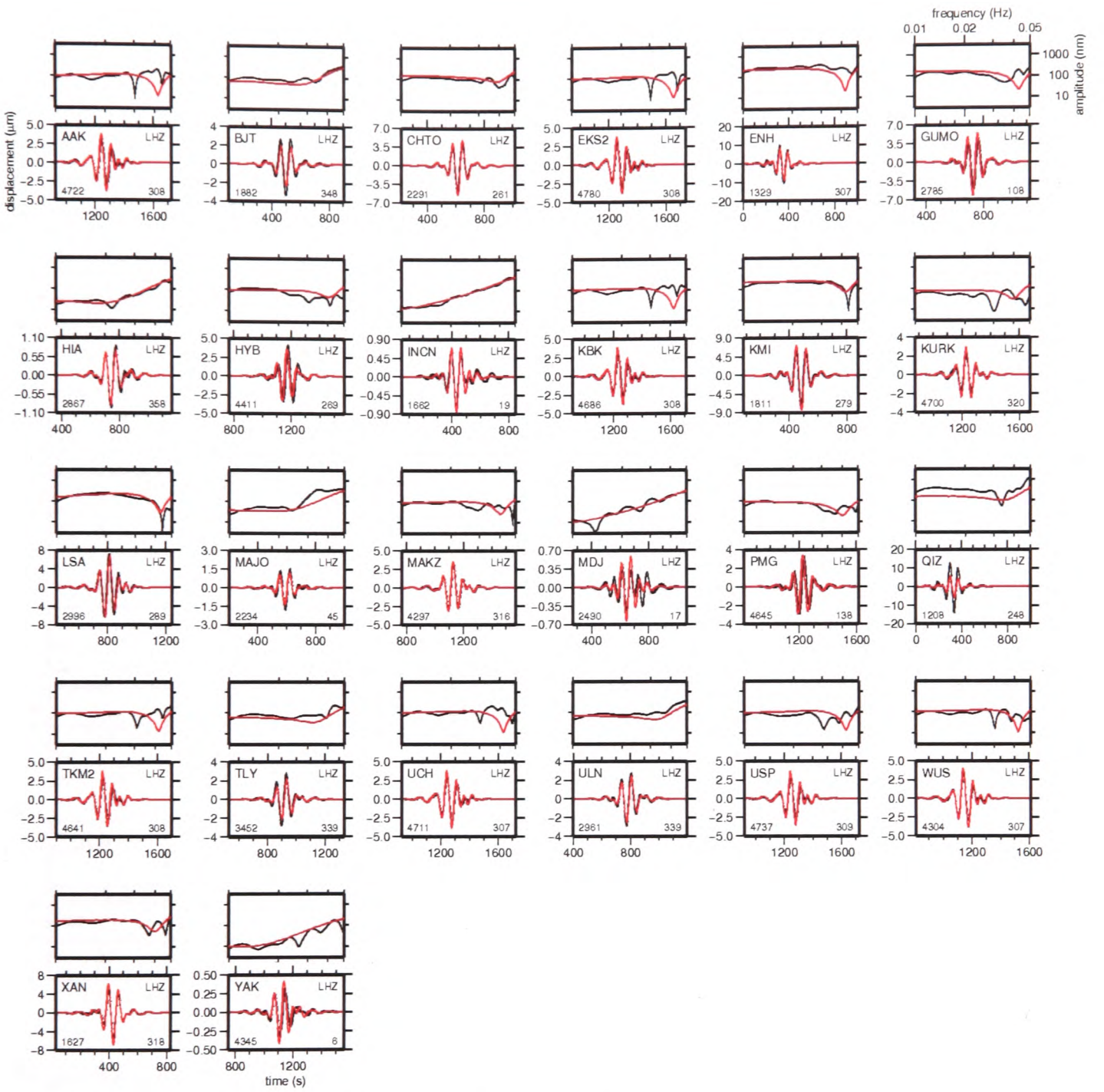
As previous figure but for LHT channel recordings.



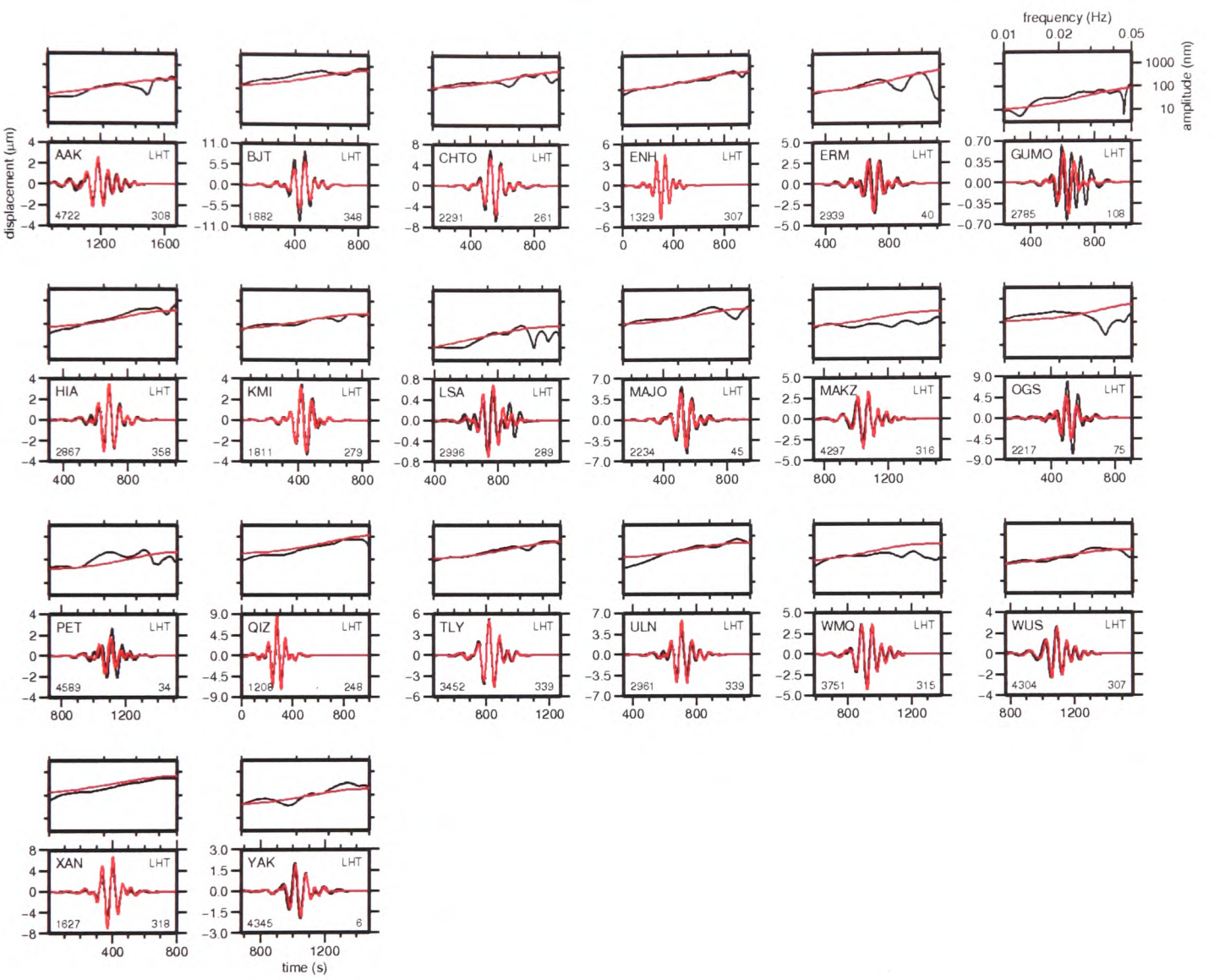
Synthetic (red) and data (black) amplitude spectra (top) and bandpass-filtered seismograms (bottom) for each station where the LHZ channel recording was used in the determination of source parameters for event 090799C.



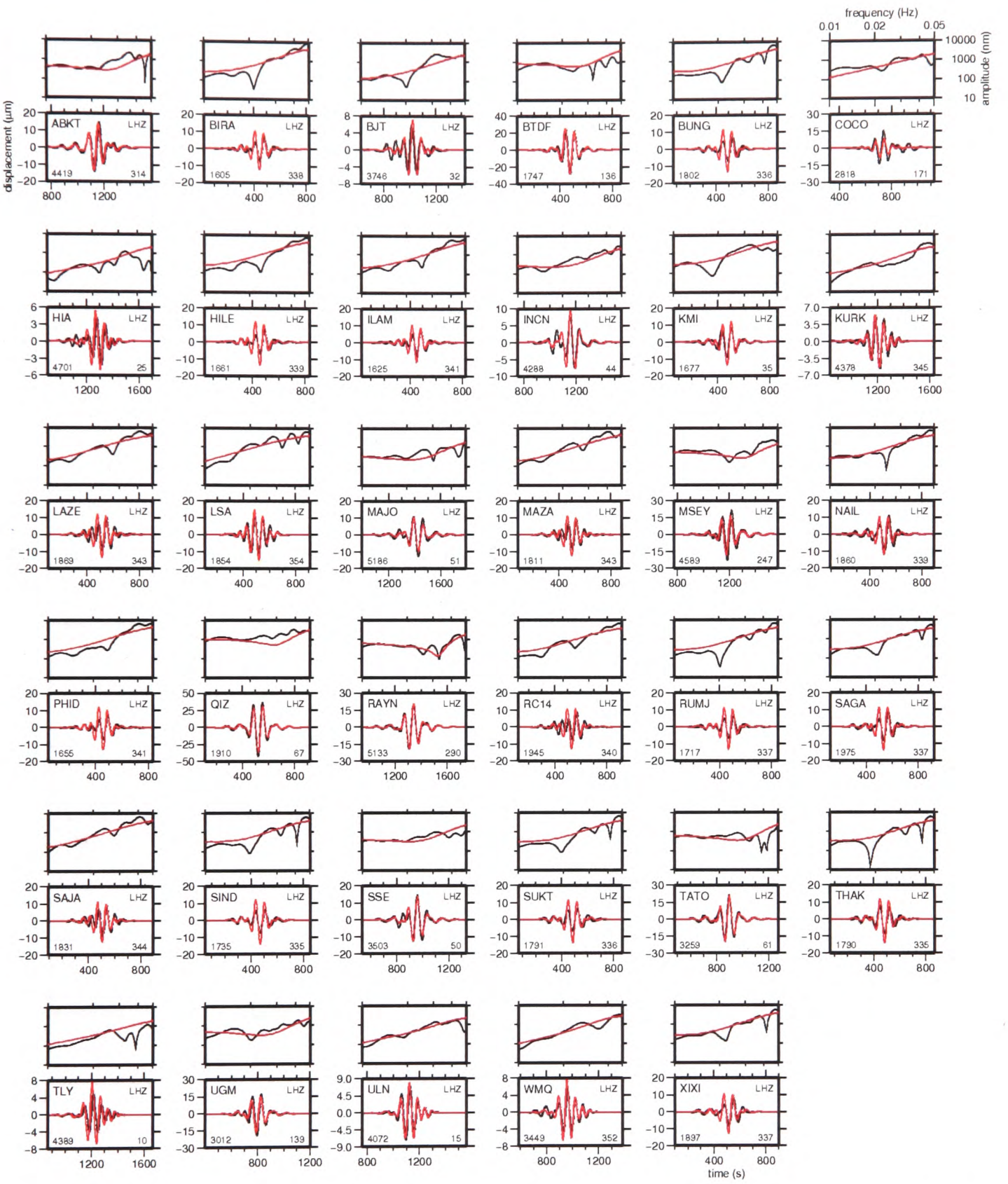
As previous figure but for LHT channel recordings.



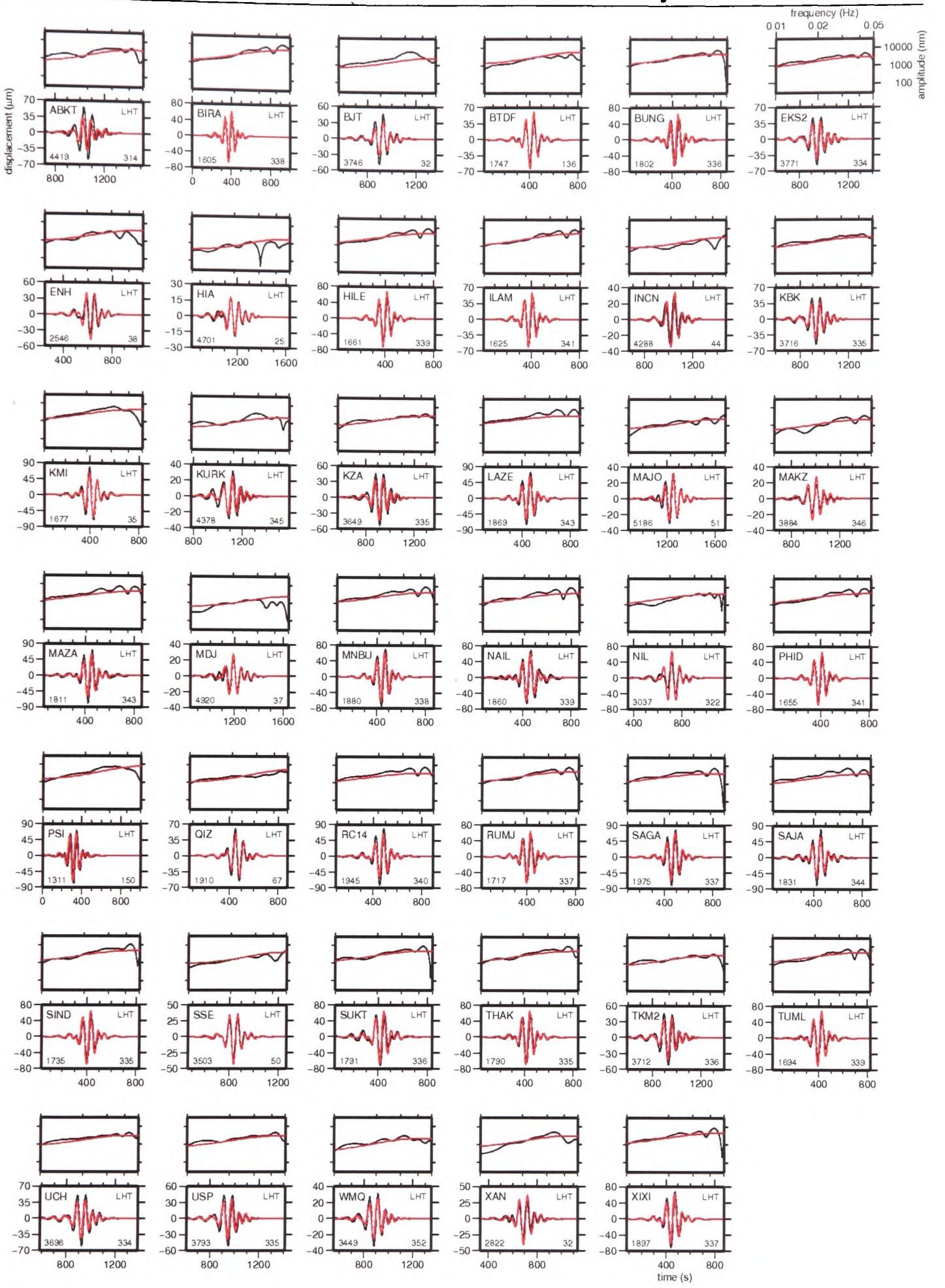
Synthetic (red) and data (black) amplitude spectra (top) and bandpass-filtered seismograms (bottom) for each station where the LHZ channel recording was used in the determination of source parameters for event 102299A.



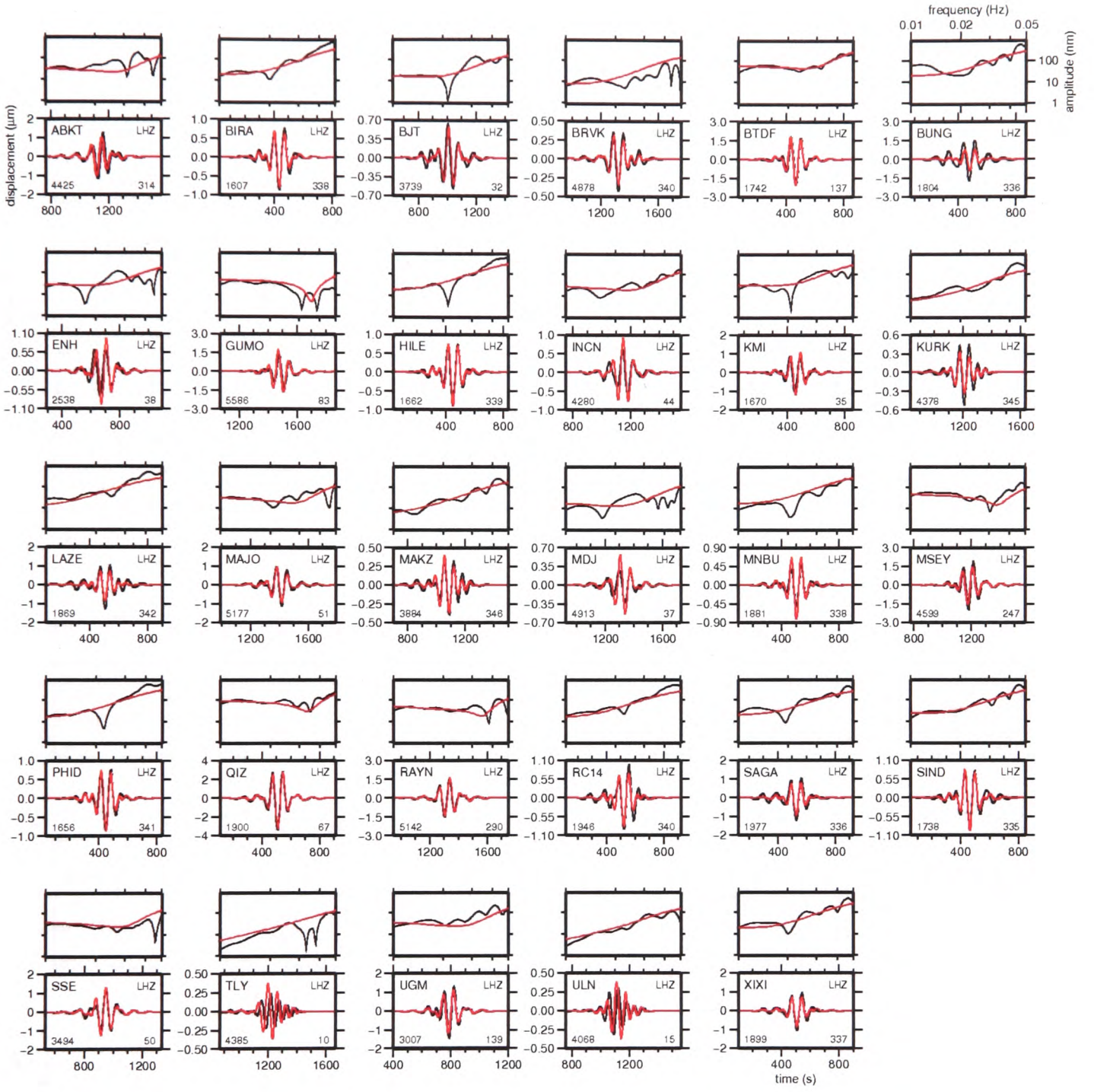
As previous figure but for LHT channel recordings.



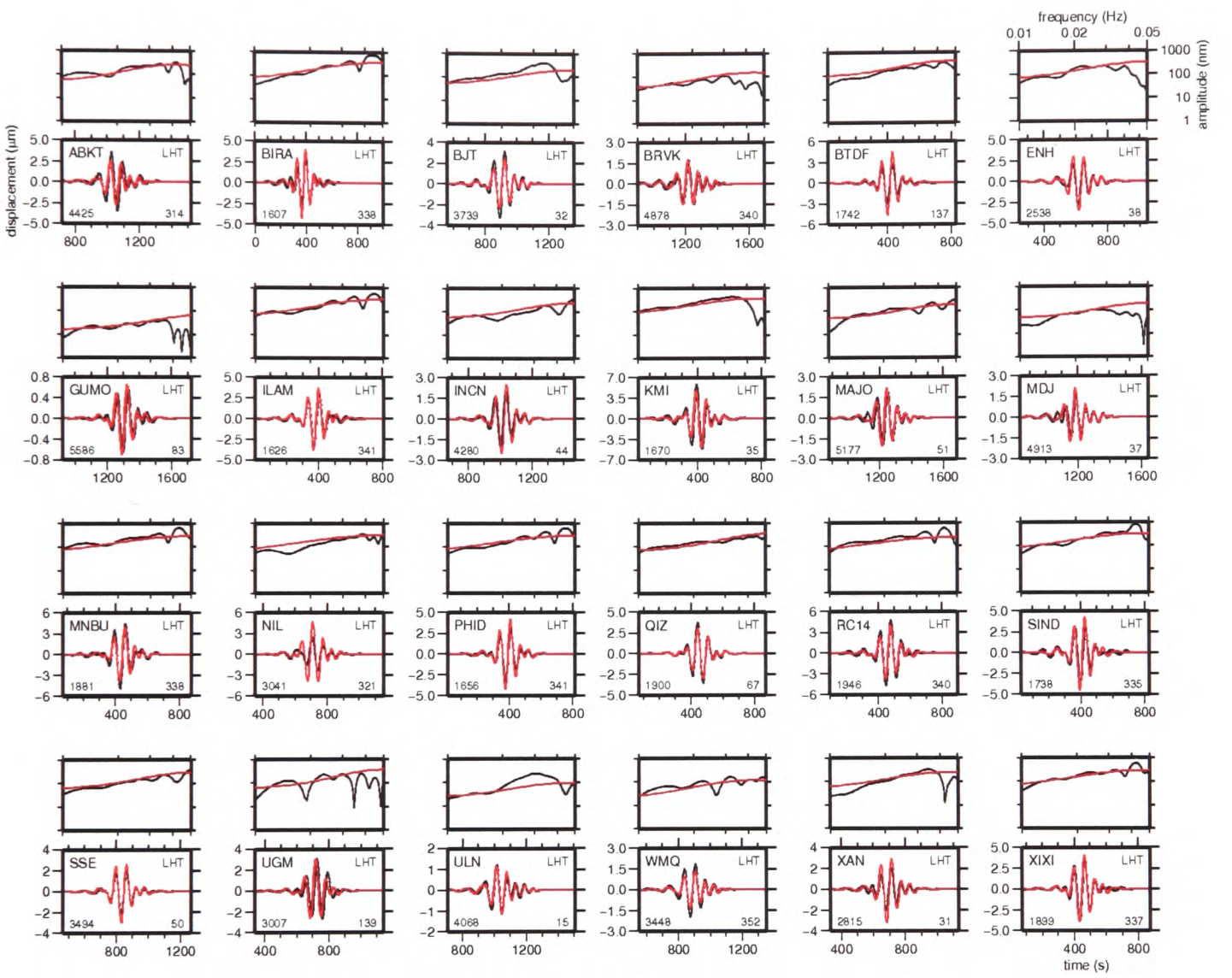
Synthetic (red) and data (black) amplitude spectra (top) and bandpass-filtered seismograms (bottom) for each station where the LHZ channel recording was used in the determination of source parameters for event 091302C.



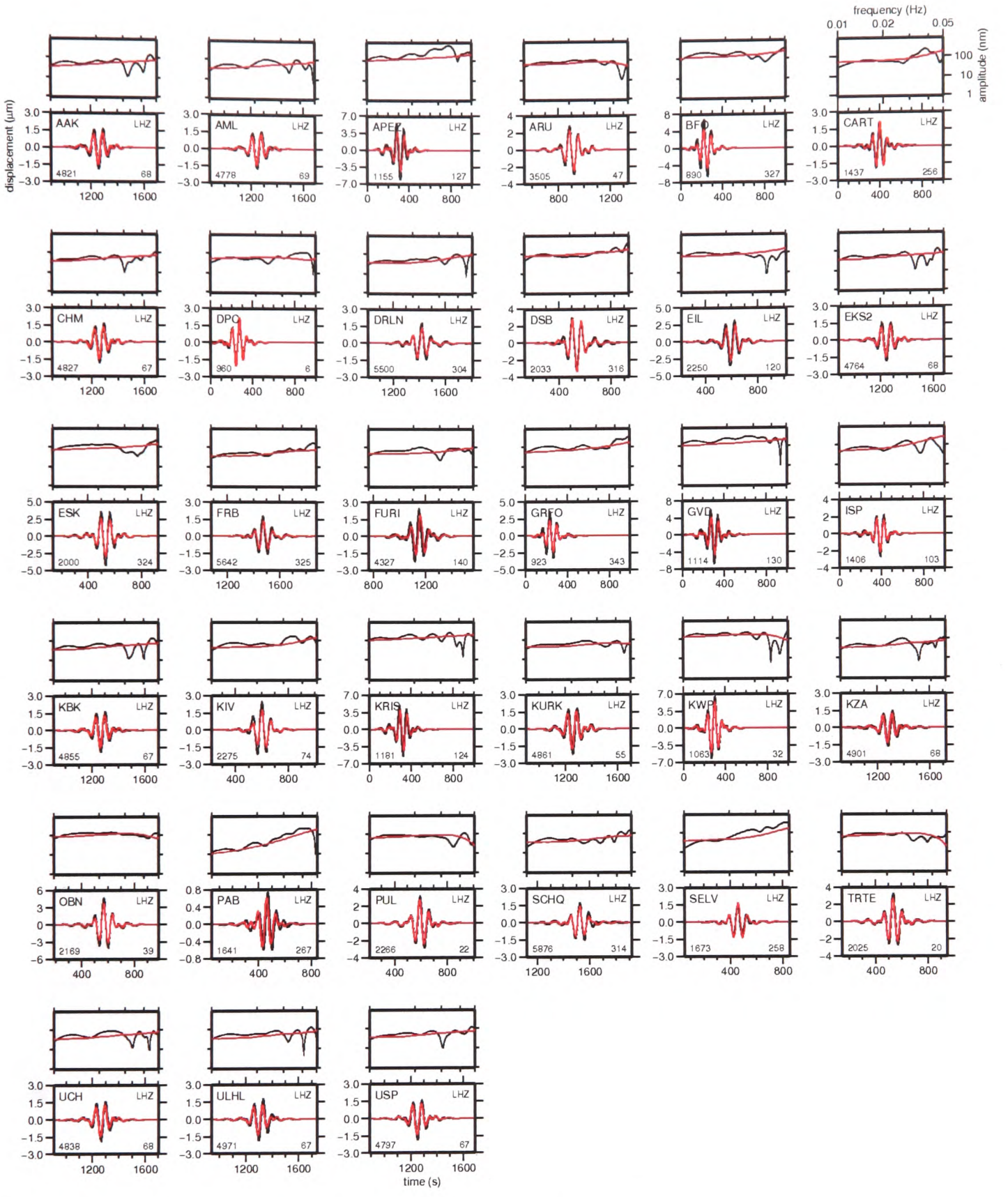
As previous figure but for LHT channel recordings.



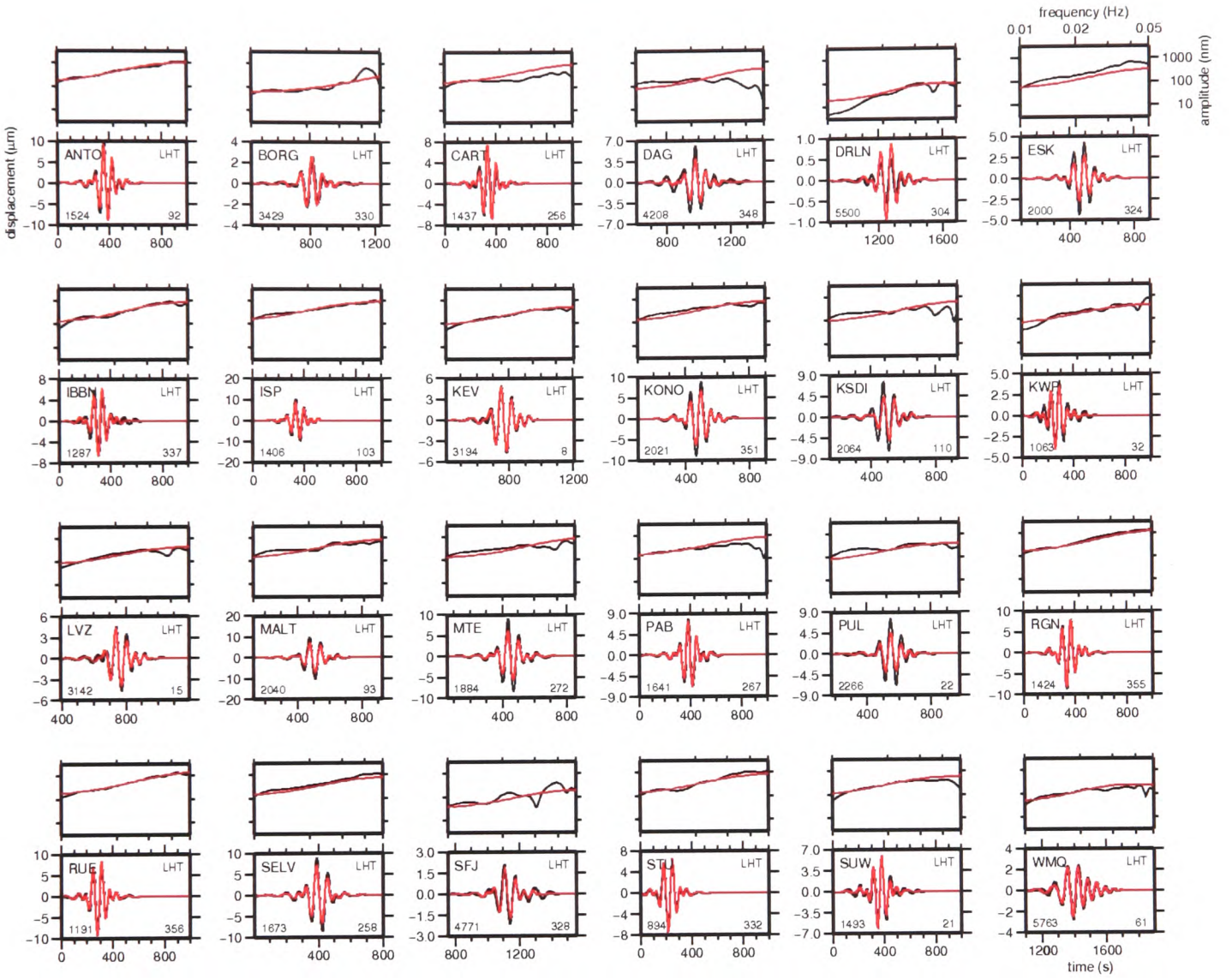
Synthetic (red) and data (black) amplitude spectra (top) and bandpass-filtered seismograms (bottom) for each station where the LHZ channel recording was used in the determination of source parameters for event 091402B.



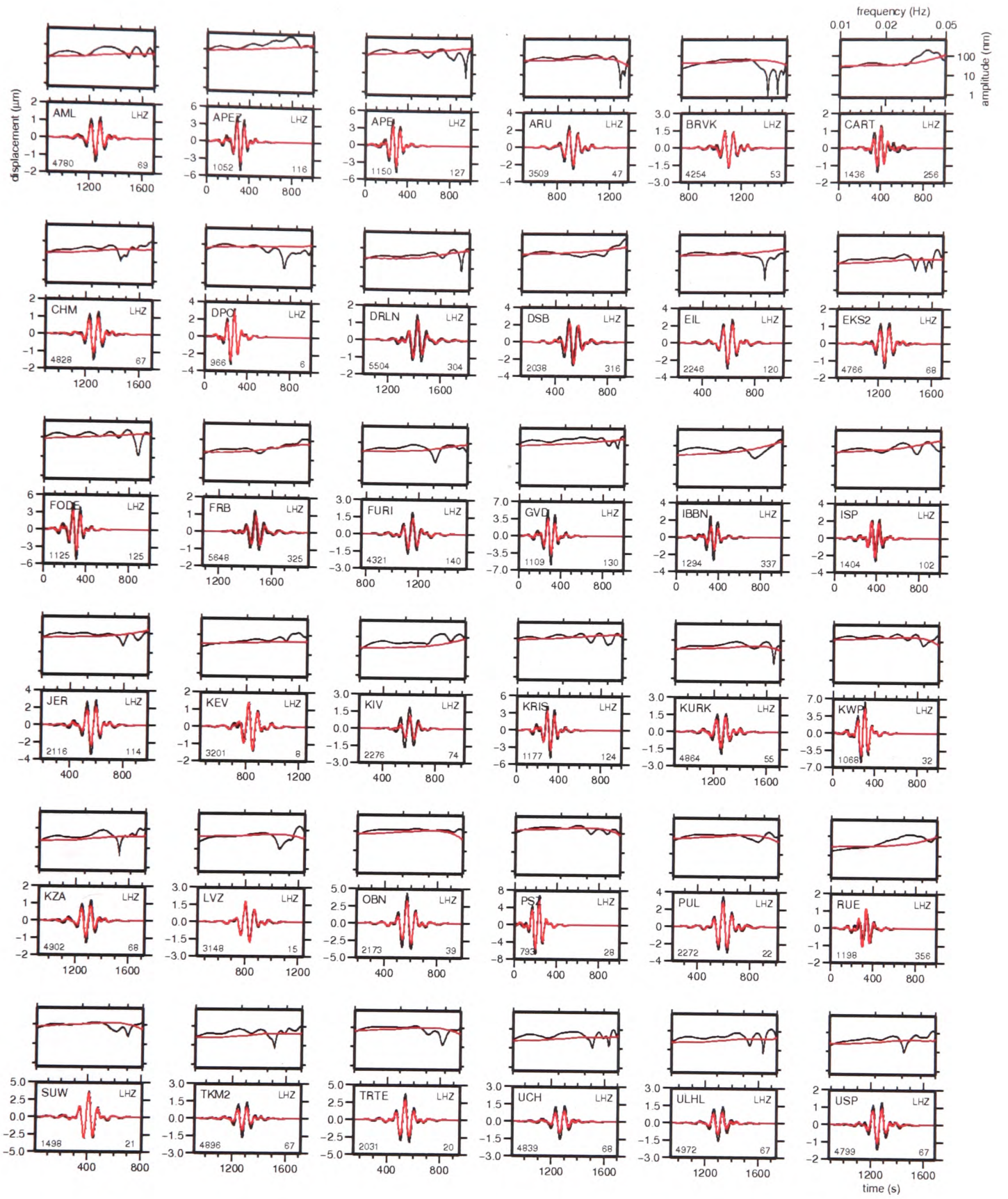
As previous figure but for LHT channel recordings.



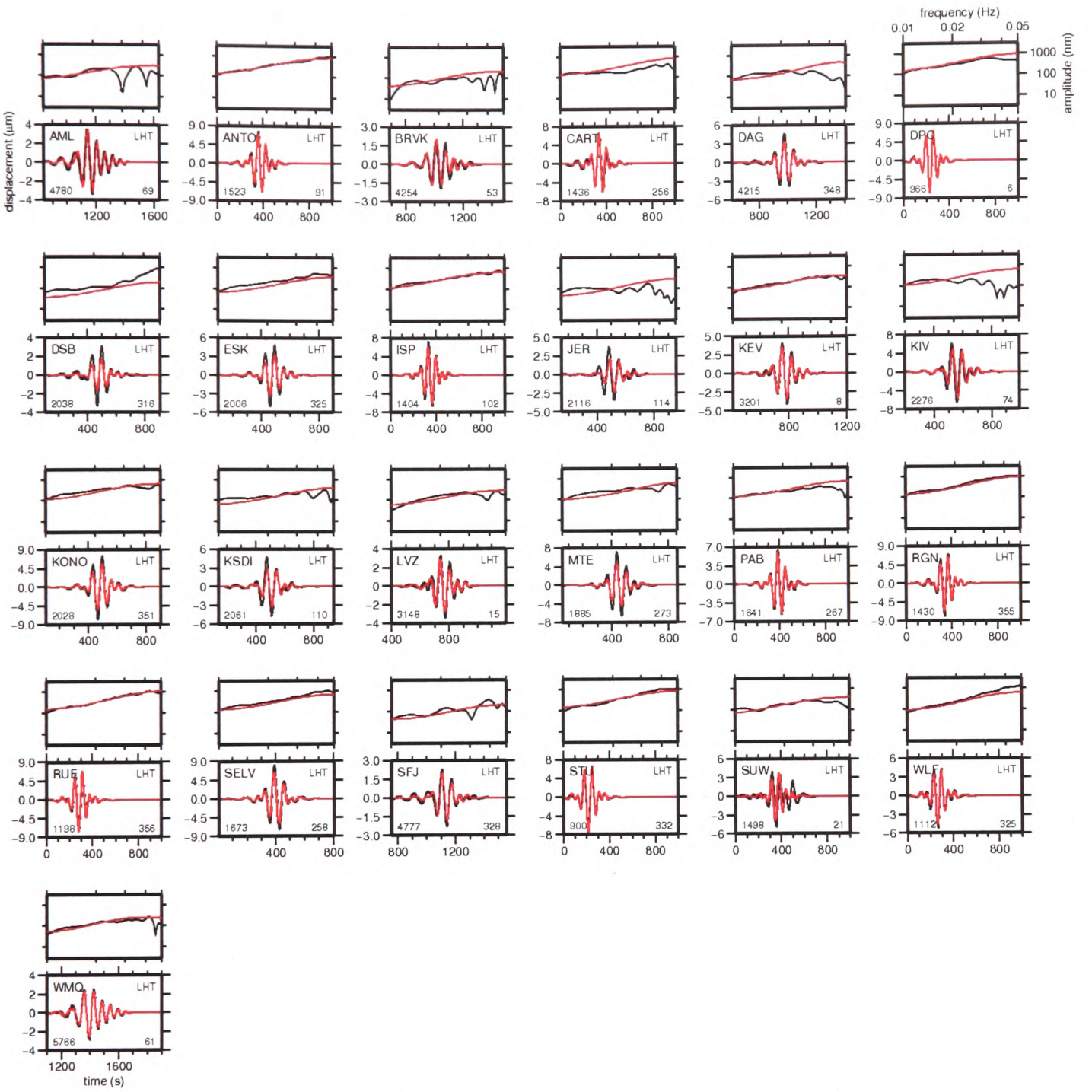
Synthetic (red) and data (black) amplitude spectra (top) and bandpass-filtered seismograms (bottom) for each station where the LHZ channel recording was used in the determination of source parameters for event 103102B.



As previous figure but for LHT channel recordings.



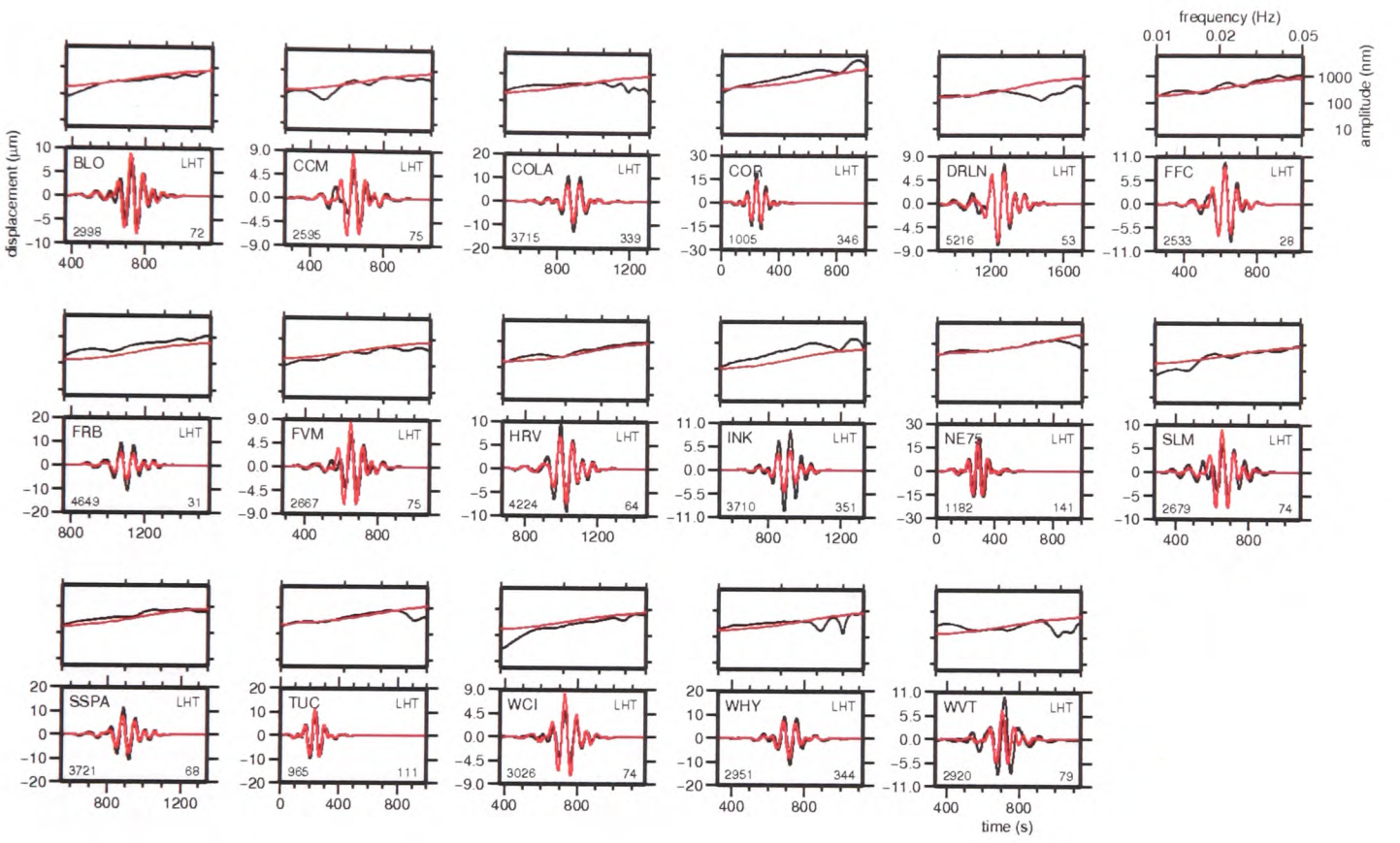
Synthetic (red) and data (black) amplitude spectra (top) and bandpass-filtered seismograms (bottom) for each station where the LHZ channel recording was used in the determination of source parameters for event 110102F.



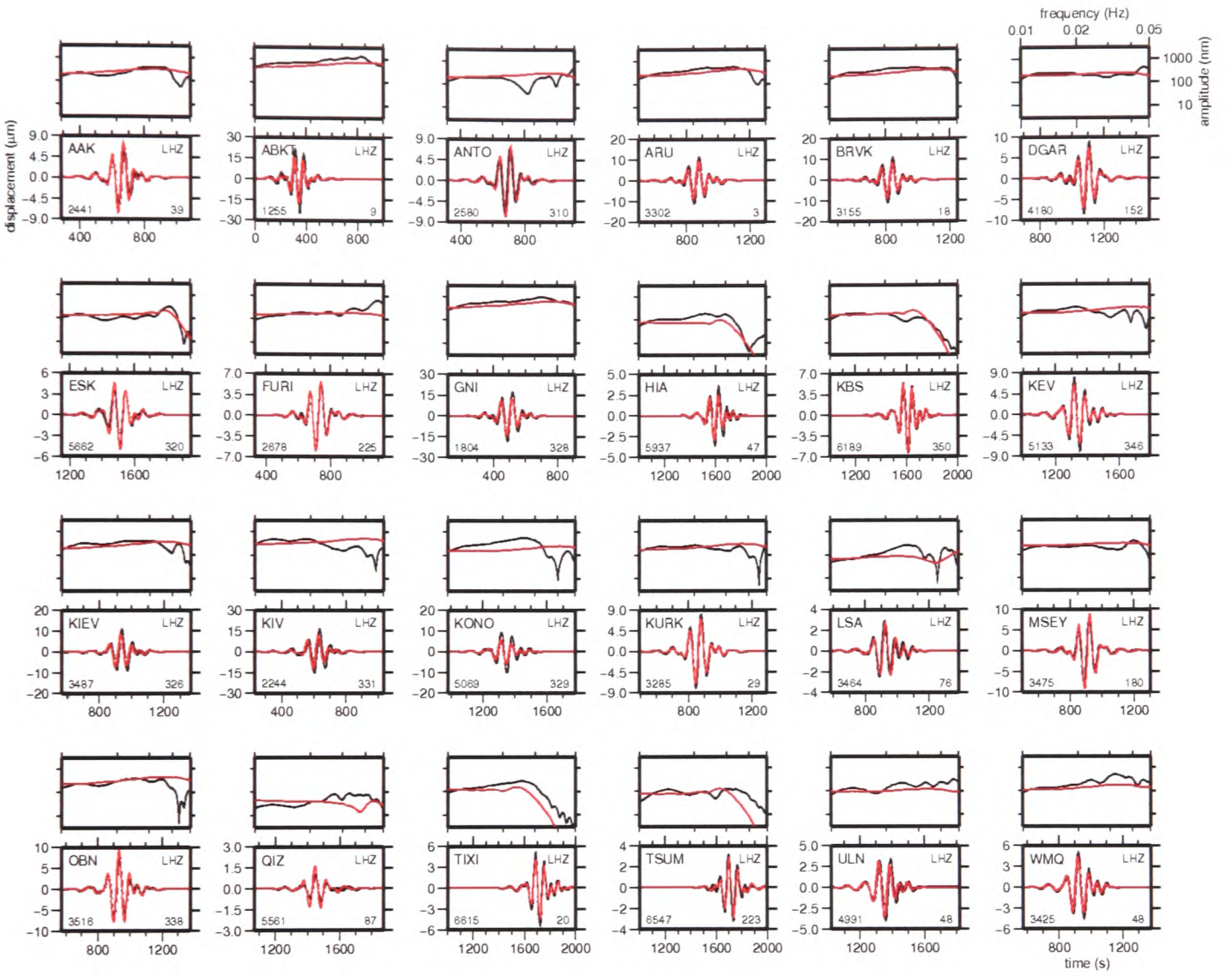
As previous figure but for LHT channel recordings.



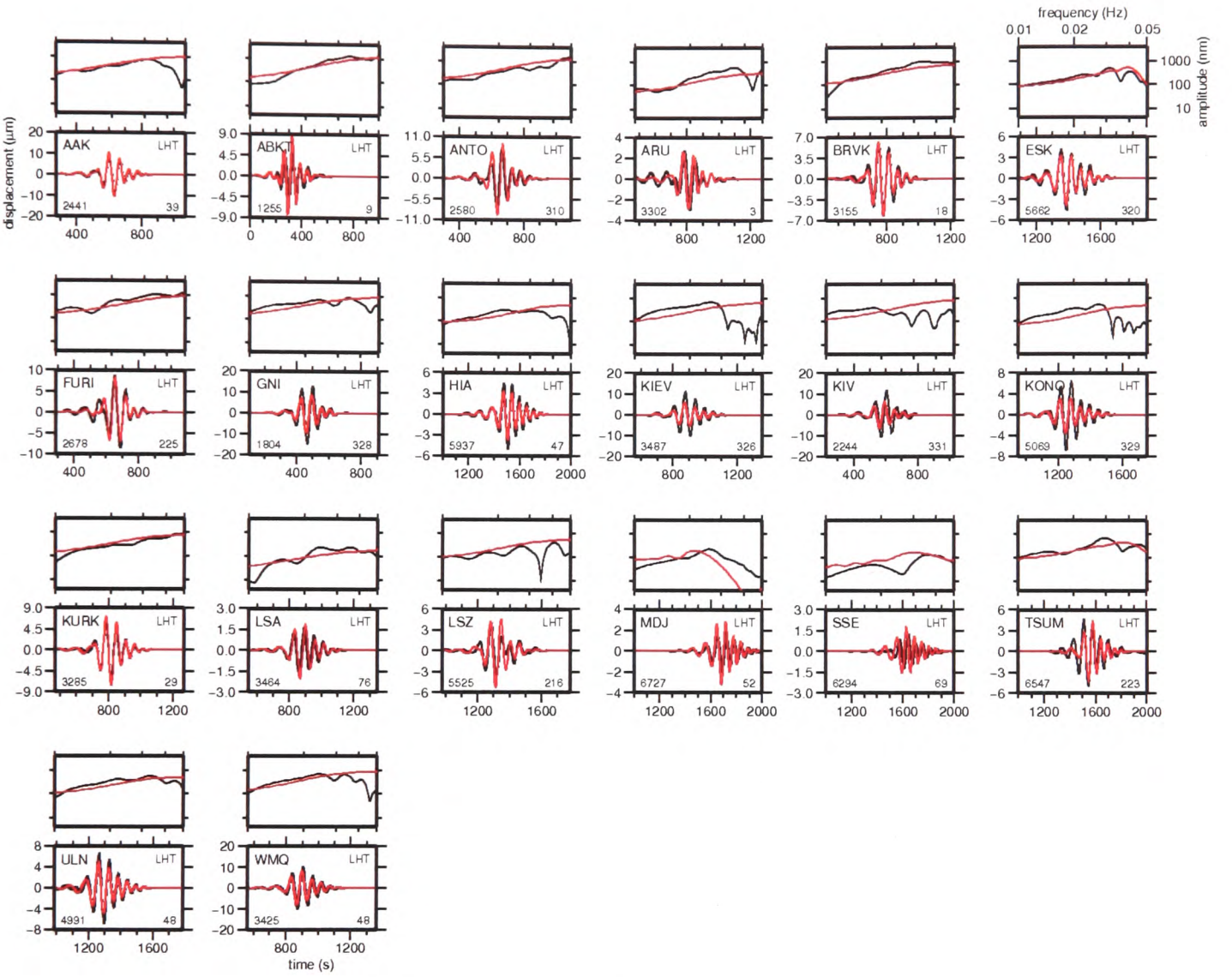
Synthetic (red) and data (black) amplitude spectra (top) and bandpass-filtered seismograms (bottom) for each station where the LHZ channel recording was used in the determination of source parameters for event 092804H.



As previous figure but for LHT channel recordings.



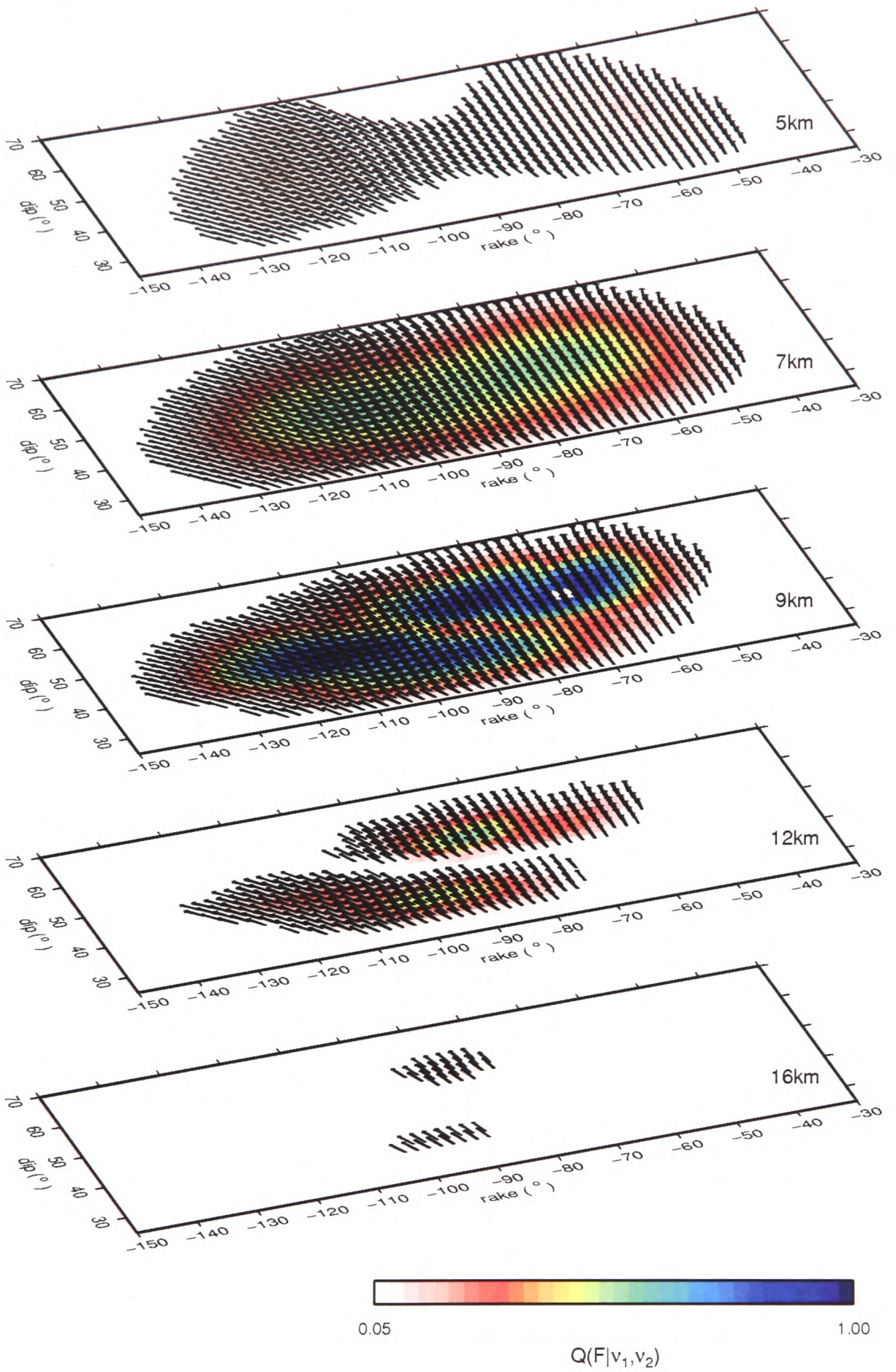
Synthetic (red) and data (black) amplitude spectra (top) and bandpass-filtered seismograms (bottom) for each station where the LHZ channel recording was used in the determination of source parameters for event 112705I.



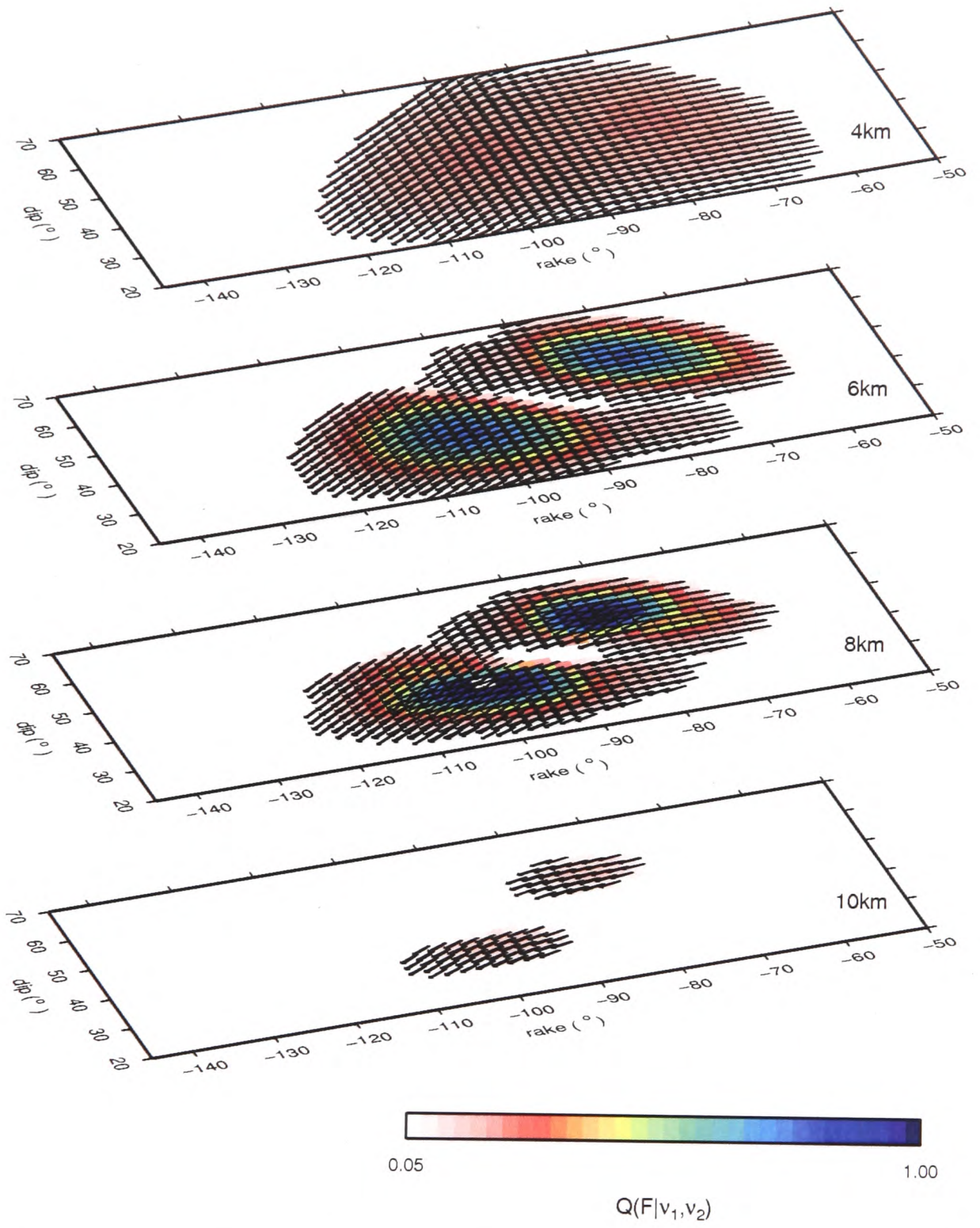
As previous figure but for LHT channel recordings.

Appendix E

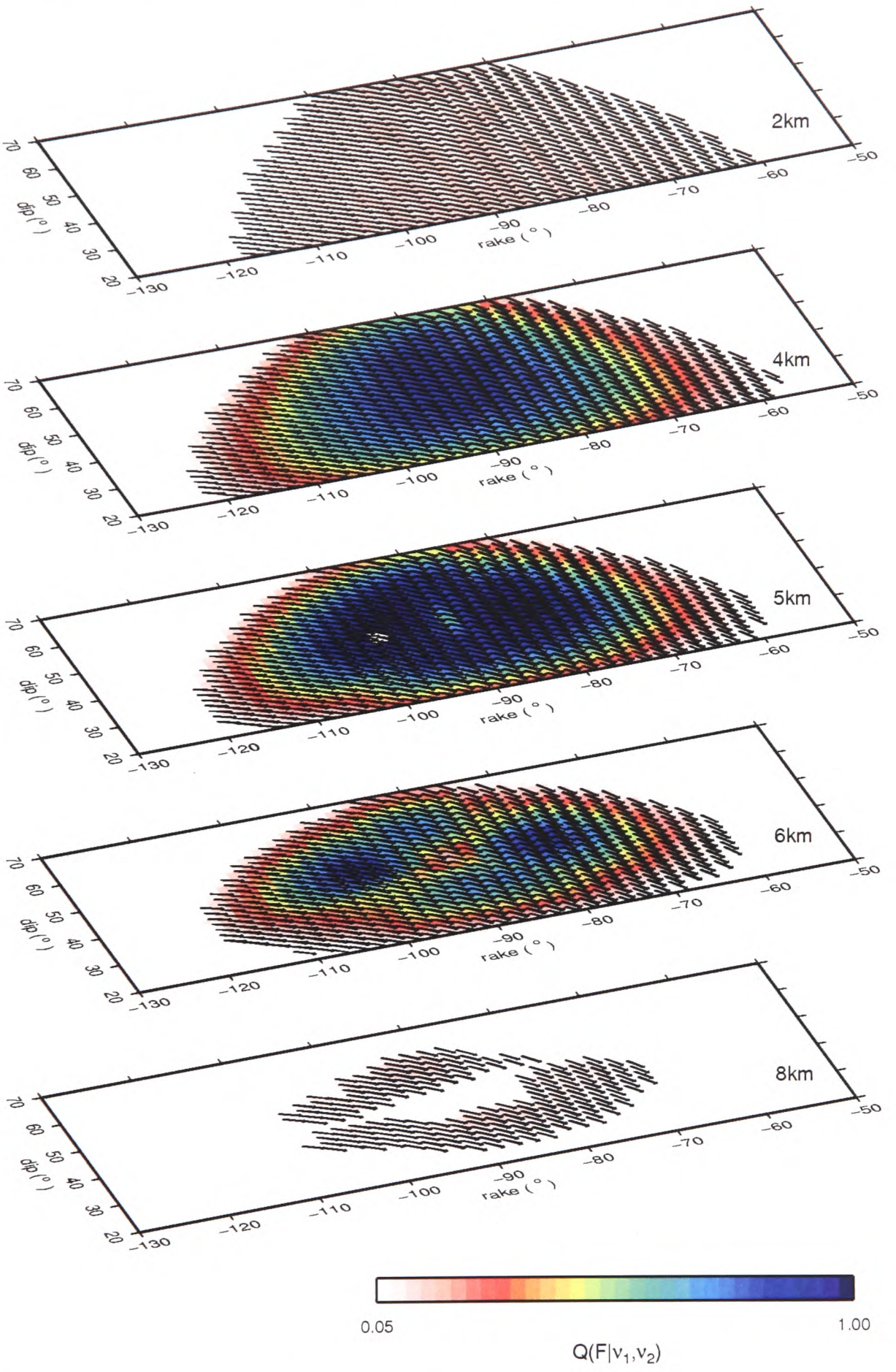
Solution Space Slices for Chapter 3 Earthquakes



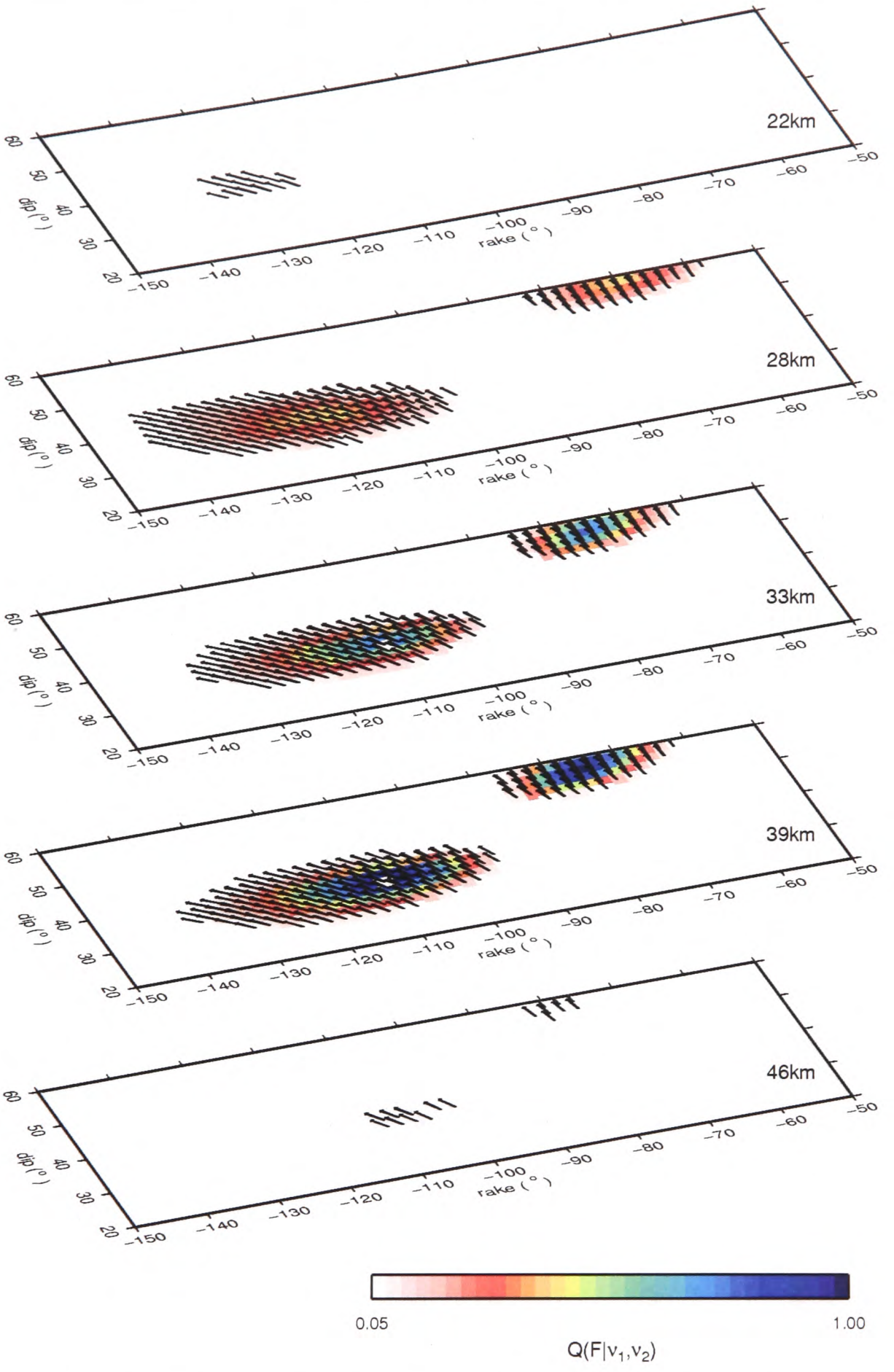
Source solutions falling within 95% confidence bounds in the study of event 080393G. Key as described in Figure 2.17.



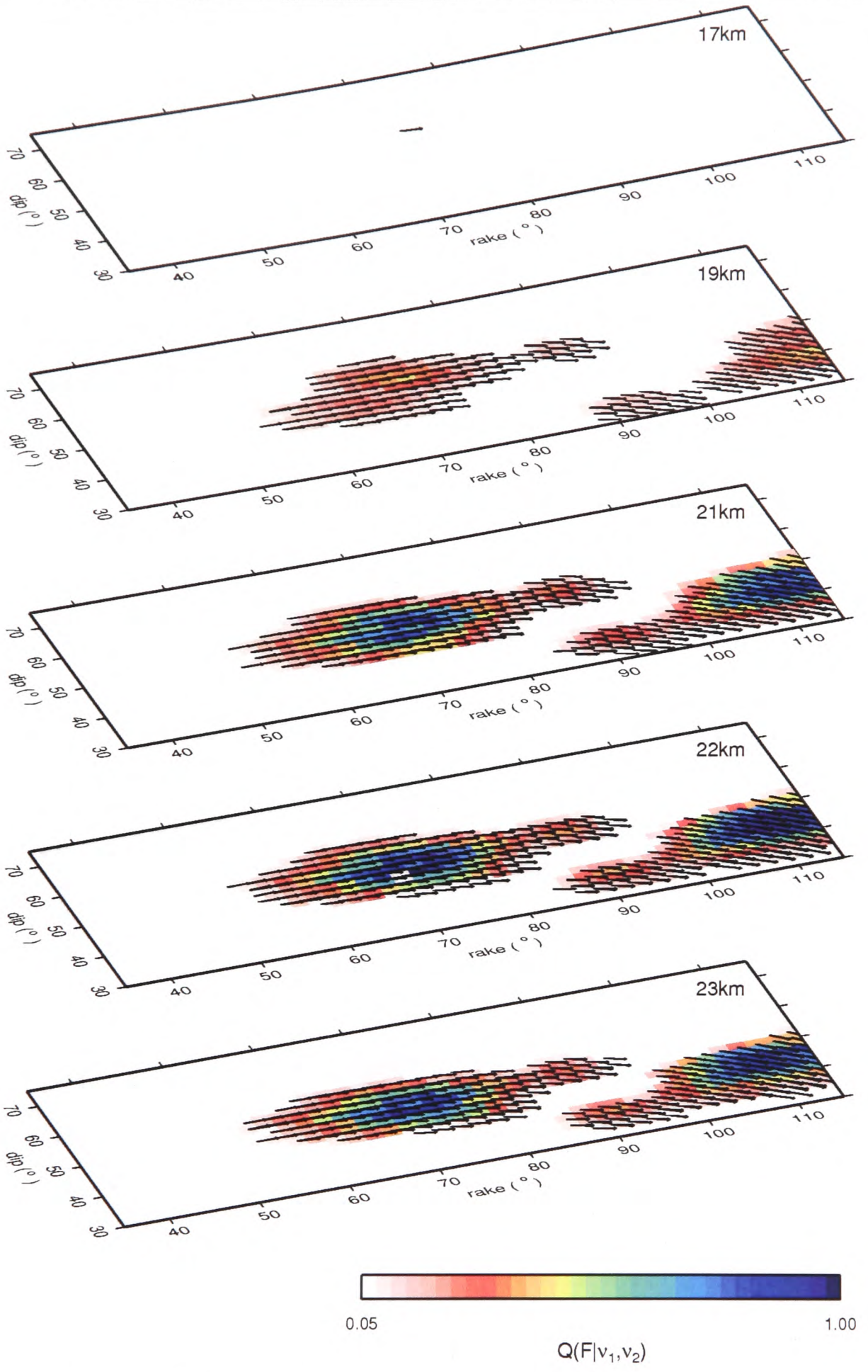
Source solutions falling within 95% confidence bounds in the study of event 051395B. Key as described in Figure 2.17.



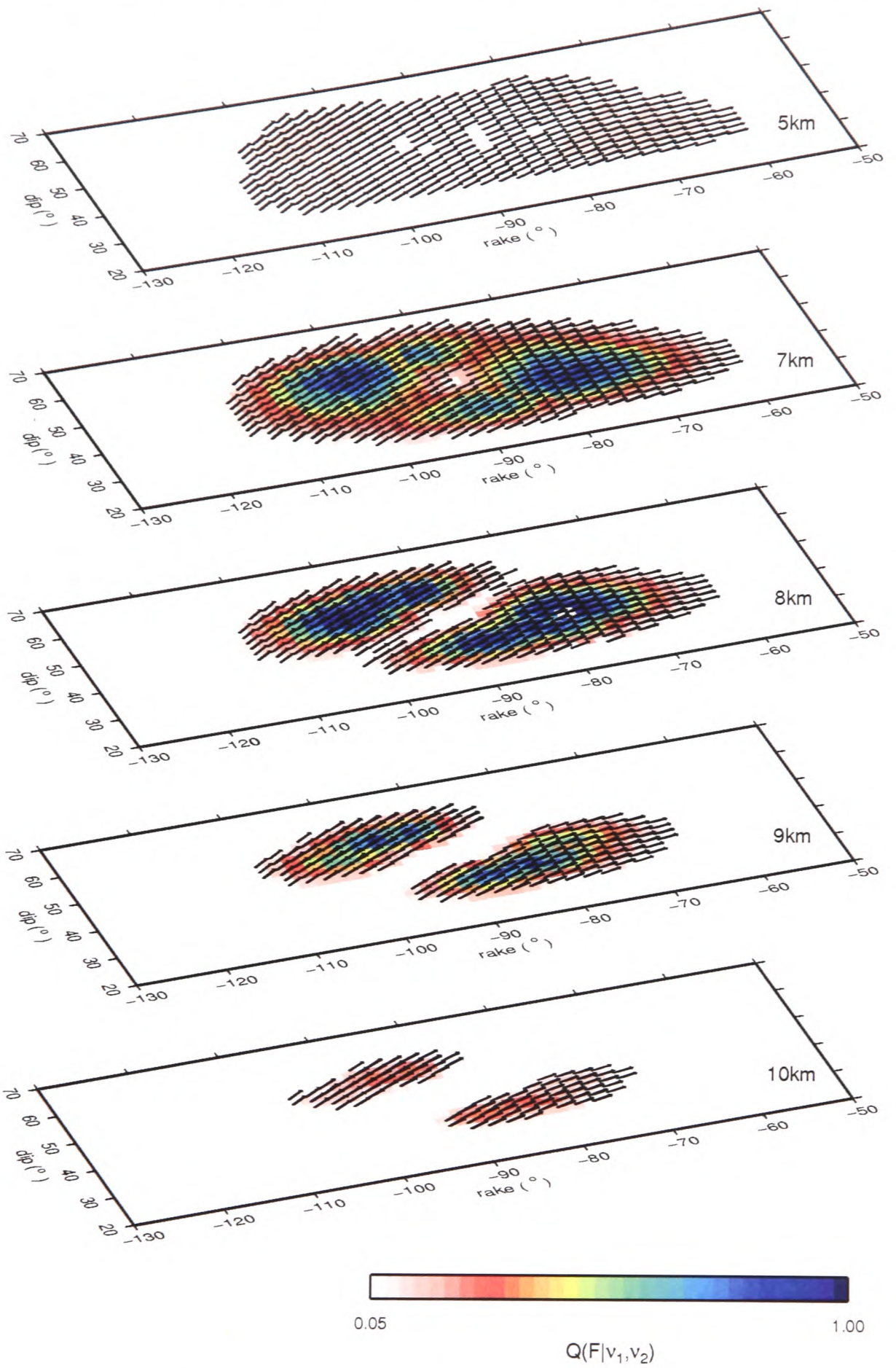
Source solutions falling within 95% confidence bounds in the study of event 100195B. Key as described in Figure 2.17.



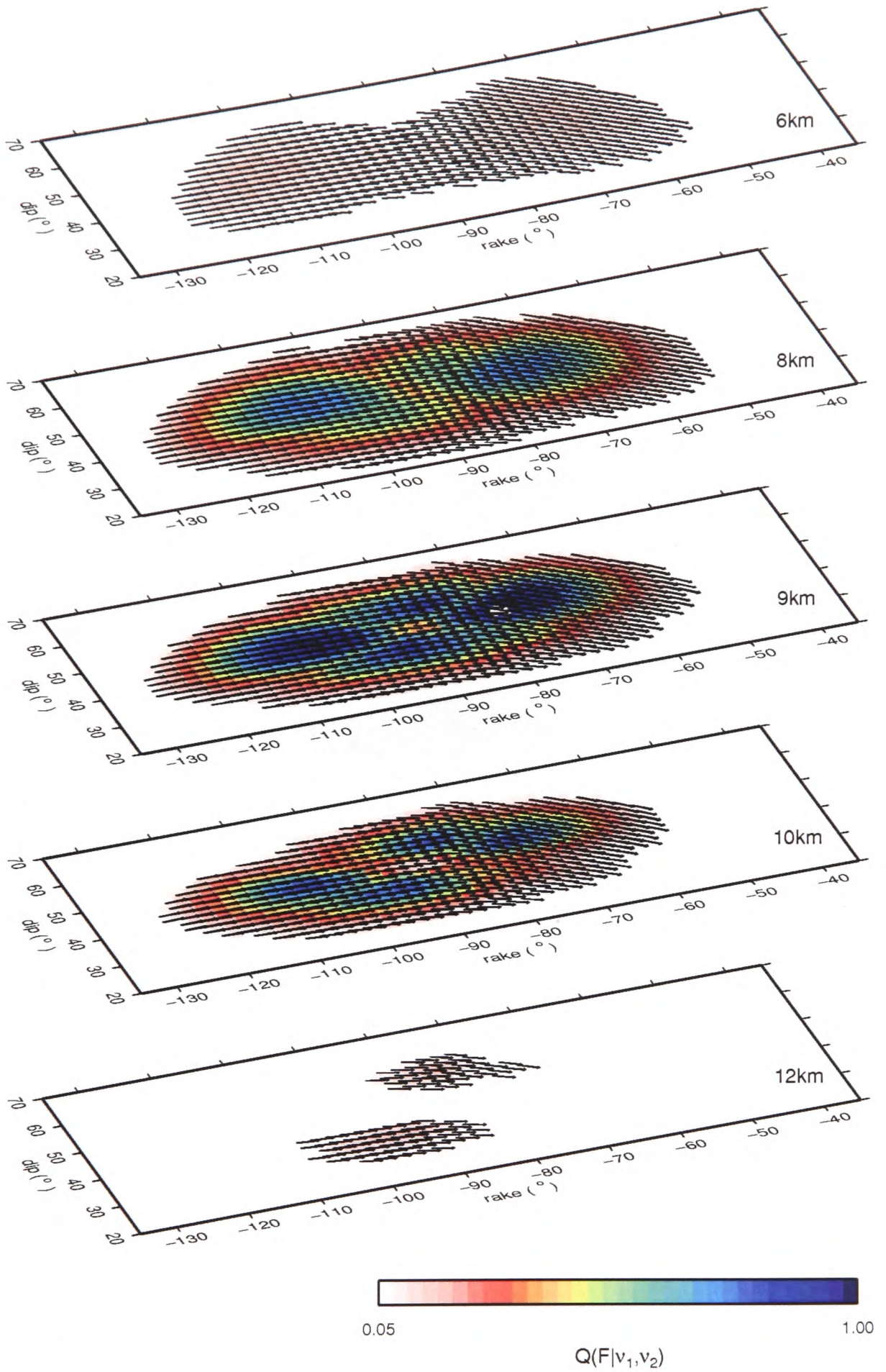
Source solutions falling within 95% confidence bounds in the study of event 092197C. Key as described in Figure 2.17.



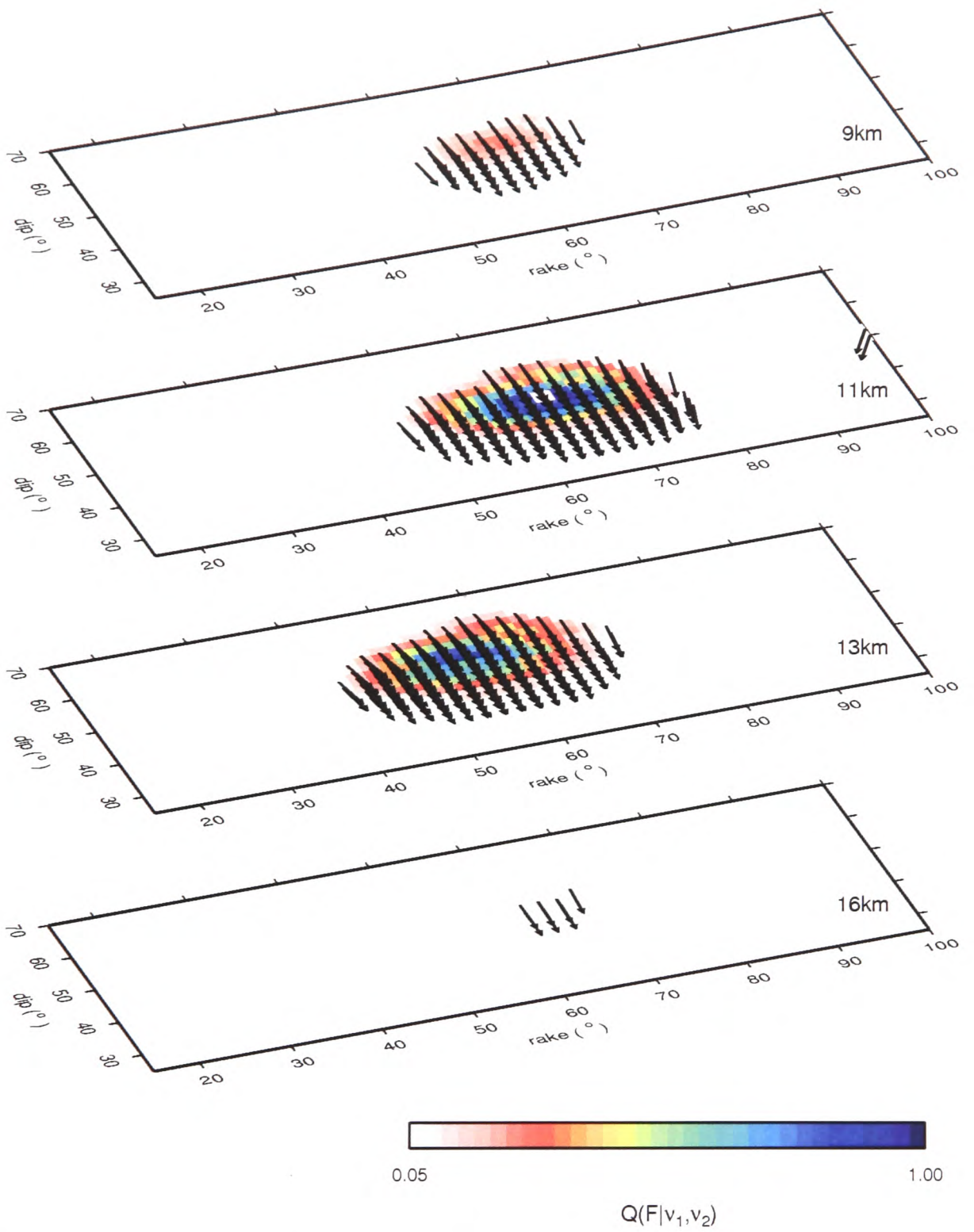
Source solutions falling within 95% confidence bounds in the study of event 013099A. Key as described in Figure 2.17.



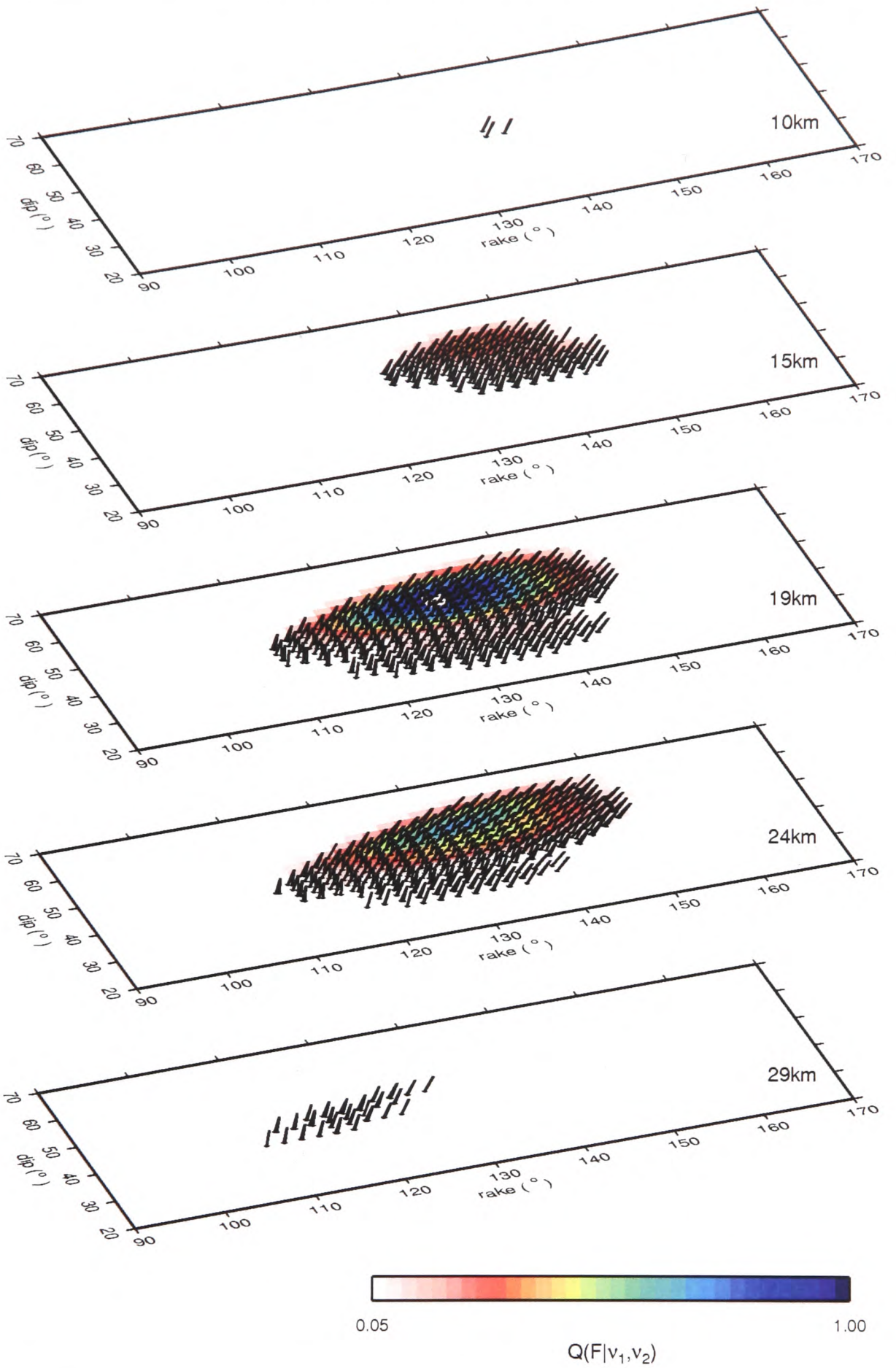
Source solutions falling within 95% confidence bounds in the study of event 022599H. Key as described in Figure 2.17.



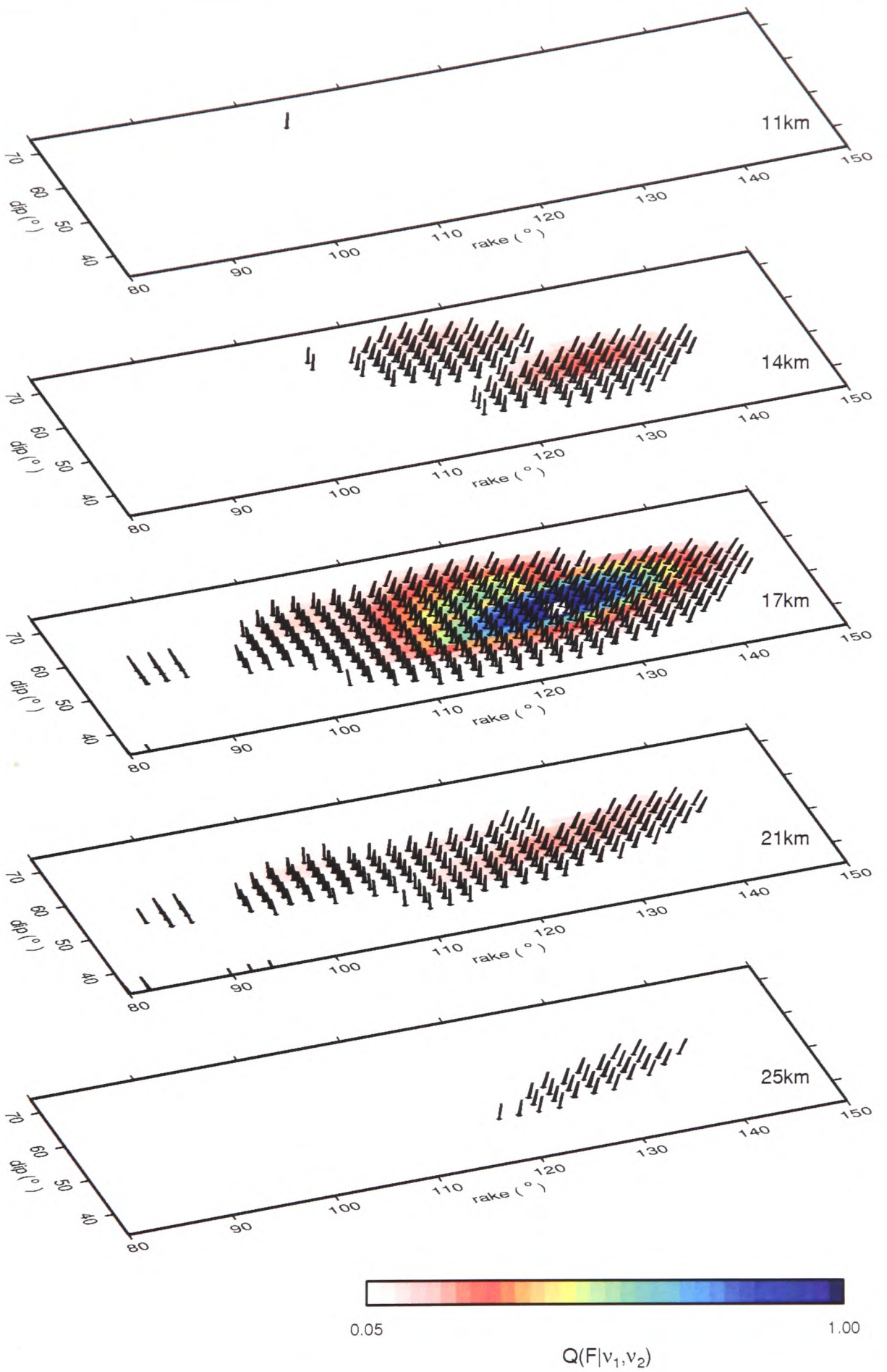
Source solutions falling within 95% confidence bounds in the study of event 090799C. Key as described in Figure 2.17.



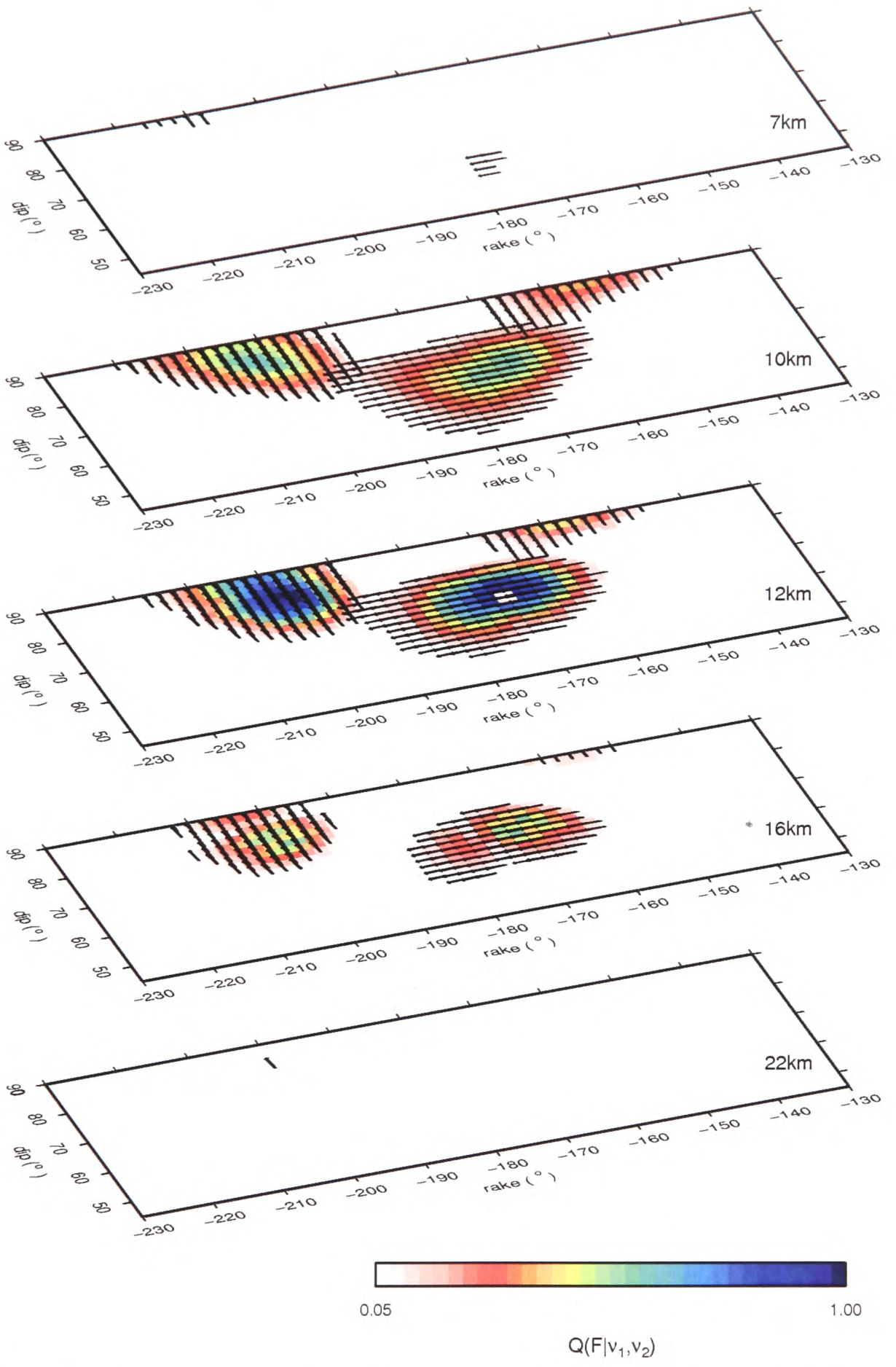
Source solutions falling within 95% confidence bounds in the study of event 102299A. Key as described in Figure 2.17.



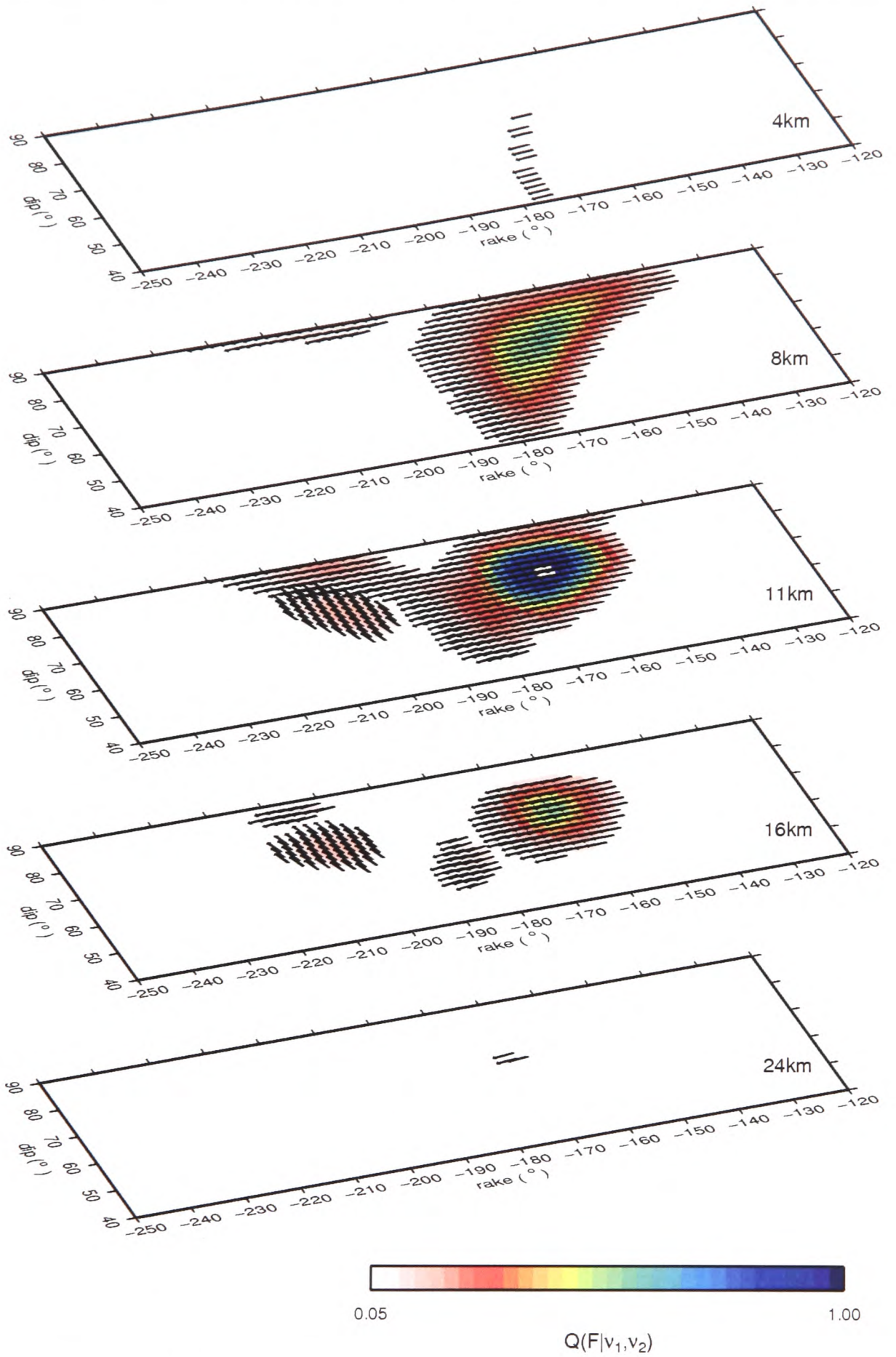
Source solutions falling within 95% confidence bounds in the study of event 091302C. Key as described in Figure 2.17.



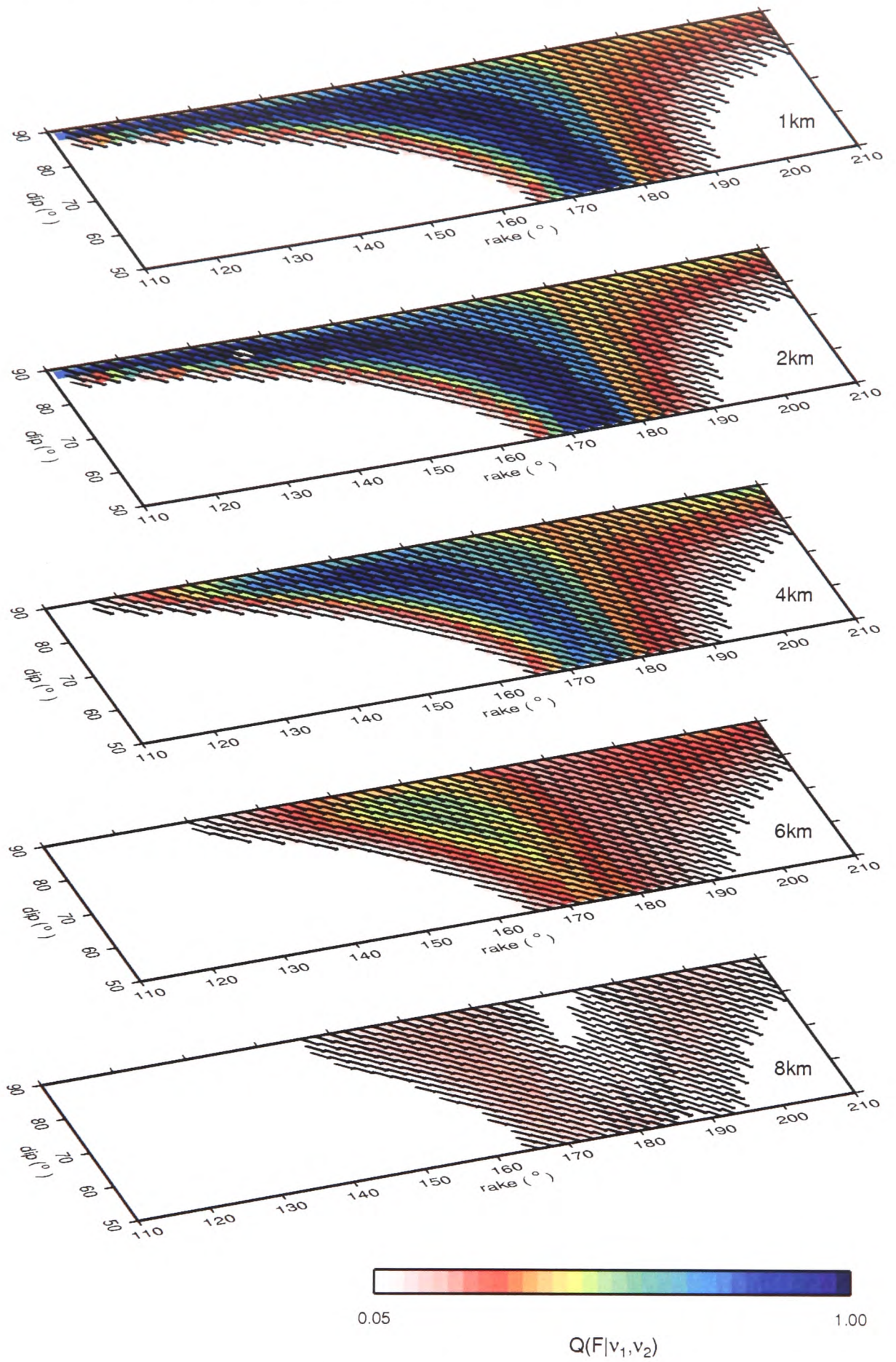
Source solutions falling within 95% confidence bounds in the study of event 091402B. Key as described in Figure 2.17.



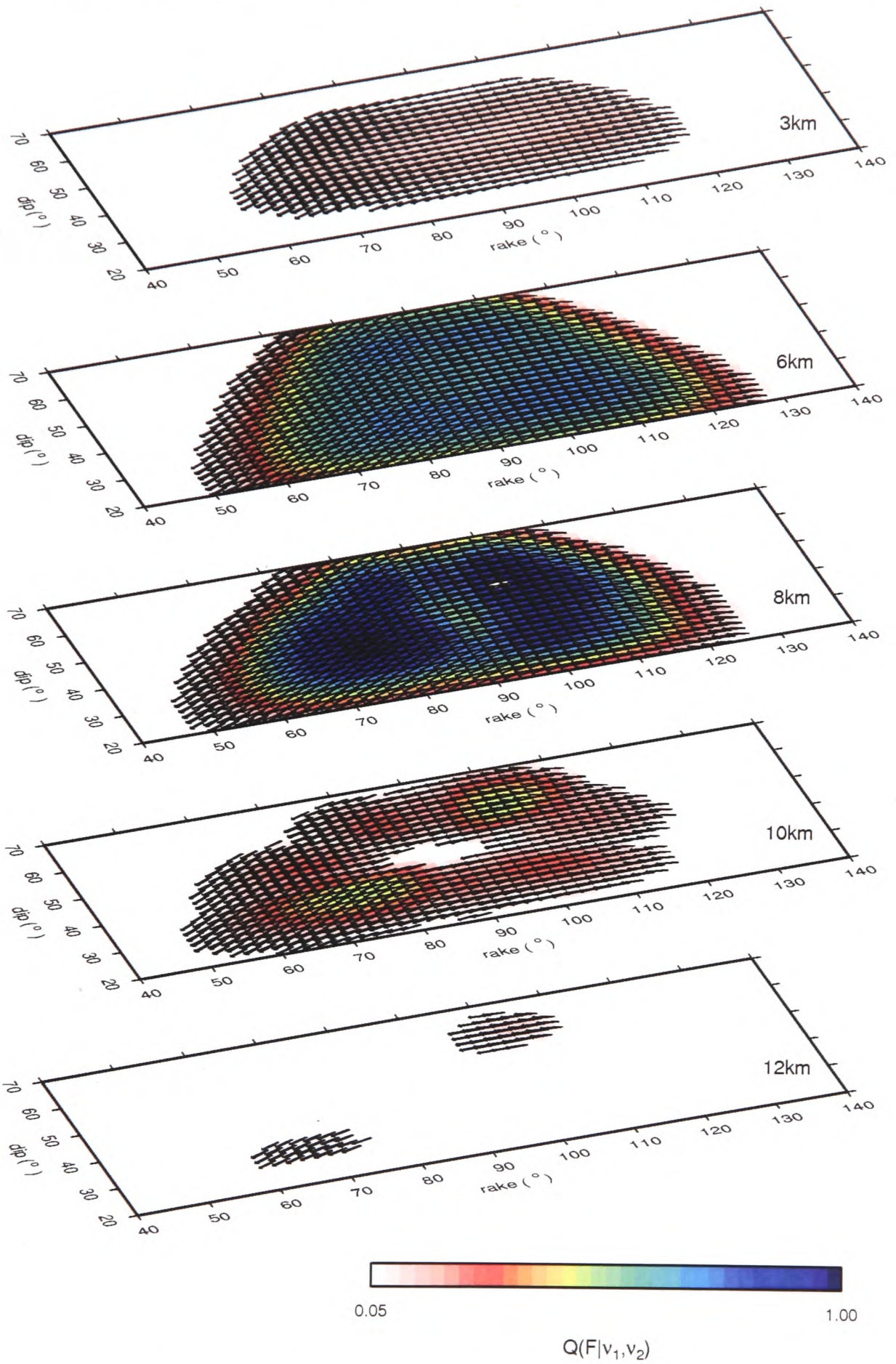
Source solutions falling within 95% confidence bounds in the study of event 103102B. Key as described in Figure 2.17.



Source solutions falling within 95% confidence bounds in the study of event 110102F. Key as described in Figure 2.17.



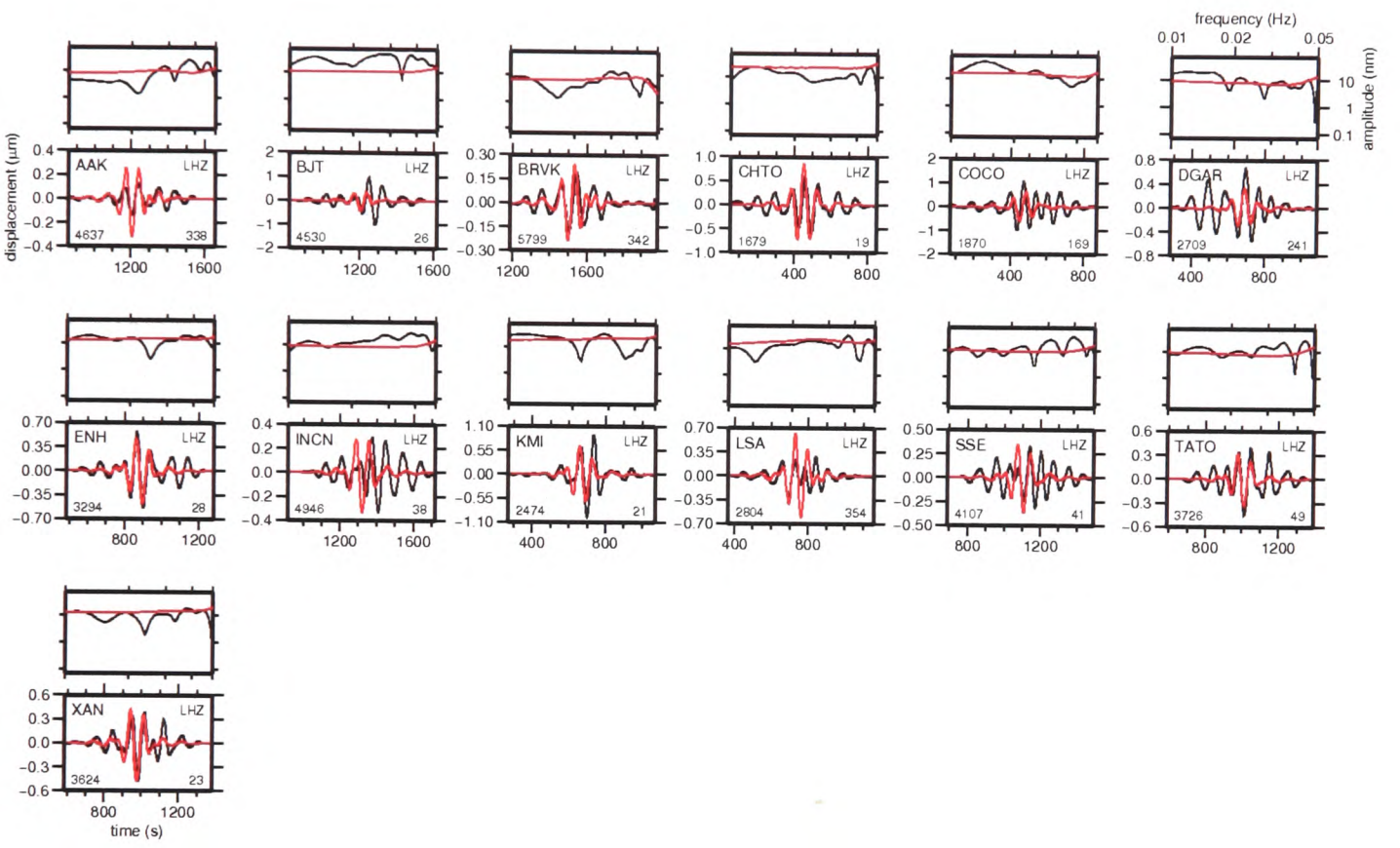
Source solutions falling within 95% confidence bounds in the study of event 092804H. Key as described in Figure 2.17.



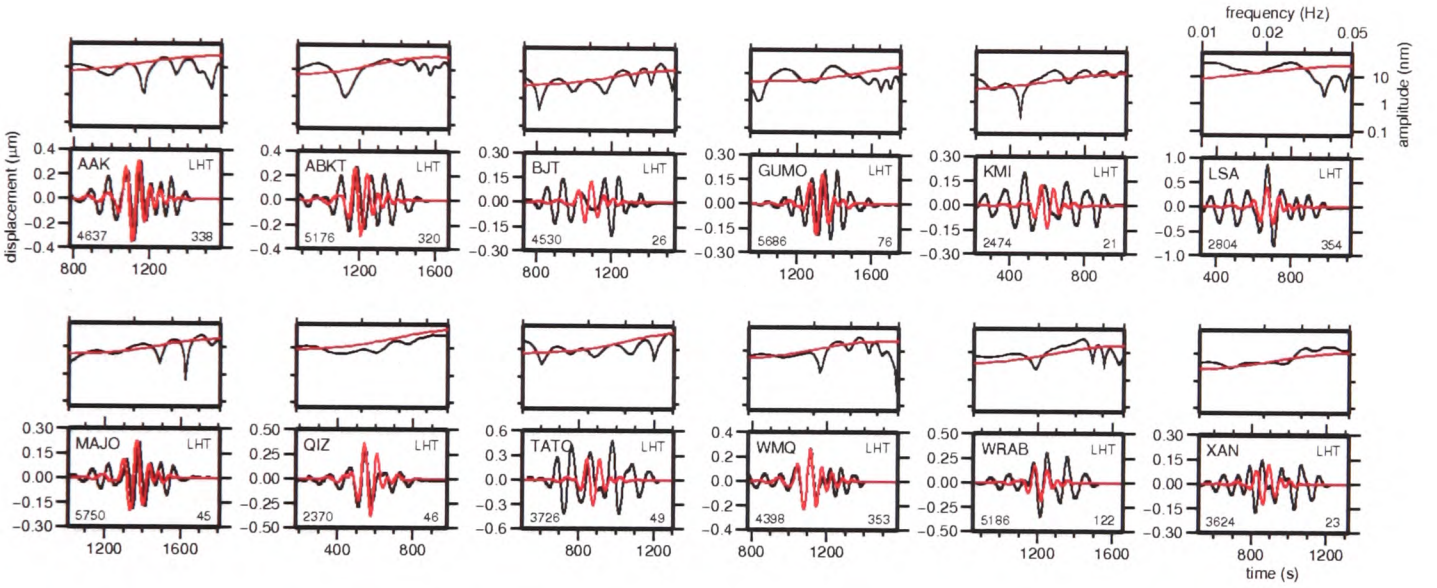
Source solutions falling within 95% confidence bounds in the study of event 112705I. Key as described in Figure 2.17.

Appendix F

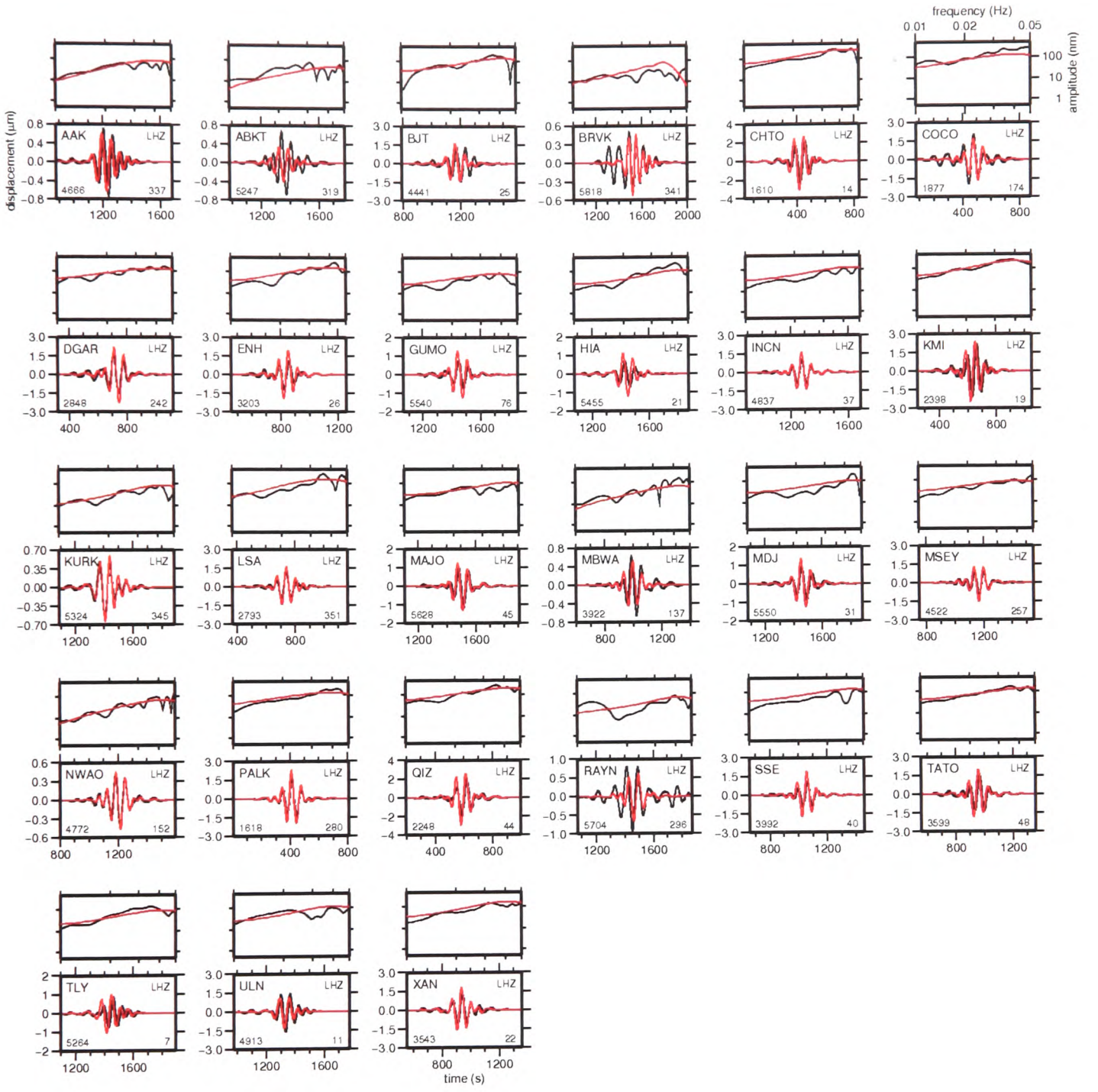
Spectra and Waveforms for Earthquakes in Chapter 4



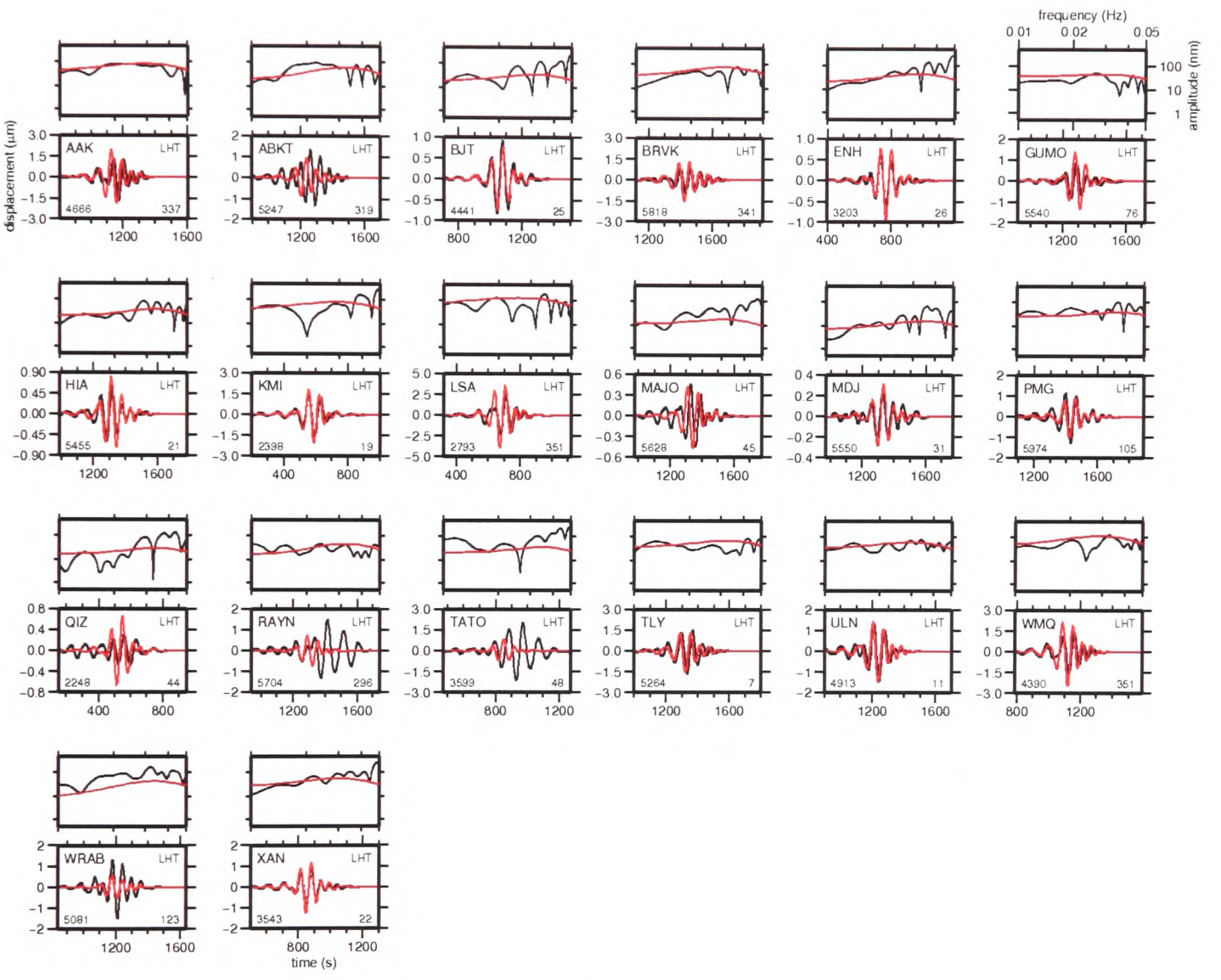
Synthetic (red) and data (black) amplitude spectra (top) and bandpass-filtered seismograms (bottom) for each station where the LHZ channel recording was used in the determination of source parameters for event 122704A.



As previous figure but for LHT channel recordings.

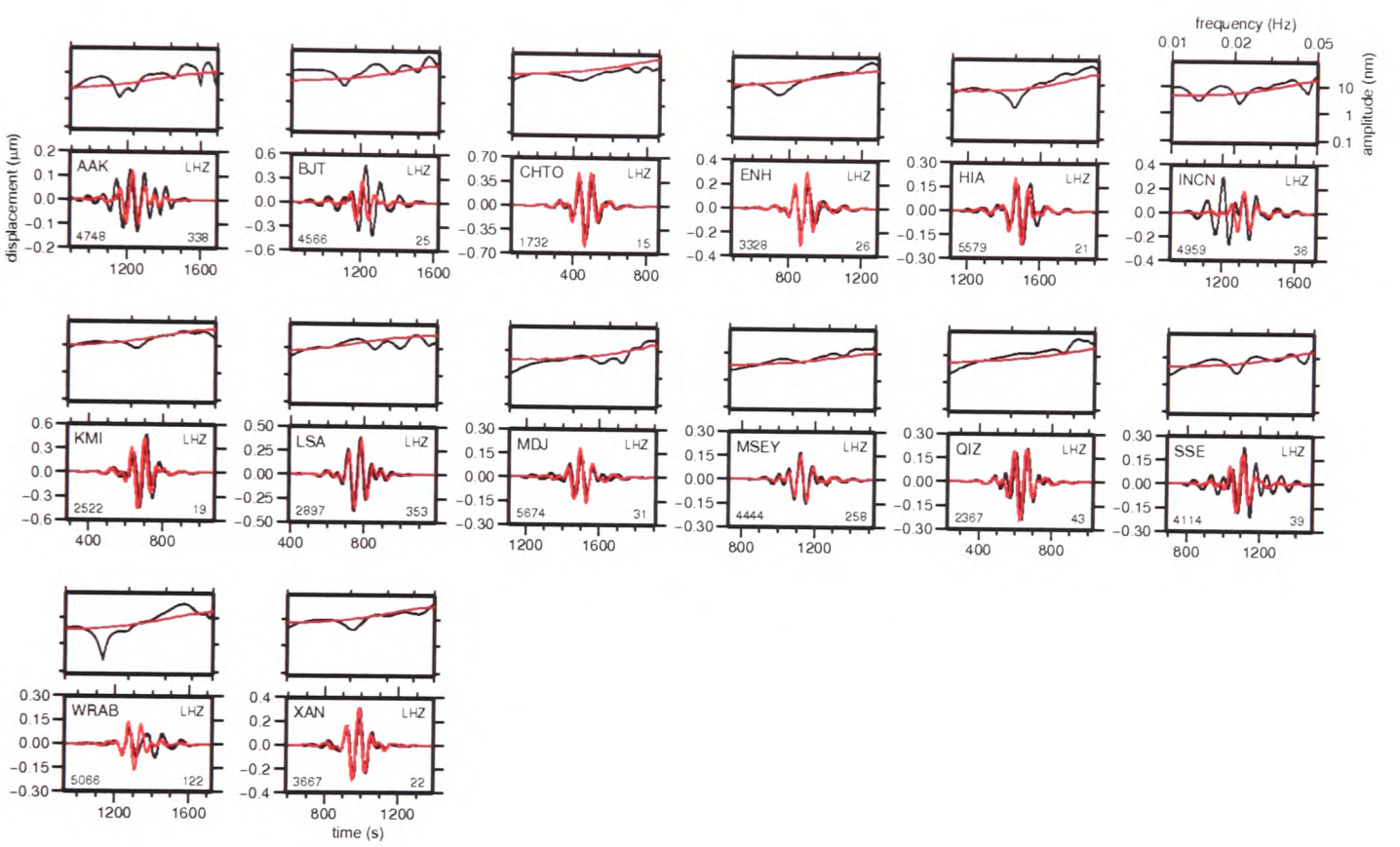


Synthetic (red) and data (black) amplitude spectra (top) and bandpass-filtered seismograms (bottom) for each station where the LHZ channel recording was used in the determination of source parameters for event 122704T.

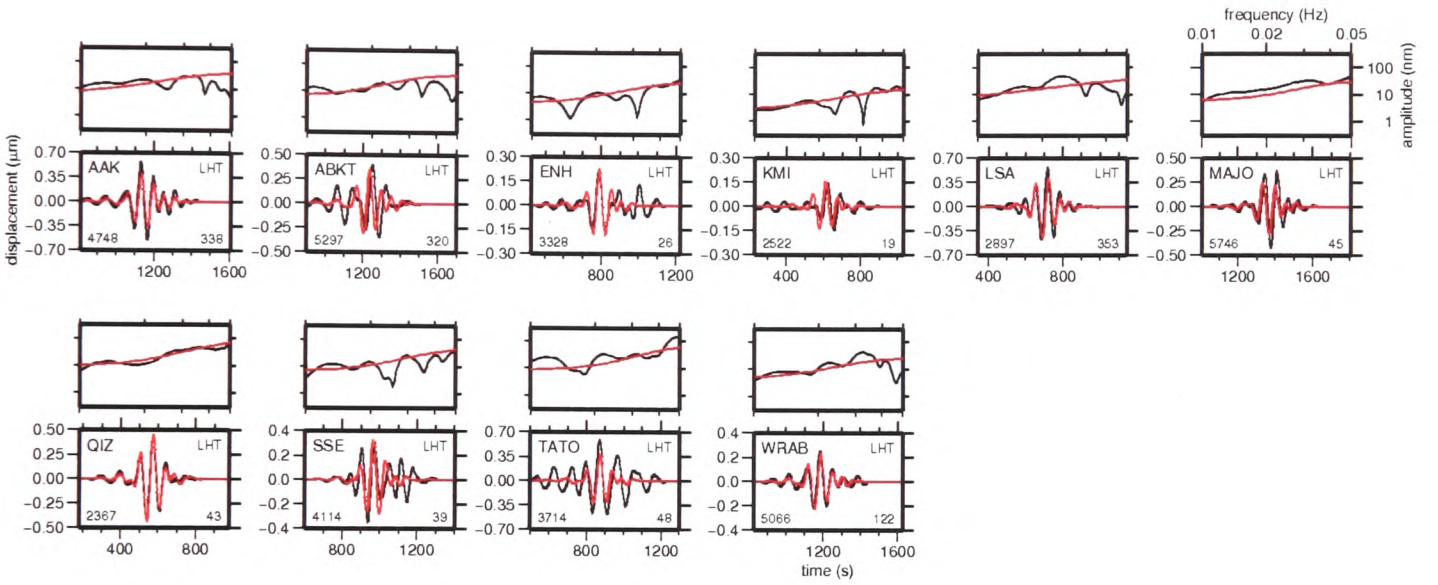


As previous figure but for LHT channel recordings.

APPENDIX F. SPECTRA AND WAVEFORMS FOR EARTHQUAKES IN CHAPTER 4

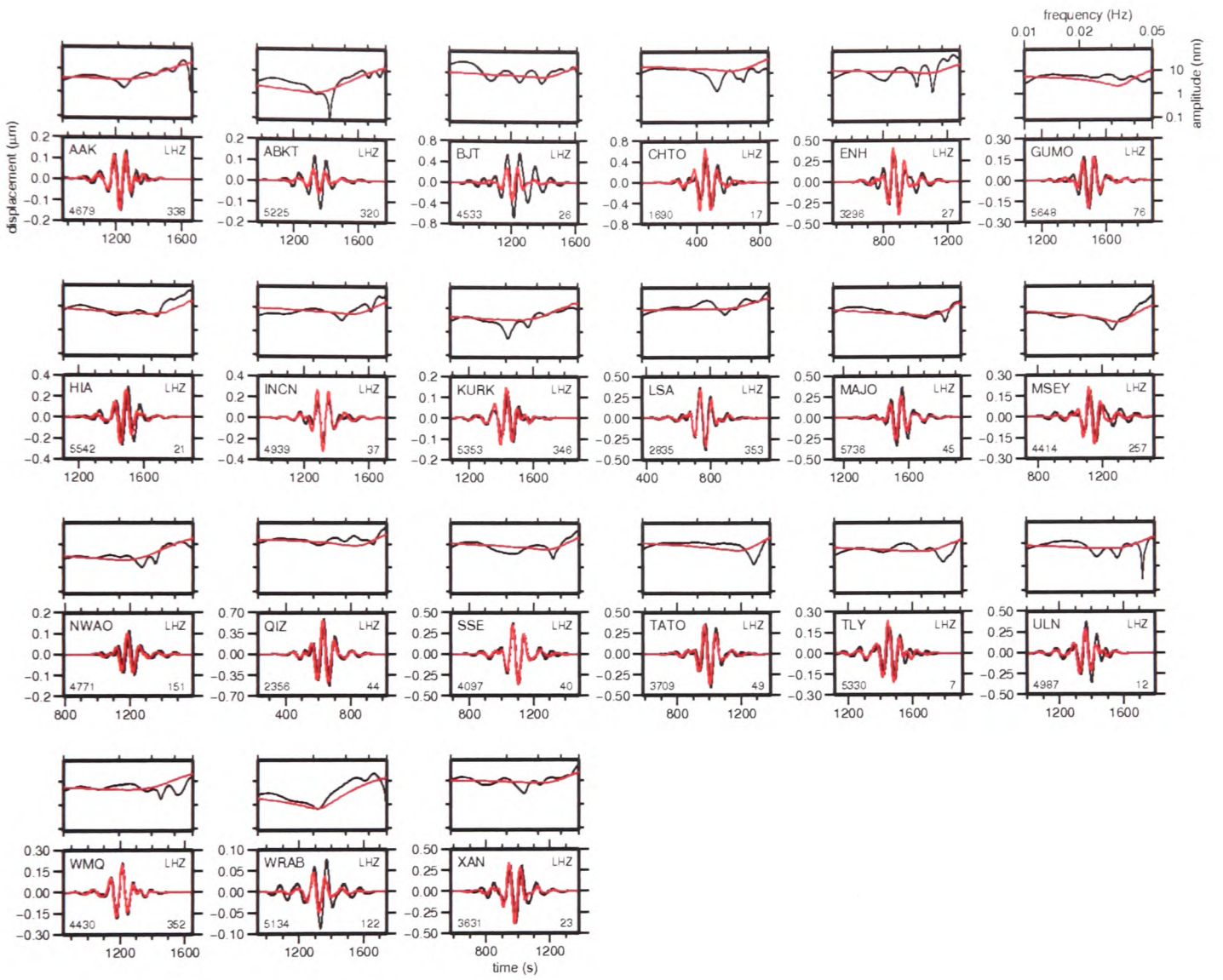


Synthetic (red) and data (black) amplitude spectra (top) and bandpass-filtered seismograms (bottom) for each station where the LHZ channel recording was used in the determination of source parameters for event 122804R.

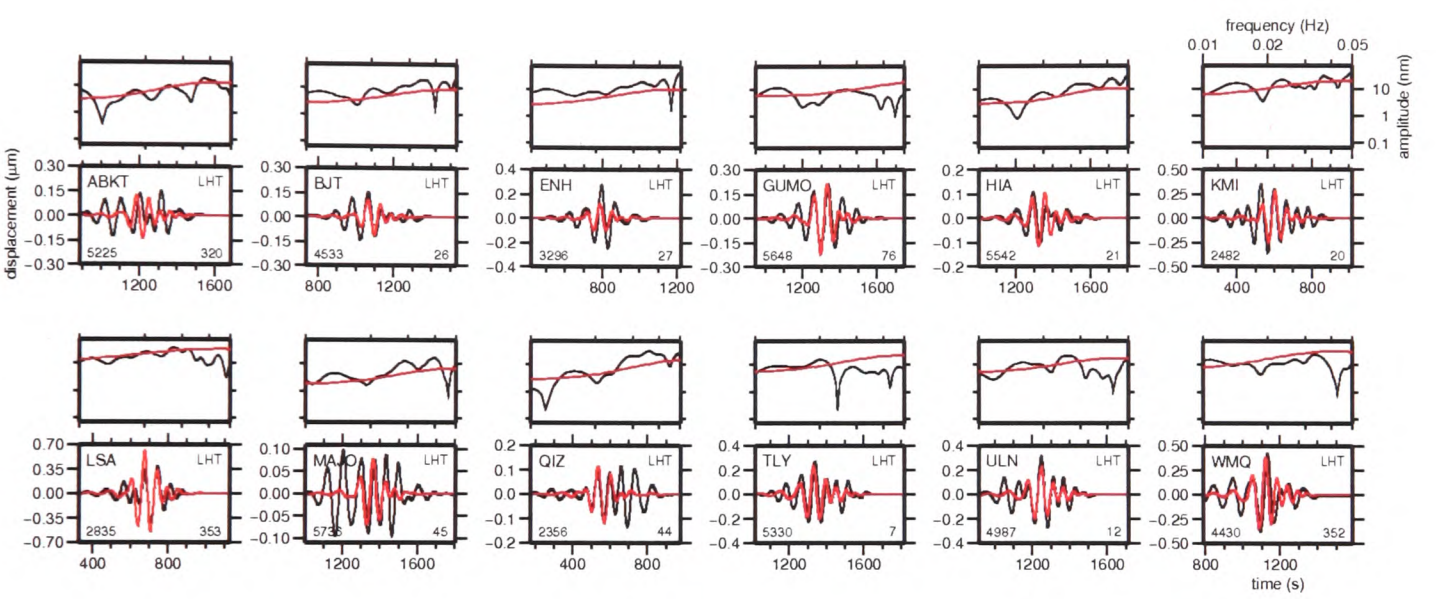


As previous figure but for LHT channel recordings.

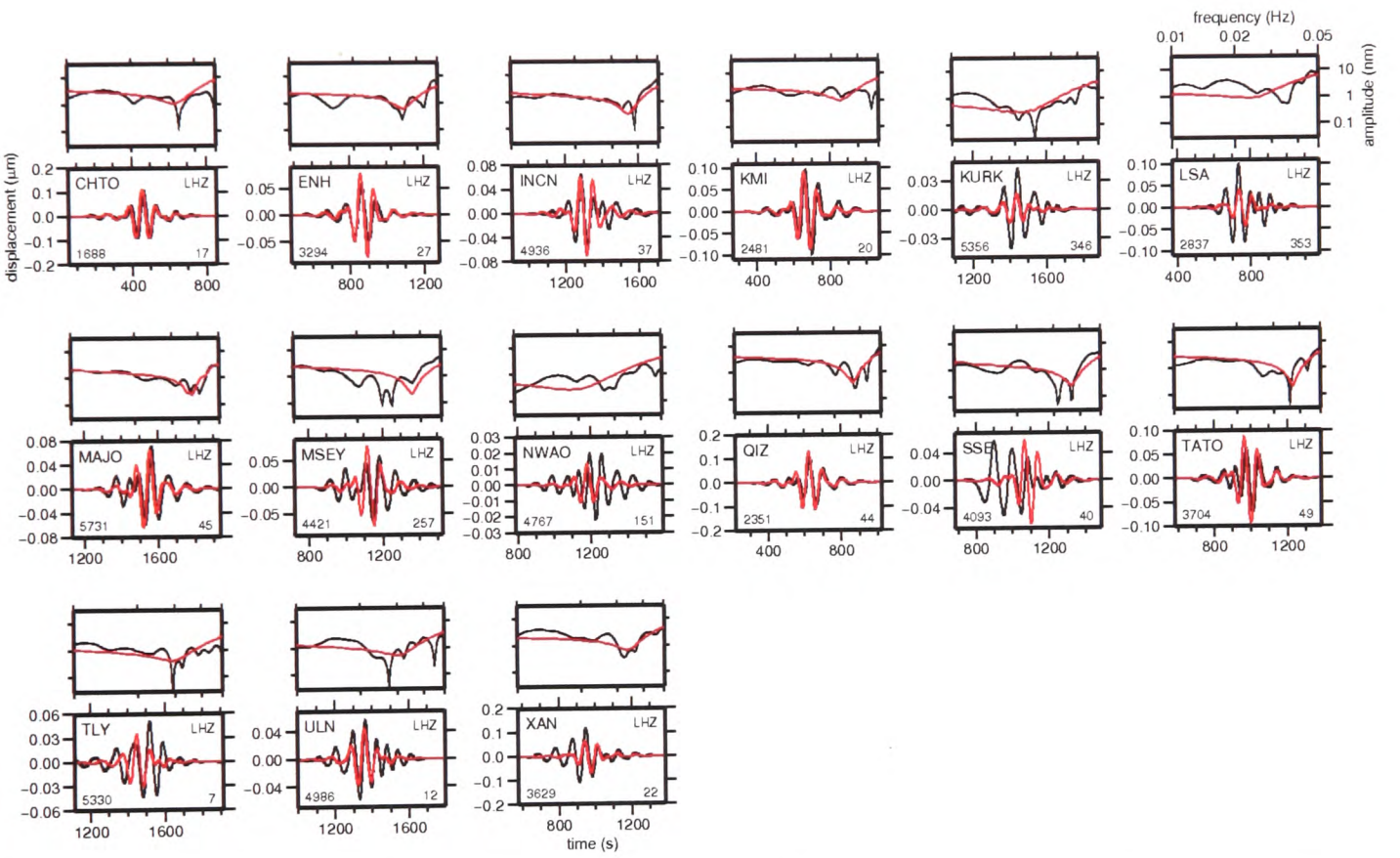
APPENDIX F. SPECTRA AND WAVEFORMS FOR EARTHQUAKES IN CHAPTER 4



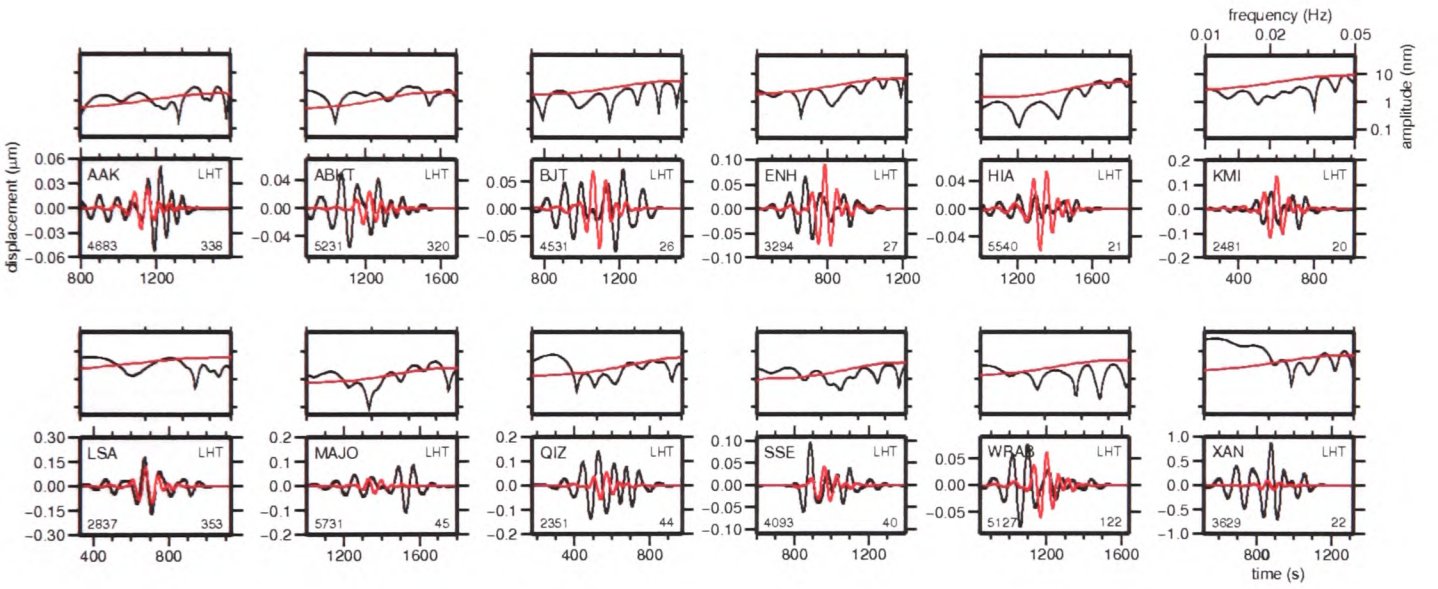
Synthetic (red) and data (black) amplitude spectra (top) and bandpass-filtered seismograms (bottom) for each station where the LHZ channel recording was used in the determination of source parameters for event 123004A.



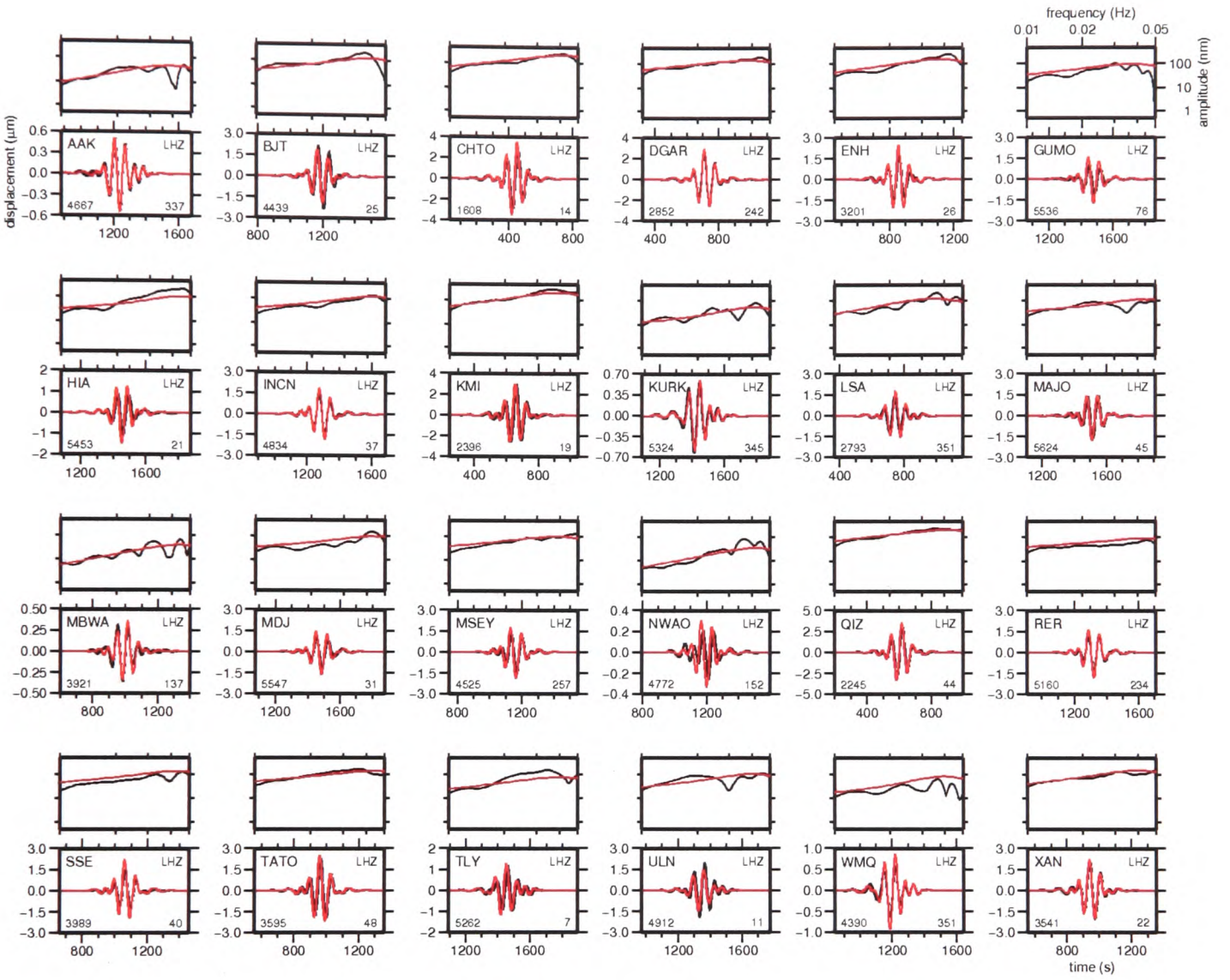
As previous figure but for LHT channel recordings.



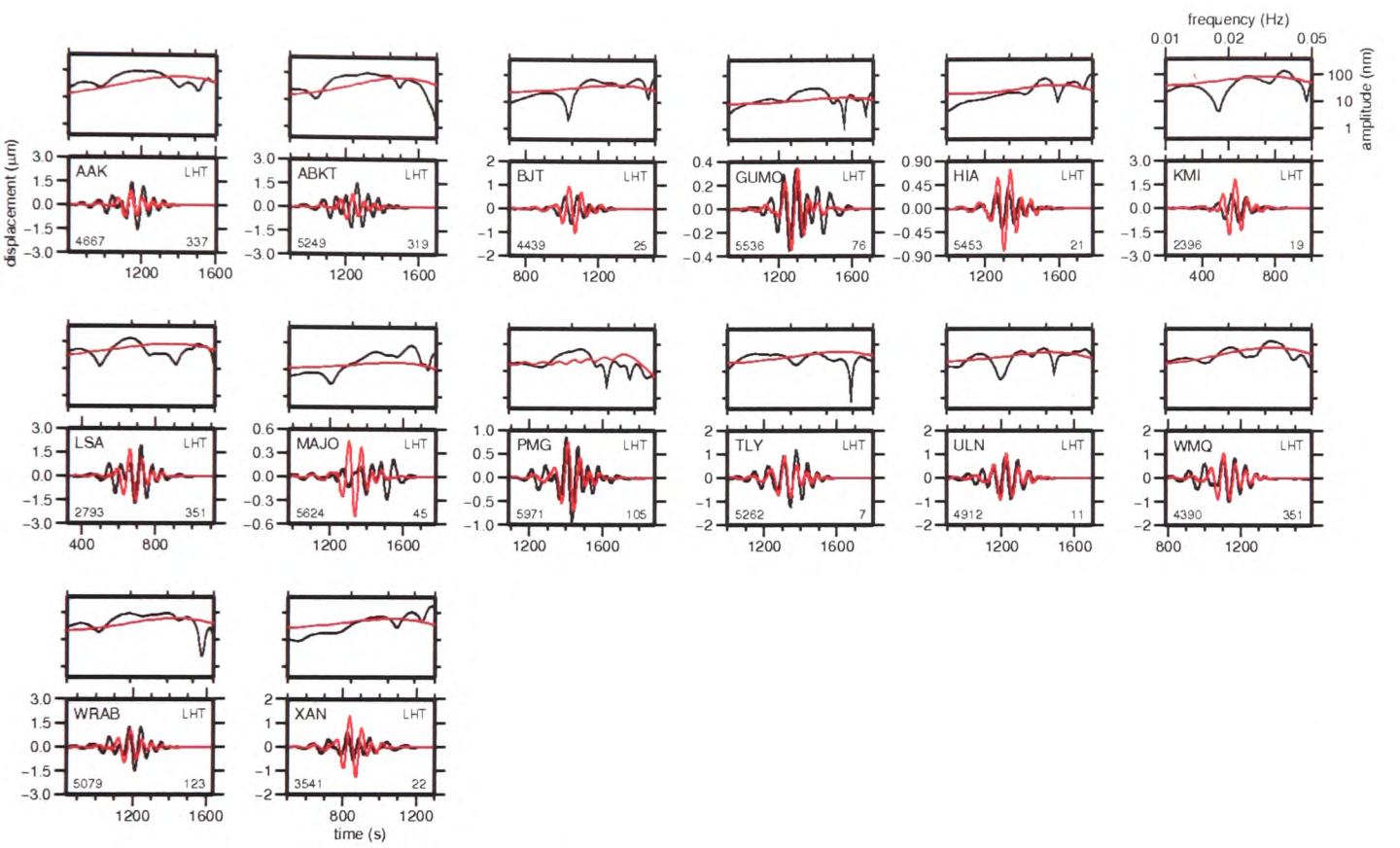
Synthetic (red) and data (black) amplitude spectra (top) and bandpass-filtered seismograms (bottom) for each station where the LHZ channel recording was used in the determination of source parameters for event 123004C.



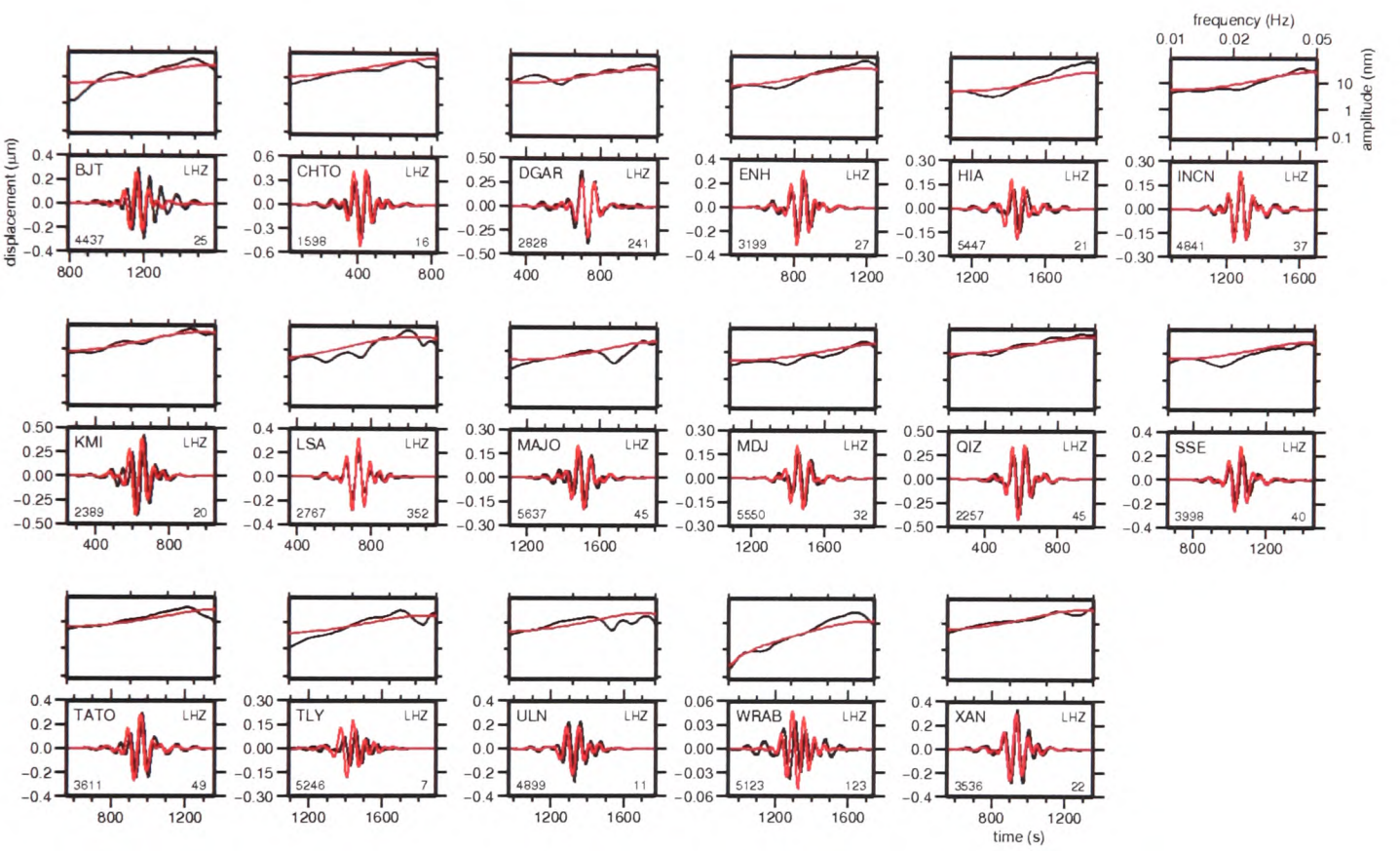
As previous figure but for LHT channel recordings.



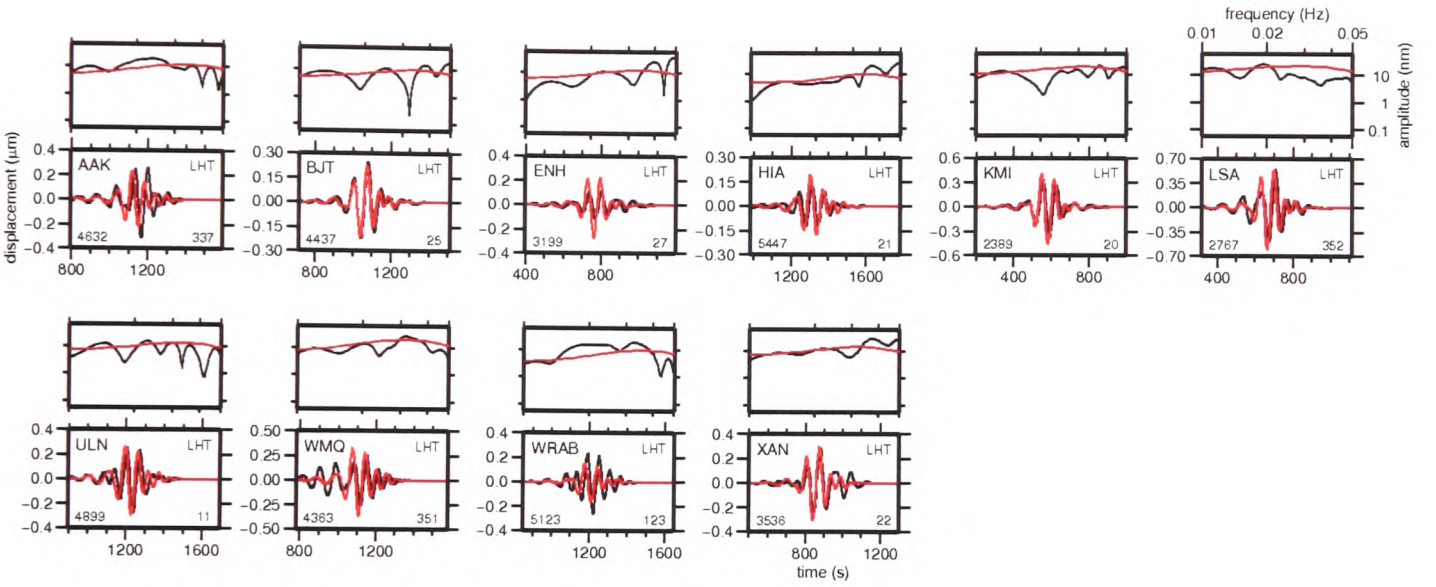
Synthetic (red) and data (black) amplitude spectra (top) and bandpass-filtered seismograms (bottom) for each station where the LHZ channel recording was used in the determination of source parameters for event 123104M.



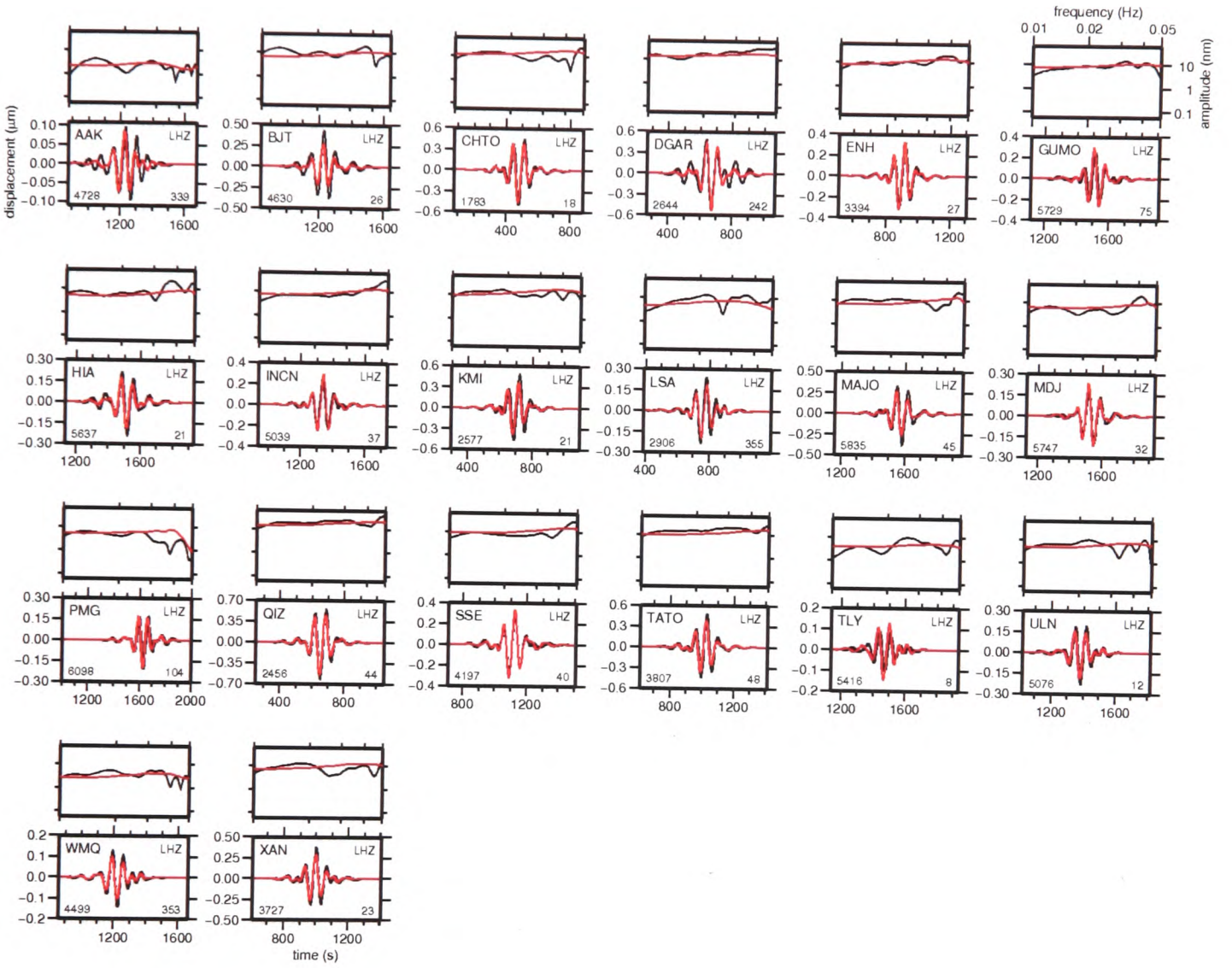
As previous figure but for LHT channel recordings.



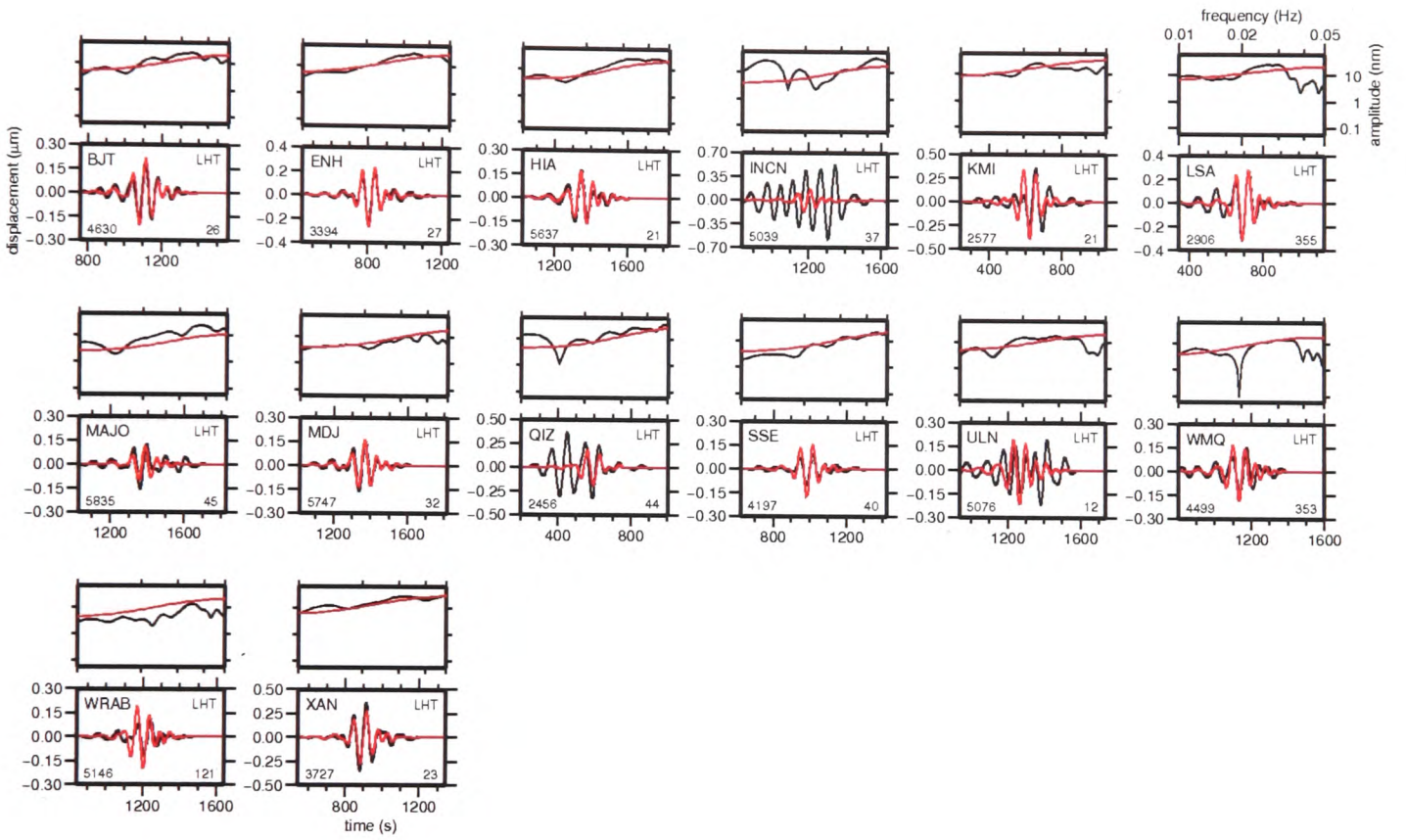
Synthetic (red) and data (black) amplitude spectra (top) and bandpass-filtered seismograms (bottom) for each station where the LHZ channel recording was used in the determination of source parameters for event 010405A.



As previous figure but for LHT channel recordings.

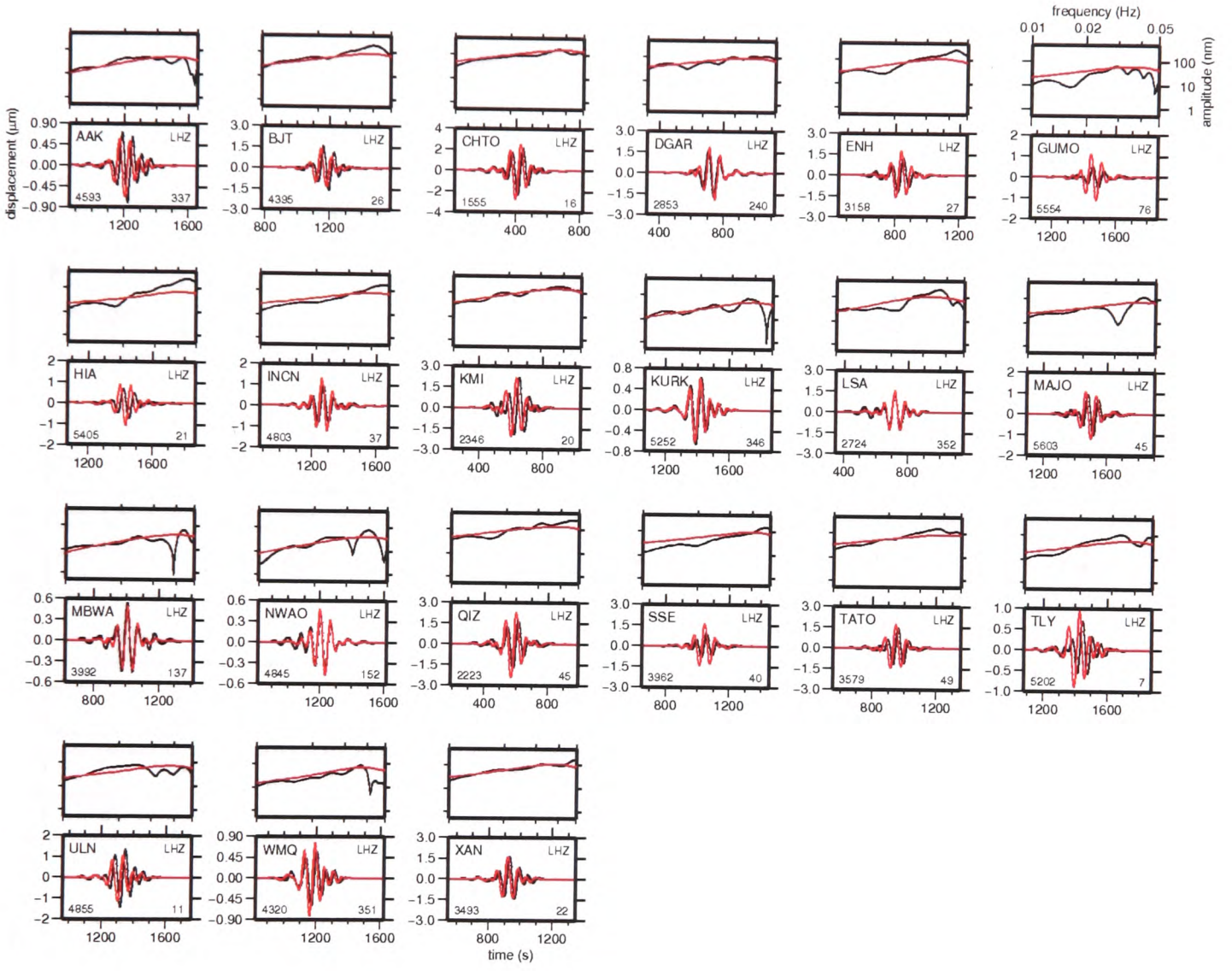


Synthetic (red) and data (black) amplitude spectra (top) and bandpass-filtered seismograms (bottom) for each station where the LHZ channel recording was used in the determination of source parameters for event 010505A.

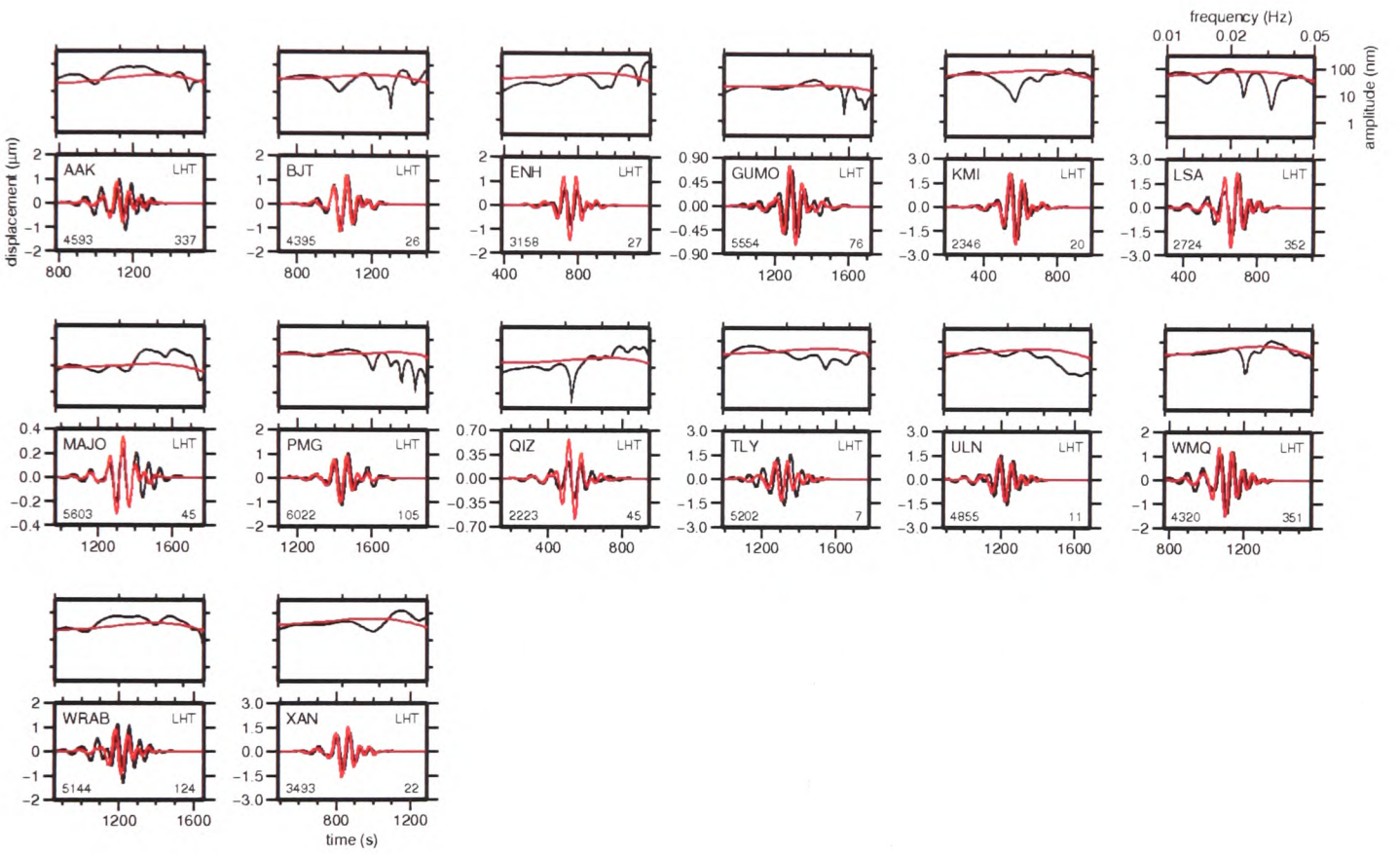


As previous figure but for LHT channel recordings.

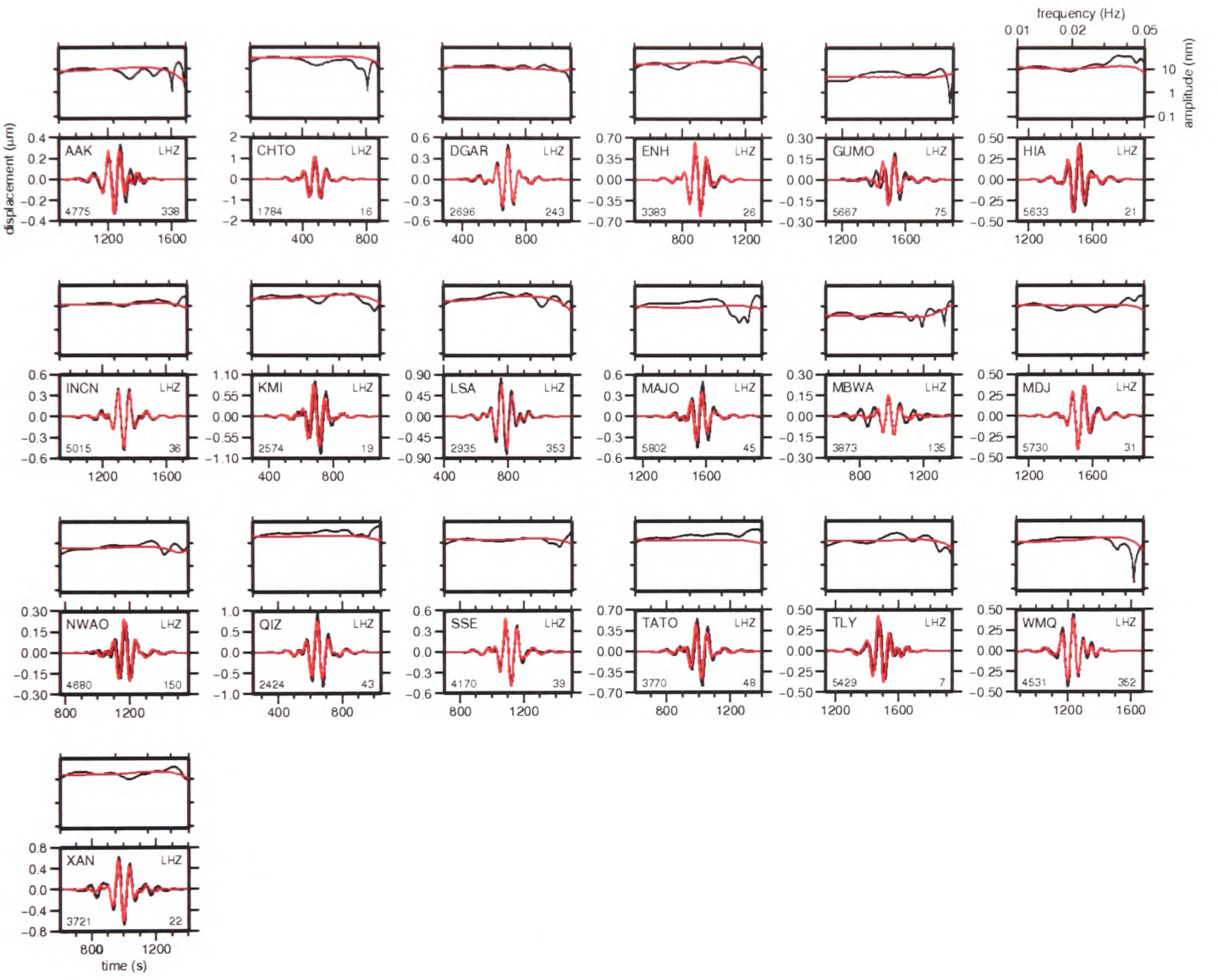
APPENDIX F. SPECTRA AND WAVEFORMS FOR EARTHQUAKES IN CHAPTER 4



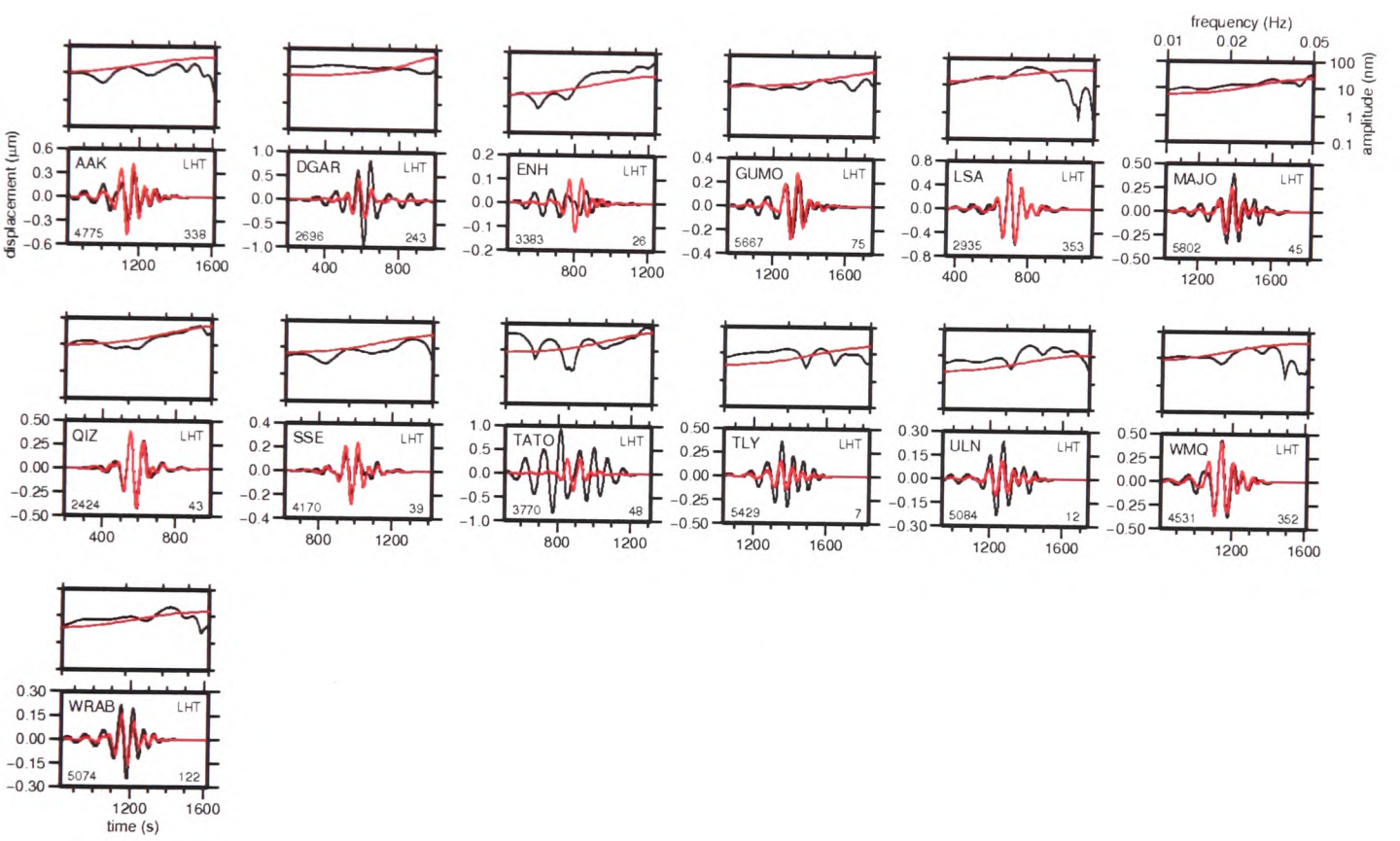
Synthetic (red) and data (black) amplitude spectra (top) and bandpass-filtered seismograms (bottom) for each station where the LHZ channel recording was used in the determination of source parameters for event 010605A.



As previous figure but for LHT channel recordings.

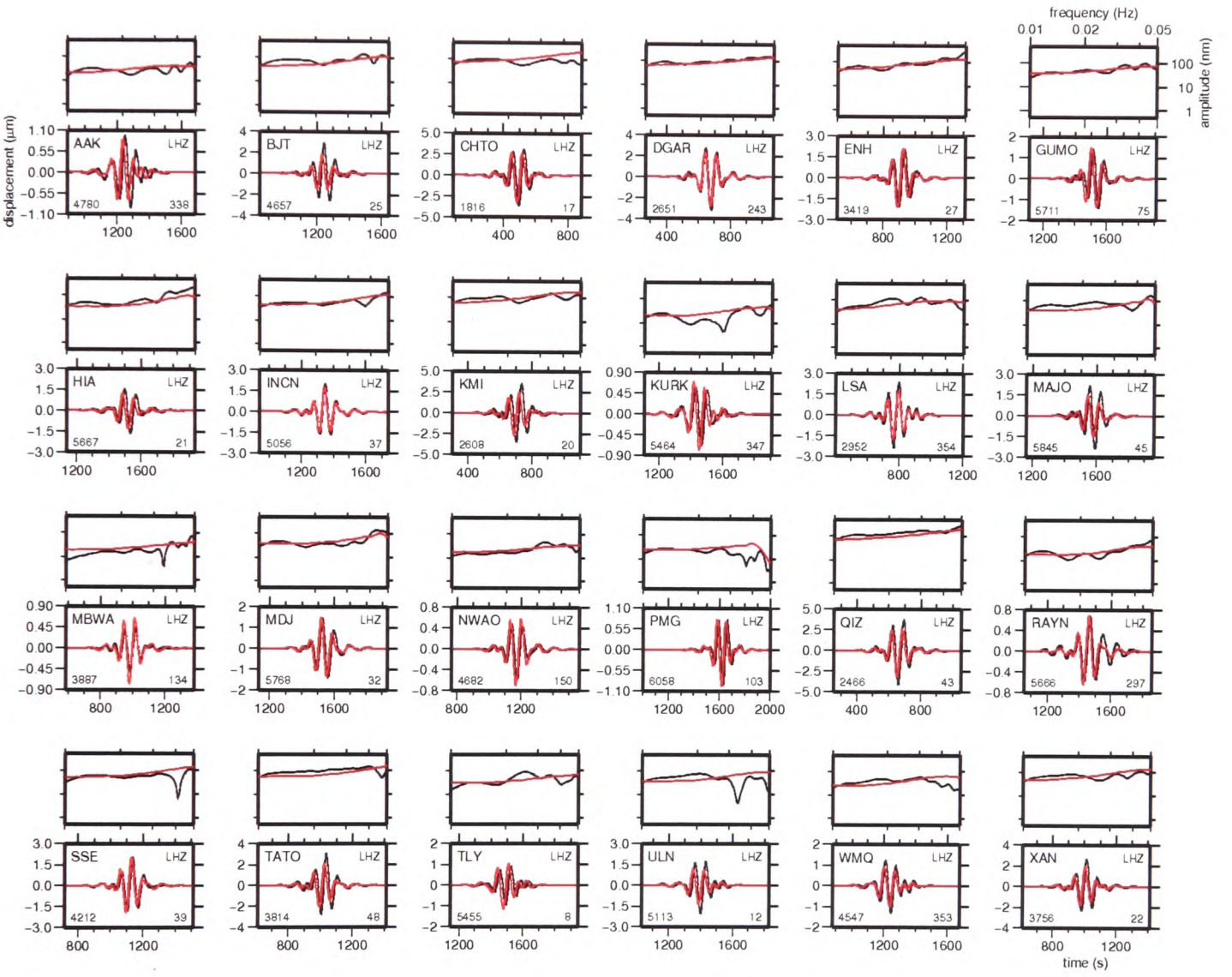


Synthetic (red) and data (black) amplitude spectra (top) and bandpass-filtered seismograms (bottom) for each station where the LHZ channel recording was used in the determination of source parameters for event 010905A.

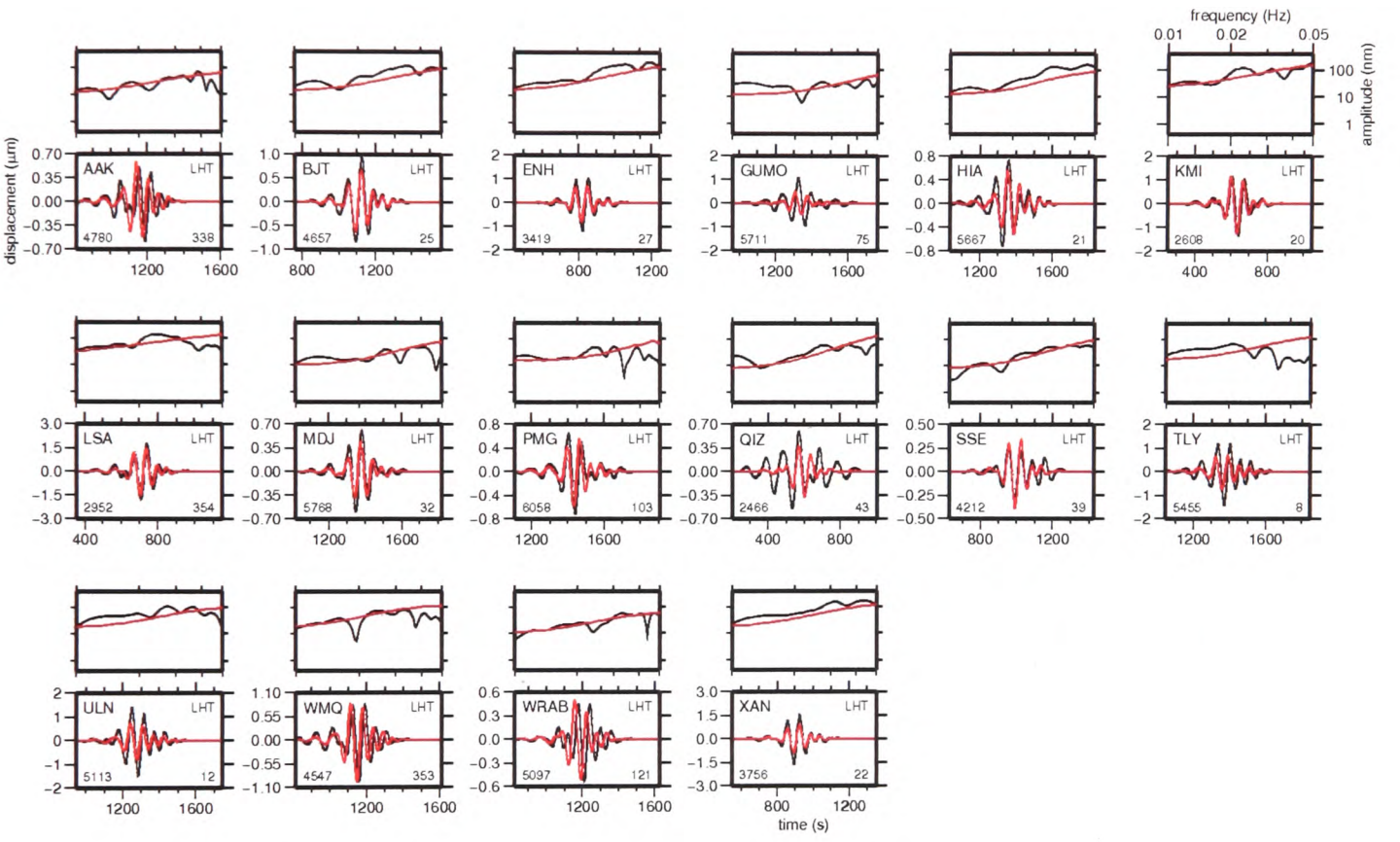


As previous figure but for LHT channel recordings.

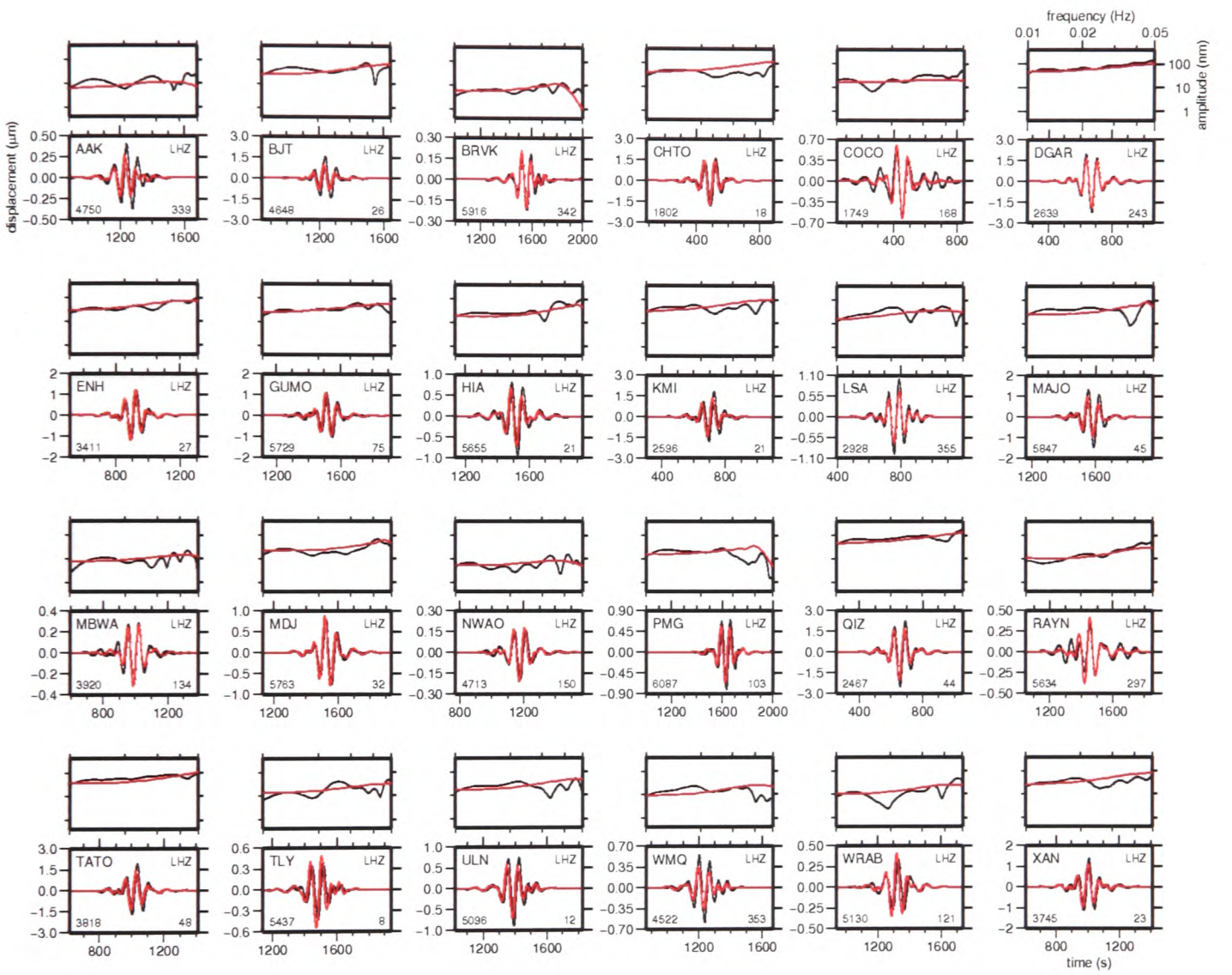
APPENDIX F. SPECTRA AND WAVEFORMS FOR EARTHQUAKES IN CHAPTER 4



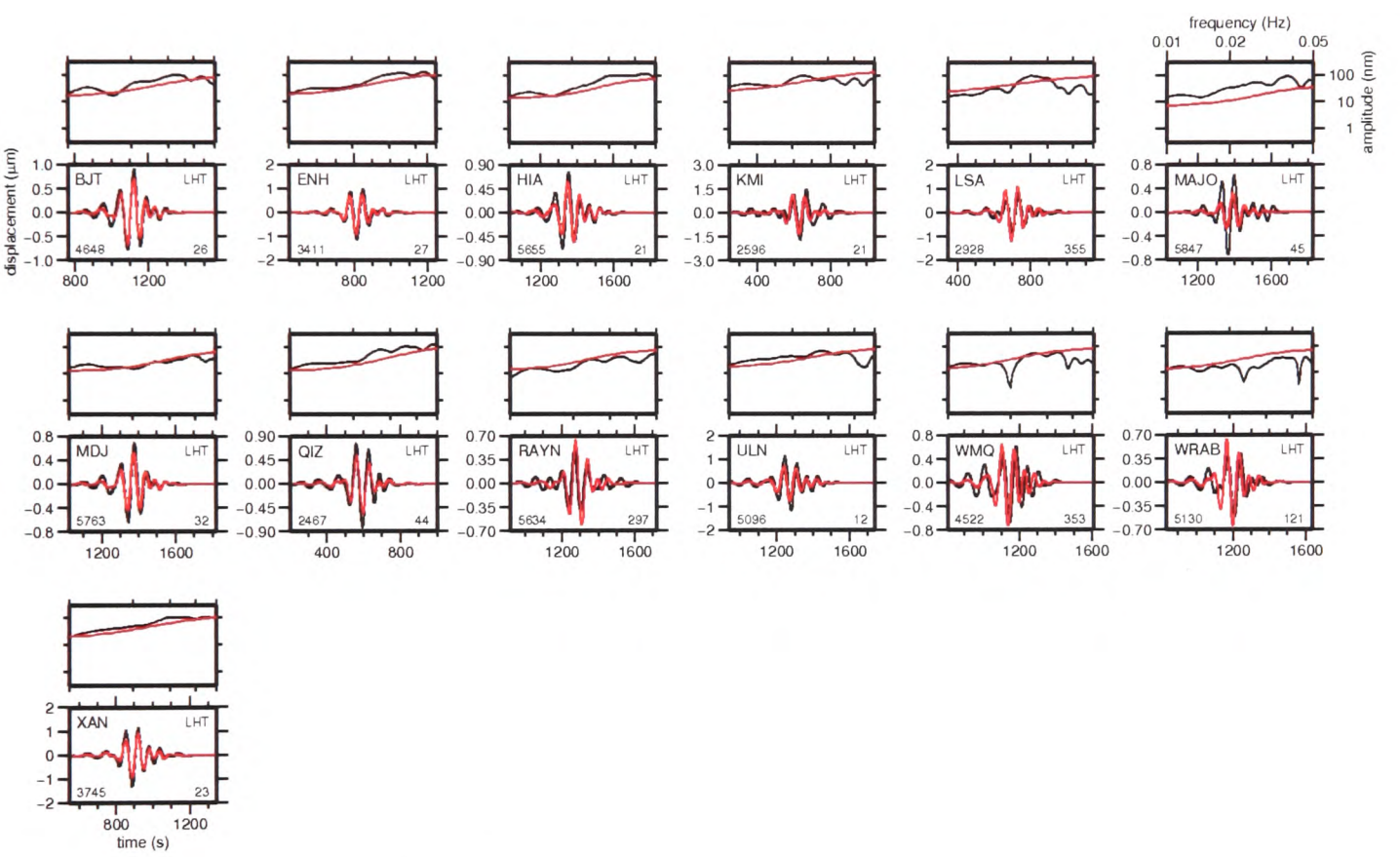
Synthetic (red) and data (black) amplitude spectra (top) and bandpass-filtered seismograms (bottom) for each station where the LHZ channel recording was used in the determination of source parameters for event 011405A.



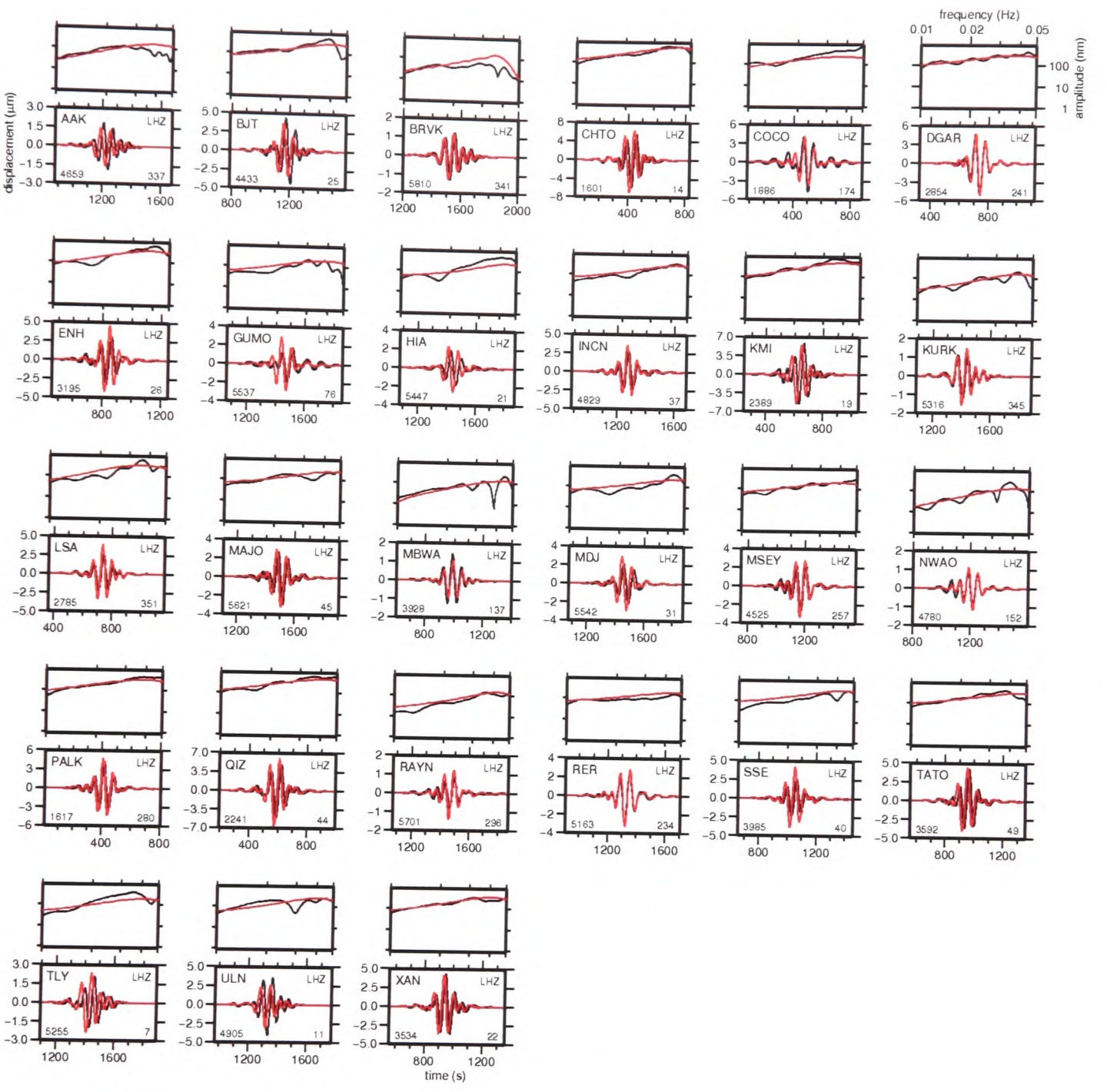
As previous figure but for LHT channel recordings.



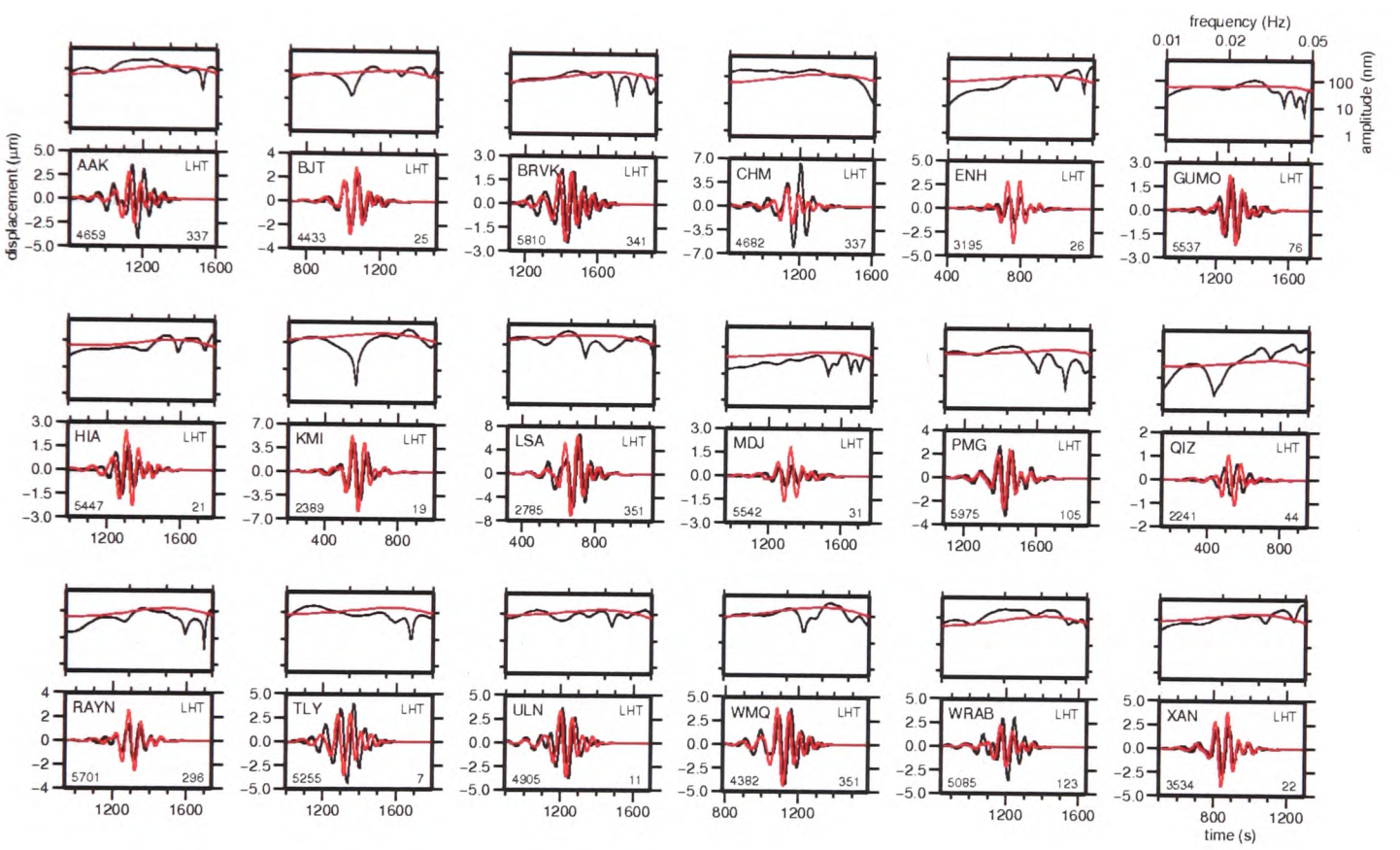
Synthetic (red) and data (black) amplitude spectra (top) and bandpass-filtered seismograms (bottom) for each station where the LHZ channel recording was used in the determination of source parameters for event 012905A.



As previous figure but for LHT channel recordings.

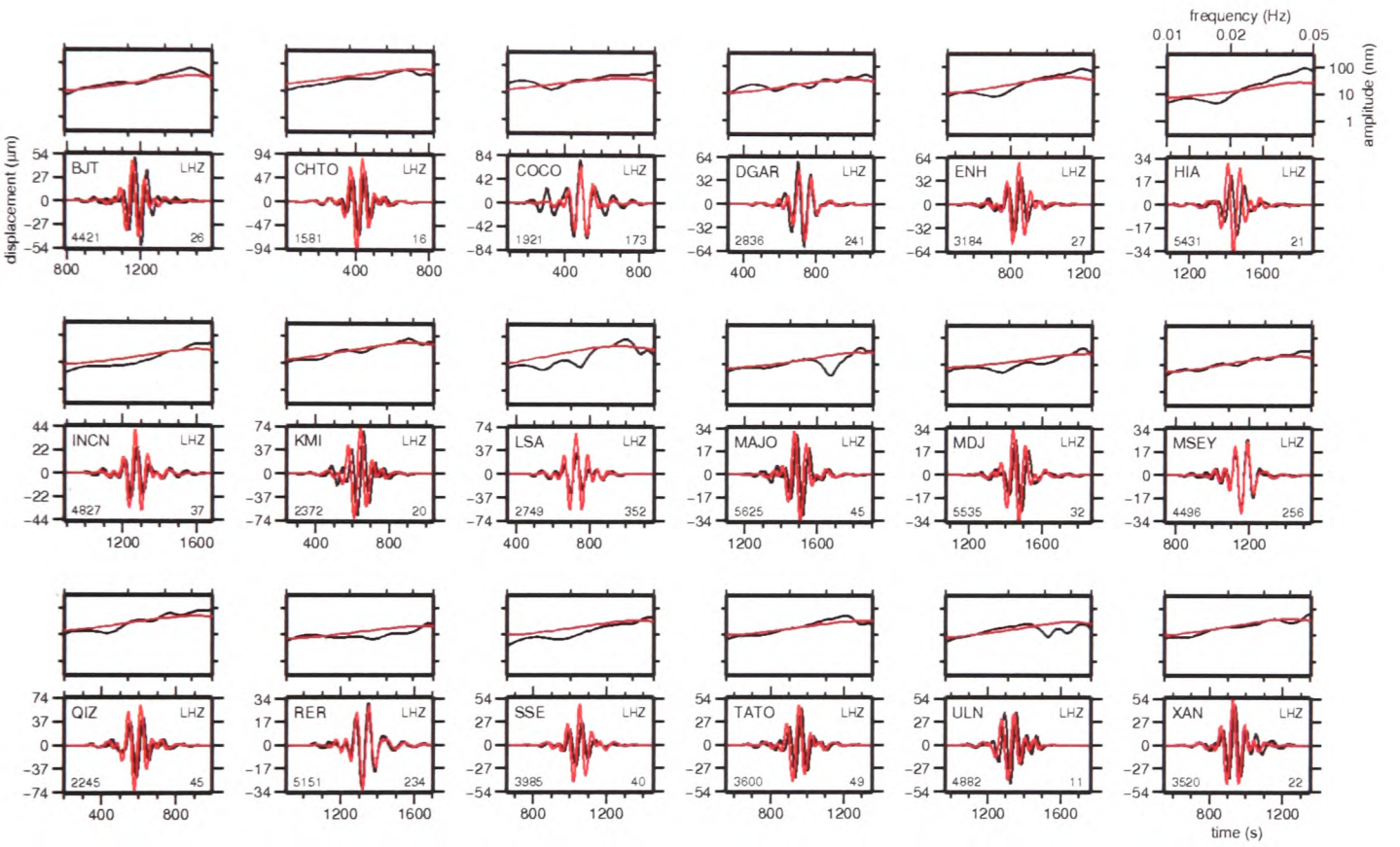


Synthetic (red) and data (black) amplitude spectra (top) and bandpass-filtered seismograms (bottom) for each station where the LHZ channel recording was used in the determination of source parameters for event 020905A.

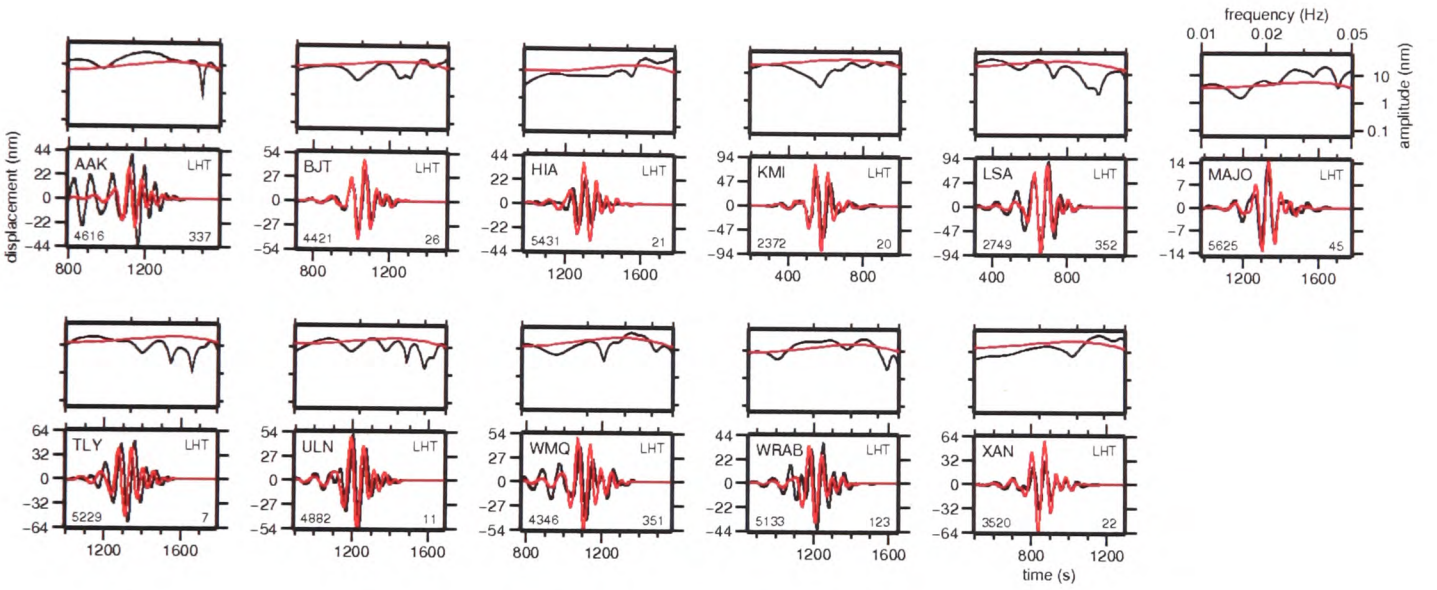


As previous figure but for LHT channel recordings.

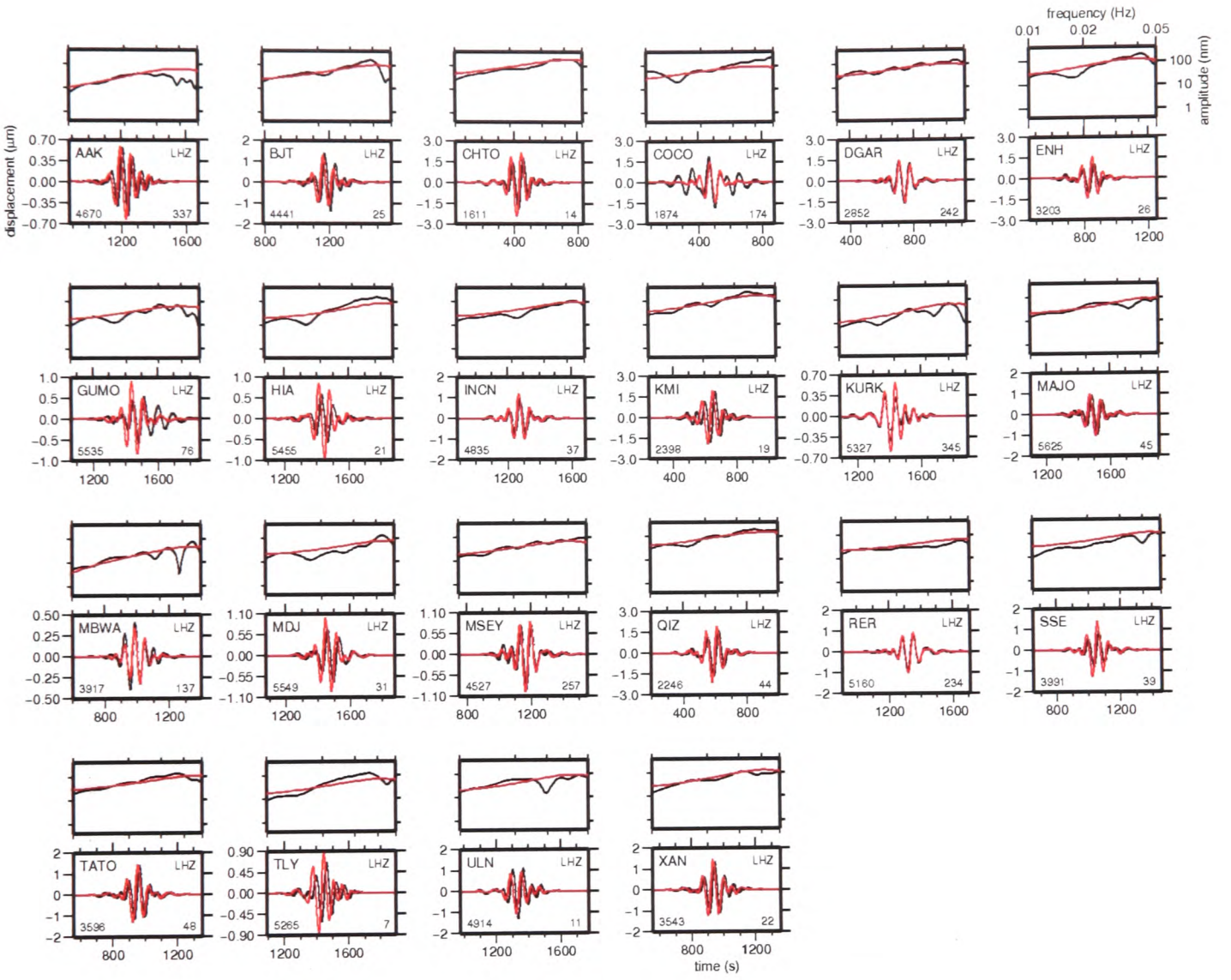
APPENDIX F. SPECTRA AND WAVEFORMS FOR EARTHQUAKES IN CHAPTER 4



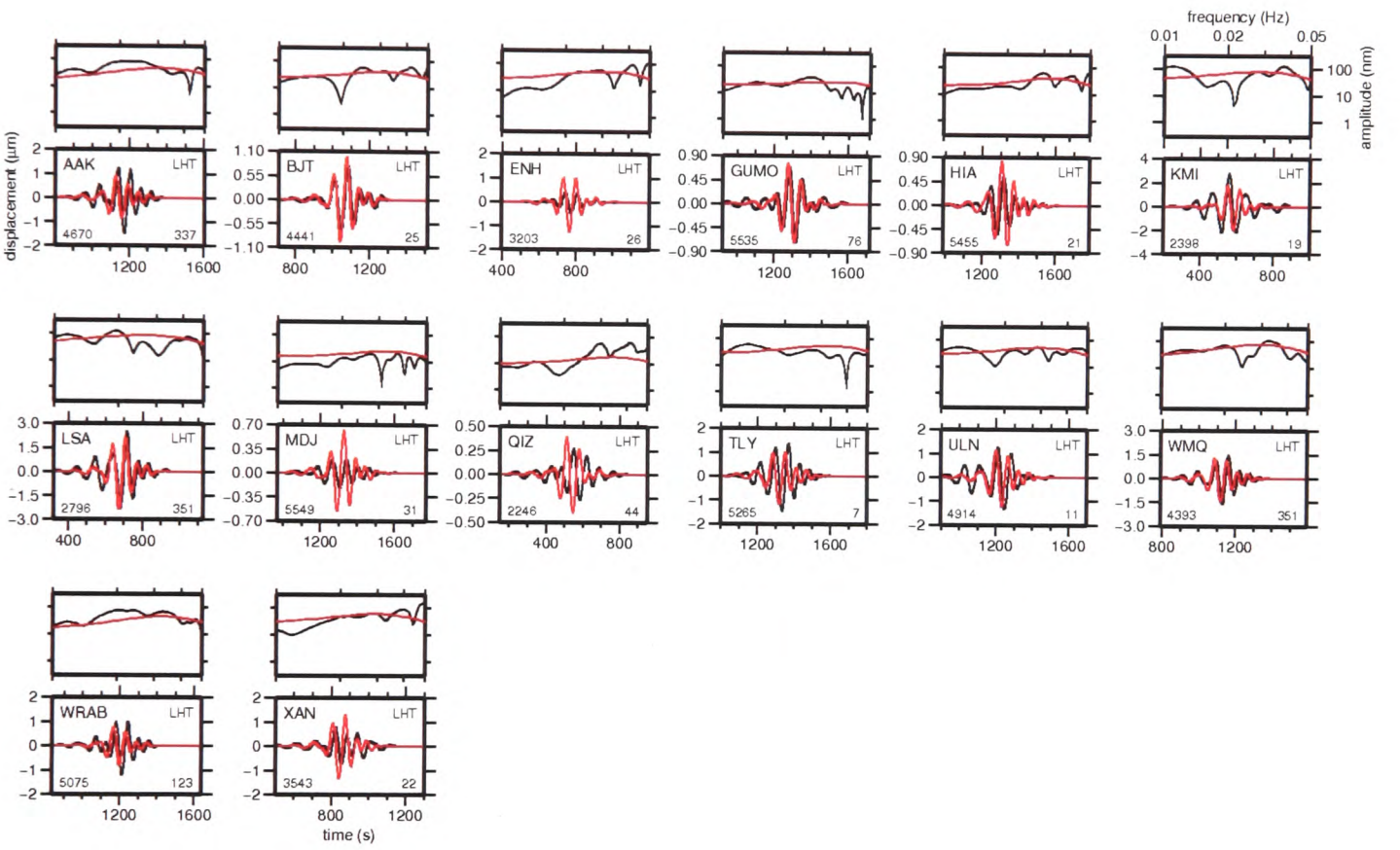
Synthetic (red) and data (black) amplitude spectra (top) and bandpass-filtered seismograms (bottom) for each station where the LHZ channel recording was used in the determination of source parameters for event 021305A.



As previous figure but for LHT channel recordings.

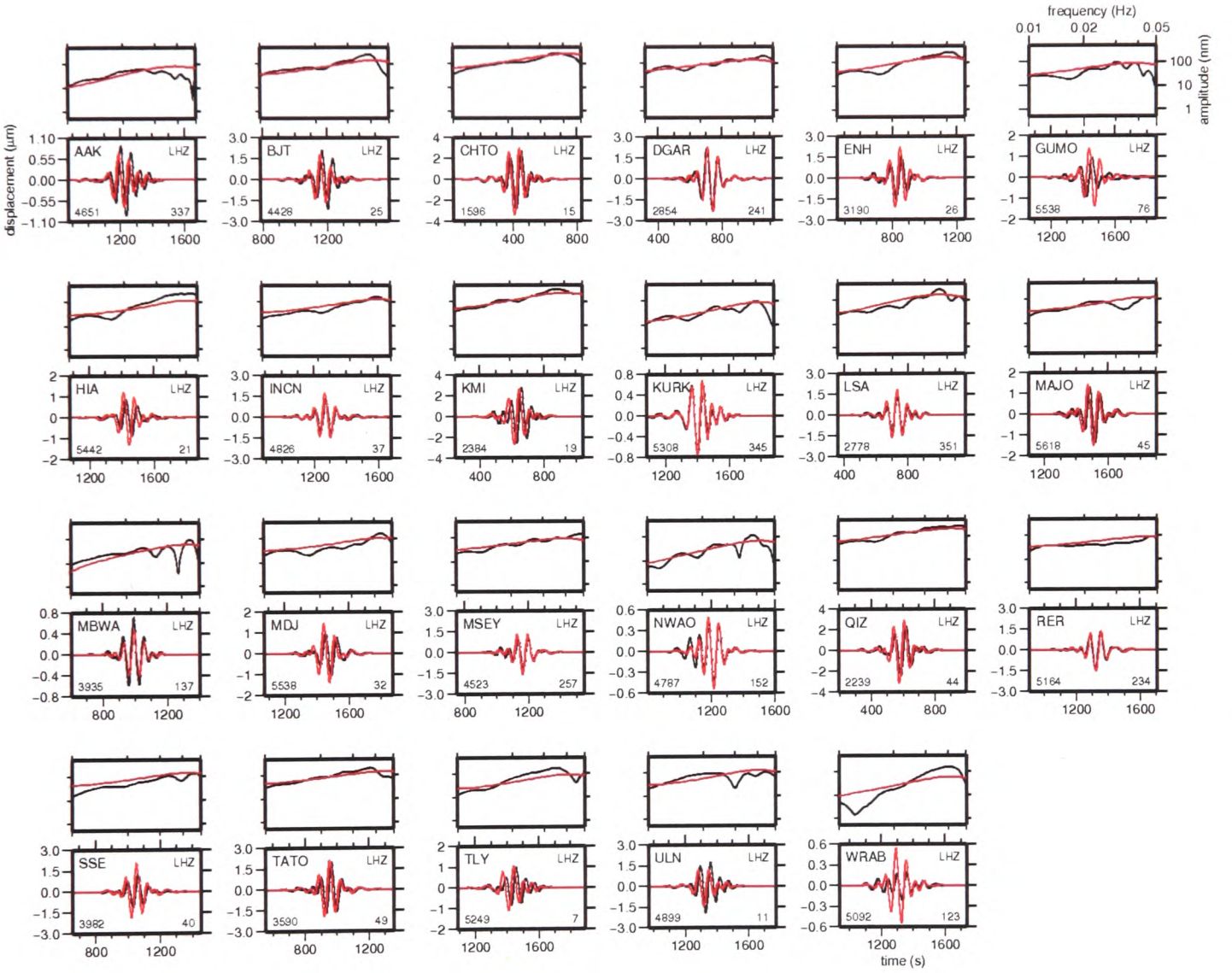


Synthetic (red) and data (black) amplitude spectra (top) and bandpass-filtered seismograms (bottom) for each station where the LHZ channel recording was used in the determination of source parameters for event 021705A.

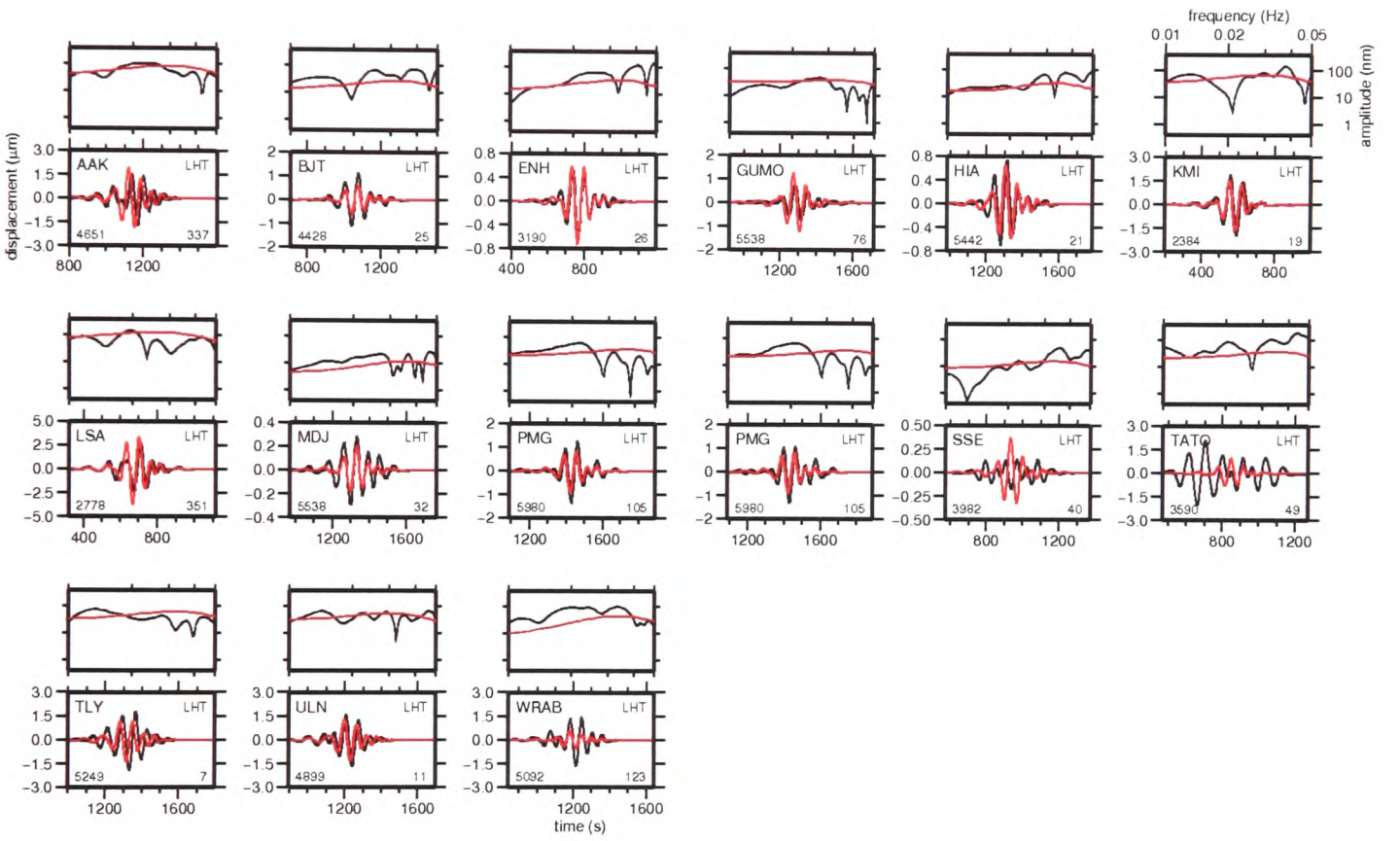


As previous figure but for LHT channel recordings.

APPENDIX F. SPECTRA AND WAVEFORMS FOR EARTHQUAKES IN CHAPTER 4



Synthetic (red) and data (black) amplitude spectra (top) and bandpass-filtered seismograms (bottom) for each station where the LHZ channel recording was used in the determination of source parameters for event 031705A.



As previous figure but for LHT channel recordings.

Appendix G

Calculations of the Subduction Zone dip in Chapter 4

What follows is a description of calculations performed to estimate the dip of the subduction zone as defined by the locations of the eight Offshore Banda Aceh aftershocks.

Given that the orientation of the transect is aligned with the likely down-dip direction of the subduction interface, assuming a planar plate boundary and trustworthy estimates of source depths; calculations of the subduction dip angle can be performed. The equation of a straight line plotted through these aftershocks is of the form:

$$h = ax + b, \tag{G.1}$$

where h is depth, x is the distance landward from the trench, a is the gradient of the straight line and b is point at which that line crosses the depth axis at the trench. By solving the following equation, estimates of a and b can be determined:

$$\begin{pmatrix} n & \sum_{i=1}^{n} x_i \\ \sum_{i=1}^{n} x_i & \sum_{i=1}^{n} x_i^2 \end{pmatrix} \begin{pmatrix} b \\ a \end{pmatrix} = \begin{pmatrix} \sum_{i=1}^{n} h_i \\ \sum_{i=1}^{n} h_i x_i \end{pmatrix}, \tag{G.2}$$

where n is the total number of aftershocks and h_i and x_i are the horizontal and vertical locations of the ith earthquake from the trench axis along the transect. In the simplest case, where the interface is rigid and of constant dip from the trench and through the earthquakes located here (i.e. $b = 0$, a suitable approximation for the depth of the trench some 300 km from the furthest aftershock), then Equation G.2 can be solved to give a dip angle (θ_d) defined

by:

$$\theta_d = \tan^{-1}\left(\frac{\sum_{i=1}^{8} h_i}{\sum_{i=1}^{8} x_i}\right). \tag{G.3}$$

Using Equation G.3 an estimate of the interface dip is made of 14°, close to the 10° and 12° suggested by Dewey et al. (2007), but significantly shallower than the $27 \pm 4°$ dip calculated by Engdahl et al. (2007).

Considering a rigid interface, whose dip angle does not change in the region of these earthquakes but is not required to intersect the trench axis (i.e. b is allowed to be non-zero), the solutions to Equation G.2 are as follows:

$$a = \frac{(n\sum_{i=1}^{n} h_i x_i) - (\sum_{i=1}^{n} x_i \sum_{i=1}^{n} h_i)}{(n\sum_{i=1}^{n} x_i^2) - (\sum_{i=1}^{n} x_i \sum_{i=1}^{n} x_i)}, \tag{G.4}$$

and

$$b = \frac{\sum_{i=1}^{n} h_i - (\sum_{i=1}^{n} x_i a)}{n}. \tag{G.5}$$

Calculations performed using these equations yield a steeper estimate of the interface dip of 22°.

Event	h_{min} (km)	h_0 (km)	h_{max} (km)	(σ)
122704T	27	52	68	10.5
123104M	33	51	73	10.2
010405A	19	46	67	12.2
010601A	31	61	84	13.5
020905A	33	53	72	9.9
021305A	22	55	77	14.0
021705A	30	50	71	10.5
031705A	26	52	74	12.2

Table G.1: Depth estimates of the eight aftershocks considered to be slab interface events, used in the determination of the likely angle of dip of the plate boundary. Values of minimum (h_{min}), optimum (h_0) and maximum (h_{max}) depth are shown, along with estimates of the standard deviations (σ) of these depth distributions.

Errors related to the location of these aftershocks in 3-D space have not yet been taken into account; there are errors associated with both the NEIC-determined hypocentres and the depth locations determined in this study. Table G.1 lists the minimum (h_{min}), optimum

(h_0) and maximum ($h_{\max}$) depth for each aftershock along with calculations of the standard deviation (σ). The values of $h_{\min}$ and $h_{\max}$ for each event correspond to the end-member depths of those solutions lying within 95% confidence bounds and are probably over-estimated. Assuming these errors are distributed normally, then this confidence bound equates to 1.96σ; as such the values of σ listed in Table G.1 are calculated using:

$$\sigma = \frac{h_{\max} - h_{\min}}{3.92}. \tag{G.6}$$

Errors associated with the NEIC location estimates vary with geographic position, but can be considered to be of similar order for these localised earthquakes. Hypocentral locations are typically accurate to a few tenths of a degree[1], so errors are assumed to be of the order of a few tens of kilometres. Using a weighted least squares routine (Press et al., 1996), which takes into account the standard deviation of both depth and distance along the transect and normalises observations by their variance, further estimates can be made of the dip of the slab interface in the Offshore Banda Aceh region.

Location variance (σ^2)	δ_0 (°)	$\delta_{\min}$ (°)	$\delta_{\max}$ (°)
0	21.8 (21.8)	-10.9 (7.1)	44.8 (34.1)
10	21.9 (22.1)	-11.1 (7.0)	45.0 (34.5)
20	21.9 (22.3)	-11.2 (6.9)	45.1 (35.0)
30	22.0 (22.6)	-11.3 (6.8)	45.2 (35.4)
40	22.1 (22.8)	-11.4 (6.7)	45.4 (35.8)
50	22.1 (23.0)	-11.6 (6.6)	45.5 (36.2)

Table G.2: Values of best-determinable interface dip (δ_0) and the errors (between $\delta_{\min}$ and $\delta_{\min}$) associated with these calculations. The values in brackets pertain to the same calculations but performed with depth σ values which are halved, i.e. what could be expected with better depth estimates. The range of acceptable dip angles decreases with this halving, nonetheless it is still of the order of 30°. Because of inaccuracies in the knowledge of the likely errors associated with the NEIC hypocentral locations, a range of values of variance (σ^2) are listed.

Table G.2 lists estimates of the plate boundary dip, along with the range of dips associated with the errors in location. It is clear that, although the variance of the location is altered significantly, the best-fitting slab dip determined remains 22°. Because of the size of the depth errors presented here, this dip angle has large errors, indeed these are sufficiently high to consider whether the determined interface angle here is at all trustworthy. More tightly constrained depth estimates would be of great help in this kind of analysis, but unfortunately it is not provided by these intermediate-period surface wave observations. The best compromise is to consider the point sources only and have faith in the best-fitting depths which are shown to broadly align down-dip in Figure 4.4.

It is thought unlikely that the interface is a planar feature; indeed it is perhaps more useful to think of the plate boundary as a 'rupture volume', a 3-D space in which faulting occurs, driven by the relative plate motion of the Indian and Sunda plates. As such, the calculation

[1] http://earthquake.usgs.gov/regional/neic/neic_bulletins.php

of an average dip of this volume of 22° is perhaps more meaningful, tectonically. The lack of constraint placed on this orientation highlights the requirement for accurate intermediate-depth hypocentre locations to complement studies, such as this one, which provide well-determined focal mechanism from which seismo-tectonic inferences can be drawn.

Bibliography

Agnieszka, K. & S. A. Sipkin. Non-double-couple earthquake mechanisms in the Nazca plate subduction zone. *Geophys. Res. Lett.*, **14**, 339–342, 1987.

Aki, K. & H. Patton. Determination of seismic moment tensor using surface waves. *Tectonophysics*, **49**, 213–222, 1979.

Aki, K. & P. Richards. *Quantitative Seismology.* W. H. Freeman and Company, San Francisco, 1980.

Ammon, C. J., C. Ji, H.-K. Thio, D. Robinson, S. Ni, V. Hjorleifsdottir, H. Kanamori, T. Lay, S. Das, D. Helmberger, G. Ichinose, J. Polet & D. Wald. Rupture process of the 2004 Sumatra-Andaman earthquake. *Science*, **308**, 1133–1139, 2005.

Ammon, C. J., G. E. Randall & J. Julia. Improving estimates of depth, magnitude, and faulting parameters of earthquakes in central Asia. *25th Seismic Research Review*, pages 24–33, 2003.

Arvidsson, R. & G. Ekström. Global CMT analysis of moderate earthquakes, $M_w \geq 4.5$, using intermediate-period surface waves. *Bull. Seismol. Soc. Am.*, **88**, 1003–1013, 1998.

Bakun, W. H. & A. G. Lindh. The Parkfield, California, Earthquake Prediction Experiment. *Science*, **229**, 619–624, 1985.

Bakun, W. H. & T. V. McEvilly. Recurrence models and Parkfield, California, earthquakes. *J. Geophys. Res.*, **89**, 3051–3058, 1984.

Bassin, C., G. Laske & G. Masters. The current limits of resolution for surface wave tomography in North America. *EOS Trans. AGU*, **F897**, 81, 2000.

Bettinelli, P., J.-P. Avouac, M. Flouzat, F. Jouanne, L. Bollinger, P. Willis & G. R. Chitrakar. Plate motion of India and interseismic strain in the Nepal Himalaya from GPS and DORIS measurements. *J. Geodesy*, **80**, 567–589, 2006.

Bilham, R. A flying start, then a slow slip. *Science*, **308**, 1126–1127, 2005.

Bowers, D. & D. A. McCormack. The mechanisms of shallow earthquakes and the monitoring of a comprehensive test ban. *Geophys. J. Int.*, **128**, 701–707, 1997.

Brune, J., A. Espinosa & J. Oliver. Relative excitation of surface waves by earthquakes and underground explosions in the California-Nevada region. *J. Geophys. Res.*, **68**, 3501–3513, 1963.

Cara, M. Filtering of dispersed wavetrains. *Geophys. J. R. Astron. Soc.*, **33**, 65–80, 1973.

Carpenter, E. W. Explosion seismology. *Science*, **147**, 363–373, 1965.

Chen, W.-P. A brief update on the focal depths of intra-continental earthquakes and their correlations with heat flow and tectonic age. *Seism. Res. Lett.*, **59**, 263–272, 1988.

Chen, W.-P. & P. Molnar. Focal depths of intracontinental and intraplate earthquakes and their implications for the thermal and mechanical properties of the lithosphere. *J. Geophys. Res.*, **88**, 4183–4214, 1983.

Chi, W.-C. & D. Dreger. Crustal deformation in Taiwan: Results from finite source inversions of six $M_w > 5.8$ Chi-Chi aftershocks. *J. Geophys. Res.*, **109**, B07305, 2004.

Chiarabba, C., P. D. Gori, L. Chiaraluce, P. Bordoni, M. Cattaneo, M. D. Martin, A. Frepoli, A. Michelini, A. Monachesi, M. Moretti, G. P. Augliera, E. D'Alema, M. Frapiccini, A. Gassi, S. Marzorati, P. D. Bartolomeo, S. Gentile, A. Govoni, L. Lovisa, M. Romanelli, G. Ferretti, M. Pasta, D. Spallarossa & E. Zunino. Mainshocks and aftershocks of the 2002 Molise seismic sequence, southern Italy. *J. Seis.*, **9**, 487–494, 2005.

Chouet, B. Dynamics of a fluid-driven crack in three dimensions by the finite difference method. *J. Geophys. Res.*, **91**, 13967–13992, 1986.

Chouet, B. & B. R. Julian. Dynamics of an expanding fluid-filled crack. *J. Geophys. Res.*, **90**, 11187–11198, 1985.

Choy, G. L. & J. Boatwright. Teleseismic and near-field analysis of the Nahanni earthquakes in the northwest territories, Canada. *Bull. Seismol. Soc. Am.*, **78**, 1627–1652, 1988.

Clarke, P. J., R. R. Davies, P. C. England, B. Parsons, H. Billiris, D. Paradissis, G. Veis, A. Cross, P. H. Denys, V. Ashkenazi, R. Bingley, M.-V. M. H.-G. Kahle and & P. Briole. Crustal strain in central Greece from repeated GPS measurements in the interval 1989-1997. *Geophys. J. Int.*, **135**, 195–214, 1998.

Clarke, P. J., D. Paradissis, P. Briole, P. England, B. Parsons, H. Billiris, G. Veis & J.-C. Ruegg. Geodetic investigation of the 13 May 1995 Kozani-Grevena (Greece) earthquake. *Geophys. Res. Lett.*, **24**, 707–710, 1997.

Cooley, J. & J. Tukey. An algorithm for the machine calculation of complex Fourier series. *Math. Comput.*, pages 297–301, 1965.

Custodio, S., P. Liu & R. J. Archuleta. The 2004 M_w6.0 Parkfield, California, earthquake: Inversion of near-source ground motion using multiple data sets. *Geophys. Res. Lett.*, **32**, L23312. doi:10.1029/2005GL024417, 2005.

Dahlen, F. A. Variation of gravity with depth in the Earth. *Phys. Rev.*, **D25**, 1735–1736, 1982.

Dahlen, F. A. & J. Tromp. *Theoretical Global Seismology.* Princeton University Press, 1998.

Dasgupta, S. & M. Mukhopadhyay. Seismicity and plate deformation below the Andaman arc, northeastern Indian Ocean. *Tectonophysics*, **225**, 529–542, 1993.

Demirtas, R., S. Karakisha & R. Yilmaz. The October 1, 1995 Dinar earthquake (M=5.9) in southwestern Turkiye. *Bull. Int. Inst. Seismol. Earthq. Eng.*, **30**, 45–58, 1996.

Dewey, J. W., G. Choy, B. Presgrave, S. Sipkin, A. C. Tarr, H. Benz, P. Earle & D. Wald. Seismicity associated with the Sumatra-Andaman Islands earthquake of 26 December 2004. *Bull. Seismol. Soc. Am.*, **97**, S25–S42, 2007.

Di Luccio, F., E. Fukuyama & N. Pino. The 2002 Molise earthquake sequence: What can we learn about the tectonics of southern Italy? *Tectonophysics*, **405**, 141–154, 2005.

Doser, D. I. & D. R. Yarwood. Deep crustal earthquakes associated with continental rifts. *Tectonophysics*, **229**, 123–131, 1994.

Douglas, A. Seismic source identification: a review of past and present research efforts. Technical report, in Identification of seismic sources - earthquake or underground explosion pp. 1-48, 1981.

Douglas, A., J. A. Hudson & V. K. Kembhavi. The analysis of surface wave spectra using a reciprocity theorem for surface waves. *Geophys. J. R. Astron. Soc.*, **23**, 207–223, 1971.

Doutsos, T. & I. Koukouvelas. Fractal analysis of normal faults in northwestern Aegean area, Greece. *J. Geodynamics*, **26**, 197–216, 1998.

Dziewonski, A., S. Bloch & M. Landisman. A technique for the analysis of transient seismic signals. *Bull. Seismol. Soc. Am.*, **59**, 427–444, 1969.

Dziewonski, A. M. & D. L. Anderson. Preliminary Reference Earth Model. *Phys. Earth Planet. Inter.*, **25**, 297–356, 1981.

Dziewonski, A. M., T.-A. Chou & J. H. Woodhouse. Determination of earthquake source parameters from waveform data for studies of global and regional seismicity. *J. Geophys. Res.*, **86**, 2825–2852, 1981.

Dziewonski, A. M. & A. L. Hales. Numerical analysis of dispersed seismic waves. *Meth. Comp. Phys.*, **11**, 39–85, 1972.

Dziewonski, A. M. & J. H. Woodhouse. An experiment in systematic study of global seismicity: centroid-moment tensor solutions for 201 moderate and large earthquakes of 1981. *J. Geophys. Res.*, **88**, 3247–3271, 1983.

Ebinger, C. J. Tectonic development of the western branch of the East African rift system. *Geol. Soc. Am. Bull.*, **101**, 885–903, 1989.

Ekström, G. & A. Dziewonski. The unique anisotropy of the pacific upper mantle. *Nature*, **394**, 168–172, 1998.

Ekström, G., J. Tromp & E. W. F. Larson. Measurements and global models of surface waves propagation. *J. Geophys. Res.*, **102**, 8137–8157, 1997.

Emmerson, B., J. Jackson, D. McKenzie & K. Priestley. Seismicity, structure and rheology of the lithosphere in the Lake Baikal region. *Geophys. J. Int.*, **167**, 1233–1272, 2006.

Engdahl, E. R., R. van der Hilst & R. P. Buland. Global teleseismic earthquake relocation with improved travel times and procedures for depth determination. *Bull. Seismol. Soc. Am.*, **88**, 3295–3314, 1998.

Engdahl, E. R., A. Villasenor, H. R. Deshon & C. H. Thurber. Teleseismic relocation and assessment of seismicity (1918-2005) in the region of the 2004 M_w 9.0 Sumatra-Andaman and 2005 M_w 8.6 Nias Island great earthquakes. *Bull. Seismol. Soc. Am.*, **97**, S43–S61, 2007.

England, P. & J. Jackson. Active deformation of the continents. *Annu. Rev. Earth. Planet Sci.*, **17**, 197–226, 1989.

Eyidogan, H. & A. Barka. The 1 October 1995 Dinar earthquake, SW Turkey. *Terra Motae*, **8**, 479–485, 1996.

Ferreira, A. M. G. Seismic surface waves in the laterally heterogeneous earth. Ph.D. thesis, University of Oxford, 2005.

Fitch, T. J. Earthquake mechanisms in the Himalayan, Burmese and Andaman regions and continental tectonics in Asia. *J. Geophys. Res.*, **75**, 2699–2709, 1970.

Foster, A. N. & J. A. Jackson. Source parameters of large African earthquakes: implications for crustal rheology and regional kinematics. *Geophys. J. Int.*, **134**, 422–448, 1998.

Fox, B. D. At what depths are the plates coupled at the Japanese subduction zones? Master's thesis, University of Oxford, 2001.

Frepoli, A. & A. Amato. Spatial variation in stresses in peninsular Italy and Sicily from background seismicity. *Tectonophysics*, **317**, 109–124, 2000.

Frohlich, C. Note concerning non-double-couple source components from slip along surfaces of revolution. *J. Geophys. Res.*, **95**, 6861–6866, 1990.

Frohlich, C. & K. D. Apperson. Earthquake focal mechanisms, moment tensors, and the consistency of seismic activity near plate boundaries. *Tectonophysics*, **11**, 279–296, 1992.

Fukushima, T., D. Suetsugu, I. Nakanishi & I. Yamada. Moment tensor inversion for near earthquakes using long-period digital seismograms. *J. Phys. Earth*, **37**, 1–29, 1989.

Gilbert, F. Excitation of the normal modes of the earth by earthquake sources. *Geophys. J. R. Astron. Soc.*, **22**, 223–236, 1970.

Hartse, H. E., A. A. Velasco & S. R. Taylor. Some interesting seismic events from western china. *21st Seismic Research Symposium*, pages 82–91, 1999.

Hatzfeld, D., V. Karakostas, M. Ziazia, G. Selvaggi, S. Leborgne, C. Berge, R. Guiguet, A. Paul, P. Voidomatis, D. Diagnourtas, I. Kassaras, I. Koutsikos, K. Makropoulos, R. Azzara, M. D. Bona, S. Baccheschi, P. Bernard & C. Papaioannou. The Kozani-Grevena (Greece) earthquake of 13 May 1995 revisited from a detailed seismological study. *Bull. Seismol. Soc. Am.*, **87**, 463–473, 1997.

Henry, C., J. H. Woodhouse & S. Das. Stability of earthquake moment tensor inversions: effect of the double-couple constraint. *Tectonophysics*, **356**, 115–124, 2002.

Herrin, E. & T. Goforth. Phase-matched filters: Application to the study of Rayleigh waves. *Bull. Seismol. Soc. Am.*, **67**, 1259–1275, 1977.

Huber, P. J. *Robust Statistics*. Wiley, 1981.

Hutchings, L., E. Ioannidou, W. Foxall, N. Voulgaris, J. Savy, I. Kalogeras, L. Scognamiglio & G. Stavrakakis. A physically based strong ground-motion prediction methodology; application to PSHA and the 1999 Mw = 6.0 Athens earthquake. *Geophys. J. Int.*, **168**, 659–680, 2007.

Inston, H. H., P. D. Marshall & C. Blamey. Optimisation of filter bandwidth in spectral analysis of wavetrains. *Geophys. J. R. Astron. Soc.*, **23**, 243–250, 1971.

Ishii, M., P. M. Shearer, H. Houston & J. E. Vidale. Extent, duration and speed of the 2004 Sumatra-Andaman earthquake imaged by the Hi-Net array. *Nature*, **435**, 933–936, 2005.

Kanamori, H. & D. L. Anderson. Importance of physical dispersion in surface wave and free oscillation problems: Review. *Rev. Geophys. Space. Phys.*, **15**, 105–112, 1977.

Kao, H. & J. Angelier. Stress tensor inversion for the Chi-Chi earthquake sequence and its implications on regional collision. *Bull. Seismol. Soc. Am.*, **91**, 1028–1040, 2001.

Kao, H. & W.-P. Chen. The Chi-Chi earthquake sequence: Active, out-of-sequence thrust faulting in Taiwan. *Science*, **30**, 2346–2349, 2000.

Kayal, J. R., S. G. Gaonkar, G. K. Chakraborty & O. P. Singh. Aftershocks and seismotectonic implications of the 13 September 2002 earthquake (M_w6.5) in the Andaman Sea Basin. *Bull. Seismol. Soc. Am.*, **94**, 326–333, 2004.

Kikuchi, M. & H. Kanamori. Inversion of complex body waves - III. *Bull. Seismol. Soc. Am.*, **81**, 2335–2350, 1991.

Kiratzi, A. & E. Louvari. Focal mechanisms of shallow earthquakes in the Aegean Sea and the surrounding lands determined by waveform modelling: a new database. *J. Geodynamics*, **36**, 251–274, 2003.

Kocyigit, A. Tectonics of Hoyran Lake (Isparta Bend) region (in turkish). *Turk. Jeol. Kurumu Bul.*, **26**, 1–10, 1983.

Kuge, K. & T. Lay. Data-dependent non-double-couple components of shallow earthquake source mechanisms: Effects of waveform inversion instability. *Geophys. Res. Lett.*, **21**, 9–12, 1994.

Landers, T. Some interesting central asian events on the $M_s : m_b$ diagram. *Geophys. J. R. Astron. Soc.*, **31**, 329–339, 1972.

Landisman, M., A. Dziewonski & Y. Sato. Recent improvements in the analysis of surface wave observations. *Geophys. J. R. Astron. Soc.*, **17**, 369–403, 1969.

Langbein, J., R. Borcherdt, D. Dreger, J. Fletcher, J. L. Hardebeck, M. Hellweg, C. Ji, M. Johnston, J. R. Murray, R. Nadeau, M. J. Rymer & J. A. Treiman. Preliminary report on the 28 September 2004, M 6.0 Parkfield, California, earthquake. *Seism. Res. Lett.*, **76**, 10–26, 2005.

Laske, G. & G. Masters. A global digital map of sediment thickness. *EOS Trans. AGU*, **78**, F483, 1997.

Lay, T., H. Kanamori, C. J. Ammon, M. Nettles, S. N. Ward, R. C. Aster, S. L. Beck, S. L. Bilek, M. R. Brudzinski, R. Butler, H. R. DeShon, G. Ekström, K. Satake & S. Sipkin. The great Sumatra-Andaman earthquake of 26 December 2004. *Science*, **308**, 1127–1133, 2005.

Levshin, A. L. & M. H. Ritzwoller. Automated detection, extraction, and measurement of regional surface waves. *Pure Appl. Geophys.*, **158**, 1531–1545, 2001.

Levshin, A. L., T. B. Yanovskaya, A. V. Lander, B. G. Bukchin, M. P. Barmin, L. I. Ratnikova & E. N. Its. *Seismic surface waves in a laterally inhomogeneous Earth*, chapter Recording, identification, and measurement of surface wave parameters, pages 131–182. Kluwer Academic Publisher, Dordrecht, 1989.

Liebermann, R. C., C. Y. Kinf, J. N. Brune & P. W. Pomeroy. Excitation of surface waves by the underground nuclear explosion LONGSHOT. *J. Geophys. Res.*, **71**, 4333–4339, 1966.

Liu, H. P., D. L. Anderson & H. Kanamori. Velocity dispersion due to anelasticity; implications for seismology and mantle composition. *Geophys. J. R. Astron. Soc.*, **47**, 41–58, 1976.

Longuet-Higgins, M. S. A theory of the origin of microseisms. *Phil. Trans. Roy. Soc. London*, **243**, 1–35, 1950.

Louvari, E. & A. Kiratzi. Source parameters of the September 7, 1999 Athens (Greece) earthquake from teleseismic data. *J. Balkan Geophysics. Soc.*, **43**, 51–60, 2001.

Maggi, A., J. A. Jackson, D. McKenzie & K. Priestley. Earthquake focal depths, effective elastic thickness, and the strength of the continental lithosphere. *Geology*, **28**, 495–498, 2000b.

Maggi, A., J. A. Jackson, K. Priestley & C. Baker. A reassessment of focal depth distributions in southern Iran, the Tien Shan and northern India: Do earthquakes really occur in the continental mantle? *Geophys. J. Int.*, **143**, 629–661, 2000a.

Marshall, P. D., E. W. Carpenter, A. Douglas & J. B. Young. Some seismic results of the LONGSHOT explosion. Technical report, AWRE Report No. 0-67/66, HMSO, London, 1966.

McCaffrey, R. & J. Nabelek. Earthquakes, gravity, and the origin of the Bali Basin: An example of a nascent continental fold-and-thrust belt. *J. Geophys. Res.*, **92**, 441–460, 1987.

McClusky, S., S. Balassanian, A. Barka, C. Demir, S. Ergintav, I. Georgiev, O. Gurkan, M. Hamburger, K. Hurst, H. Kahle, K. Kastens, G. Kekelidze, R. King, V. Kotzev, O. Lenk, S. Mahmoud, A. Mishin, M. Nadariya, A. Ouzounis, D. Paradissis, Y. Peter, M. Prilepin, R. Reilinger, I. Sanli, H. Seeger, A. Tealeb, M. N. Toksoz & G. Veis. Global Positioning System constraints on plate kinematics and dynamics in the eastern Mediterranean and Caucasus. *J. Geophys. Res.*, **105**, 5695–5720, 2000.

Mendiguren, J. A. Inversion of surface wave data in source mechanism studies. *J. Geophys. Res.*, **82**, 889–894, 1977.

Meyer, B., R. Armijo, D. Massonnet, J. B. de Chabalier, C. Delacourt, J. C. Ruegg, J. Achache, P. Briole & D. Papanastassiou. The 1995 Grevena (Northern Greece) earthquake: Fault model constrained with tectonic observations and SAR interferometry. *Geophys. Res. Lett.*, **23**, 2677–2680, 1996.

Molnar, P. & P. England. Temperatures, heat flux, and frictional stress near major thrust faults. *J. Geophys. Res.*, **95**, 4833–4856, 1990.

Mooney, W. D., G. Laske & T. G. Masters. Crust 5.1: A global crustal model at 5°5°. *J. Geophys. Res.*, **103**, 727–748, 1998.

Morelli, A., G. Ekström & M. Olivieri. Source properties of the 1997-98 Central Italy earthquake sequence from inversion of long-period and broad-band seismograms. *J. Seis.*, **4**, 365–375, 2000.

Muller, R. D., W. R. Roest, J. Y. Royer, L. M. Gahagan & J. Sclater. Digital isochrons of the world's ocean floor. *J. Geophys. Res.*, **102**, 3211–3214, 1997.

Nettles, M. & G. Ekström. Faulting mechanism of anomalous earthquakes near Bardarbunga Volcano, Iceland. *J. Geophys. Res.*, **103**, 17973–17984, 1998.

Nguyen, B. V. & R. B. Herrmann. Determination of source parameters for central and eastern North American earthquakes (1982-1986). *Seism. Res. Lett.*, **63**, 567–586, 1992.

Ni, S., H. Kanamori & D. Helmberger. Seismology: energy radiation from the Sumatra earthquake. *Nature*, **434**, 582–582, 2005.

Nissen, E., M. Ghorashi, J. jackson & B. Parsons. The 2005 Qeshm Island earthquake (Iran) - a link between buried reverse faulting and surface folding in the Zagros simply folded belt. *Geophys. J. Int.* doi:10.1111/j.1365-246X.2007.03514.x, 2007.

Nyblade, A. A. & C. Langston. East African earthquakes below 20 km depth and their implications for crustal structure. *Geophys. J. Int.*, **121**, 49–62, 1995.

Oncel, A. O., H. Koral & O. Altering. The Dinar earthquake (M_w = 6.2; October 1, 1995; Afton-Turkey) and earthquake hazard of the Dinar-Civil fault. *Pure Appl. Geophys.*, **152**, 91–105, 1998.

Panza, G. F. & A. Sarao. Monitoring volcanic and geothermal areas by full seismic moment tensor inversion: are non-double-couple components always artefacts of modelling? *Geophys. J. Int.*, **143**, 353–364, 2000.

Papadimitriou, P., N. Voulgaris, I. Kassaras, G. Aviaries, N. Delibasis & K. Makropoulos. The Mw = 6.0, 7 September 1999 Athens earthquake. *Natural Hazards*, **27**, 15–33, 2002.

Papadopoulos, G. A., G. Dramatise, D. Papanastassiou, I. Kalogeras & G. Stavrakakis. Preliminary results about the catastrophic earthquake of 7 September 1999 in Athens, Greece. *Seism. Res. Lett.*, **71**, 318–329, 2000.

Papazachos, B. C., B. G. Karakostas, A. A. Kiratzi, E. E. Papadimitriou & C. B. Papazachos. A model for the 1995 Kozani-Grevena seismic sequence. *J. Geodynamics*, **26**, 217–231, 1998.

Park, J.-O., T. Tsuru, S. Kodaira, P. R. Cummins & Y. Kaneda. Splay fault branching along the Nankai subduction zone. *Science*, **297**, 1157–1160, 2002.

Pasyanos, M. E., D. S. Dreger & B. Romanowicz. Toward real-time estimation of regional moment tensors. *Bull. Seismol. Soc. Am.*, **86**, 1255–1269, 1996.

Patton, H. J. Reference point method for determining the source and path effects of surface waves. *J. Geophys. Res.*, **82**, 889–894, 1977.

Patton, H. J. Bias in the centroid moment tensor for central Asian earthquakes: Evidence from regional surface wave data. *J. Geophys. Res.*, **103**, 26963–26974, 1998.

Patton, H. J. & G. Zandt. Seismic moment tensors of western U.S. earthquakes and implications for the tectonic stress field. *J. Geophys. Res.*, **96**, 18245–18259, 1991.

Pavlides, S. B., G. Papadopoulos & A. Ganas. The fault that caused the Athens September 1999 Ms = 5.9 earthquake: Field observations. *Natural Hazards*, **27**, 61–84, 2002.

Peacock, S. & A. Douglas. Two-stage rupture of the 1999 m_w 6.0 Southern Lake Baikal earthquake. *Geophys. J. Int.*, **in press**, 2007.

Pilant, W. L. & L. Knopoff. Observations of multiple seismic events. *Bull. Seismol. Soc. Am.*, **54**, 19–39, 1964.

Pinar, A. Source inversion of the October 1, 1995, Dinar earthquake (M_s = 6.1): a rupture model with implications for seismotectonics in SW Turkey. *Tectonophysics*, **292**, 255–266, 1998.

Pinar, A. & N. Turkelli. Source inversion of the 1993 and 1995 Gulf of Aqaba earthquakes. *Tectonophysics*, **283**, 279–288,. 1997.

Press, F., G. Dewart & R. Gilman. A study of techniques for identifying earthquakes. *J. Geophys. Res.*, **68**, 2909–2928, 1963.

Press, W. H., S. A. Teukolsky, W. T. Vetterling & B. P. Flannery. *Numerical Recipes in Fortran 77, The Art of Scientific Computing, 2nd ed.* Cambridge University Press, Cambridge, 1996.

Radziminovitch, N., J. Deverchere, V. Melnikova, V. San'kov & N. Giljova. The 1999 Mw 6.0 earthquake sequence in the southern Baikal rift, Asia, and its seismotectonic implications. *Geophys. J. Int.*, **161**, 387–400, 2005.

Rajendran, C. P., A. Earnest, K. Rajendran, R. D. Das & S. Kesavan. The 13 September 2002 North Andaman (Digilipur) earthquake: An analysis in the context of regional seismicity. *Cur. Sci.*, **84**, 919–924, 2003.

Resor, P. G., D. D. Pollard, T. J. Wright & G. C. Beroza. Integrating high-precision aftershock locations and geodetic observations to model coseismic deformation associated with the 1995 Kozani-Grevena earthquake, Greece. *J. Geophys. Res.*, **110**, B09402. doi: 10.1029/2004JB003263, 2005.

Rigo, A., J.-B. de Chabalier, B. Meyer & R. Armijo. The 1995 Kozani-Grevena (northern Greece) earthquake revisited: An improved faulting model from synthetic aperture radar interferometry. *Geophys. J. Int.*, **157**, 727–736, 2004.

Ritsema, J. & T. Lay. Rapid source mechanism determination of large (M(w) not less than 5) earthquakes in the western united states. *Geophys. Res. Lett.*, **20**, 1611–1614, 1993.

Ritsema, J., H. van Heijst & J. Woodhouse. Complex shear wave velocity structure imaged beneath Africa and Iceland. *Science*, **286**, 1925–1928, 1999.

Romanowicz, B. A global tomographic model of shear attenuation in the upper mantle. *J. Geophys. Res.*, **100**, 12,375–12,394, 1995.

Royden, L. Coupling and decoupling of crust and mantle in convergent orogens: Implications for strain partitioning in the crust. *J. Geophys. Res.*, **101**, 17679–17706, 1996.

Royden, L. H., B. C. Burchfiel, R. W. King, E. Wang, Z. Chen, F. Shen & Y. Liu. Surface deformation and lower crustal flow in eastern Tibet. *Science*, **276**, 788–790, 1997.

Rymer, M. J., J. C. T. III, J. A. Treiman, J. R. Arrowsmith, K. B. Clahan, A. M. Rosinski, W. A. Bryant, H. A. Snyder, G. S. Fuis, N. A. Toke & G. W. Bawden. Surface fault slip associated with the 2004 Parkfield, California, earthquake. *Bull. Seismol. Soc. Am.*, **96**, S11–S27, 2006.

Sargeant, S. L. P. W., A. Douglas & J. Evans. The source mechanism of the Athens earthquake, September 7, 1999, estimated from *p* seismograms recorded at long range. *Natural Hazards*, **27**, 35–45, 2002.

Selby, N. D., D. Bowers, A. Douglas, R. Heyburn & D. Porter. Seismic discrimination in Southern Xinjiang: The 13 March 2003 Lop Nor earthquake. *Bull. Seismol. Soc. Am.*, **95**, 197–211, 2005.

Shapiro, N. M. & M. H. Ritzwoller. Monte-Carlo inversion for a global shear-velocity model of the crust and upper mantle. *Geophys. J. Int.*, **151**, 88–105, 2002.

Shin, T.-C. & T. Teng. An overview of the 1999 Chi-Chi, Taiwan, earthquake. *Bull. Seismol. Soc. Am.*, **91**, 895–913, 2001.

Shumway, R. H. On detecting a signal in N stationary correlated noise series. *Technometrics*, **13**, 499–519, 1971.

Sieh, K. E. Slip along the San Andreas fault associated with the great 1857 earthquake. *Bull. Seismol. Soc. Am.*, **68**, 1421–1448, 1978.

Silver, P. G. Seismic anisotropy beneath the continents: Probing the depths of geology. *Annu. Rev. Earth. Planet. Sci.*, **24**, 385–432, 1996.

Sipkin, S. A. Estimation of earthquake source parameters by the inversion of wave-form data: synthetic seismograms. *Phys. Earth Planet. Inter.*, **30**, 242–259, 1982.

Sipkin, S. A. Estimation of earthquake source parameters by the inversion of waveform data: Global seismicity, 1981-1983. *Bull. Seismol. Soc. Am.*, **76**, 1515–1541, 1986.

Socquet, A., C. Vigny, N. Chamot-Rooke, W. Simons, C. Rangin & B. Ambrosius. India and Sunda plates motion and deformation along their boundary in Myanmar determined by GPS. *J. Geophys. Res.*, **111**(B05406). doi:10.1029/2005JB003877, 2006.

Stevens, J. L. & K. L. McLaughlin. Optimization of surface wave identification and measurement. *Pure Appl. Geophys.*, **158**, 1547–1582, 2001.

Taymaz, T., J. Jackson & D. McKenzie. Active tectonics of the north and central Aegean Sea. *Geophys. J. Int.*, **106**, 433–490, 1991.

Thio, H.-K. & H. Kanamori. Moment-tensor inversions for local earthquakes using surface waves recorded at TERRAscope. *Bull. Seismol. Soc. Am.*, **85**, 1021–1038, 1995.

Tichelaar, B. W. & L. J. Ruff. Seismic coupling along the Chilean subduction zone. *J. Geophys. Res.*, **96**, 11997–12022, 1991.

Tichelaar, B. W. & L. J. Ruff. Depth of seismic coupling along subduction zones. *J. Geophys. Res.*, **98**, 2017–2038, 1993.

Trampert, J. & J. H. Woodhouse. Global phase velocity maps of Love and Rayleigh waves between 40 and 150 seconds. *Geophys. J. Int.*, **122**, 675–690, 1995.

Tsai, V. C., M. Nettles, G. Ekström & A. M. Dziewonski. Multiple CMT source analysis of the 2004 Sumatra earthquake. *Geophys. Res. Lett.*, **32**(L17304). doi:10.1029/2005GL023813, 2005.

Tsai, Y.-B. Determination of focal depths of earthquakes in mid-oceanic ridges from amplitude spectra of surface waves. Ph.D. thesis, Mass. Inst. of Technol., Cambridge, 1969.

Tsai, Y.-B. & K. Aki. Precise focal depth determination from amplitude spectra of surface waves. *J. Geophys. Res.*, **75**, 5729–5743, 1970.

Tsai, Y.-B. & K. Aki. Amplitude spectra of surface waves from small earthquakes and underground nuclear explosions. *J. Geophys. Res.*, **76**, 3940–3952, 1971.

Tselentis, G.-A. & J. Zahradnik. The Athens earthquake of 7 September 1999. *Bull. Seismol. Soc. Am.*, **90**, 1143–1160, 2000.

Udias, A. *Principles of Seismology.* Cambridge University Press, 1999.

Utkucu, M., A. Pinar & O. Alptekin. A detailed slip model for the 1995, October 1, Dinar, Turkey, earthquake ($M_s = 6.1$) determined from inversion of teleseismic P and SH waveforms. *Geophys. J. Int.*, **151**, 184–195, 2002.

Vallee, M. & F. D. Luccio. Source analysis of the 2002 Molise, southern Italy, twin earthquakes (10/31 and 11/01). *Geophys. Res. Lett.*, **32**, L12309, 2005.

van der Vink, G. E. & J. Park. Nuclear test ban monitoring: New requirements, new resources. *Science*, **263**, 634–635, 1994.

von Herzen, R., C. Ruppel, P. Molnar, M. Nettles, S. Nagihara & G. Ekström. A constraint on the shear stress at the Pacific-Australian plate boundary from heat flow and seismicity at the Kermadec forearc. *J. Geophys. Res.*, **106**, 6817–6833, 2001.

Wallace, T. C. A reexamination of the moment tensor solutions of the 1980 mammoth lakes earthquakes. *J. Geophys. Res.*, **95**, 11171–11176, 1985.

Warren, L. M. & P. M. Shearer. Using the effects of depth phases on p-wave spectra to determine earthquake depths. *Bull. Seismol. Soc. Am.*, **95**, 173–184, 2005.

Weidner, D. J. & K. Aki. Focal depth and mechanism of mid-ocean ridge earthquakes. *J. Geophys. Res.*, **78**, 1818–1831, 1973.

Wiens, D. A. & S. Stein. Age dependence of oceanic intraplate seismicity and implications for lithospheric evolution. *J. Geophys. Res.*, **88**, 6455–6468, 1983.

Woodhouse, J. H. Surface waves in a laterally varying layered structure. *Geophys. J. R. Astron. Soc.*, **37**, 461–490, 1974.

Woodhouse, J. H. *Seismological Algorithms*, chapter The calculation of eigenfrequencies and eigenfunctions of the free oscillations of the Earth and Sun, pages 321–370. Academic Press, San Diego, CA, 1988.

Wright, T. J., B. E. Parsons, J. A. Jackson, M. Haynes, E. J. Fielding, P. C. England & P. J. Clarke. Source parameters of the 1 October 1995 Dinar (Turkey) earthquake from SAR interferometry and seismic bodywave modelling. *Earth Planet. Sci. Lett.*, **172**, 23–37, 1999.